Direct Numerical Simulations of Shock Trains

Doctoral Thesis

Alexander Gillespie

AERODYNAMICS & FLIGHT MECHANICS
UNIVERSITY OF SOUTHAMPTON

Submitted in Fulfilment of the
Requirements for the Degree of
Doctor of Philosophy

June 2021

Abstract

Shock wave boundary layer interactions (SBLIs) are physical phenomena which occur in many applications of supersonic flow. One particular category of SBLI involves systems of linked shock waves which are arranged within an enclosed duct or channel (such as the internal flow through the inlet of a supersonic engine). Shock trains - as these SBLI structures are known - are the primary focus of this work. In particular, the results of direct numerical simulations (DNS) and implicit large eddy simulations (ILES) of shock trains are presented here in order to provide insights into their behaviour. Simulations are performed with a freestream Mach number of 2.0 and a baseline inflow Reynolds number (based on momentum thickness) of 500.

The first part of the research involves a detailed validation of the underlying numerical methods. By considering the development of the turbulent boundary layer and formation of the shock train for different grid resolutions and numerical methods we are able to quantify uncertainties in the results. The internal structure of the shock train is found to be less sensitive than its equilibrium location. Following this, a detailed parameter study considers the effect of back pressure, Reynolds number and boundary layer confinement. These parameters are found to have very little effect on the internal structure shock train, including the angle of the leading shock which occurs at the limit of a Mach reflection (between 40° and 43°). By studying the effects of spanwise confinement we are able to show that the sidewalls reduce the strength of the individual shocks, resulting in a lower wall pressure gradient and the shock train length being approximately doubled. This effect is not fully explained by the blockage of the sidewall boundaries. Comparing the wall pressure results of each case with an established empirical model finds generally good agreement.

The final part is devoted to investigating the time-dependent behaviour of shock trains. By subjecting shock trains to step changes in back pressure we are able to characterise the response. When correcting for back pressure lag effects we find that the response speed of the leading shock wave is largely independent of the initial conditions and direction of pressure change. The initial response is primarily governed by the back pressure step size, although spanwise confinement also plays an important role. Sinusoidal back pressures are applied to the shock train which allows us to show that, due to a filtering effect, lower forcing frequencies cause larger shock oscillation amplitudes. Back pressure changes are propagated upstream via the subsonic region at approximately Mach 0.3 and the resulting forcing/response lag causes an upstream shift in average shock position, such that the shock train length can be up to 35% higher on average. Lastly, a detailed spectral analysis of the shock train wall pressure reveals a number of flow features including a region of low frequency oscillation below the leading shock.

Acknowledgements

Firstly, I would like to express my sincere appreciation to my supervisor, Prof. Neil Sandham, for his advice and guidance throughout the course of this project. I must acknowledge the financial support and reliable feedback of MBDA UK, with special thanks to Dr. Scott Shaw. I would like to acknowledge both the UK Turbulence Consortium (2018 & 2019 allocations) and the Cambridge Service for Data Driven Discovery (EPSRC Tier-2 capital grant EP/P020259/1) for providing computational time for this project. For their valuable assistance near the start of my degree, I must thank Dr. Satya Jammy and Dr. David Lusher. I am grateful to my viva examiners, Prof. Yufeng Yao and Dr. Zhiwei Hu, for their reviewing efforts and excellent feedback. Finally, I would like to pay gratitude to my girlfriend, Eleanor, and to my family for their ongoing love and support.

A.G.
Glasgow, 10th June 2021.

Declaration of Authorship

I, Alexander Gillespie, declare that the thesis entitled *Direct Numerical Simulations of Shock Trains* and the work presented in the thesis are both my own, and have been generated by me as the result of my own original research. I confirm that:

- This work was done wholly or mainly while in candidature for a research degree at the University of Southampton.
- Where any part of this thesis has previously been submitted for a degree or any other qualification at this University or any other institution, this has been clearly stated.
- Where I have consulted the published work of others, this is always clearly attributed.
- Where I have quoted from the work of others, the source is always given. With the exception of such quotations, this thesis is entirely my own work.
- I have acknowledged all main sources of help.
- Where the thesis is based on work done by myself jointly with others, I have made clear exactly what was done by others and what I have contributed myself.
- Aspects of this work have been included in the following papers intended for publication:
  - A. Gillespie and N. D. Sandham, "Shock train response to high frequency back pressure forcing", *AIAA Journal*, submitted.
  - A. Gillespie and N. D. Sandham, "Numerical study of the effect of side-walls on shock train behaviour", in preparation.

Signed:

_____

Date:

_____

Contents

List of Figures

List of Tables

List of Symbols and Abbreviations

Latin Symbols

a	Fluctuation amplitude matrix
B	Blockage
C	Sutherland constant
c	Local speed of sound
C_f	Coefficient of skin friction
C_T	TENO scheme cut-off parameter
E	Total energy
F	Frequency, two-point correlation function
F, f	Flux term
H	Duct/channel height
h	Duct/channel half-height
I	Integral length scale
i, j, k	Index values
L, l	Length
L_{sep}	Separation length
l_{ST}	Shock train length
M	Mach number

N, n	Number of grid points
p	Pressure
p_b	Back pressure
Pr	Prandtl number
q	Heat flux
R	Specific gas constant, Reynolds stress tensor
r	Normally-distributed random number
Re	Reynolds number
S	Distance from shock train leading edge
St	Strouhal number
T	Temperature
t	Time
T_0	Period of oscillation
t_0	Time of back pressure change (§6 only)
t_1	Leading shock lag time (§6 only)
u, v, w	Velocity components
u^*	Unscaled velocity fluctuations
u_τ	Friction velocity
W	Duct/channel width
x, y, z	Cartesian coordinates
x_1	Initial leading shock position (§6 only)

Greek Symbols

α	Flow deflection angle
β	Shock angle, grid stretching factor

δ^*	Displacement thickness
δ_{99}	Boundary layer thickness
γ	Heat capacity ratio
κ	Von Kármán constant
μ	Dynamic viscosity
ω	Vorticity
ϕ, ψ	Intermediate correlation variables
ρ	Density
τ	Stress tensor
θ	Momentum thickness

Abbreviations

AR	Aspect ratio
BC	Boundary condition
BP	Back pressure
CDNS	Coarse direct numerical simulation
CFD	Computational fluid dynamics
CPU	Central processing unit
CUDA	Compute unified device architecture (Nvidia)
DNS	Direct numerical simulation
FIT	Free interaction theory
FTT	Flow through time
GPU	Graphics processing unit
HPC	High performance computing
ILES	Implicit large eddy simulation

LES	Large eddy simulation
MPI	Message passing interface
OPS	Oxford parallel structured software
PIV	Particle image velocimetry
PSD	Power spectral density
RANS	Reynolds-averaged Navier-Stokes
RK	Runge-Kutta
RMS	Root mean square
SBLI	Shock wave boundary layer interaction
TBL	Turbulent boundary layer
TENO	Targeted essentially non-oscillatory
WENO	Weighted essentially non-oscillatory
WPSD	Weighted power spectral density

Subscripts

1	Inlet conditions
2	Conditions at shock train leading edge
3	Conditions at first shock
∞	Freestream value
bl	Boundary layer
$c, comp$	Compressible
e	boundary layer edge value
i, inc	Incompressible
i, j, k	Nested indices
m	Lower boundary condition

p	Upper boundary condition
r, ref	Dimensional reference value
$T, total$	Total/stagnation value
vd	Van Driest-transformed value
$w, wall$	Wall value

Superscripts

$'$	Fluctuating component
$*$	Sonic condition
$+$	Viscous wall unit

Chapter 1

Introduction

1.1 Motivation

THE STUDY of supersonic flow serves to aid in the design and maintenance of supersonic aircraft, spacecraft and missiles. The interaction of supersonic air and solid boundaries involves highly complicated turbulent flow structures which must be well understood in order to ensure that such vehicles can operate successfully in this environment. The body of research on internal supersonic flow is mainly concerned with shock wave boundary layer interactions (SBLIs) due to their ubiquity and consequences for pressure and thermal loading, where mistakes or misunderstandings can be catastrophic. Figure 1.1 shows a sketch of a scramjet engine, demonstrating the typical SBLI structures which may exist in the internal flow of a supersonic vehicle. The diagram is based on the NASA X-43 experimental scramjet (see figure 1.2) which was designed to operate at around Mach 7.

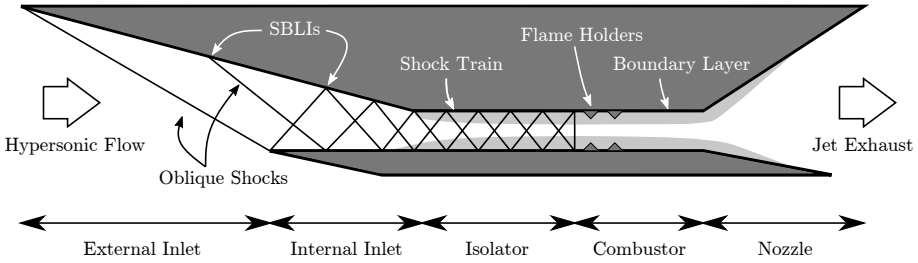

FIGURE 1.1: Schematic diagram of a typical scramjet propulsion system.

Each section of the engine where supersonic or hypersonic flow occurs has a number of SBLIs associated with it, although the majority of the interactions occur within the first three sections where the flow compression occurs. The inlet sections provide the initial compression via oblique shock waves generated from the angular

surfaces. The isolator section further compresses the flow with a series of reflected shocks (referred to as a shock train) and guards against instabilities from the combustion process reaching the inlet. It is the isolator section of the engine that this project is concerned with. In particular, this project is focused on numerical simulations of shock trains within straight, constant-area, rectangular ducts that represent a canonical configuration for studying the physical phenomena.

FIGURE 1.2: Artistic render of the NASA X-43A hypersonic vehicle (courtesy of NASA).

1.2 Objectives

Shock trains are the focus of a considerable amount of scientific research and their behaviour is reasonably well-documented. There remains, however, much to be understood regarding, the boundary layer confinement effects, dynamic back pressure effects, and the flow physics underpinning the behaviour of shock trains. It is these problems that this project attempts to understand. The main objectives for the project are listed below:

1. Develop and characterise eddy resolving (DNS or near DNS) simulations of shock trains.

2. Better understand the unique effect of sidewalls and spanwise confinement.

3. Provide a detailed examination of other governing parameters (back pressure, Reynolds number, confinement ratio).

4. Gain an insight into the time-dependent shock train behaviour, particularly via back pressure forcing.

1.3 Thesis Outline

This thesis is comprised of seven chapters, including three research chapters. Chapter 2 documents the historical context and state-of-the-art knowledge on shock trains and SBLIs, with a focus on relevance to the current work. In chapter 3 we describe in detail the computational methods used to run the simulations - including the code, grid meshes and boundary conditions.

In chapter 4 we present validations of the code, boundary conditions, grid refinement and numerical scheme. This fulfils the first objective of the research project. Such is the computational cost of running these kind of simulations, only a few examples currently exist in the published literature. The validation process also ensures the reliability of the simulations in latter chapters.

While the main governing parameters of shock trains are generally well understood, they are rarely studied in the level of detail or numerical accuracy that is afforded by the current simulations. Therefore, chapter 5 contains a number of parametric studies, providing detailed examinations of the effects of back pressure, Reynolds number, confinement ratio on the shock train behaviour. One of the lesser-understood aspects of shock trains is the unique effects of the sidewalls and this problem is addressed in this chapter where we compare shock trains in finite- and infinite-span ducts. Additional sections in this chapter are devoted to: analysing the use of a double symmetry condition for modelling ducted supersonic flow; comparing the results of the parameter studies to a commonly-used semi-empirical model; and providing detailed a examination of the shock train structure.

Chapter 6 is the final research chapter and is focused on the physics governing the dynamic behaviour of the shock train. In this chapter we are able to study and characterise the response of the moving shock train to different time-dependent back pressures (step increases, step decreases and sinusoidal waveforms). Additionally, we provide a simple 1D model for the dynamic shock response and perform a Fourier analyses of both static and oscillating shock trains. The overall conclusions of the research and suggestions for future work are given in chapter 7.

1.4 Key Contributions

In regard to the project objectives, the main contributions to the field of supersonic gas dynamics are listed below:

- Efficient generation of turbulent boundary layers on highly parallelised codes through improvements to an existing turbulence generation algorithm.

- Development of a sponge zone boundary condition to allow for a back pressure to be applied to a ducted flow.
- Development of a set of implicit large eddy simulation (ILES) test cases for studying shock train behaviour at relatively low computational cost.
- A detailed parameter study evaluating the effects of Back pressure, Reynolds number and boundary layer confinement on the shock train structure. We find that the shock spacing and the shape of the supersonic region is highly conserved for the range of parameters studied. Additionally, in each case, the leading shock angle occurs at or near to the Mach reflection limit (between 40° and 43°.
- A study of the effect of sidewalls on shock train structure. In the present configuration, the sidewalls have a very strong effect on the length and internal structure of the shock train. We propose that the sidewalls reduce the strength of the individual shock waves, thereby reducing the overall pressure gradient through the shock train which must then be longer to accommodate the same pressure rise.
- A characterisation and study of the effect of back pressure step forcing. The shock train response his highly dependent on the size of the pressure change and there is a strong degree of symmetry between step up and step down scenarios. We find when there are sidewalls, the response is slower but only in the case where the back pressure is stepped down.
- A study of the effect of sinusoidal back pressure forcing at a range of frequencies. The Response is highly frequency depended given that higher frequency disturbances are much more easily dissipated as they move through the turbulence mixing region. The forcing-response time lag plays a very important role and appears to be responsible for an upstream offset in the average shock positions. We observe a region of natural low frequency motion at the foot of the leading shock which becomes excited by the lowest forcing frequency.

The following journal papers have been generated as a result of the research conducted:

- A. Gillespie and N. D. Sandham, "Shock train response to high frequency back pressure forcing", *AIAA Journal*, submitted.
- A. Gillespie and N. D. Sandham, "Numerical study of the effect of sidewalls on shock train behaviour", in preparation.

Chapter 2

Literature Review

2.1 Historical Context

Shock wave reflections on solid boundaries were observed as early as 1875 by Ernst Mach, although it wouldn't be for another 65 years that the interaction between shocks waves and boundary layers themselves would be first documented. This is most commonly attributed to Ferri (1940) with similar observations being made in subsequent years by, for example, Liepmann (1946), Ackeret et al. (1947) and Fage and Sargent (1947). These early studies involved wind tunnel experiments looking at transonic flow over aerofoil surfaces and hence the recorded SBLIs existed within the limited pockets of supersonic flow. In order to conduct a more systematic approach to studying these phenomena, investigations in following years were conducted in straight, rectangular wind tunnel sections at purely supersonic speeds. Examples of such studies are found in Bardsley and Mair (1951), Barry (1951) and Liepmann et al. (1951).

These experimental arrangements provide the main canonical layouts still utilised in the majority of SBLI work today; namely straight, rectangular sections with external shock generators, ramps and steps. The main rationale for this is that flow in this arrangement is (in theory) mostly two-dimensional, in that there is limited variation in conditions along the spanwise direction (the z-direction in the Cartesian frame). This idea helps to simplify the flow field and allow for better generalisations and better consistency between studies. It is worth noting that many working supersonic inlets developed in the 20th century have shared this basic geometry (for example the rectangular inlets on the Aérospatiale/BAC Concorde or Grumman F-14 Tomcat).

Probably the earliest recorded instance of a shock train was in a study by Neu-

mann (1949) who considered the behaviour of normal shock waves within internal pipe flow. Although it was expected that there would be a very sudden pressure rise over a single shock wave, it was observed instead that the pressure rose gradually, occurring over 8-12 pipe diameters. The presence of multiple shocks was noted by both Lukasiewicz (1953) and Shapiro (1953), with the latter describing "a series of bifurcated normal shocks". It was around this time that the term "pseudo-shock" was first used to describe the shock train (Crocco, 1958) due to the fact that the pressure rise at the wall resembled that of more typical forms of SBLI.

Wind tunnel research on SBLIs and shock trains over the past 80 years has undergone clear long-term cycles whereby improvements in experimental technology have led to fresh insights into the flow structure and therefore better understanding of the physics governing SBLIs. A non-exhaustive list of examples is as follows:

- Developments in schlieren and shadowgraph imagery delivered better visualisation of SBLIs and detailed characterisations from a side-on perspective. This led to, for example, the development of the Free Interaction Theory by Chapman et al. (1958).
- The introduction of high-frequency pressure transducers in the 1960s meant that researchers could observe the inherent unsteadiness of SBLIs (e.g. Kistler, 1964), a feature that was not apparent until then and still forms a significant area of interest to this day.
- Surface flow visualisation methods, which use special formulae of oil to trace out the streamlines on wind tunnel walls, are able to provide valuable information on the 3D flow patterns at the surface (see for example Reda and Murphy, 1973).
- Developments in recent decades in particle image velocimetry (PIV) and stereo PIV which track the motion of suspended particles in the wind tunnel flow has allowed researchers to observe in high-definition the two-dimensional and three-dimensional flow fields and has brought new information on the structure of SBLIs (see Ganapathisubramani et al., 2007; Humble et al., 2009).

Current research on shock interactions conducted in supersonic wind tunnels make use of several (if not all) of these methods in different combinations to analyse the flow structure. Yet, that still often leaves limitations should a researcher want to know the flow conditions at any given point. In addition, wind tunnel experiments (despite having run times of around a minute or less) can incur large operational

costs and the lack of such experimental facilities puts a limit on the amount of research that can be conducted at any given time.

The limitations of wind tunnel testing can be addressed, in part, by eddy-resolving simulations which are able to capture the full time-history of the entire flow field. Running simulations is limited by the availability of generic-use HPC (high performance computing) systems rather than that of purpose-built facilities. In recent decades the processing capacity of computers has risen exponentially, thereby making it much easier and far cheaper to run large simulations. Currently (as of November 2020), the highest capacity HPC systems are capable of delivering a peak performance of $10 - 100$ petaflops ($10^{16} - 10^{17}$ floating point operations per second). This continual improvement in performance has meant that researchers are able to simulate SBLIs in 3D, capturing the surrounding flow field in sufficient resolution to perform large eddy simulations (LES) and even direct numerical simulations (DNS).

Despite some initial scepticism as to whether supersonic flow fields could be accurately simulated, it was observed in 1979 by Horstman and Hung (1979), in the first detailed study of its type, that simulations were able to accurately predict flow properties (such as Mach number, pressure, velocity) when compared to recorded experimental data. Since then, the development of sub-grid scale turbulence models and shock-capturing numerical schemes has improved the accuracy of numerical work (Dolling, 2001). In addition, improvements in processor speeds and memory capacity allows for increasingly high mesh densities which greatly increases the accuracy of the simulation as well as providing much richer data fields for analysis. As an illustration: the simulations conducted by Horstman and Hung (1979) used a total of 21,000 grid points compared to contemporary studies which may use around 100-1000 million grid points for a similar configuration.

The computational domains considered by contemporary work on SBLIs generally follow the same canonical layouts used in wind tunnels: straight rectangular sections. Most studies aim to try and replicate wind tunnel conditions by introducing boundary layers and particular geometric features (such as ramps or steps). This is the general arrangement of the cases studied in this project.

2.2 Shock Wave Boundary Layer Interactions

In this section, we will discuss classical SBLIs, where boundary layers interact with only one shock wave. Although the focus of this project is on systems of shock waves, the wider context of SBLI research is key to the understanding of shock trains.

Classical SBLIs can be categorised in a number of ways but the most fundamental difference is the type of shock wave the boundary layer interacts with: normal or oblique. Oblique SBLIs can be categorised further as incident-reflected, swept, ramp-induced, and forward-facing step-induced (Babinsky and Harvey, 2011). Four of these canonical types are illustrated in figure 2.1 within the context of a supersonic compression intake which induces a shock train in order to compress the flow.

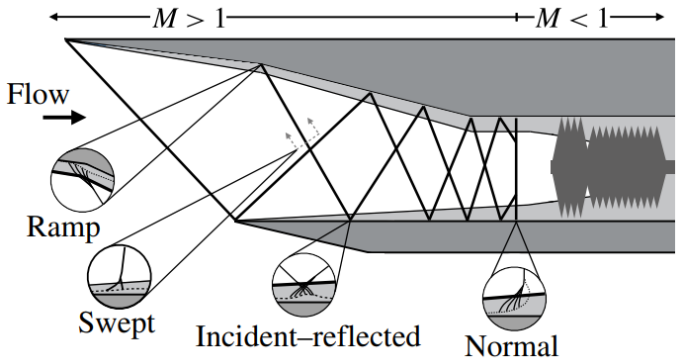

FIGURE 2.1: Diagram depicting the various types of SBLI (Grossman and Bruce, 2018) and where they are typically found in a supersonic inlet. The detailed view of the swept SBLI considers the boundary layer on the sidewall.

2.2.1 Normal SBLI

Normal shock waves are defined by the fact that they impart no deflection on the flow (unlike oblique shocks). They fully decelerate the flow to subsonic speeds and occur usually due to the presence of an imposed back pressure (such as a downstream throat in a supersonic wind tunnel). Figure 2.2 shows a schlieren photograph of such an interaction alongside a sketch detailing the main flow features.

Due to the large pressure rise over a very short distance, the shock wave exerts a strong adverse pressure gradient on the boundary layer which encourages viscous dissipation and therefore a tendency for the boundary layer to thicken across the SBLI as shown in the sketch. The pressure gradient often causes the flow to separate, as in in the example on the right where the flow separates at point **S** and reattaches at point **R**. The separation/thickening of the boundary layer causes a series of weak compression waves, which begin to form at the sonic line and coalesce into the oblique shock ($\boldsymbol{C_1}$) which itself meets the main normal shock ($\boldsymbol{C_3}$) at the triple point **I**. In order to satisfy the flow deflection criteria, there is an additional

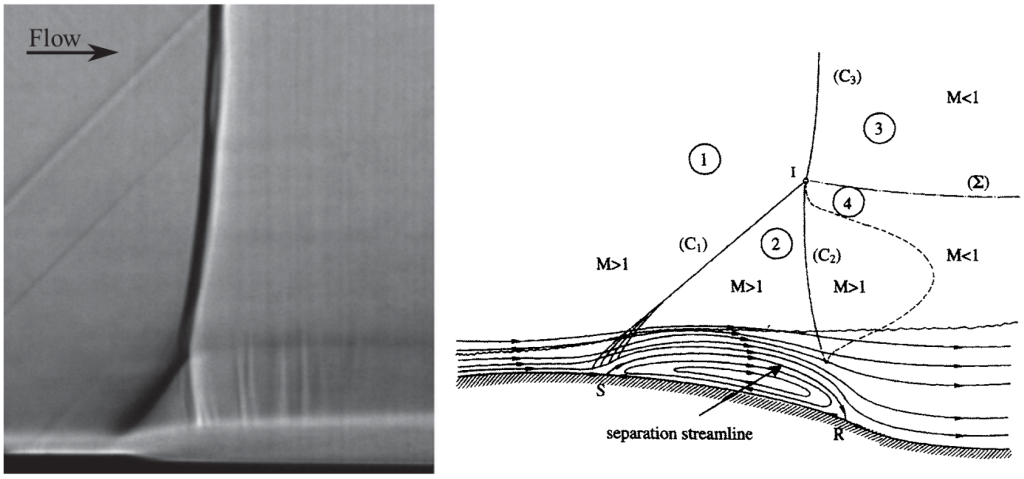

FIGURE 2.2: Schlieren photograph (Bruce et al., 2011) and sketch (Ben-Dor et al., 2001) of a normal SBLI. The regions highlighted are as follows: (1) - freestream; (2) - inter-shock region; (3) - post-shock flow; (4) - post-interaction flow.

trailing shock, $\boldsymbol{C_2}$, as well as a post-shock slip line (Σ). The flow downstream of the interaction is subsonic although it is often re-accelerated above Mach 1 within a short distance.

Most normal shock waves are not purely normal in the strictest sense but in fact have a slight but noticeable curvature towards boundaries (due to the presence of the SBLI). The curvature is usually not significant enough to impart any meaningful flow deflection outside of the boundary layer, however the transverse flow velocity near the boundary layer can lead to pockets of re-accelerated supersonic flow.

Since the location of normal SBLIs is not constrained by physical geometry, their position is highly unsteady. This is exacerbated by the fact that the flow downstream is subsonic and is therefore capable of transmitting disturbances upstream - commonly leading to unstable feedback loops. Most experiments and simulations induce the normal shock by means of downstream blockage or back pressure and slight changes to these arrangements will cause the shock wave to move as it adjusts its effective Mach number to meet the new conditions (Bruce and Babinsky, 2008). Experimental studies of this type in supersonic wind tunnels require the implementation of flow control methods in order to keep the shock wave in place (e.g. Bruce et al., 2011).

2.2.2 Oblique SBLI

Oblique shock waves are caused by a sudden flow deflection in supersonic flow. The flow deflection can be come from a number of different causes, but they are generally classified as being induced by ramps (sharp changes in boundary angle), steps (sudden jumps in boundary height) or pressure changes (such as the confluence of internal and external flows at the mouth of an aircraft engine nozzle). In this section we are concerned with the most common type of oblique SBLI: the incident-reflected SBLI where an oblique shock (usually generated by a ramp) comes into contact with a solid boundary.

Two depictions of such interactions are shown in figure 2.3. As in the inviscid case of shock reflections, the flow deflection downstream of the incident shock must be corrected with a second (reflected) shock when it meets a solid surface. Unlike the inviscid case, however, the flow structure is complicated by the viscous and subsonic flow of the inner boundary layer. The sharp pressure rise across the incident shock causes viscous dissipation to increase, creating a thickened boundary layer (as with the normal SBLI) as well as a temporary thickening of the subsonic region. Downstream of the interaction the flow relaxes back to a steady state but with a larger boundary layer thickness and generally a lower shape factor (defined as $H = \delta^*/\theta$ where δ^* and θ are the displacement and momentum thicknesses).

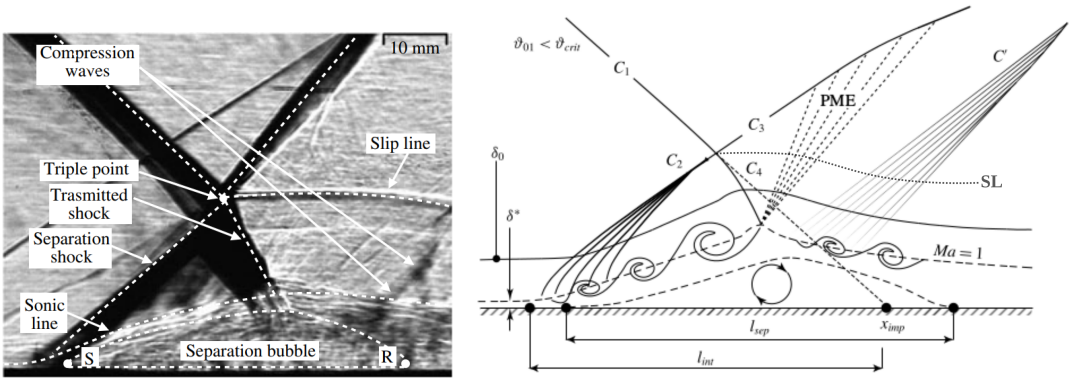

FIGURE 2.3: Annotated schlieren image of an oblique SBLI (Grossman and Bruce, 2018) with a corresponding sketch (adapted from Matheis and Hickel, 2015) showing key flow features.

As the intensity of the incident shock (and hence the adverse pressure gradient) increases, the boundary layer reaches a point where flow nearest the wall will reverse, causing it to separate from the wall. Both images in figure 2.3 show a shock-induced separation caused by an incident oblique shock. The separation occurs at point **S**

followed by a reattachment at point **R**. In both the separated and non-separated cases, the boundary layer thickening leads to a series of compression waves which together form the separation shock ($\boldsymbol{C_2}$) which itself becomes the transmitted shock ($\boldsymbol{C_3}$) after the shock-shock interaction with the incident shock. At the shock-shock interface, continuity in all properties is maintained except for the streamwise velocity. This discontinuity gives rise to a slip line (**SL**) which follows the path of the streamlines. At the point where the incident shock ($\boldsymbol{C_1}$) meets the separation bubble, it is reflected as a Prandtl-Meyer expansion wave (**PME**) due to the need to satisfy continuity at the sonic boundary. As the velocity on the dividing streamline (limit of the separation bubble) increases, the flow eventually reattaches to the solid boundary - this requires another flow deflection, giving rise to the reattachment shock ($\boldsymbol{C'}$). As with the normal SBLI, the downstream equilibrium boundary layer is considerably thicker, with its velocity profile distributed away from the wall.

Figure 2.4 shows how the wall pressure varies in x over the incident-reflected SBLI. It is clear that there are two distinct pressure rises, one each from the separation and reattachment shocks, leading to a pressure rise of Δp_T over the whole interaction region. The reduction in pressure after the peak in pressure is due to the expansion wave caused by the trailing edge of the shock generator. One important finding in SBLI research has been the discovery of Free-Interaction Theory (FIT) by Chapman et al. (1958). FIT states that the pressure rise up to the point of separation is dependent only on the conditions at that point, and is independent of any downstream conditions. This finding has been tested and appears to hold true for a wide variety of conditions (Babinsky and Harvey, 2011, chapter 2).

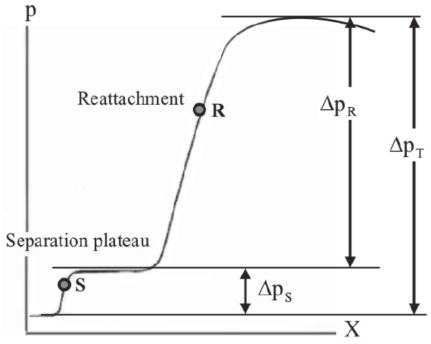

FIGURE 2.4: Typical distribution of wall pressure across an oblique SBLI (Babinsky and Harvey, 2011). Typically, the majority of the pressure rise is due to the reattachment shock.

Although some experiments and simulations have made the assumption that SBLI behaviour within finite ducts (i.e. the sidewalls are resolved) is fully 2D, this

is now considered untrue, especially for highly confined ducts. The presence of the sidewalls introduces two particularly important flow features (shock interaction with the sidewall boundary; corner separations) which cause the flow to be highly three-dimensional, even affecting the flow at the centreline. Wang et al. (2015) performed a detailed LES study on the sidewall effects and found that the physical structure of the SBLI was greatly altered near the corners. Additionally, the sidewalls were able to increase the streamwise extent of the shock-induced separation by around 30% when compared to a infinite-span arrangement. It has been suggested by Babinsky et al. (2013) that the corner separation regions (occurring further upstream of the main SBLI) create their own compression waves which meet near the centreline, thereby affecting the shock strength of the core interaction (and by implication, the size of the interaction).

2.3 Shock Trains

2.3.1 Overview

A shock train is a common phenomenon found in internal supersonic flows and occurs when a series of shocks occur in sequence. These shock systems can form in a wide variety of situations and hence are the focus of a considerable amount of scientific research. One particular type of shock train occurs when a series of incident-reflected SBLIs exist within a sufficiently long channel where shocks are successively reflected off opposing walls (this is the compression mechanism that is found in many supersonic compression intakes). Another class of shock train (and the type which this project is concerned with) involves a series of normal or oblique shock waves in constant area ducts where the shocks form due to a combination of an imposed back pressure and high level of boundary layer confinement (thickness of the boundary layer relative to the duct height). This particular case is common in the isolator section of scramjet engines where the flow is compressed ahead of the combustor.

It is well known from classical aerodynamics that a normal shock is created when a strong back pressure applied to supersonic channel flow. However, given sufficient confinement ratio (boundary layer thickness divided by duct half-height: δ_{99}/h) and a sufficiently high Mach number (typically $M > 1.5$), the presence of the SBLI will cause the shock to bifurcate, forming an additional shock further downstream. Increasing the confinement or Mach number further will cause even more shocks, which then comprise a shock train.

The shock train structure is illustrated in figure 2.5 which shows a series of shocks within a confined constant-area channel. As expected, the initial shock immediately causes the boundary layer to thicken and separate, forming a normal SBLI with the familiar λ shape. However, the reflection of the trailing shock on the subsonic boundary creates an expansion wave which re-accelerates the core flow above Mach 1. The reflection of this expansion on the opposing wall then causes another shock to form, and the process then repeats. This continues, with successively weaker shocks, until either the subsonic layer reaches the centreline of the channel or the imposed exit pressure conditions are reached. Depending on the shock train structure, the flow at the very centreline can become subsonic earlier than flow closer to the region - as seen in the mixing region in figure 2.5. This occurs due to the stronger stagnation pressure losses associated with the normal shock near the centre of the channel.

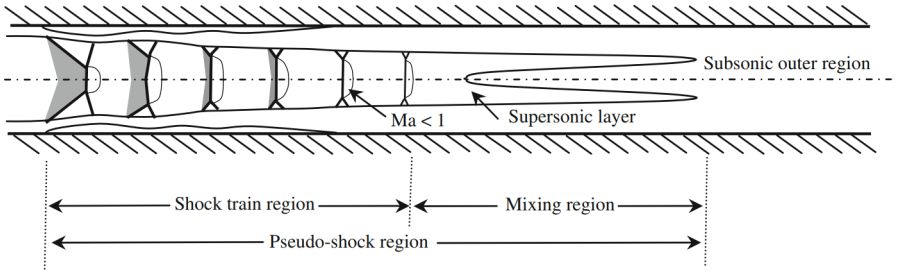

FIGURE 2.5: Illustration of a shock train system showing the gradual flow compression and distinction between supersonic (core) and subsonic (outer) regions (Weiss et al., 2010).

An important feature of shock trains is the strong distinction between the supersonic and subsonic layers. The supersonic layer is characterised by repeated accelerations and decelerations through shocks and expansions, while the subsonic layer is a highly turbulent region of flow with considerable mixing and viscous interaction. This difference is most stark when comparing the pressure measurements at the centreline (where the pressure change is highly oscillatory) and at the wall (where there is a gradual pressure rise). Since the wall pressure rise is comparable to that of typical SBLI, shock trains are often referred to as *pseudoshocks*, however the pressure gradients involved are generally much lower.

Each of the shock waves comprising the shock train have their own associated boundary layer interaction structure. Figure 2.6 compares the three main forms of the leading SBLI structure found in shock trains. Type 1 is the most common form, occurring in the majority of observed shock trains. The exact form of the SBLI is driven by geometric factors (i.e. Mach number and duct height) but is also sensitive to the implementation of the numerical scheme - each of the 3 shock trains

in figure 2.6 were formed by implementing different sub-grid LES models on the same underlying test conditions (Gnani et al., 2018b). The subsequent shock waves are usually curved normal shocks and frequently involve λ-foot structures at the interaction with the boundary layer.

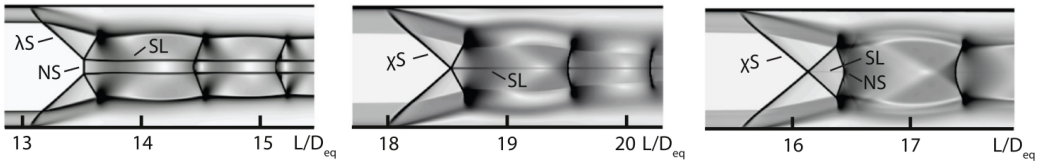

(a) Type 1: Mach stem.

(b) Type 2: Crossing oblique waves.

(c) Type 3: Crossing oblique waves with normal shock.

FIGURE 2.6: Numerical schlieren images of typical SBLI structures of the leading shock (Gnani et al., 2018b). NS = normal shock; XS = crossing oblique shocks; λS = lambda shock; SL = slip line.

2.3.2 Key Parameters and Modelling

The main governing parameters affecting the behaviour and structure of shock trains are generally considered to be: Freestream Mach number (M_1), exit/inlet pressure ratio (p_b/p_1) and confinement ratio (δ_{99}/h).

The Mach number strongly effects the SBLI structure and higher Mach numbers ($M > 2$) are more commonly associated with the dominance of oblique shocks - types 2 and 3 in figure 2.6 - (Carroll and Dutton, 1990; Hunt and Gamba, 2018). Additionally, higher Mach number shock trains often exhibit more unsteady behaviour, where the system has as a tendency to drift upstream towards the inlet (Carroll and Dutton, 1990). In general, higher Mach numbers produce longer shock trains with wider spacing between the shocks (Cox-Stouffer and Hagenmaier, 2001; Weiss et al., 2010) due to the shallower Mach angles and shock angles.

When considering the shock train to be a physical response to a prescribed pressure condition, it is intuitive that a larger ratio between exit and inlet pressure should produce a more significant shock train response. Indeed, it can be shown that shock train length (typically defined as the distance between the outlet and the location where the wall pressure rises 10% above the freestream) varies linearly with back pressure, assuming that other variables can be kept constant (Klomparens et al., 2015). It can also be observed that the streamwise distribution of pressure at the wall is independent (up to a point) of the actual back pressure imposed, provided

that the distribution is normalised by the location of the initial pressure rise (Carroll and Dutton, 1990; Klomparens et al., 2015). This suggests that the assumptions of Free-Interaction Theory are applicable to shock trains, as well as classical SBLIs.

The confinement ratio is found to have a noticeable influence on the length of the shock train as well as the distance between shocks. With the use of schlieren photographs, Carroll and Dutton (1988, 1990) were able to show that the overall length of the interaction scaled with the confinement ratio, with more boundary layer dominated flows exhibiting a higher number of weaker shocks. A more recent study (Fiévet et al., 2017) performed using direct numerical simulations on a similar layout at $M = 2$, confirmed the findings in Carroll and Dutton (1990) while also demonstrating the upstream displacement of the entire shock structure at increased levels of confinement. Numerical schlieren images from this study are shown in figure 2.7 showing that a thicker upstream boundary layer is associated with an upstream shift of the shock train as well as larger gaps between shocks.

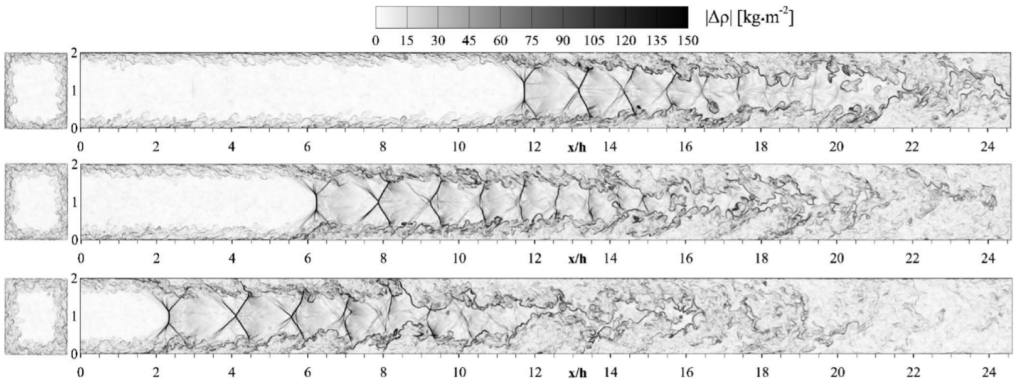

FIGURE 2.7: Effect of boundary layer confinement on a shock train in a $M = 2$ duct (Fiévet et al., 2017). The confinement ratios are (from top to bottom) 0.25, 0.28 and 0.34.

Although Reynolds number (calculated from boundary layer thickness or momentum thickness) also affects the structure of the shock train, the influence is very weak. It is estimated that in circular and rectangular ducts, the shock train length only scales with $Re^{1/4}$ (Billig, 1993; Matsuo et al., 1999) meaning that with an order of magnitude increase in Reynolds number one would only expect the shock train length to increase (relative to the duct height) by around 80%. By exploiting this weak scaling, researchers have been able to successfully reproduce wind tunnel experiments with numerical simulations at much lower (and therefore affordable) Reynolds numbers (Morgan et al., 2014; Roussel, 2016).

There have been a number of attempts at developing empirical and analytical models to understand and predict the behaviour of shock trains. The first of these was developed by Crocco (1958) (the Shockless Model) who made the assumption that the static pressure rise over the shock train is equal to that of a normal shock wave and that the distribution of pressure is driven by the dissipation in the boundary layer. Generally, this model is found to be too simplistic and the assumption of the static pressure rise does not actually hold in most situations. Waltrup and Billig (1973) took the approach of designing an empirical model which accounted for the main shock train parameters. This was done by running a range of experiments in a circular duct in order to test different conditions. The resulting relationship is given by

$$\frac{(x/D)(M_1^2-1)Re_\theta^{1/4}}{(\theta/D)^{1/2}} = 50\left(\frac{p}{p_1}\right) + 170\left(\frac{p}{p_1}\right)^2, \tag{2.1}$$

where D is the duct diameter. This describes the relationship between the main variables (streamwise position, Mach number, Reynolds number, confinement ratio and pressure ratio) at all points along the wall. It confirms the results of the parametric studies discussed in this section (e.g. that confinement ratio varies linearly with shock train length). One of the authors of the study subsequently adapted the model to fit rectangular ducts (Billig, 1993), producing a very similar result:

$$\frac{(x/h)(M_1^2-1)Re_\theta^{1/4}}{(2\theta/h)^{1/2}} = 50\left(\frac{p}{p_1}\right) + 170\left(\frac{p}{p_1}\right)^2. \tag{2.2}$$

The value of θ is taken to be the maximum momentum thickness on any of the surfaces whereas h is taken to be the lowest of the duct half-width or half-height. For this reason, the model does not fully account for the particular aspect ratio of the duct cross section. For example, the model would predict an identical shock train response for a square duct and very high aspect ratio duct, as long as the maximum θ and minimum h values are the same.

The Shockless Model has been improved on by Ikui et al. (1974) who developed the so-called Diffusion Model. In this case the core flow is assumed to be non-isentropic and the overall length of the shock train was made possible to calculate. This model was further improved by the same group (Ikui et al., 1981) (the Modified Diffusion Model), who accounted for the friction losses of the upstream boundary layer to improve the accuracy of the model.

A detailed review of a number of shock train models was performed by Matsuo et al. (1999) who also developed their own - the Mass Averaging Model. In this case

all of the properties mass-averaged over the cross section of the duct and the shock train analysed as a control volume. The model provides an estimation of the static and total pressure ratios over the shock train, however no information can be given about the conditions within the shock train itself.

In comparisons with wind tunnel experiments (Klomparens et al., 2015; Weiss et al., 2010), the models by Waltrup and Billig (1973), Ikui et al. (1974) and Matsuo et al. (1999) are all found to produce reasonably good predictions of the shock train pressure distributions. In general the two Billig models are considered to be more useful given that they take into account a wider range of input variables while also providing a prediction of the entire pressure distribution. In figure 2.8 the pressure curves predicted by the models are compared against established datasets (taken from Billig, 1993). It is clear that the circular duct model provides a more reliable prediction, especially at very high pressure ratios. It is likely that the high degree of scatter in figure 2.8b is due to the differing aspect ratios of the rectangular ducts (see following section).

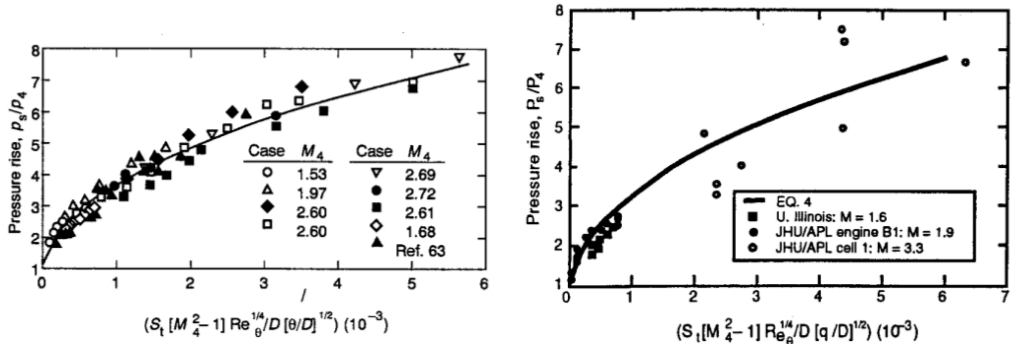

(a) Cylindrical ducts. (b) Rectangular ducts.

FIGURE 2.8: Comparison of the Billig models with established shock train data (Billig, 1993). Based on the scatter, the prediction is more reliable for cylindrical ducts.

2.3.3 Sidewalls and Spanwise Confinement

Another significant factor affecting the behaviour of shock trains is thought to be the spanwise confinement of the duct, and therefore, the influence of the sidewalls. Much like in more typical SBLI arrangements, the flow physics associated with the sidewalls (corner flow, sidewall separation) is thought to have a strong effect on the bulk flow near the centreline especially in the case of highly confined ducts.

Cox-Stouffer and Hagenmaier (2001) published a RANS study on shock trains where the Mach number and aspect ratio (W/H) were varied. For the highest Mach number (3.2) they found that increasing aspect ratio (by widening the duct) was associated with shock train systems which were longer and settle further upstream. For the lower Mach number (2.0) however, the effect was more complicated with the lowest aspect ratio (square duct) settling furthest upstream. These effects are illustrated in figure 2.9. Additionally it was noted that the underlying mechanism that causes the shock train to move upstream is absent in any configurations than aim to mitigate the sidewall influence (i.e. periodic boundary conditions). The implication is that any work aiming to study the phenomenon of unstart in isolators should resolve the sidewalls.

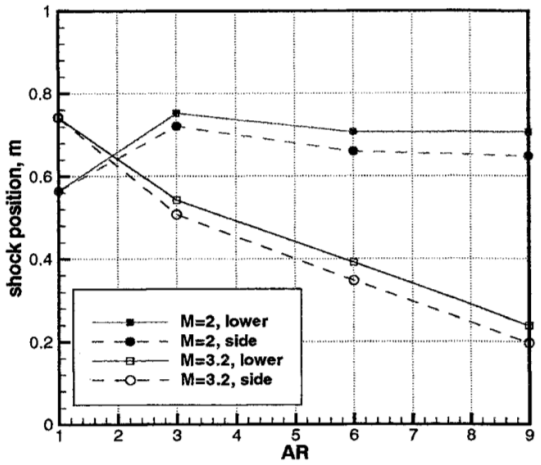

FIGURE 2.9: Aspect ratio effects on shock train position for two different Mach numbers.

The sidewall influence has been studied more recently by Morgan et al. (2014) where shock trains were analysed with both span-periodic conditions and sidewalls. By comparing the results to wind tunnel measurements, the sidewall case was found to match more closely to the experiments than the span-periodic case. Specifically, the span-periodic case underestimated the boundary layer growth rate, thereby predicting a lower level of confinement and producing a shorter shock train, even with a larger back pressure applied. Additionally it was shown that the corner vortices present with the application of sidewalls (referred to as secondary flow) were able to extend beyond the boundary layer edge, and thereby influence the core flow. Another study by Gnani et al. (2018b) confirms the inaccuracy of 2D/quasi 2D arrangements compared to fully 3D, with the 3D case exhibiting much larger pressure increases/decreases through the centreline of the shock train. The inaccuracies compound over the subsequent shocks, leading to the 2D case overestimating the

downstream Mach number and slightly underestimating the exit pressure.

It has been suggested by Vane and Lele (2013) that the difference between cases with and without sidewalls can be explained by the overall blockage of the cross section. By doubling the height of the boundary layer of a span-periodic case (thereby approximating the overall blockage with sidewalls) they found good agreement with wind tunnel measurements. This finding would imply that, at least in some configurations, the corner flow plays a much lesser role in the shock train behaviour compared to the additional viscous effects of the sidewall boundary layers.

2.3.4 Dynamic Shock Train Behaviour

The bulk of shock train research is concerned with their static behaviour i.e. studying instantaneous or time-averaged flow fields. However, due to the real world applications of shock trains (and the associated turbulent and vibrational forces), the flow cannot be considered to merely exist in a steady state and so understanding time-dependent effects is crucial.

A time-dependent back pressure can be used to study the impact of the combustion cycles within the combustor section, which is located close to the exit of the isolator. Applying a sinusoidal pressure function at the exit (by means of a numerical boundary condition or a hydraulic device) will cause the shock train to oscillate at the applied frequency in the streamwise direction. The oscillation pattern is that of an imperfect sinusoid, with an observed bias towards upstream movement both in terms of the response speed and the oscillation amplitude (Gnani et al., 2018a). Additionally there appears to be a hysteresis effect of the shock position between upstream and downstream motion (Klomparens et al., 2016). Generally, lower frequencies are found to produce larger oscillation amplitudes (Gnani et al., 2018a) of the shock train position.

Most of the current research on back pressure forcing is concerned with a fairly narrow band of low frequencies - between 0.5 and 20Hz corresponding to Strouhal numbers based on duct half width (non-dimensionalised frequency, $St_h = hf/u_1$) of the order 10^5 to 10^3. At this frequency range the shock train moves as a quasi-rigid body since the time delay between the head and tail of the shock train is negligible (Edelman and Gamba, 2018). A study by Jiao et al. (2018) has considered the effects higher frequency forcing in the range $50-1000$Hz ($St_h \sim 10^3-10^2$) where this time delay becomes non-negligible. Here the highest shock oscillation amplitude was found at 200Hz and the smallest at 1000Hz. It was noted that the peak oscillation occurring at an intermediate frequency suggested the presence of an excitation effect

within the shock train.

In addition to back pressure forcing, there has also been a consideration of inflow perturbations by Fiévet et al. (2017). As part of this study, the inflow boundary layer thickness was varied over time as a sinusoidal function between 20 and 1000Hz. The variations in inflow pressure caused an oscillation in the shock train position - this is visualised in figure 2.10. At particularly high frequencies the shock train acted as a low-pass filter and the size of the oscillations was small. Lower frequencies were generally responsible for larger oscillations although the peak occurred at around 93Hz due to an observed resonance-like effect (possibly similar to the effect seen by Jiao et al., 2018).

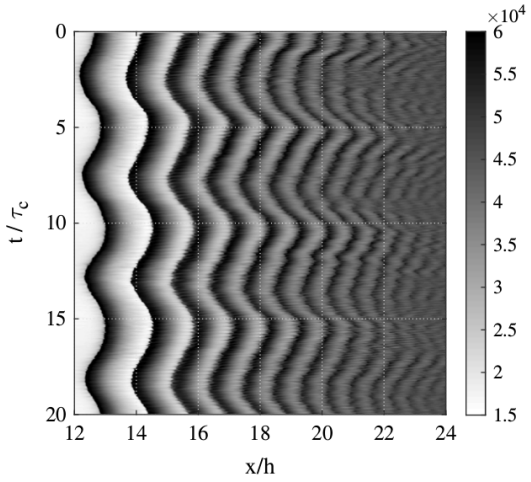

FIGURE 2.10: Contours of centreline pressure in $x-t$ space of a shock train response to a 93Hz inflow forcing (Fiévet et al., 2017).

A common focus of research on incident-reflected SBLI flows is the analysis of the frequency space and the unsteady behaviour of the shock structure. Spacial distributions of wall pressure power spectral density (PSD) provide a useful insights into the unsteadiness. It is well understood that the shock interaction is responsible for a broadband increase in fluctuation intensity. Additionally, there is a significant peak in low frequency motion corresponding to location of the shock foot - this is observed both in simulations (Touber and Sandham, 2009) and wind tunnel experiments (Dupont et al., 2006). This unsteadiness occurs at a frequency of the order $0.01u_1/\delta_{99}$ which is several orders of magnitude below the characteristic frequency of the inflow boundary layer. The precise source of this phenomenon is not fully understood, although a number of potential explanations have been proposed. For example, in the past it was thought that the low frequency motion may relate to a breathing motion of the separation region (Piponniau et al., 2009) or occur due

to perturbations by large inflow boundary layer structures (superstructures hypothesis, see Ganapathisubramani et al., 2009). Currently, the favoured explanation is that disturbances around the point of separation are "filtered" such that only low frequencies are selected (Touber and Sandham, 2011). The source of disturbances can therefore come from either upstream or downstream events.

Similar frequency analysis has also been performed on shock trains, although the extend of the research is much more limited. Figure 2.11 shows the distribution of wall pressure PSD as a function of space and frequency for a Mach 1.6 shock train from Roussel (2016). The non-dimensional frequency (Strouhal number, $St_L = Lf/u_1$) allows for more generalisable conclusions and the reference length is taken as the estimated interaction length of the leading shock. One notable feature of this plot is the ridges of constant frequency, which Roussel deduced to be due to acoustic resonance modes which occur due to the enclosed nature of the shock train problem. Additionally, the largest intensity of PSD occurs under the leading shock wave at around $x^* = 0.5$ and the frequency range matches that of the low frequency motion of canonical SBLIs (typically around $St_L = 0.03$). This has also been observed by Xiong et al. (2017) where the frequency range was independent of a number of flow conditions (back pressure, duct geometry). These results suggest that the same physical mechanism of low frequency unsteadiness occurs in both oblique SBLIs and shock trains.

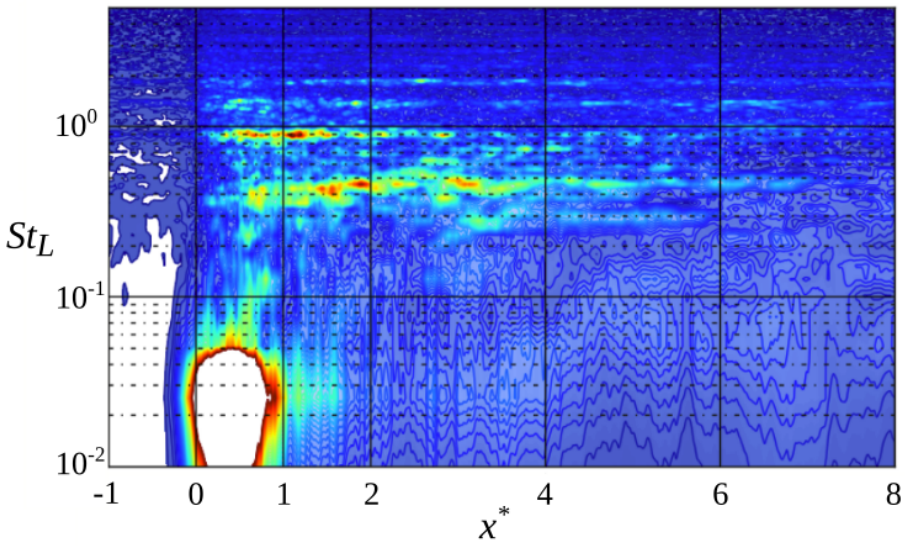

FIGURE 2.11: Spacial and frequency distribution of shock train PSD derived from wall pressure (adapted from Roussel, 2016). The largest fluctuation intensity occurs at the leading shock.

2.4 Summary and Open Questions

The study of SBLIs has been an active area of research since the late 1940s. In that time significant technological progress has been made, allowing for vast improvements in both the computational and experimental domains. Research groups now have access to very high-fidelity CFD codes, enormous computational resources, and detailed wind tunnel measurement apparatus with which to study these flow fields. This has led to the formation of a considerable body of knowledge, such that much of the governing physics of SBLIs (and, in particular, shock trains) is now very well understood. Despite this, there are aspects to shock train behaviour that remain mysterious and which therefore require a greater understanding. Additionally, the technological aspect to the research requires further incremental improvement. The open questions which relate to the motivation behind the current work are outlined below:

- Numerical simulations involving shock trains are typically done with LES or RANS codes which do not fully capture the physics of the turbulent flow. Expanding on the limited work conducted at the DNS level is therefore worthwhile but not necessarily a trivial task. Two questions can therefore be posed: 1) Is it possible to set up a computationally-inexpensive DNS (or implicit-LES) shock train test case? 2) What are the accuracy penalties caused by the grid resolution and simulation parameters (i.e. Reynolds number)?

- Although the effect of sidewalls has been studied in some detail, there are still several unknowns. For example, how exactly do the sidewalls affect the shock train structure and can their presence be accounted for purely by the additional blockage induced by the sidewall boundary layers?

- The study of time-dependent back pressure applied to shock trains has thus-far been focused on sinusoidal waveforms in the $1-10$Hz range. Would looking at other forms of back pressure forcing as well as sinusoidal forcing at higher frequencies reveal anything about the dynamic behaviour of shock trains?

Chapter 3

Computational Methods

3.1 OpenSBLI

The simulations in this project are performed using OpenSBLI (Jacobs et al., 2017; Lusher et al., 2018), a finite difference solver developed within the Aerodynamics & Flight Mechanics research group at the University of Southampton. In-house and open-source codes have the advantage of total user control (i.e. being able to rewrite any part of the code) yet there is a burden of responsibility whereby the code base must be maintained and adapted to software updates and hardware changes. This cost is most acute when running large CFD simulations on HPC facilities which use large clusters of CPUs or GPUs working in parallel to solve the simulation. For any given type of processor there may a number of libraries (e.g. MPI & OpenMP for CPUs and CUDA & OpenCL for GPUs) which provide the capacity for parallelisation. Adapting the code to any of these libraries requires a significant rewrite of the code base, which is time-consuming and error-prone. With the rapid improvement in processor capacity in recent years there is an increasing need for flexibility to run code on different architectures. However, to take full advantage of this, researchers are required to be experts in parallel computing as well as in their own scientific discipline.

This is the problem that OpenSBLI aims to address. By utilising the OPS library (Oxford Parallel Structured Software, Reguly et al., 2014) it is possible to take a generic discretisation of a numerical problem (written in OPSC, the OPS programming language) and use the OPS system to adapt it for a wide range of parallel architectures. OpenSBLI provides another abstraction by allowing the user to define the flow problem in a set-up file written in Python which then automatically generates the required OPSC code. This provides the advantages of both in-house and off-the-shelf codes in that a user does not need to have an in-depth understand-

ing of the code to run a simulation, yet another user who is more experienced with the code back-end can rewrite any part of it, should they wish.

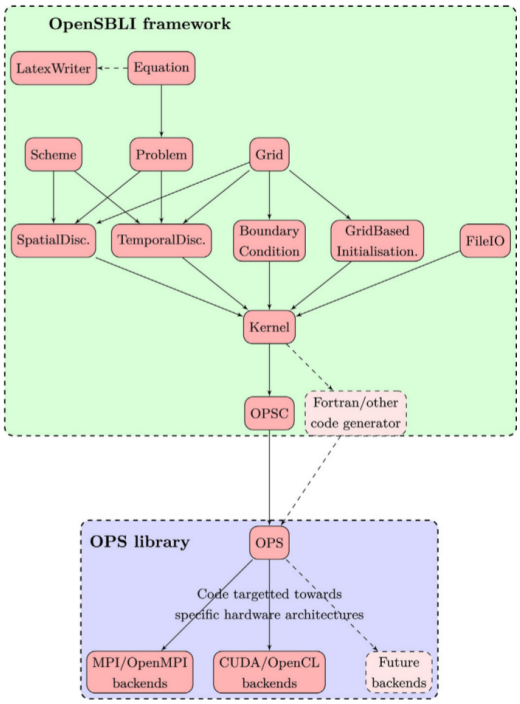

FIGURE 3.1: Overview of the design of the OpenSBLI system showing the interactions between the core classes (Jacobs et al., 2017). Targeting towards the specific HPC architecture is handled by the OPS translator.

Figure 3.1 shows the general structure of the OpenSBLI system with the interactions between key classes and with the OPS library. Within the Python set-up file the user defines the numerical scheme, governing equations, initial conditions, boundary conditions and the grid coordinates. All equations within the set-up file are written in Einstein (or index) notation and are implemented in the equation class from the Sympy library. The advantage of this is that equations can be defined in a more concise form rather than the expanded form in typical in-house solvers. Additionally, substitutions of variables are performed in the back-end meaning that longer equations can be written in multiple parts, reducing the chance of errors and allowing the code to be more readable. All of the simulation equations are written to a LaTeX file meaning that debugging of the equation sets can be done fairly easily. Initial conditions and grid coordinates can be described using equations or by reading from a source file. Boundary conditions are defined on each of the boundary surfaces with many of the common types available (e.g. Dirichlet, Neumann,

isothermal wall).

Upon running the set-up file, the problem is discretised with the core simulation classes written as computational kernels in the OPSC language. The code is then further translated into the required architecture-specific language which can then be compiled and run on the chosen platform. It is therefore possible to run identical problems, from the same set-up script, on completely different parallel architectures without having to rewrite any code.

OpenSBLI has been validated with a number of shock wave and turbulence problems including the Taylor-Green vortex (TGV) problem (Jacobs et al., 2017) and both laminar and transitional SBLIs (Lusher et al., 2018). The latest version of OpenSBLI can be found at https://opensbli.github.io

3.2 Governing Equations

All of the simulations in this project are solved using the compressible, dimensionless Navier-Stokes equations which relate the principal state variables $(\rho, \rho u_i, \rho E)$. They are described in tensor notation by

$$\frac{\partial \rho}{\partial t} + \frac{\partial \rho u_j}{\partial x_j} = 0, \tag{3.1}$$

$$\frac{\partial \rho u_i}{\partial t} + \frac{\partial (\rho u_i u_j + p\delta_{ij})}{\partial x_j} - \frac{\partial \tau_{ij}}{\partial x_j} = 0, \tag{3.2}$$

$$\frac{\partial \rho E}{\partial t} + \frac{\partial (\rho E + p) u_j}{\partial x_j} - \frac{\partial q_j}{\partial x_j} - \frac{\partial \tau_{ij} u_i}{\partial x_j} = 0, \tag{3.3}$$

where ρ, T and E are respectively density, temperature and total energy, u_i are the velocity components, and δ_{ij} is the Kronecker delta function. The pressure (p), the viscous stress tensor (τ_{ij}) and heat flux (q_i) are given by

$$p = (\gamma - 1)(\rho E - \frac{1}{2}\rho u_j u_j), \tag{3.4}$$

$$\tau_{ij} = \frac{\mu}{Re}\Big(\frac{\partial u_i}{\partial x_j} + \frac{\partial u_j}{\partial x_i} - \frac{2}{3}\delta_{ij}\frac{\partial u_k}{\partial x_k}\Big), \tag{3.5}$$

$$q_j = \frac{\partial T}{\partial x_j}\Big(\frac{\mu}{(\gamma-1)M^2 PrRe}\Big), \tag{3.6}$$

where Re is the Reynolds number, Pr is the Prandtl number, M is the freestream Mach number, γ is the heat capacity ratio and μ is the viscosity, defined by Sutherland's law

$$\mu = T^{3/2}\frac{1+C}{T+C}, \tag{3.7}$$

with C denoting the Sutherland constant, obtained by

$$C = \frac{T_s}{T_r}. \tag{3.8}$$

Here T_s is the Sutherland temperature (110.4K) and T_r is the reference temperature (288.0K). Finally, pressure, density and temperature are related by the dimensionless ideal gas law:

$$p = \frac{\rho T}{\gamma M^2}. \tag{3.9}$$

In the current implementation, velocity, density, temperature and viscosity are non-dimensionalised by the freestream quantities (u_r, ρ_r, T_r), with pressure non-dimensionalised by $\rho_r u_r^2$. All distances are non-dimensionalised by the displacement thickness of the van Driest-transformed inflow profile, δ^*_{vd} which is defined by equation 3.35 in section 3.5.2. All of the simulations model air with $\gamma = 1.4$ and $Pr = 0.72$.

3.3 Numerical Schemes

3.3.1 Shock Capturing

The simulations are solved in OpenSBLI using explicit finite difference methods. Implementing standard finite difference schemes in simulations involving supersonic flow leads to unstable behaviour around shocks and other discontinuities. OpenSBLI has the capacity to implement both weighted essentially non-oscillatory (WENO) and targeted essentially non-oscillatory (TENO) shock capturing methods which allow shocks to be resolved while limiting the artificial dissipation common amongst shock capturing methods. Only the 6th-order TENO scheme is used in this project (documented in Fu et al., 2016) and it is summarised below. The shock capturing is only applied to the Euler terms and both the stress tensor term (equation 3.5) and heat flux term (equation 3.6) are computed using a 4th order explicit central scheme.

In order to describe the shock capturing methods, it is necessary to first introduce a hyperbolic equation of the form

$$\frac{\partial \boldsymbol{u}}{\partial t} + \nabla \cdot \boldsymbol{F}(\boldsymbol{u}) = 0, \tag{3.10}$$

where $\boldsymbol{F}(\boldsymbol{u})$ represents the flux term. Simplifying the problem to a single dimension and reconstructing the flux term means the following approximation can be made at grid point i:

$$\frac{\partial u_i}{\partial t} + \frac{1}{\Delta x}(f_{i+\frac{1}{2}} - f_{i-\frac{1}{2}}) = 0. \tag{3.11}$$

The TENO method determines the centre point fluxes ($f_{i\pm\frac{1}{2}}$) using a weighted sum of fluxes on candidate stencils ($f^{(r)}_{i+\frac{1}{2}}$). For a scheme of order K there will be $K-2$ candidate stencils for each flux term. Figure 3.2 shows the staggered stencils (S_r) and their positions over a 1D grid.

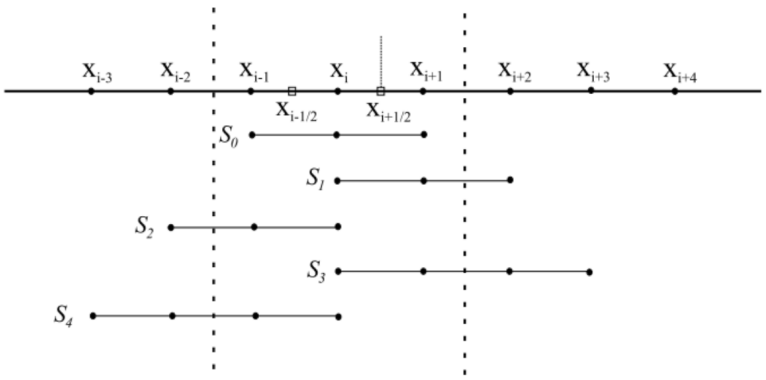

FIGURE 3.2: Sketch of candidate stencils (S_r) for TENO schemes (Fu et al., 2016).

The combined flux term is given by

$$f_{i+\frac{1}{2}} = \sum_{r=0}^{K-3} \omega_r f^{(r)}_{i+\frac{1}{2}}. \tag{3.12}$$

Here, ω_r are the stencil weights which are required to sum to 1 (i.e. $\Sigma\omega_r = 1$). The individual flux terms, $f^{(r)}_{i+\frac{1}{2}}$, are obtained from interpolations given by

$$f^{(r)}_{i+\frac{1}{2}} = \sum_{j=0}^{K-3} c_{rj}\overline{f}_{i-r+j}, \tag{3.13}$$

where $\overline{f}_{i-r+j}$ are the cell averages and c_{rj} are the coefficients as outlined by table 2.1 in Shu (1998).

The scheme uses a discrete delta function in order to remove stencils by weighting them at zero if they fall below a certain threshold smoothness. The weighting function is given by

$$\omega_r = \frac{\delta_r d_r}{\sum_{j=0}^{K-3} \delta_j d_j}, \tag{3.14}$$

where d_r are optimal weight values given in table 2 in Fu et al. (2016). The delta function, δ_r, is defined by

$$\delta_r = \begin{cases} 0 & : \chi_r < C_T \\ 1 & : \text{otherwise.} \end{cases} \tag{3.15}$$

Here, C_T is a cut-off parameter which defines whether a particular stencil will have a non-zero weight. Lower values of C_T will allow for a lower rate of dissipation, at the cost of larger inaccuracies around discontinuities and therefore the ideal value is just below that which the code can run without stability issues. The standard value used in this project is $C_T = 10^{-6}$, although some simulations (involving moving shock waves) are also run using $C_T = 10^{-5}$. χ_r is a smoothness measure determined by a normalisation process:

$$\chi_r = \frac{\gamma_r}{\sum_{j=0}^{K-3} \gamma_r}, \tag{3.16}$$

with the local weights, γ_r given by

$$\gamma_r = \left(C + \frac{\tau_K}{\beta_r + \epsilon}\right)^q. \tag{3.17}$$

The parameters C and q can be varied in order to limit the level of dissipation. In Fu et al. (2016) it was found that the combination $C = 1$ and $q = 6$ was optimal. The local smoothness indicator, β_r, is used to detect discontinuities within any of the stencils, allowing the respective ω_r value to be close to zero. It is defined by

$$\beta_r = \sum_{j=1}^{2r-1} \Delta x^{2j-1} \int_{x_{i-1/2}}^{x_{i+1/2}} \left(\frac{d^j}{dx^j} f_k(x)\right)^2 dx. \tag{3.18}$$

Finally, τ_K is a global smoothness value relating to the values of β_r (Castro et al., 2011). Substituting the scheme order for $2r-1$, the global smoothness value is given by

$$\tau_{2r-1} = \begin{cases} \|\beta_0 - \beta_{r-1}\| & : \mathrm{mod}(r,2) = 1 \\ \|\beta_0 - \beta_1 - \beta_{r-2} + \beta_{r-1}\| & : \mathrm{mod}(r,2) = 0. \end{cases} \tag{3.19}$$

3.3.2 Temporal Discretisation

The time advancement is performed with an explicit, low-storage, 3rd order Runge-Kutta (RK3) scheme. The low storage form was originally derived by Williamson (1980) and it has the advantage of limiting the number of intermediate variables which need to be stored, thereby reducing memory requirements and improving the processing performance. To describe the scheme we first consider an example differential equation:

$$\frac{\partial u}{\partial t} = F(t, u(t)), \tag{3.20}$$

with initial value

$$u(t_0) = u_0. \tag{3.21}$$

The problem is descretised with fixed time step Δt and the time advancement finds u^{n+1} which is the solution to u^n at the next time step:

$$u^{n+1} = u(t^{n+1}) = u(t^n + \Delta t). \tag{3.22}$$

An m-th order RK scheme computes the time advancement over m stages. For the low-storage form, stages $j = 1, ..., m$ are computed in the following way:

$$du^{(j)} = A_j du^{(j-1)} + \Delta t F(u^{(j-1)}), \tag{3.23}$$

$$u^{(j)} = u^{(j-1)} + B_j du^{(j)}), \tag{3.24}$$

where A_j and B_j are storage variables (see table 3.1). $u^{(0)}$ is initialised as u^n and $du^{(0)}$ as 0. Finally, the solution for the next time step is simply

$$u^{n+1} = u^{(m)}. \tag{3.25}$$

j	A_j	B_j
1	0	1/3
2	-5/9	15/16
3	-153/128	8/15

TABLE 3.1: Storage coefficients for the 3rd-order low-storage RK3 scheme.

3.4 Domain Description

3.4.1 Grid

This project is concerned with two principal domain layouts: channel and duct cases. These are visualised in figure 3.3 which shows pictorial representations of the grid meshes. Additionally, the quarter duct arrangement (which is used in only one test case) is shown. Both principal cases have solid boundaries on the top and bottom (y^+ and y^-) surfaces and the grid is refined at these boundaries in order to resolve the turbulence. The duct case has additional solid boundaries on the sides (z^+ and z^- boundaries) whereas the channel case does not. The quarter duct is used to simulate only one corner of the duct and thus only the y^- and z^- boundaries are solid surfaces.

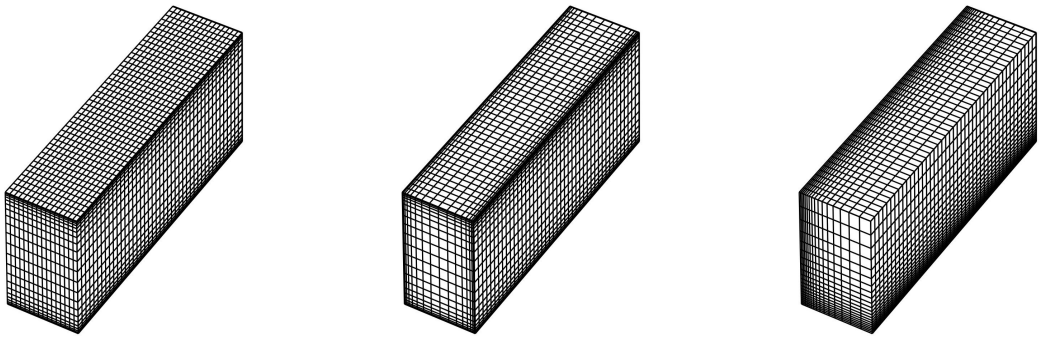

(a) Channel. (b) Full duct. (c) Quarter duct.

FIGURE 3.3: Sketches of the three main numerical domains used in this project.

The grid stretching is achieved via symmetric stretching functions where the grid coordinates (in this case y) are defined as:

$$y = l_y \frac{1 - \tanh\left(\beta_y\left(1 - \frac{2j}{n_y - 1}\right)\right)}{\tanh(\beta_y)}, \tag{3.26}$$

where l_y is the height of the domain, n_y is the number of grid points in the y direction, β_y is the stretching factor and j is the index value in the range $0 : n_y - 1$. Where there is no grid stretching, the grid coordinates are equispaced. For the quarter duct, the grid stretching is asymmetrical and is instead achieved with the following function:

$$y = l_y \frac{\sinh\left(\frac{\beta_y j}{n_y - 1}\right)}{\sinh(\beta_y)}. \tag{3.27}$$

3.4.2 Boundary Conditions

The boundary condition for the wall boundaries is a non-slip isothermal condition which sets all momentum components to zero and fixes the temperature (T_{wall}) to the recovery temperature (with recovery coefficient $r = Pr^{1/3}$). The energy component can then be calculated with

$$\rho E = \frac{\rho T_{wall}}{\gamma(\gamma - 1)M^2}. \tag{3.28}$$

This applies to the bottom and top walls (y_m, y_p) in both of the principal arrangements as well as the sidewalls (z_m, z_p) in the duct arrangement. For the channel, in lieu of sidewalls, there is a periodic condition applied in the z direction which mimics a quasi-infinite span arrangement. The quarter duct has isothermal wall boundary conditions at the y_m and z_m boundaries and symmetry conditions at the y_p and z_p boundaries. The symmetry condition mirrors the flow variables in the halo points and sets the relevant transverse momentum component (ρv, ρw) to zero.

For the quarter duct case, there is an additionally applied filter at the corner of the two symmetry planes. This is used to provide numerical stability by limiting the growth of unnatural disturbances. The filter is applied to the solution vector, U such that:

$$U = (1 - \sigma)U_{uf} + \sigma U_f, \tag{3.29}$$

where σ is the mixing ratio and U_f and U_{uf} are respectively the filtered and unfiltered solutions. U_f is the average of the directional filters, U_{fx_i}:

$$U_f = (U_{fx} + U_{fy} + U_{fz})/3. \tag{3.30}$$

The directional filters here are 10th-order filters, the coefficient of which are found by expanding the term $(a - b)^{10}/2^{10}$. In the current work a mixing ratio of 0.01 was sufficient to stabilise the code and the filter was applied zonally to a 4×4

box of grid points around the corner point.

At the outflow plane of each case (x_p), an extrapolation condition is applied, whereby the flow variables are copied into the halo points. For cases involving shock trains, there is an additional sponge treatment in order to establish the required back pressure - this is discussed in section 3.6. All simulations implement a turbulent inflow condition at the inflow boundary (x_m) which is outlined in the following section. A summary of the boundary conditions implemented in different scenarios is given in table 3.2 and a visual representation of the computational domain is given in figure 3.4.

Domain	ST/ZPG	x_m	x_p	y	z
Channel	ZPG	TI	Ex	Wall	Periodic
Channel	ST	TI	Ex & sponge	Wall	Periodic
Full duct	ZPG	TI	Ex	Wall	Wall
Full duct	ST	TI	Ex & sponge	Wall	Wall
Quarter duct	ST	TI	Ex & sponge	Wall/symmetry	Wall/symmetry

TABLE 3.2: Summary of boundary conditions used in the project. ST = shock train, ZPG = zero-pressure-gradient, TI = turbulent inflow, Ex = extrapolation.

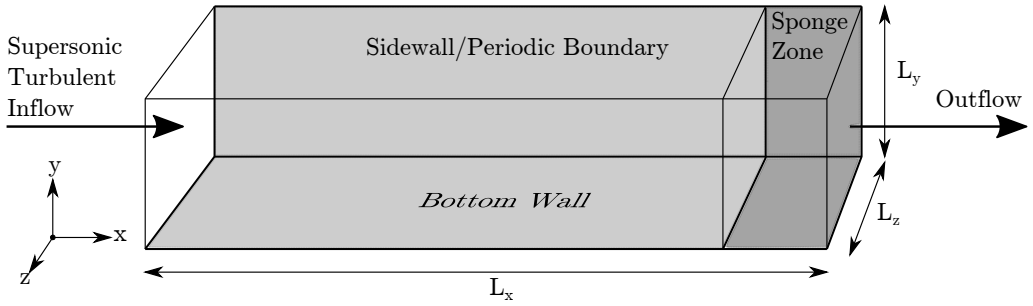

FIGURE 3.4: Schematic diagram of the computational domain and the applied boundary conditions.

3.5 Turbulence Generation

3.5.1 Overview

Since this project is concerned with simulating turbulent boundary layers, there is a requirement to generate physically correct turbulent flow shortly downstream of the

inflow. Since there is no analytical solution to the Navier-Stokes equations, there is no straightforward way to generate accurate turbulent structures algorithmically.

There are two main approaches to the problem of turbulence generation. One method requires an auxiliary recycling/rescaling simulation to be run either before or alongside the main simulation. This auxiliary simulation allows a turbulent boundary layer to develop before having a velocity field extracted as the inflow of the main simulation. This is the technique outlined by Lund et al. (1998) who developed a simplified version of the method originally formulated by Spalart (1988). While this method produces a physically correct TBL directly at the inflow, due to the rescaling process from the auxiliary simulation there is a propensity for the target integral thicknesses to 'drift' as time goes on when the method is applied to compressible flow (Sagaut et al., 2004). Additionally, the recycling process may introduce artificial low-frequency information into the domain. This is a significant disadvantage when studying the low-frequency motion inherent in SBLI problems.

The second approach to the problem concerns the generation of a synthetic turbulent flow at the inflow boundary. The general approach is to impose a random signal onto an analytically-determined mean velocity profile. Purely random, uncorrelated signals applied in this way will decay rapidly and cause to the flow to re-laminarise so there is a need for the random signals to have the realistic statistical moments and energy spectra so that the generated data has the same correlation lengths and energy distribution of a real turbulent flow. The formulation of this approach, as defined by Lund et al. (1998), is described by

$$U_i = \bar{U}_i + a_{ij} u_j^*, \tag{3.31}$$

where U_i are the components of the total velocity profile, $\bar{U}_i$ is the mean profile, u_j^* are the components of the unscaled velocity fluctuations with the correct spacial and temporal correlation lengths and a_{ij} is an amplitude matrix (to scale the fluctuations to the correct boundary layer fit) such that

$$\begin{aligned} a_{11} &= \sqrt{R_{11}} \\ a_{21} &= R_{21}/a_{11} \\ a_{22} &= \sqrt{R_{22} - a_{21}^2} \\ a_{31} &= R_{31}/a_{11} \\ a_{32} &= (R_{32} - a_{21}a_{31})/a_{22} \\ a_{33} &= \sqrt{R_{33} - a_{31}^2 - a_{32}^2}, \end{aligned} \tag{3.32}$$

with the Reynolds stress tensor defined as:

$$R_{ij} = \overline{\rho u_i' u_j'}, \tag{3.33}$$

where u_i' is a fluctuating component of velocity and the $\overline{()}$ notation denotes time-averaging.

The values of the matrix a_{ij} can be determined using existing data of a turbulent boundary layer, therefore what remains is the method to apply the correlations. A common method to achieve this is the so-called digital filter approach proposed by Klein et al. (2003) where a 3D field of random disturbances is filtered to ensure the correct correlation structure. This technique has been a considerable source of interest over the past decade or so and forms the basis of many contemporary inflow methods - see Veloudis et al. (2007) for example. One drawback of the Klein method was its need to filter a full 3D velocity field at each time step, therefore adding a considerable computational cost. An improvement on the method was developed and published by Xie and Castro (2008) where only the 2D inflow data plane was filtered, with the temporal structure determined with an exponential correlation method. A further simplification was made by the same research group (Kim et al., 2011) who applied the exponential correlation to the whole field, saving on computational expense while still producing a sufficiently accurate turbulent boundary layer.

Synthetic turbulence methods are not without their disadvantages; due to the limitations of the method of correlation algorithm, the flow immediately downstream of the inflow is un-physical and generally requires a relaxation distance of around 10 - 20 boundary layer thicknesses which can add otherwise unnecessary length to the domain. Additionally, there is a general difficulty in controlling the target skin friction and integral displacements downstream of the relaxation zone (Lund et al., 1998). This usually requires some form of trial-and-error before the required boundary layer characteristics are generated.

Despite the shortcomings, it was deemed that the synthetic turbulence approach was the most appropriate to apply to this project, due to its better suitability to compressible flows and its relative simplicity when compared to the auxiliary simulation approach. Additionally, the synthetic turbulence method avoids a potential issue of artificial low-frequency signals. The specific implementation of this method was chosen to be that of Kim et al. (2011) primarily due to the general simplicity of the method.

3.5.2 Mean Profile Generation

The first stage of the inflow generation process is to compute a mean boundary layer profile based on the input Mach and Reynolds numbers. When applying this to the OpenSBLI framework, the process only needs to be performed once, prior to the simulation. The method presented here was initially developed by Li (2003) and further improved by Touber (2010).

First it is necessary to define the van Driest coordinate system, which transforms a boundary layer profile between compressible and incompressible forms. The transformation is given by

$$u_{vd}(y) = \int_{u(y=0)}^{u(y)} \sqrt{\frac{\rho(y)}{\rho(y=0)}} du'. \tag{3.34}$$

Additionally, we will define the van Driest displacement thickness which serves as the reference length scale for the numerical simulations:

$$\delta^*_{vd} = \int_0^\infty (1 - u_{vd}(y_{vd}))dy_{vd}. \tag{3.35}$$

Hence, the Reynolds number based on this value can be given by

$$Re = \frac{\rho_r u_r \delta^*_{vd}}{\mu_r}, \tag{3.36}$$

with r denoting the reference values at the inflow.

The process of finding the mean profile starts with a guess of $u^+_{vd,e}$, that is, the wall-unit scaled van Driest velocity at the boundary layer edge. The guess does not have to be particularly accurate since the correct value is iteratively determined later on. An array is then generated, equispaced between 0 and $u^+_{vd,e}$ such that

$$u^+_{vd} = [0, \ldots, u^+_{vd,e}]. \tag{3.37}$$

An intermediate coordinate system, $\xi^+(u^+_{vd})$, can then be computed:

$$\xi^+(u^+_{vd}) = u^+_{vd} + \exp(-\kappa b) \exp\left(\kappa u^+_{vd} - 1 - \kappa u^+_{vd} - \frac{1}{2}(\kappa u^+_{vd})^2 - \frac{1}{6}(\kappa u^+_{vd})^3\right), \tag{3.38}$$

where $b = 5.17$ is the log law constant and $\kappa = 0.41$ is the von Kármán constant.

This coordinate system can then be transformed into the van Driest form in wall units:

$$y^+_{vd}(u^+_{vd}) = \frac{\xi^+(u^+_{vd})\xi^+(u^+_{vd,e})}{\xi^+(u^+_{vd,e}) - \xi^+(u^+_{vd})}. \tag{3.39}$$

The final value (boundary layer edge/freestream) in this coordinate system is chosen to be an arbitrarily large value representing the far-field. The pure van Driest form can then be computed using the definition of the input Reynolds number (equation 3.36)

$$y_{vd} = \frac{y^+_{vd}u^+_{vd,e}}{Re}. \tag{3.40}$$

The next step is to solve for the dimensionless boundary layer thickness:

$$\delta_0 = \frac{u^+_{vd,e}\xi^+_e}{\alpha Re}, \tag{3.41}$$

where α is an intermediate value given by

$$\alpha = \exp\Big(\frac{2Re}{690 + 1.5Re}\Big) - 1. \tag{3.42}$$

This then allows the van Driest velocity profile to be computed:

$$u_{vd}(y_{cd}) = 1 - f + \frac{u^+_{vd}}{u^+_{vd,e}}f, \tag{3.43}$$

where

$$f = \exp\Big(- 3\big(\exp(\eta^{1/\kappa})\big)\Big), \tag{3.44}$$

and

$$\eta = \frac{y_{vd}}{\delta_0}. \tag{3.45}$$

Since the van Driest velocity is the reference length scale for the simulation, it is required to be, by definition, equal to one. Therefore the above process from equation 3.37 to 3.45 must be iterated until the guessed value of $u^+_{vd,e}$ results in the following condition:

$$\delta^*_{vd} = \int_0^\infty (1 - u_{vd})dy_{vd} = 1. \tag{3.46}$$

Although the process is fairly long-winded, this condition is relatively simple to reach using a simple iterative method. This then allows the correct van Driest profile to be found which must then be converted into the physical profiles of velocity,

temperature and density.

This second task begins with finding the adiabatic wall temperature, T_{aw}:

$$T_{aw} = 1 + \frac{\gamma - 1}{2} M^2. \tag{3.47}$$

The relationship between temperature and velocity within the boundary layer is given by the Crocco-Busemann relation:

$$T(u) = a + bu + cu^2, \tag{3.48}$$

where

$$\begin{aligned} a &= T_w \\ b &= T_{aw} - T_w \\ c &= 1 - T_{aw}, \end{aligned} \tag{3.49}$$

and T_w is the prescribed wall temperature, which may include a recovery factor ($r = 1, T_w = T_{aw}$ for an adiabatic wall).

From the definition of the van Driest transform in equation in 3.34, the van Driest velocity in wall units is given by

$$u^+_{vd}(y) = \int_{u^+(y=0)}^{u(y)} \sqrt{\frac{\rho(y)}{\rho(y=0)}} du'^+. \tag{3.50}$$

By considering that the ideal gas law within the boundary layer is $\rho T = const.$, the Crocco-Busemann equation can be substituted into equation 3.50, yielding

$$\begin{aligned} u^+_{vd} &= u^+_e \sqrt{T_w} \int_0^u \frac{du'}{\sqrt{a + bu' + cu'^2}} \\ &= u^+_e \sqrt{\frac{-T_w}{c}} \Big[\arcsin\Big(\frac{b}{\sqrt{b^2 - 4ac}}\Big) - \arcsin\Big(\frac{2cu + b}{\sqrt{b^2 - 4ac}}\Big) \Big]. \end{aligned} \tag{3.51}$$

Since $u = 1$ at the boundary layer edge, the value of u^+_e can be solved for:

$$u^+_e = \frac{u^+_{vd,e} \sqrt{-c}}{\sqrt{T_w} \Big[\arcsin\Big(\frac{b}{\sqrt{b^2-4ac}}\Big) - \arcsin\Big(\frac{2cu+b}{\sqrt{b^2-4ac}}\Big) \Big]}. \tag{3.52}$$

This allows the full, compressible velocity profile to be computed:

$$u(u_{vd}) = \frac{(\sqrt{b^2-4ac})\sin\left[\arcsin\left(\frac{b}{\sqrt{b^2-4ac}}\right) - \arcsin\left(\frac{2cu+b}{\sqrt{b^2-4ac}}\right)\right]}{2c}. \tag{3.53}$$

From this profile, the distribution of temperature can be found using equation 3.48. Assuming isobaric conditions across the inflow, density can be found using

$$\rho = \frac{1}{T}. \tag{3.54}$$

The penultimate task is to compute the physical coordinate system from the van Driest values. From equation 3.40 we find that

$$y^+_{vd} = \frac{y_{vd}Re}{u^+_{vd,e}} = \frac{yRe\rho_w}{u^+_e\mu_w}, \tag{3.55}$$

where ρ_w and μ_w are the density and dynamic viscosity values at the wall. By applying the ideal gas law and Sutherland's law for viscosity we arrive at

$$y = \frac{y_{vd}u^+_e}{u^+_{vd,e}} T_w^{5/2} \frac{1+C}{T_w+C}, \tag{3.56}$$

where C is the chosen Sutherland constant.

Lastly, the generated profiles of u, T and ρ can be interpolated on to the real mesh of the simulation.

In addition to calculating the distribution of $\bar{u}$, some methods (e.g. Touber, 2010) use semi-analytical techniques to determine the average distribution of wall-normal velocity, $\bar{v}$. The intention is to take into account the effect of the gradual streamwise thickening of the boundary layer, thereby avoiding a weak pressure wave right at the inflow of the domain. This is achieved by estimating the boundary layer growth over a certain distance and then solving for $\bar{v}(y)$ using the continuity equation. However, when applying the same method used by Touber (2010) in test simulations, the prediction of the $\bar{v}(y)$ profile was found to be significantly larger than the actual profile observed in the simulations, therefore providing no benefit in preventing inaccuracies at the inflow. Attempts to capture empirical distributions of $\bar{v}(y)$ and use them at the inflow resulted in similar problems. Therefore, no such method is implemented in any of the results shown here and $\bar{v}(y)$ for all the simulations is set to zero.

3.5.3 Fluctuating Profile Generation

The method for generating turbulent fluctuations is outlined in this section. An example of the code used for this method is given in appendix B.1.

Original Method

As explained in section 3.5.1 there are two steps to generating fluctuations in the synthetic turbulence method: determining the fluctuation amplitudes and generating the unscaled fluctuations. The values in the matrix a_{ij} as defined in equation 3.32 were obtained using DNS data produced from Schlatter and Örlü (2010) which is available to download for a range of Reynolds numbers. The first step therefore is to choose the dataset most suitable for the target Reynolds number of the simulation. The specific Reynolds number (based on momentum thickness) used by Schlatter and Örlü (2010) is given by

$$Re_\theta = \frac{\rho_r U_r \theta}{\mu_r}. \tag{3.57}$$

Since the simulation performed by S&O was incompressible, this is equivalent to the following definition in compressible flow:

$$Re_\theta = \frac{\rho_w U_{vd,e} \theta_{vd}}{\mu_w}. \tag{3.58}$$

These values can be determined from the mean profile and hence the correct match of Reynolds numbers can be made.

The fluctuation data provided gives profiles of y^+, $\bar{U}^+$ and the four main Reynolds stress vectors: u^+_{rms}, v^+_{rms}, w^+_{rms}, $(uv)^+_{rm}$ where rms and rm denote the root-mean-square and root-mean values. Using the y^+ profile generated from the mean profile, the first job is to fit the profiles to that of the simulation. Then, the Reynolds stress profiles are converted from wall units and scaled by a factor of $\sqrt{\rho_w/\rho(y)}$ to account for the incompressible DNS data being applied to a compressible boundary layer. Once the full Reynolds stress profiles are known, the components of a_{ij} can be found of each y coordinate. Since only the dominant Reynolds stress components are considered, the matrix can be simplified such that

$$\begin{aligned} a_{11} &= \sqrt{R_{11}} \\ a_{21} &= R_{21}/a_{11} \\ a_{22} &= \sqrt{R_{22} - a_{21}^2} \\ a_{33} &= \sqrt{R_{33}}. \end{aligned} \tag{3.59}$$

The correlation method involves finding the unscaled fluctuation field for each velocity component, $u_j(y,z)$ at each time step. The specific method used in this project applies exponential correlation functions in the y, z and temporal dimensions to reproduce the 2-point correlation behaviour of turbulent flow. The method, as defined by Kim et al. (2011), is given by the flowing set of equations:

$$\phi_j(t,y+1,z) = \phi_j(t,y,z)\exp\left(\frac{-1}{n_{yj}}\right) + r_j(t,y,z)\Big[1-\exp\left(\frac{-2}{n_{yj}}\right)\Big]^{1/2}, \tag{3.60}$$

$$\psi_j(t,y,z+1) = \psi_j(t,y,z)\exp\left(\frac{-1}{n_{zj}}\right) + \phi_j(t,y,z)\Big[1-\exp\left(\frac{-2}{n_{zj}}\right)\Big]^{1/2}, \tag{3.61}$$

$$u_j^*(t+1,y,z) = u_j^*(t,y,z)\exp\left(\frac{-1}{n_{tj}}\right) + \psi_j(t,y,z)\Big[1-\exp\left(\frac{-2}{n_{tj}}\right)\Big]^{1/2}, \tag{3.62}$$

where $n_{yj} = I_{yj}/\Delta y$, $n_{zj} = I_{yj}/\Delta z$ and $n_{tj} = T_j/\Delta t$ are the number of grid points required to resolve the largest length scales. T_j is the Lagrangian time scale defined as $T_j = I_{xj}/U$ with U being the local mean velocity. The values I_{ij} is the matrix of integral length scales chosen for the specific problem.

The variables ϕ_j are ψ_j intermediate values used to apply the correlation method. The variable r_j represents a field of uncorrelated random numbers generated for each velocity component at each time step. The values of r_j are required to be normally distributed with a mean of 0 and a standard deviation of 1 - i.e.

$$\left(\overline{r_j(t,y,z)^2}\right)^{1/2} = RMS(r_j) = 1.0. \tag{3.63}$$

This is an important property since it is the same condition that the fluctuations, u_j^* must hold once the correlation method has been applied.

The choices of integral length scales for this project are outlined in table 3.3. The values are the similar to the ones used by Touber (2010) who applied a similar synthetic turbulence method to a Mach 2.3 boundary layer and found the method to be flexible to the choice of length scales.

Modifications for Current Project

In essence, the method outlined in equations 3.60 - 3.62 involves a sequence of summations in each Cartesian direction. This is depicted in figure 3.5 which shows a summation along grid points in the z direction.

Visualising the method in this way reveals two things. Firstly, there is no way for the boundary values of $\phi_j(t,0,z)$ and $\psi_j(t,y,0)$ to be updated; all other points

I_{ij}	x	y	z
u	10.0	4.0	4.0
v	1.5	1.75	1.0
w	1.5	1.0	1.75

TABLE 3.3: Choice of integral length scales for each velocity component in each direction.

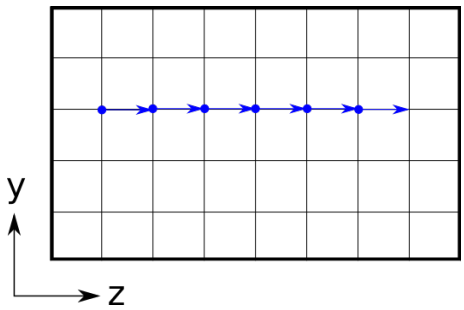

FIGURE 3.5: Visualisation of the correlation method applied to a sequential code.

are updated with the points before them. Unless they are updated at each time step then the values immediately adjacent will be biased one way or the other and hence the RMS values at theses coordinates will be incorrect. It is unclear how this issue was dealt with in Kim et al. (2011), however a modification was made for this project, by implementing a periodic condition in the values of ϕ_j and ψ_j such that:

$$\phi_j(t,0,z) = \phi_j(t,N_y-1,z)\exp\left(\frac{-1}{n_{yj}}\right) + r_j(t,0,z)\left[1-\exp\left(\frac{-2}{n_{yj}}\right)\right]^{1/2}, \tag{3.64}$$

$$\psi_j(t,y,0) = \psi_j(t,y,N_z-1)\exp\left(\frac{-1}{n_{zj}}\right) + \phi_j(t,y,0)\left[1-\exp\left(\frac{-2}{n_{zj}}\right)\right]^{1/2}, \tag{3.65}$$

where N_y and N_z are respectively the number of grid points in the y and z directions (changes from equations 3.60 and 3.61 are highlighted in red). To use ϕ_j as an example, at the zeroth index in y there is no "previous" value of ϕ_j to use and therefore the value at $N_y - 1$ is taken instead.

The second issue is that the method is designed for purely sequential codes where all the calculations on the grid are computed one after the other on the same processor. However, the scale of simulations in this project necessitates the use of parallel codes where the domain is distributed between multiple processors. This is shown in figure 3.6 where the grid is decomposed into different processors (outlined

in red). The problem is that since the method is computed simultaneously, values from one processor are required for calculation in another. Due to limitations in bandwidth, communication between processors occurs only between iterations. In addition, processors would be required to wait for other processors to finish thereby destroying the advantage of parallelisation. For these reasons it is clear that the method as originally proposed is not well suited for efficient parallel applications.

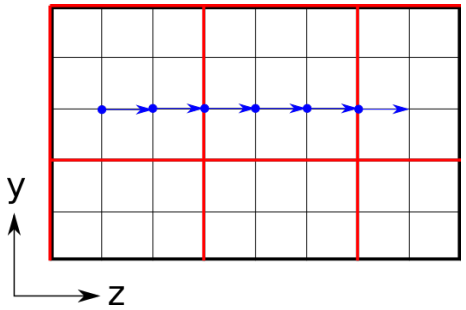

FIGURE 3.6: Visualisation of the correlation method applied to a parallel code. The red outlines represent the parallelisation of the domain across multiple processors.

To solve this issue another modification was made to the method which updates the values of ϕ_j and ψ_j using stored values from the previous time step:

$$\phi_j(t, y+1, z) = \phi_j(t-1, y, z)\exp\left(\frac{-1}{n_{yj}}\right) + r_j(t, y, z)\left[1 - \exp\left(\frac{-2}{n_{yj}}\right)\right]^{1/2}, \quad (3.66)$$

$$\psi_j(t, y, z+1) = \psi_j(t-1, y, z)\exp\left(\frac{-1}{n_{zj}}\right) + \phi_j(t, y, z)\left[1 - \exp\left(\frac{-2}{n_{zj}}\right)\right]^{1/2}. \quad (3.67)$$

This modification technically reduces the accuracy of the method due to the variation between time steps. However, due to the size of the convective time step ($u_e\Delta t$) compared to the grid spacing in the boundary layers (Δy and Δz) and the dominance of the streamwise length scale, the variation between iterations is much smaller than between grid points. This suggests that the modifications are reasonable but that there is a need for verification - this is found in section 4.1.1.

3.5.4 Adaptation for Sidewalls

The methods described in the previous sections are concerned with generating a flat plate boundary layer with homogeneity in the z direction. Due to the fact that this project is in part concerned with the influence of sidewalls and finite ducts, there is the additional requirement of being able to generate turbulent boundary layers

around corners as well as the top and bottom walls.

Generating inflow data for the sidewalls and top wall is a reasonably simple task; the main difficulty comes in generating blended inflow data at the corners such that there is a smooth transition between walls. In the present work this is done in two stages: blending of the mean profiles and blending of the fluctuation amplitudes. The method defined below considers only the corner between the bottom wall and z^- sidewall, but in principle it can apply to any number of corners.

With the method laid out in the previous sections 3.5.2 a mean profile for the bottom wall boundary layer can be generated: $\overline{u_y}$, $\overline{T_y}$ and $\overline{\rho_y}$. Similarly we can generate a fluctuation amplitude matrix, A_y, which has non-zero components:

$$\begin{aligned} a_{11} &= \sqrt{R_{11}} \\ a_{21} &= R_{21}/a_{11} \\ a_{22} &= \sqrt{R_{22} - a_{21}^2} \\ a_{33} &= \sqrt{R_{33}}. \end{aligned} \tag{3.68}$$

By flipping the axes y and z and changing v for w we can generate similar values for the sidewall boundary layer: $\overline{u_z}$, $\overline{T_z}$, $\overline{\rho_z}$ and A_z. Note that the components of A_z will be:

$$\begin{aligned} a_{11} &= \sqrt{R_{11}} \\ a_{22} &= \sqrt{R_{33}} \\ a_{31} &= R_{21}/a_{11} \\ a_{33} &= \sqrt{R_{22} - a_{21}^2}. \end{aligned} \tag{3.69}$$

The blended velocity profile, $\overline{u}$ is determined by multiplying the individual profiles:

$$\overline{u(j,k)} = \frac{\overline{u_y(j)} * \overline{u_z(k)}}{\overline{u_e}}. \tag{3.70}$$

From this new distribution, we can determine temperature and density using equations 3.48 and 3.54.

The general blending method for the fluctuation amplitudes is defined by

$$A(j,k) = D_1 b A_y(j) + D_2(1-b)A_z(k). \tag{3.71}$$

The blending function, b, ensures a smooth transition between distributions. It is given by

$$b = 0.5\Big(1 - \sin\Big(\frac{\pi(d_y - d_z}{2\delta_0}\Big)\Big), \tag{3.72}$$

with d_y and d_z being the distances to the nearest y and z boundary respectively and δ_0 being the boundary layer thickness.

The damping functions D_1 and D_2 prevent any overly large fluctuations within the corners. They are defined by

$$D_1 = \begin{cases} \left(\frac{d_z}{\delta_0}\right)^{1/4} & : d_z \leq \delta_0 \\ 1.0 & : d_z > \delta_0 \end{cases} \tag{3.73}$$

$$D_2 = \begin{cases} \left(\frac{d_y}{\delta_0}\right)^{1/4} & : d_y \leq \delta_0 \\ 1.0 & : d_y > \delta_0. \end{cases} \tag{3.74}$$

Illustrations of the blending methods are displayed in figures 3.7 and 3.8 which compares the case of a simple flat plate boundary layer with a bottom wall/side wall combination. The examples used are $\overline{u}$ and A_{11} which is the amplitude of the streamwise fluctuations, u'.

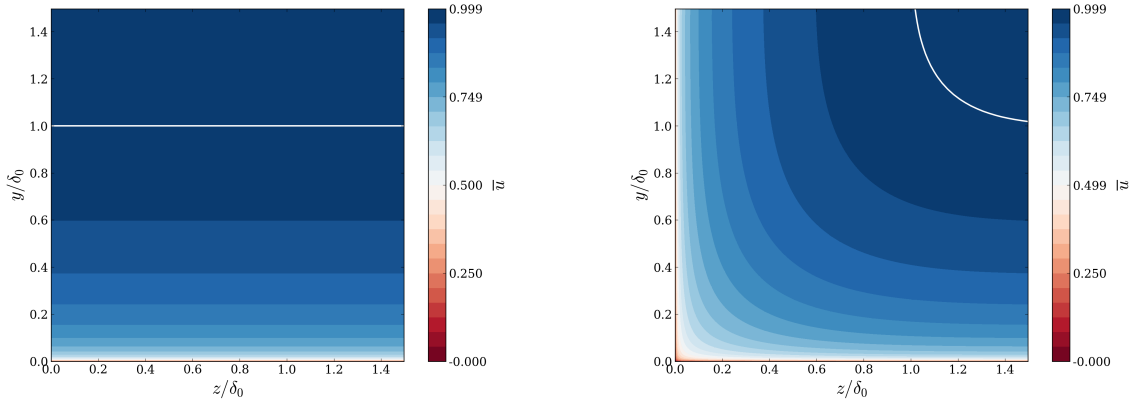

(a) Bottom boundary layer only.

(b) Blended boundary layers.

FIGURE 3.7: Blending of streamwise velocity within the corner region. The white line indicates the edge of the boundary layer (δ_{99}).

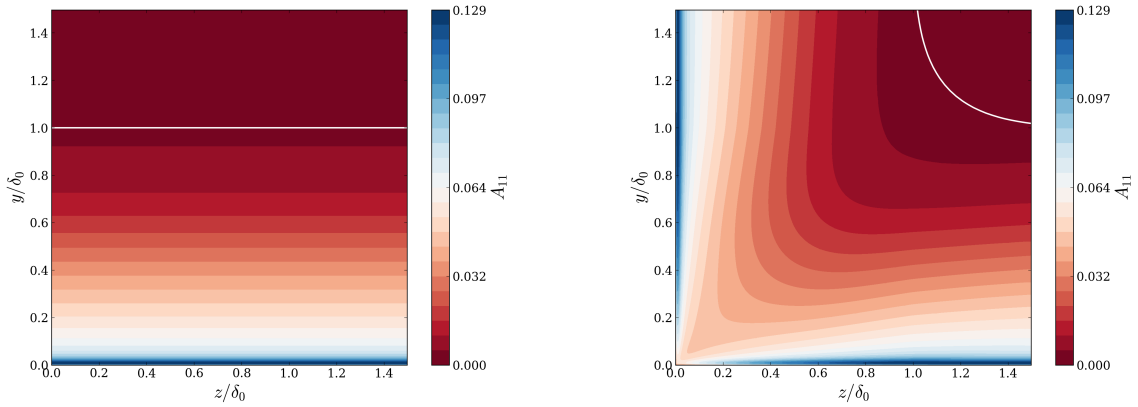

(a) Bottom boundary layer only.

(b) Blended boundary layers.

FIGURE 3.8: Blending of the A_{11} component of fluctuation amplitude within the corner region.

3.6 Sponge Zone

In order to generate shock trains in the simulation, a pressure ratio must be enforced over the domain. Due to the inflow method, the inlet pressure is fixed to that of the freestream Mach number ($p_1 = 1/\gamma M^2$) so the overall pressure ratio can be set by prescribing a certain back pressure at the exit of the domain. The main difficulty in applying this condition is in avoiding instability issues at the outflow plane associated with reflections and regions of separation. For example, setting a condition at the outflow plane that pressure values should be fixed to a chosen target pressure will simply result in instability issues when applied to a supersonic turbulent flow.

There are a number of approaches that researchers have taken to avoid these issues. For example, applying a non-reflective characteristic boundary condition (see Fiévet et al., 2017). In this project we take a simpler approach and enforce the back pressure by means of a sponge zone where pressure condition is applied more gradually. In order to demonstrate this, we will use the generic variable q for which the sponge is applied to. The value of q at streamwise position x is forced towards the required target value q_{target} at iteration number n via the following formula:

$$q_n(x) = q_{n-1}(x) + (q_{target} - q_{n-1}(x))w(x). \tag{3.75}$$

The term $w(x)$ here is a spacially-varied weight term which allows the sponge to more robustly enforce the target value near the exit of the domain. This value can

vary from 0 to 1, with $w(x) = 0$ having no effect and $w(x) = 1$ setting $q = q_{target}$. For our purposes, this variable takes the form

$$w(x) = a\Delta t\Big(\frac{1}{2} - \frac{1}{2}\cos\Big(\pi\frac{x - x_{sponge}}{l_{sponge}}\Big)\Big)^b. \tag{3.76}$$

Here x_{sponge} is the coordinate at the start of the sponge zone, l_{sponge} is the overall length of the sponge zone and a and b are weight parameters used to tune the sponge zone to the simulation. The parameter a is used to scale the overall strength of the sponge while b is used to shift the distribution towards or away from the outlet. The time step, Δt, is included in order to account for the fact that simulations with lower time steps will implement the sponge function more frequently and therefore having effectively stronger sponges.

The sponge zone can theoretically be applied to any flow variable, including density and momentum. The results discussed here however only make use of the sponge zone for the pressure term, setting a target back pressure of p_{target} or p_b. This variable is usually fixed to a certain value but is also varied in time for certain simulations. The values of a, b and l_{sponge} should be tuned to any individual simulation such that the required conditions at the outflow are met, while the simulation remains stable. The particular values used in this project are $a = 0.05$, $b = 1.0$ and $l_{sponge} = 2h$. An example of the code used for the sponge zone is given in appendix B.2.

Chapter 4

Validations

4.1 Turbulent Boundary Layer

A first part of the validation process is to assess the development of the turbulent boundary layer in the absence of any shock waves. This is primarily to judge the inflow turbulent boundary layer generation, however it also provides an opportunity to consider what phenomena may be directly caused by the turbulence. This process is conducted with two different cases; the first is a simple channel arrangement with solid boundaries on the top and bottom and a periodic condition imposed in the z-direction (span-periodic); the other is a fully enclosed square duct with solid boundaries on all four sides. Boundary layers are generated on all solid boundaries. Both cases will be assessed here and comparisons made between the two.

All of the simulations discussed in this chapter have been run with a freestream Mach number of $M = 2.0$ and a Reynolds number of $Re_\theta = 500$. The Reynolds number is deliberately low (near to the lower bound where turbulence can be sustained) in order to allow for large grid sizes while still resolving the small scale turbulence. There is no sponge zone active in any of the cases so all pressure gradients are caused by the natural boundary layer growth.

4.1.1 Supersonic Channel

Qualitative Analysis

Using the half-height, h, as the reference length, the channel case has a cuboid arrangement with lengths of $16h \times 2h \times 1h$ (x, y, z). The initial confinement ratio is set at $\delta_{99}/h = 0.28$, meaning that the boundary layers occupy roughly one third of the channel cross-section. Two different grid resolutions are considered here, referred to as ILES and DNS. The details of these are summarised in table 4.1. These

grid resolutions are also considered in the main grid refinement study (section 4.3). As with all of the cases studied in the current work, a minimum of three FTT cycles are performed prior to any data analysis in order to wash out any transient flow.

Grid	N_x	N_y	N_z	Δx^+	Δy^+ (min/max)	Δz^+	Δt
ILES	800	320	60	9	0.8/5	8	0.016
DNS	1600	480	120	4.5	0.5/4.0	4	0.008

TABLE 4.1: Summary of grid resolutions used to study the turbulent boundary layer. Viscous grid spacing values are calculated with the local u_τ value at $x = 6h$.

Visualisations of the flow can be seen in figure 4.1 (as with all cases, flow is left to right). The development of the boundary layer can be seen clearly - the artificial structures produced by the inflow method develop into larger, more coherent structures further downstream. There is also considerable boundary layer growth between the inlet and exit. This higher confinement leads to a larger pressure near the end of the domain - see figure 4.1c. The density gradient (calculated as the Pythagorean sum of $\partial\rho/\partial x_i$) is visualised in figure 4.1b and provides the best view of the structures in the outer part of the boundary layer which develop between $x = 2h$ and $x = 4h$.

Another feature that can be seen clearly is the pattern of weak Mach waves which propagate from the bottom and top of the inlet and cross over at approximately $x = 2h$. These waves are an artefact of the uncorrected wall-normal velocity profile (prescribed as zero at the inflow) which must adjust to the natural rate of boundary layer growth. As will be discussed further in this chapter, we find that these waves do not produce any significant lasting effects on the downstream flow.

An additional visualisation of the flow field is considered in figure 4.2 which considers various cross sections of the bottom half of the domain. Three flow properties are considered: Mach number, temperature and density gradient. Moving from left to right shows the development of the boundary layer from the inflow to $x = 5h$. This view provides a good qualitative view of how un-physical the generated flow structures are; although certain turbulent statistics may be correct, the flow field more closely resembles white noise than a real turbulent boundary layer.

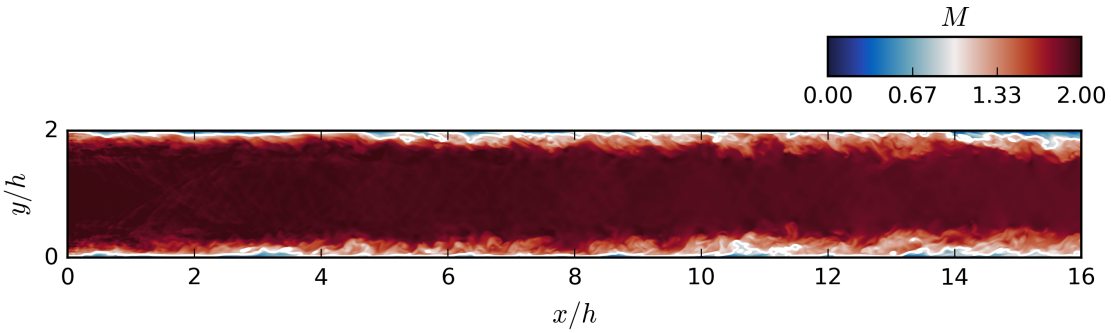

(a) Mach number.

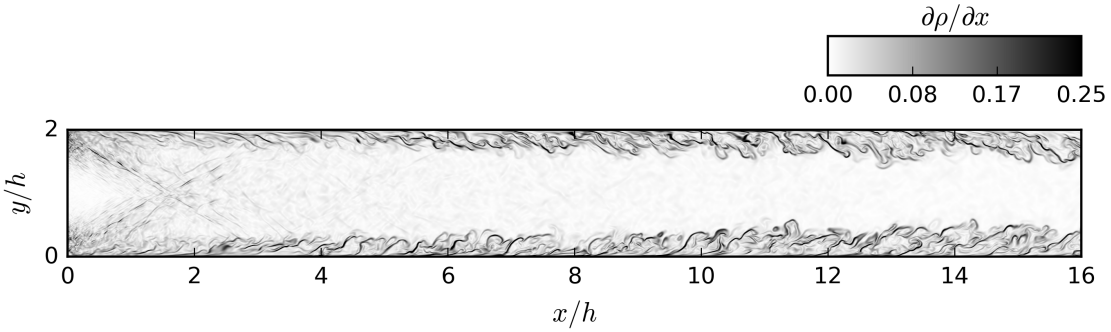

(b) Density gradient.

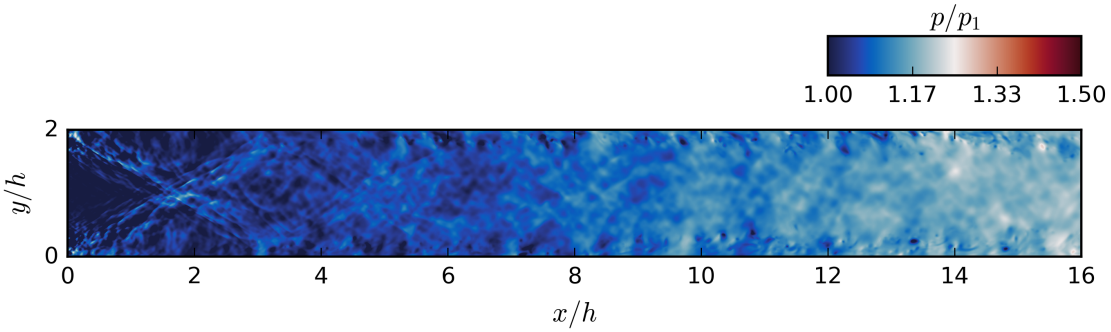

(c) Static pressure.

FIGURE 4.1: Contours of instantaneous flow properties showing the development of turbulent flow structures and gradual thickening of the boundary layer. Data is taken from the DNS case at the mid-span x-y plane.

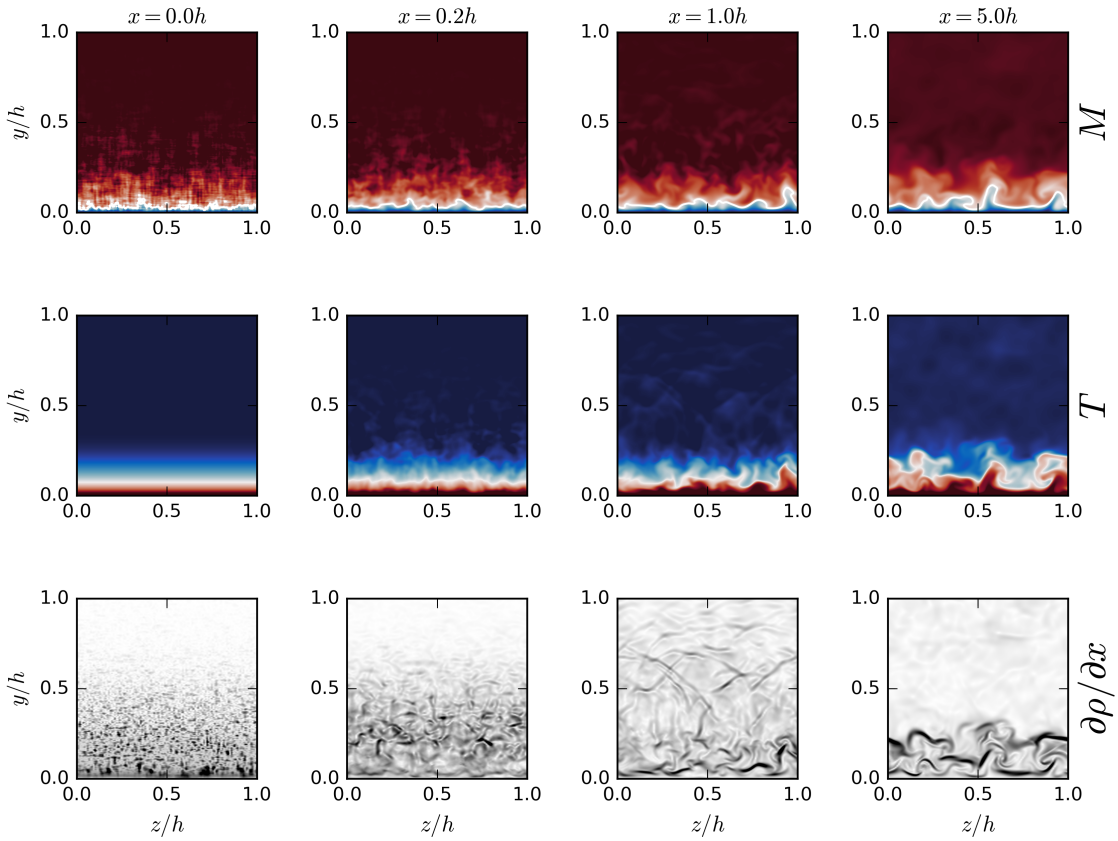

FIGURE 4.2: Flow field contours in the y-z plane taken at various streamwise locations of the DNS case. From top to bottom: Mach number, temperature and density gradient. This view of the flow field gives a clear impression of the turbulence development process.

Time-averaged Flow Properties

The purpose of this validation is threefold: firstly to ensure that the turbulence generation method is able to produce a physically correct turbulent boundary layer. Secondly, to determine the approximate streamwise location where this occurs (i.e. to understand which sections of the domain can or cannot be analysed in later experiments). The third requirement is to find out the natural rate of development of various flow properties (such as boundary layer thickness) to provide a useful counter-factual when analysing the shock train behaviour in following chapters.

With these considerations in mind, the rest of this section provides a quantitative study of time-averaged flow properties in the supersonic channel case. Both grid resolutions are compared and data from each has been captured (after reaching

a converged state) over 4 convective cycles (flow-though time) which amounts to a time period of $64h/u_1$, where u_1 is the freestream velocity at the inflow. In addition, data is averaged in the spanwise direction, due to the homogeneity of the flow.

Figure 4.3 plots the streamwise variation of a number of flow properties for both the ILES and DNS grids. There is a clear region of volatility shortly downstream of the inlet (present in each of the charts) which illustrates the development of the analytically-produced boundary layer. The natural growth of the boundary layer thickness (figures 4.3d and 4.3e) increases the confinement ratio in the channel, directly leading to an increase in wall pressure by roughly 18% (figure 4.3a) and decrease in Mach number at the centreline (figure 4.3b). The presence of the inflow compression waves show up in the two spikes/dips in the pressure and Mach number curves. The strength of these compression waves appears to be very weak and the flow recovers immediately, suggesting that the permanent effect of these waves can be neglected. The shape factor (distribution seen in figure 4.3f) appears to be the most sensitive parameter to the inflow compression waves although it eventually settles down to a constant downward slope beyond $x = 8h$ with very little variation between the grid resolutions.

Skin friction provides good information about the state of the boundary layer flow very close to the wall. The distribution of skin friction in figure 4.3c shows a very large variation in this development region, a feature which is common for these synthetic turbulence methods. After approximately $x = 6h$ the distribution appears to converge to a constant slope, suggesting that this is the length of the development region for this particular property.

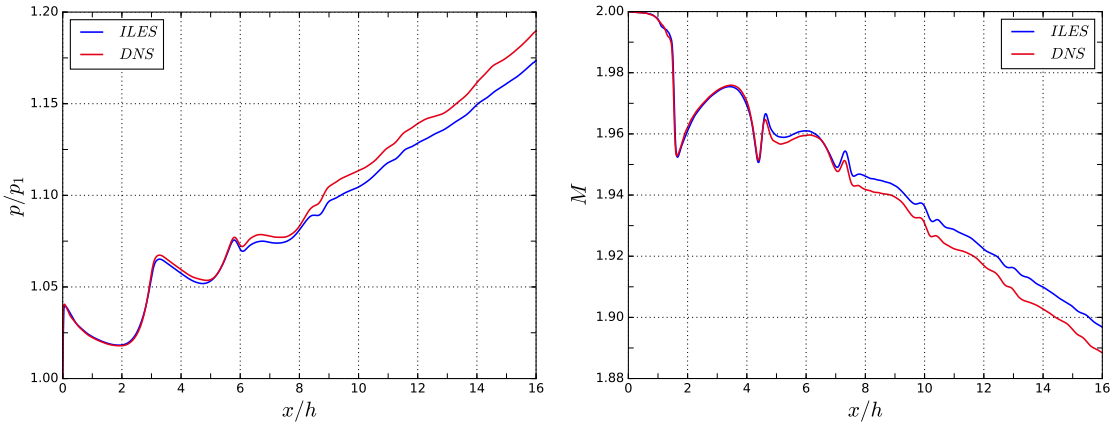

(a) Wall static pressure.

(b) Centreline Mach number.

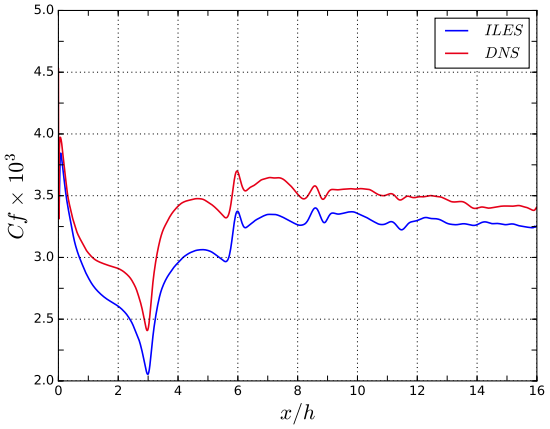

(c) Skin friction coefficient.

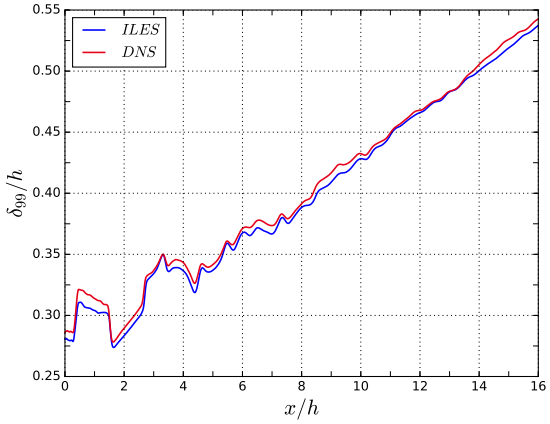

(d) Boundary layer thickness (δ_{99}).

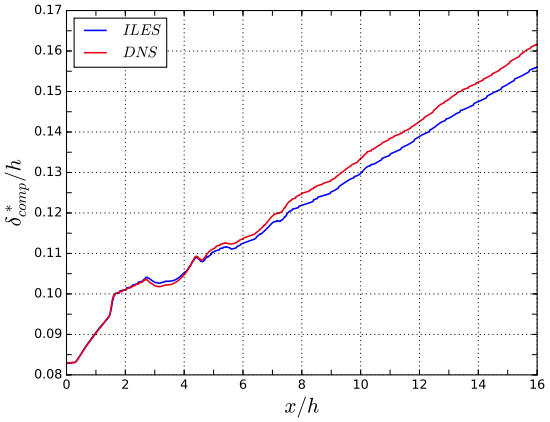

(e) Displacement thickness.

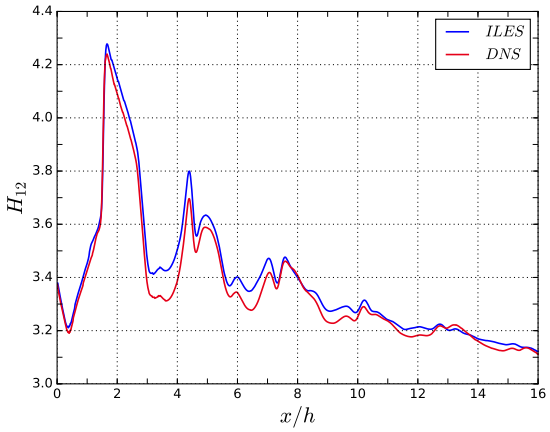

(f) Shape factor.

FIGURE 4.3: Streamwise variation of various time- and span-averaged flow properties within the supersonic channel case. The most noticeable difference between the two grid resolutions is in the skin friction distribution.

It is the skin friction distribution which also shows the largest discrepancy between the two grid resolutions. The difference between the two is significant, with the ILES case underestimating C_f by approximately 5% after the development region. This suggests that the near-wall turbulence is not fully resolved when running at the ILES resolution, despite the fact that the measured viscous grid spacings are very low (see table 4.1). This is further confirmed by the fact that the difference can be seen clearly in the distributions of displacement thickness (affected by the near-wall velocity deficit), while the distributions of boundary layer thickness are very similar. The low displacement thickness at the ILES resolution also leads to a

lower wall pressure near the end of the duct due to there being slightly lower flow momentum in the boundary layer. A more rigorous analysis of the grid convergence can be found in section 4.3.

Turbulent Statistics

In order to fully validate the inflow method it is necessary to study the boundary layer turbulence in detail. Time-averaged velocity profiles at various streamwise locations are plotted in figure 4.4. The profiles have been van Driest scaled (transformation described by equation 3.34) in order to account for the high degree of compression in the boundary layer. Additionally, the profiles are in viscous wall units, as is standard. Also plotted here is the law of the wall and log law relationships ($B = 5.17$; $\kappa = 0.41$). The different locations have been chosen in order to illustrate the process the boundary layer undertakes before converging.

The inflow profile at $x = 0$ (figure 4.4a) suggests that the method of generating the mean velocity profile is poorly suited to such a low Reynolds number. There is significant divergence in the wall region and there is no log law fit for either grid resolutions. Despite this, the log law fit further downstream (figure 4.4b) is significantly worse, with a U^+_{vd} edge value of around 25. This location is right in the middle of the boundary layer development region and it was noted previously that this corresponds to a huge variation in the skin friction - this relates to the viscous scaling factor, hence why the slope here is very large. Moving downstream further to $x = 5.0h$ (figure 4.4c), the velocity profile has once again settled down to a reasonable level and the recognisable double inflection curve has formed. The boundary layer converges to the correct log law slope by $x = 8.0h$ (figure 4.4d), although this is strictly for the DNS grid only. This is the velocity profile which endures throughout the remainder of the channel, with the U^+_{vd} edge value in the DNS case slowly rising to 21 at the exit.

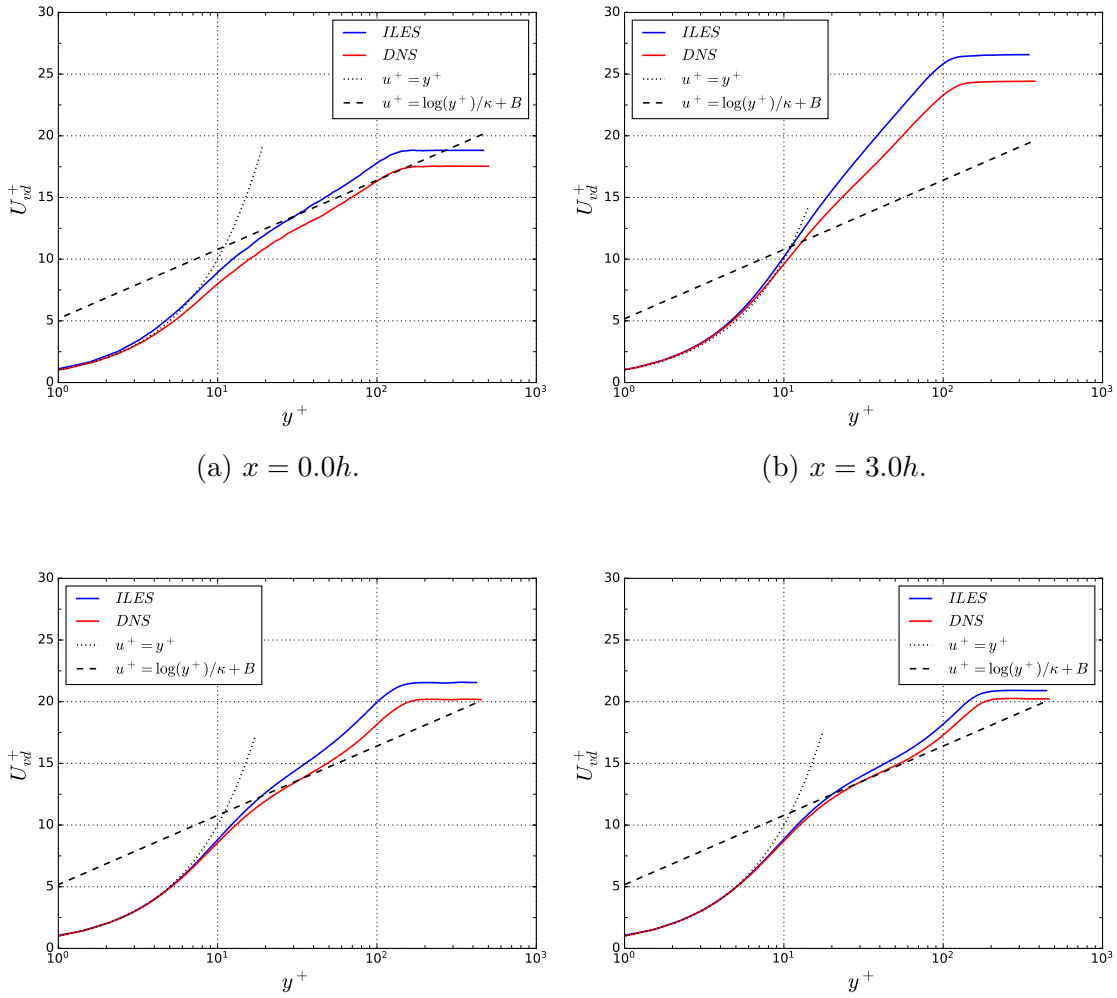

(a) $x = 0.0h$. (b) $x = 3.0h$.

(c) $x = 5.0h$. (d) $x = 8.0h$.

FIGURE 4.4: Plots of van Driest-transformed velocity profiles at various streamwise positions. Also plotted are the log law and law of the wall slopes. All data is time- and span-averaged.

The differences in grid resolution are once again obvious in each of these plots. The consistently higher U_{vd}^+ distribution for the ILES grid is consistent with the lower skin friction in figure 4.3c since the velocity in wall units is inversely scaled with the square root of wall shear stress:

$$u^+ = u(\rho/\tau_w)^{1/2}. \tag{4.1}$$

The Reynolds stress statistics for each of the cardinal directions are plotted in figure 4.5 at the same streamwise locations as discussed above. The solid, dashed

and dotted lines represent the computed RMS of u', v' and w' respectively. The profiles are given in viscous wall units and the RMS profiles have been additionally scaled by the following density parameter, ξ:

$$\xi = (\rho(y)/\rho_w)^{1/2}. \tag{4.2}$$

This is a common technique to account for the compressibility of high Mach number boundary layers. The scaling allows for very good comparisons with incompressible boundary layers (see for example Wenzel et al., 2018).

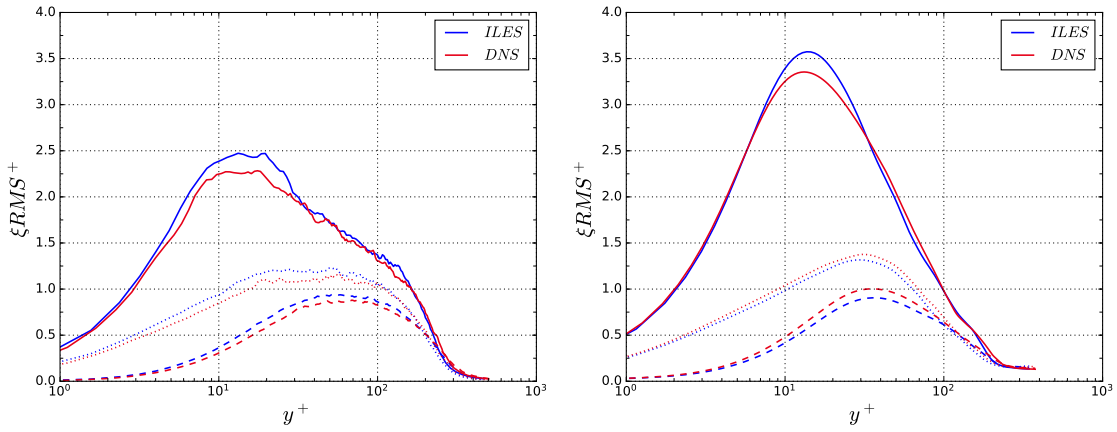

(a) $x = 0.0h$. (b) $x = 3.0h$.

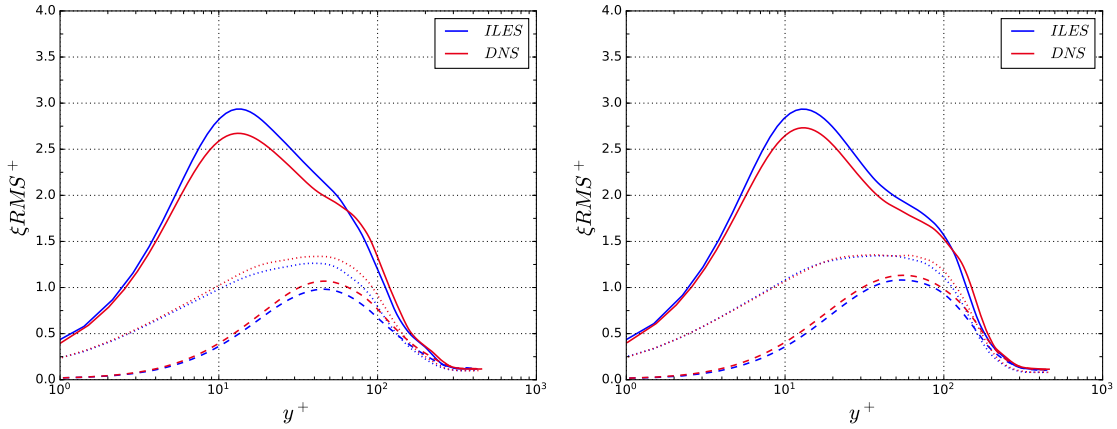

(c) $x = 5.0h$. (d) $x = 8.0h$.

FIGURE 4.5: Density-scaled RMS profiles of turbulent fluctuations. Solid, dashed and dotted lines respectively represent RMS curves of u', v' and w'.

In general, the turbulent fluctuations evolve in a similar way to the velocity profile; the initial (prescribed) distribution (figure 4.5a) is disrupted during the de-

velopment region (figure 4.5b) before settling down and converging further along the domain (figures 4.4c and 4.4d). The grid differences are also present here, with the lower τ_w leading to an overestimation of the streamwise fluctuations. The fact that the initial and converged profiles are much more similar to each other than the intermediate profile at $x = 3h$ suggests that it is not important to be particularly accurate with the prescribed fluctuation amplitudes - i.e. if the initial distribution is not preserved in the development region, then the inflow method is likely to be flexible to the choice of RMS inputs.

The final study of turbulence statistics considered in this section is an assessment of turbulent length scales via two-point correlations. The standard correlation function, f_{ij}, of velocity component i in direction j is given by

$$f_{ij} = \frac{R_{ij}}{RMS(u_i)}. \tag{4.3}$$

The function R_{ij} is itself given by

$$R_{ij} = \overline{u_i'(\vec{x})u_i'(\vec{x} + r_j)}, \tag{4.4}$$

where r_j is correlation length in the given direction.

Correlation functions for the DNS case are plotted in figure 4.6. Since the flow is only homogeneous in span, only the three correlations in the z direction are given. The data has been captured over the whole span and between $y^+ = 5$ and $y^+ = 70$ in the wall normal direction. The prescribed two-point correlation at the inflow is given in black, with the chosen integral length scales drawn as the vertical dashed lines. Starting off as a purely exponential form (as defined by the inflow method), the correlation function quickly develops a typical rounded peak and the size of the length scales noticeably increase towards the end of the domain. Although this might suggest that some of the input length scales to the inflow method are poorly chosen, the fact that the larger length scale forms within $4h$ of the inflow (i.e. inside the development region) shows that the method is most likely flexible to the choice of length scale. This finding has also been noted by Touber (2010) who implemented a similar turbulence generation method. That all of the correlations level off at zero is a good indication that the domain is long enough in z to contain the largest flow structures.

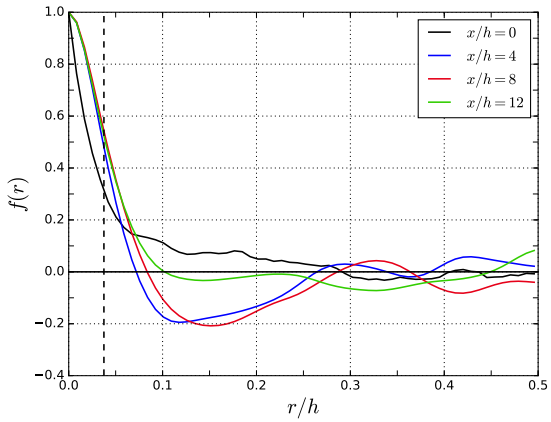

(a) $f(u,z)$.

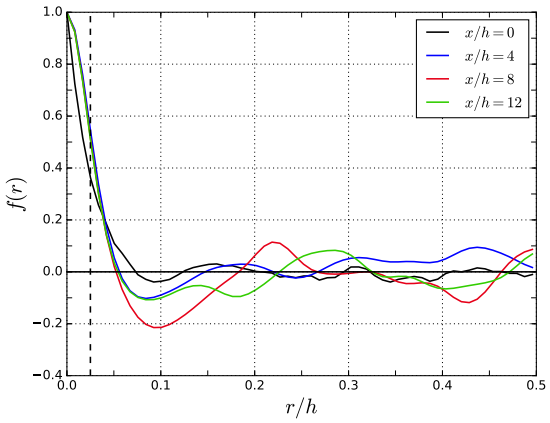

(b) $f(v,z)$.

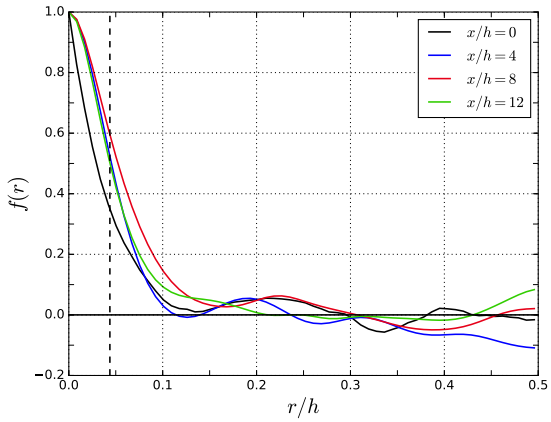

(c) $f(w,z)$.

FIGURE 4.6: Spanwise two-point correlation functions for each velocity component. Dashed vertical lines indicate the input integral length scale values.

4.1.2 Comparison with Established DNS Data

In this section we will compare the results of the supersonic channel to existing reference data. The primary source of this comes a DNS study by Wenzel et al. (2018) who have compiled very detailed information on zero-pressure-gradient boundary layers for various Mach numbers and Reynolds numbers. For the Mach number of the current cases ($M = 2.0$) Wenzel et al. (2018) collected data over the range $Re_\tau = 158{-}482$ and published local boundary layer profiles at $Re_\tau = 252, 359$ & 450. Figure 4.7a shows the spacial distribution of Re_τ for both the ILES and DNS grids in the current work. The range of values $Re_\tau = 130{-}260$ means there is a

good degree of overlap with the reference dataset and allows for a direct comparison with the $Re_\tau = 252$ boundary layer profile.

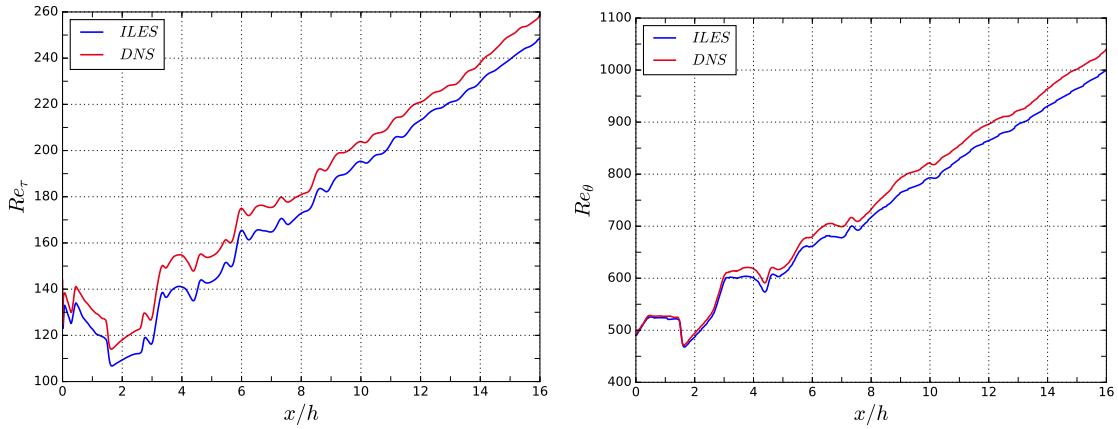

(a) Re_τ. (b) Re_θ.

FIGURE 4.7: Spatial distribution of Reynolds number for the supersonic channel case.

A comparison of the boundary layer profiles are shown in figure 4.8. Data is taken from the end of the domain $x = 16h$ which corresponds to $Re_\tau = 248$ and 258 for the ILES and DNS cases respectively and these are compared to the reference data at $Re_\tau = 252$. All of the profiles are adjusted for density changes although this would not change the comparison given the identical Mach numbers. In general there appears to be a very good fit with the reference profiles, especially with the DNS resolution. The minor exception to this is occurs around $y^+ = 100$ where there is a slight overshoot of the RMS profile. This effect may well be caused by the confinement effects in the channel - at this location the boundary layers occupy around 50% of the channel cross section whereas the arrangement in Wenzel et al. (2018) involves no confinement at all in the wall-normal direction.

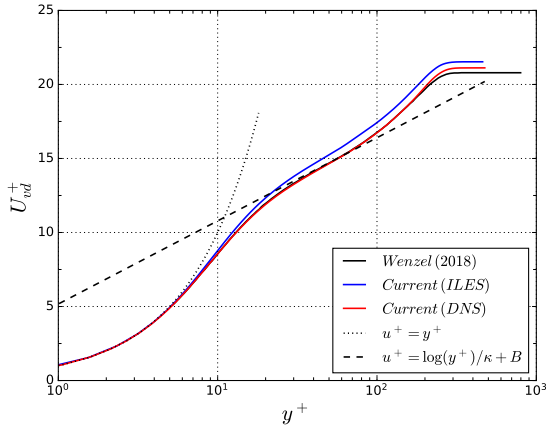

(a) Van Driest-scaled mean velocity profile.

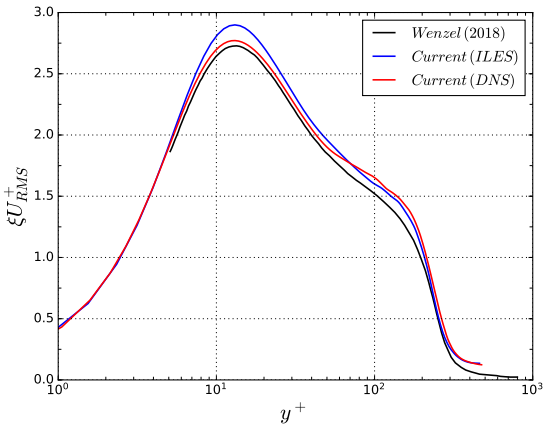

(b) Density-scaled RMS of u'.

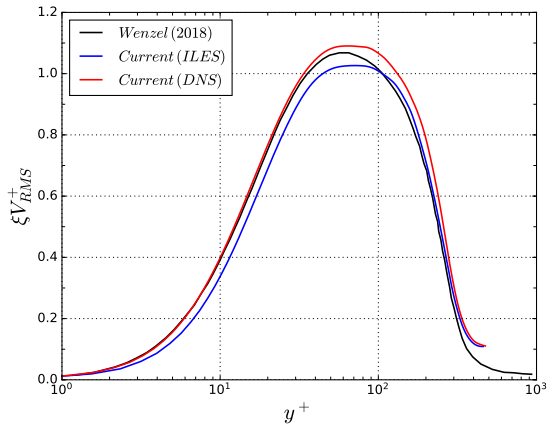

(c) Density-scaled RMS of v'.

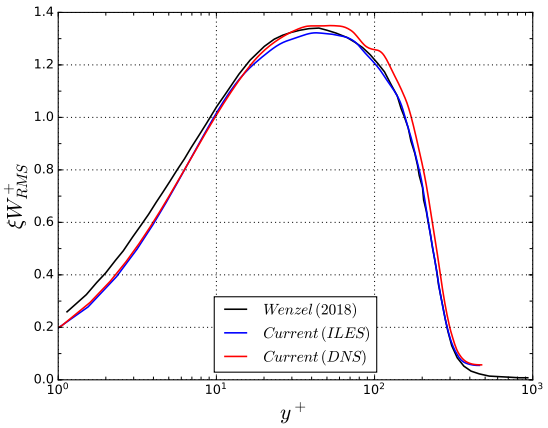

(d) Density-scaled RMS of w'.

FIGURE 4.8: Mean and RMS velocity profiles at $x = 16h$ compared with the reference data from Wenzel et al. (2018). All profiles are adjusted for Mach number/compressibility effects.

In addition to boundary layer profile data, Wenzel et al. (2018) published streamwise distributions of a number of flow properties. In order to provide more generalised comparisons, the streamwise coordinate system of this data is Re_θ instead of x. A comparison of three properties to the current work is shown in figure 4.9. The data is plotted downstream of $Re_\theta = 700$ which corresponds to the edge of the development region at approximately $x = 6h$.

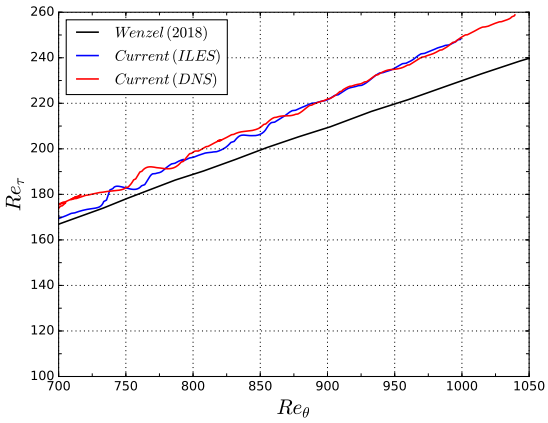

(a) Friction Reynolds number.

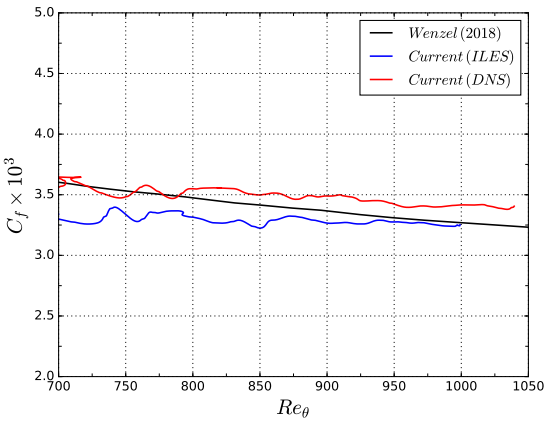

(b) Skin friction coefficient.

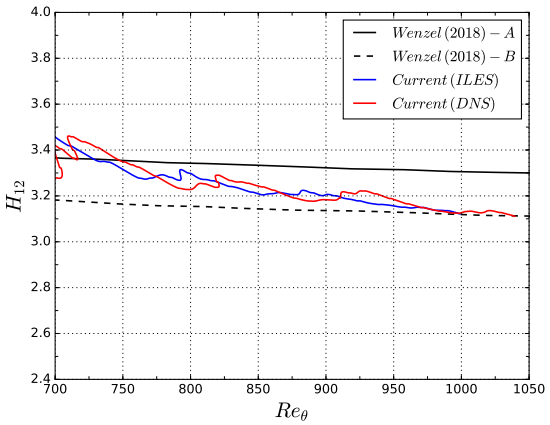

(c) Incompressible shape factor.

FIGURE 4.9: A comparison of flow properties in Re_θ space. The differences with the reference data appears to be due to the confinement effects of the channel which reduces the rate at which the boundary layer thickens.

Although there is a gap in the distributions of Re_τ between the two grid resolutions, this is proportional to the gap in Re_θ which allows the slopes in figure 4.9a to collapse together. This slope is however distinct from that of the reference data. Given the good agreement in the boundary layer profile in figure 4.8a, this difference is most likely caused by differences in Re_θ rather that Re_τ. Due to the high degree of confinement that occurs in the channel, it is probable that there is a lower rate of boundary layer growth compared with the counterfactual, therefore leading to a lower distribution of the momentum thickness towards the end of the domain. A similar effect is seen with the skin friction curve in figure 4.9b, where the reference data diverges from the DNS case results.

In figure 4.9c we compare the distributions of incompressible shape factor, H_{12}. Here, two reference slopes are provided which differ by the definition of displacement and momentum thickness. Taking incompressible displacement thickness as the example, slope A uses the standard definition which integrates the boundary layer all the way to the far-field:

$$\delta^* = \int_0^{\delta_e} \Big(1 - \frac{\overline{u}}{u_e}\Big) dy. \tag{4.5}$$

The definition for slope B on the other hand makes a distinction between the boundary layer edge/freestream (as defined by Spalart and Strelets, 2000), δ_e, and the 99% boundary layer thickness and only integrates as far as the latter:

$$\delta^* = \int_0^{\delta_{99}} \Big(1 - \frac{\overline{u}}{u_e}\Big) dy. \tag{4.6}$$

This distinction is what leads to the noticeable gap between the two curves. The particular definition in the present work is that of slope B, except that the boundary layer edge location is taken as the centreline since there is no far-field. Despite this, it is clear that the shape factor distribution trends towards slope A as it approaches the end of the domain. This is most likely due to the fact that, as the flow nears the outlet and the boundary layer thickens towards the centreline, the δ_e value taken at the centreline trends to δ_{99} rather than the hypothetical freestream value.

4.1.3 Supersonic Duct

Duct/Channel Comparison

Tests on the supersonic duct were performed using a case with dimensions of $24h \times 2h \times 2h$ - differing from the channel case by being 50% longer in x and 100% wider in z. The domain is longer in order to match the duct cases involving shock trains studied in following chapters. Identical boundary layers are generated on all four walls. Due to the memory constraints of the HPC resources, it was only feasible to run a single grid resolution (ILES). Both the Mach number and Reynolds number are consistent with the previous channel cases.

The mid-span flow field is illustrated in figure 4.10. The duct is long enough that the exit is almost entirely dominated by boundary layer flow, although the majority of the flow still remains supersonic. The higher confinement is amplified further by the presence of the sidewall boundary layers. The confinement is large enough to significantly raise the exit pressure (+100%) and if left to run long enough a shock train will eventually form at the exit without any sponge treatment. This effect

however is slow to materialise and all results discussed here are captured be after the boundary layers have converged but before the emergence of the shock train.

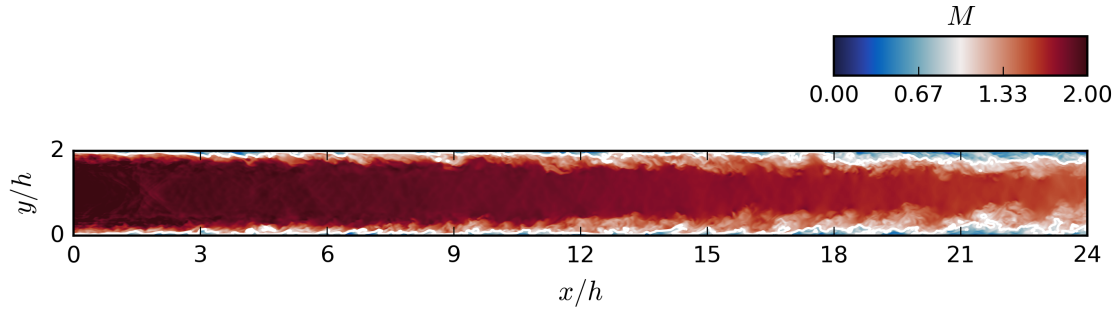

(a) Mach number.

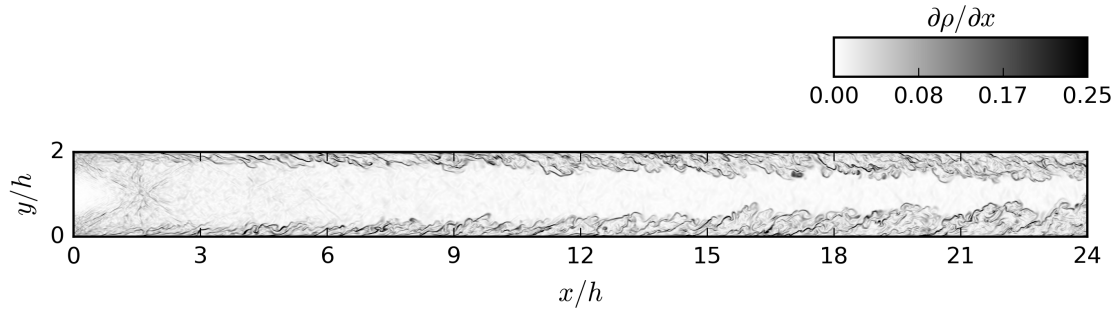

(b) Density gradient.

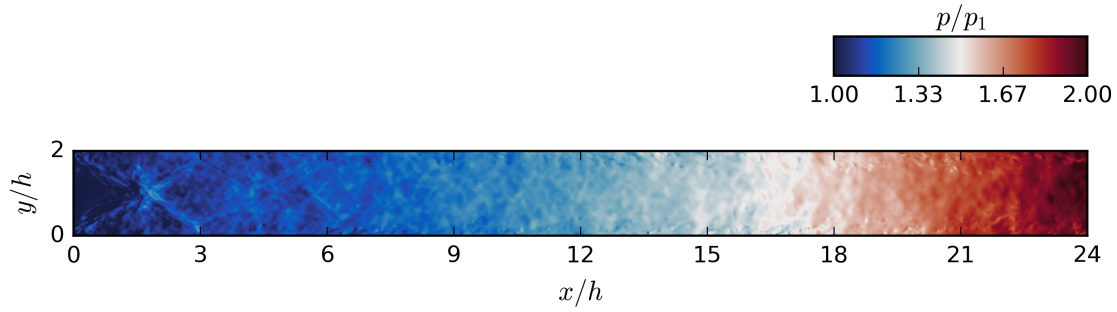

(c) Static pressure.

FIGURE 4.10: Contours of instantaneous flow properties in the x-y plane of the supersonic duct case. Data is from the mid-span plane.

Comparing the results of duct and channel cases allows us to isolate any phenomena which are directly caused by the presence of the sidewalls. Streamwise distributions of key variables are given in figure 4.11, comparing results from the channel and duct cases. Data from the duct case has only been averaged in time

due to the non-homogeneity in the spanwise direction; data is taken from the wall bisector plane at $z = h$ and is plotted up to $x = 16h$. The averaging period for the duct was four convective cycles ($t_{avg} = 96h/u_1$).

Other than the higher pressure which has been previously noted, the duct case exhibits a consistently lower Mach number at the centreline (a consequence of the higher pressure) and more significant disturbances from the inflow compression waves. This is due to the fact that there are a total of four compression waves (one from each boundary) which all meet in the middle of the duct.

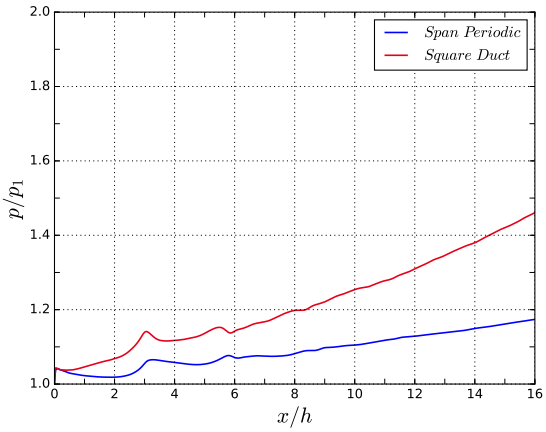

(a) Wall static pressure.

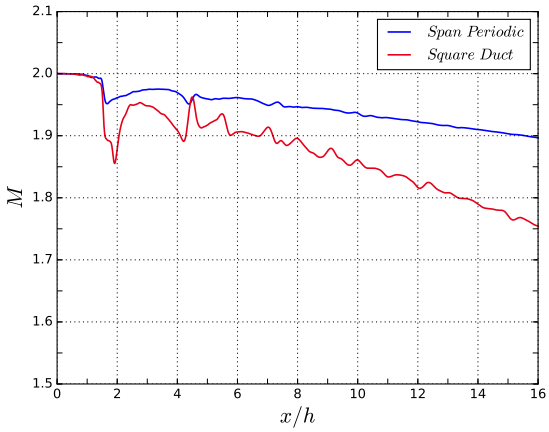

(b) Centreline Mach number.

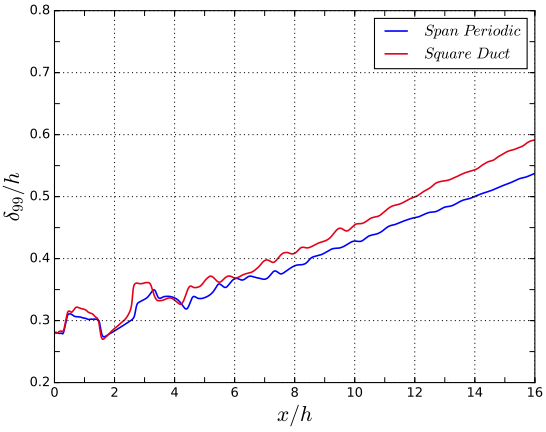

(c) Boundary layer thickness (δ_{99}).

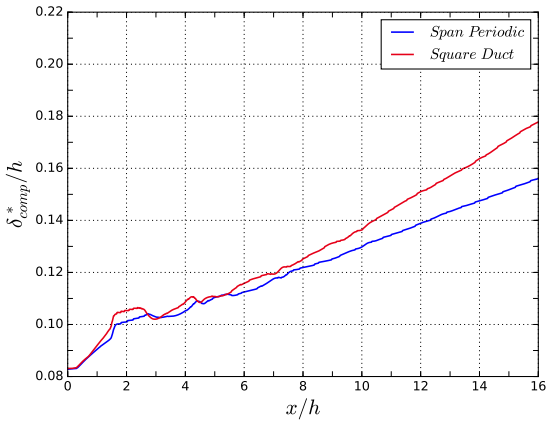

(d) Displacement thickness.

FIGURE 4.11: Comparison of streamwise variation of various time-averaged flow properties between the duct and ILES channel cases.

The duct case also has higher integral thicknesses (figures 4.11c and 4.11d) which is likely caused by the steeper adverse pressure gradient. This results in a feedback loop where the sidewall boundary layers induce a higher pressure via confinement, with the higher pressure causing the boundary layers to thicken even more. As noted previously, this particular arrangement eventually leads to an exit pressure which is high enough to trigger a shock train - this particular phenomenon will be discussed in section 6.1.1.

Development of Secondary Flow Structures

The presence of Prandtl's secondary flow (of the 2nd kind) has been identified in a variety of ducted flows, including in the supersonic regime (see for example Morgan, 2012; Wang et al., 2015). Such structures are also present in the current work and this is visualised in figure 4.12. In this figure streamlines of transverse flow velocity (v, w) are plotted at various streamwise locations. In each corner of the duct a vortex pair is formed, symmetrical about the corner bisectors. The peak (time-averaged) velocity in each vortex is typically around 2% of the freestream velocity as flow is drawn towards and then away from in corners. There is incipient secondary flow at the $x = 4h$ position and a complete vortex structure by $x = 6h$. From there the vortices continue to grow in size until they occupy more-or-less the entire cross section by $x = 20h$. At this point the vortices are constrained by those in opposing corners and so remain at a constant size.

Figure 4.13 provides another perspective of the vortex development. Here, transverse flow velocity ($\sqrt{v^2 + w^2}$) is plotted against the location along the corner bisector, λ, at the evenly spaced streamwise locations. Each curve represents an average across all four corners and each chart shows the development along sections of the duct. In the first quadrant (4.13a) the structure of the velocity profiles starts to develop, forming a clear velocity peak. In the second quadrant (4.13b) the velocity profile remains steady as the overall vortex size continues to increase. During the third quadrant (4.13c) the peaks broaden and reduce in height. The vortex structures begin to interfere with each other and a second velocity peak forms with a saddle point approximately midway between the corner and centre point. Over the final quadrant (4.13d) the main velocity peak continues to broaden even more and the second peak disappears. The trend suggests that the vortices will continue to develop and mature even after occupying the entire duct.

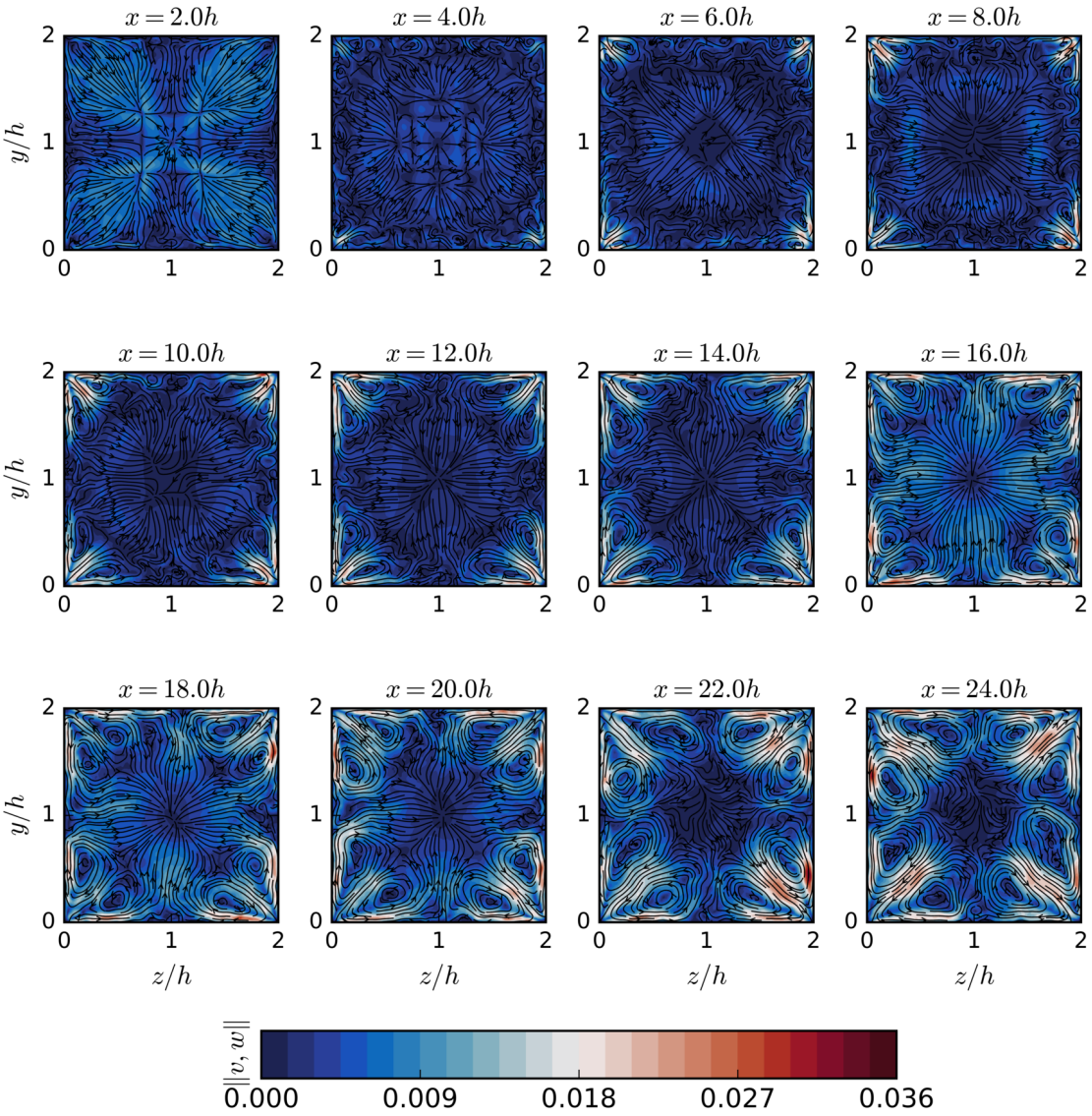

FIGURE 4.12: Velocity streamlines showing the emergence and development of secondary flow structures. Plots are coloured by transverse velocity magnitude, $\sqrt{v^2 + w^2}$.

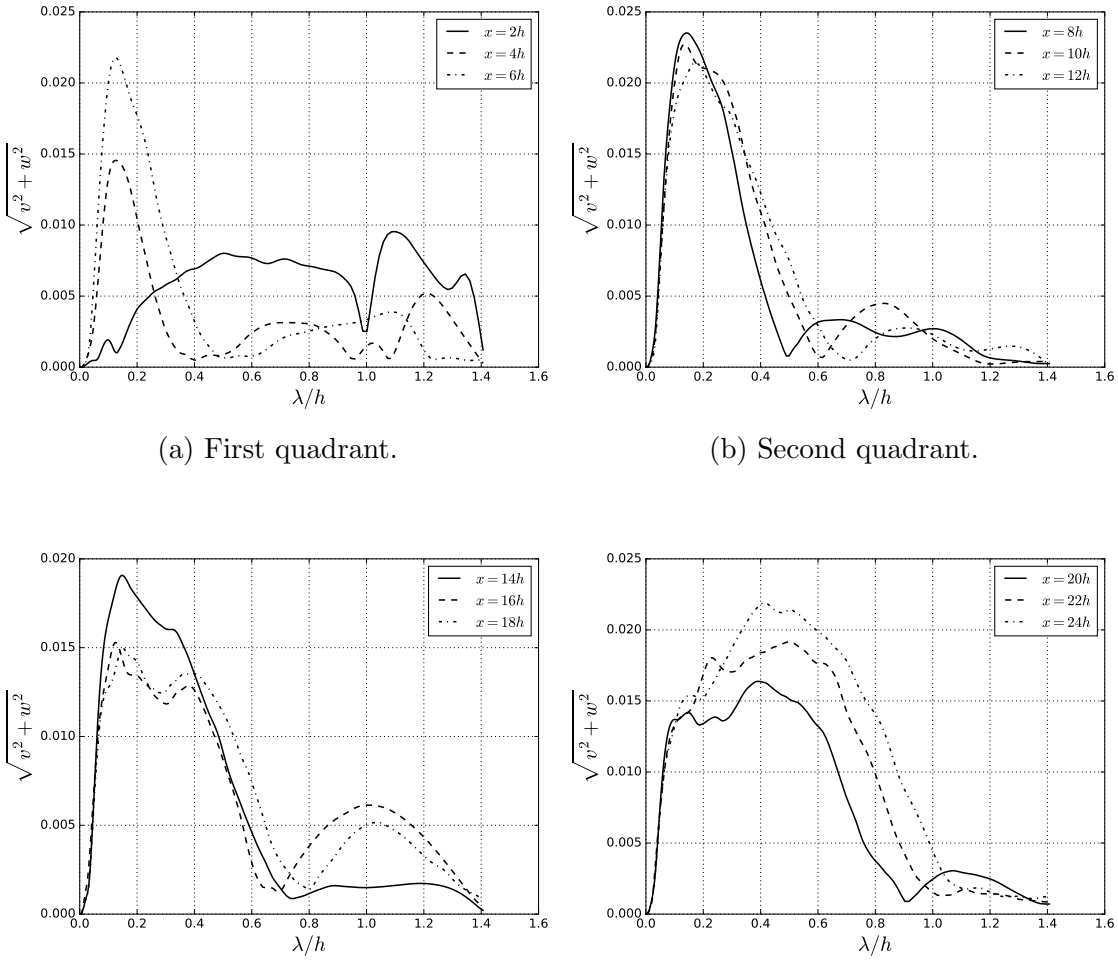

(a) First quadrant.

(b) Second quadrant.

(c) Third quadrant.

(d) Fourth quadrant.

FIGURE 4.13: Plots of transverse flow velocity ($\sqrt{v^2 + w^2}$) against distance along the corner bisector. Plots are split into four equal sections along the duct.

4.2 Shock Train

4.2.1 Flow Field Analysis

All cases in this section are run using the same channel arrangement outlined in section 4.1.1. The sponge zone is active and induces a pressure ratio (p_b/p_1) of 3.0 across the length of the domain. This results in a shock train forming in the latter half of the channel, with the wave front of the shock train settling at a position of $x = 7h$.

The converged flow field of the shock train (CDNS case - see section 4.3) is presented in figure 4.14. Here we can see that four separate shock waves form, causing a significant thickening of the boundary layer. A significant portion of the flow cross-section becomes subsonic, although a supersonic core remains all the way to the exit. The first shock, composed of two oblique shocks and a primary normal shock (see also figure 2.6c), causes a permanent separation bubble to form as shown by the solid white lines in figure 4.14a. Further downstream there are additional pockets of transient separation inside the subsonic region. The remaining shocks in the shock train are purely normal shocks.

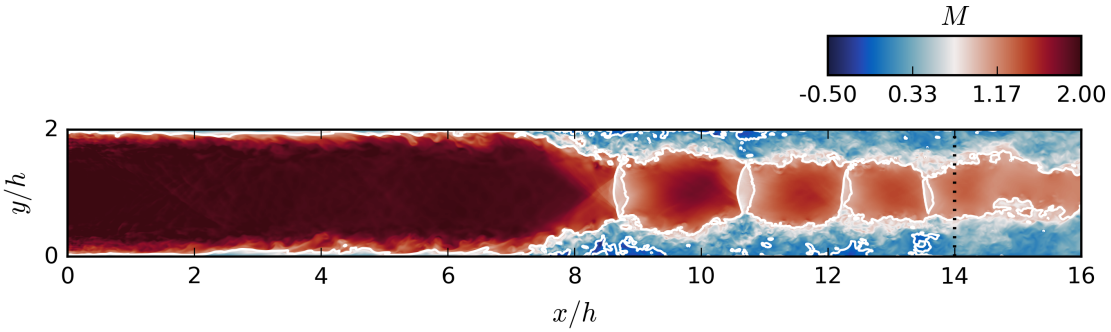

(a) Mach number. Sonic lines and separation regions are drawn in white.

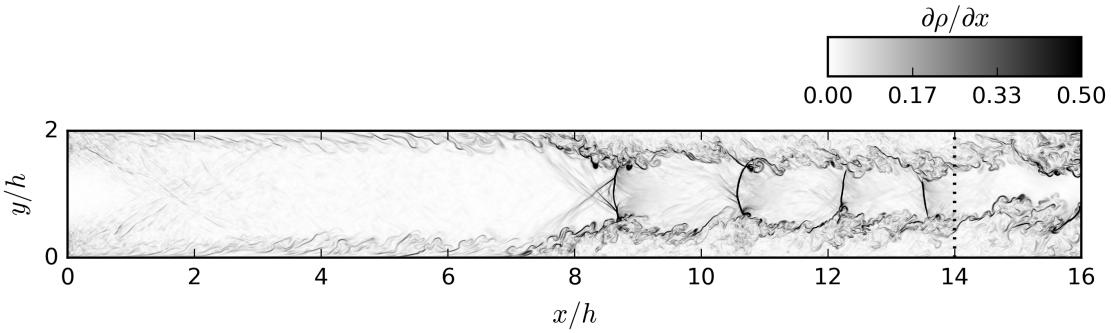

(b) Density gradient.

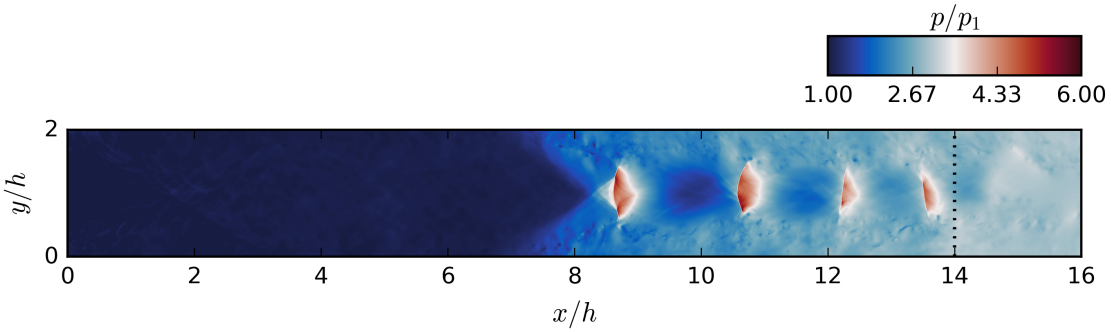

(c) Static pressure.

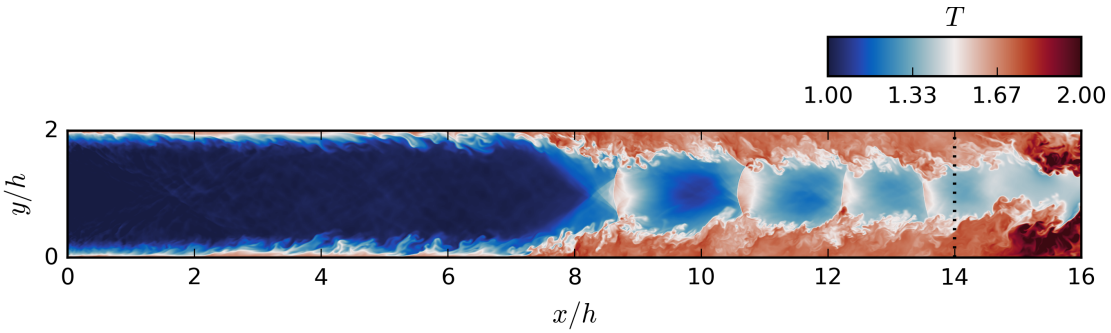

(d) Temperature.

FIGURE 4.14: Contours of instantaneous flow properties in the x-y plane of the span-periodic shock train case. The shock train is composed of four individual shock waves with the leading edge stabilising at approximately $x = 7h$. The limit of the sponge zone is indicated by the dashed line.

4.2.2 Statistical Data

A plot of time- and span- averaged pressure distribution at both the wall and centreline is shown in figure 4.15. This resembles the canonical pressure distribution of shock trains; the wall pressure rises in a gentle arc while the freestream pressure has peaks and troughs as it crosses each of the shock waves and expansion regions. Both distributions settle at the same target back pressure ($p_b/p_1 = 3.0$) as enforced by the sponge zone.

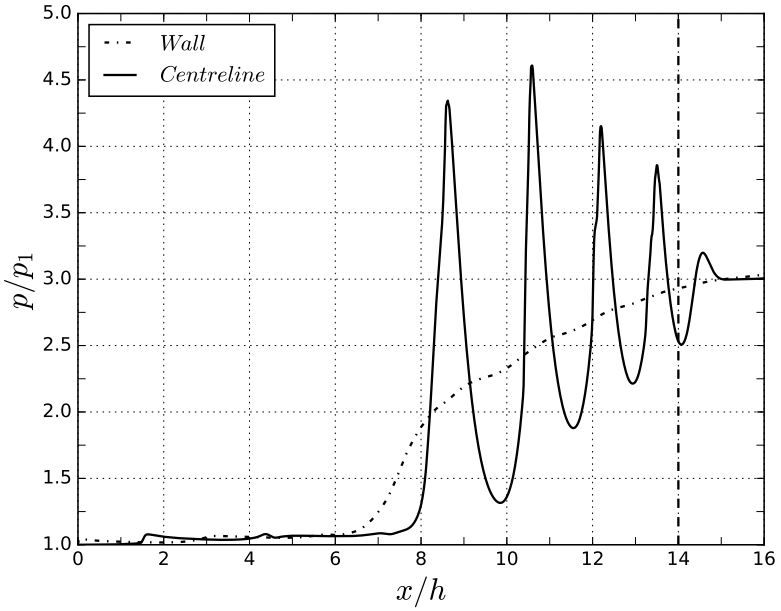

FIGURE 4.15: Plot of centreline and wall pressure through the shock train. The limit of the sponge zone is indicated by the vertical dashed line.

The initial pressure rise at the wall (i.e. the furthest upstream extent of the shock train) is located between $x = 6h$ and $x = 7h$. Due to the findings in section 4.1.1, at this stage all of the main parameters of the boundary layer have converged to a satisfactory state. The disturbances caused by the inflow compression waves are present but clearly dwarfed by the pressure changes within the shock train. Something which is also apparent is the high degree of recovery that the flow experiences immediately after each of the shock waves; there is a very rapid expansion following the shock wave contraction. This expansion mechanism is a direct consequence of the confinement and is what allows multiple shocks to coexist.

Additional plots are given in figure 4.16 showing Mach number and skin friction distributions. The change in centreline Mach number tells a similar story to that of the centreline pressure. The natural increase in confinement along the channel leads to a slight reduction in the Mach number ahead of the shock train. At this point the Mach number sharply drops to below 1 as it crosses the first shock wave, before recovering to $M = 1.8$ which is roughly 95% of its pre-shock level. There are three further contraction-expansion cycles before the pressure conditions demanded by the sponge zone are met. The flow exits the domain at the centreline at approximately $M = 1.2$. Supersonic exit flow is atypical of pressure-induced shock trains where the high degree of boundary layer confinement near the end of the domain is enough to force a fully subsonic flow. In this situation however, the boundary layer thickness

remains low enough to allow a core of supersonic flow.

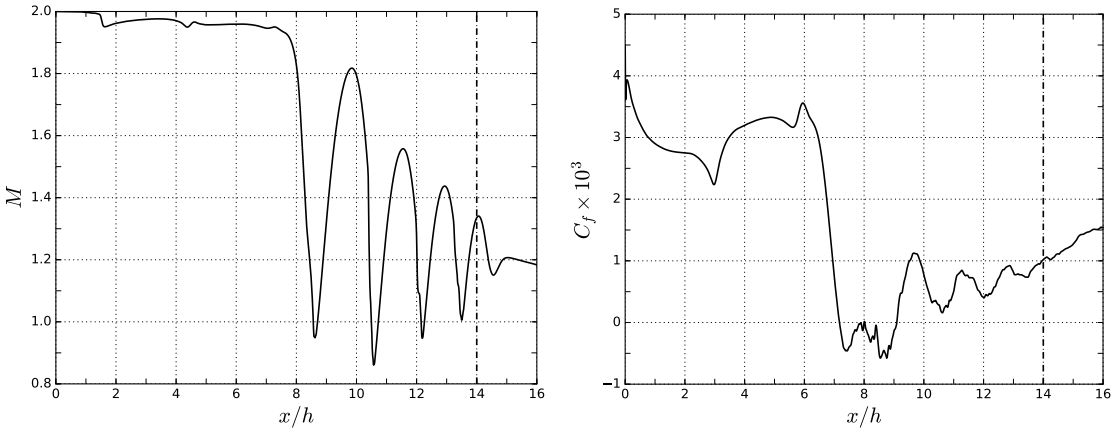

(a) Centreline Mach number. (b) Skin friction coefficient.

FIGURE 4.16: Plots of time- and span-averaged Mach number and skin friction across the shock train. The $C_f < 0$ region indicates a separation bubble.

The distribution of skin friction in figure 4.16b provides information about the flow at the wall through the shock train. The large pressure gradient of the first shock causes the skin friction to drop sharply below zero, indicating a region of reversed flow which is approximately $2h$ long. After the flow reattaches, the skin friction remains low and fairly volatile as it slowly rises to the exit. The volatility of the distribution under the shock train indicates that this region is dominated by unsteady turbulent flow.

Contour plots of time-averaged flow properties can be seen in figure 4.17. The statistical data provides a clearer view of the structure of the shock train than the instantaneous flow field. The distinction between subsonic and supersonic regions is very clear in figure 4.17a. The ramp-like structure of the head of the subsonic region causes compression waves to form, which converge at the first shock. The supersonic regions between the shocks are distinctly barrel-shaped, each getting progressively smaller as the subsonic region grows in size. The bulging in the middle of these shock cells are directly due to the expansions which immediately follow the shock waves.

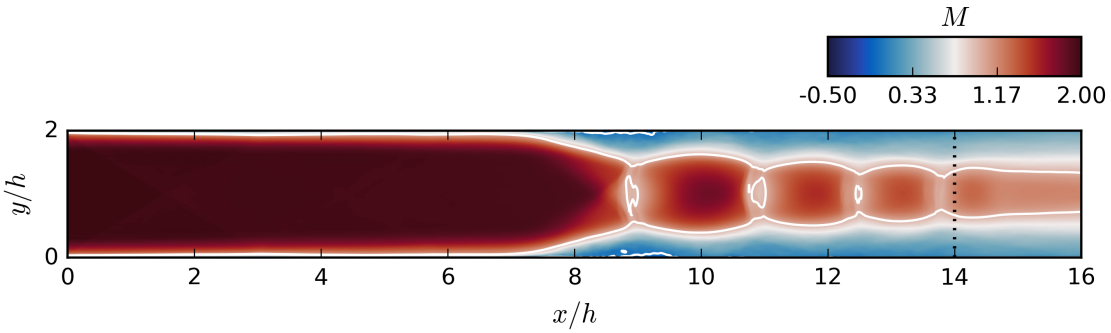

(a) Mach number. Sonic lines and separation regions are drawn in white.

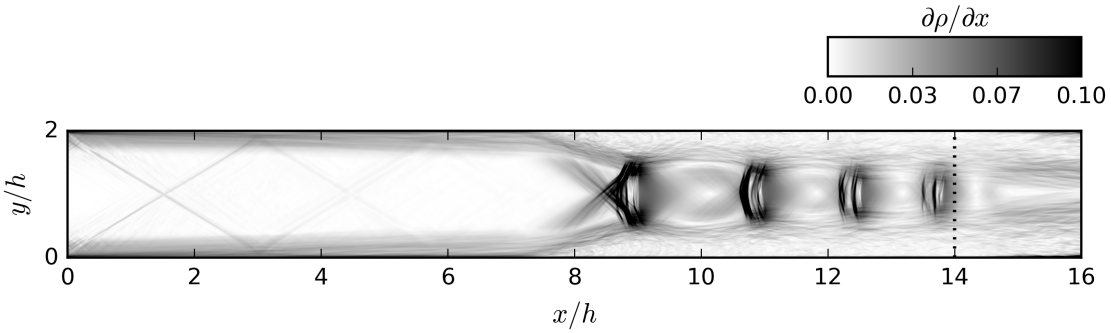

(b) Density gradient.

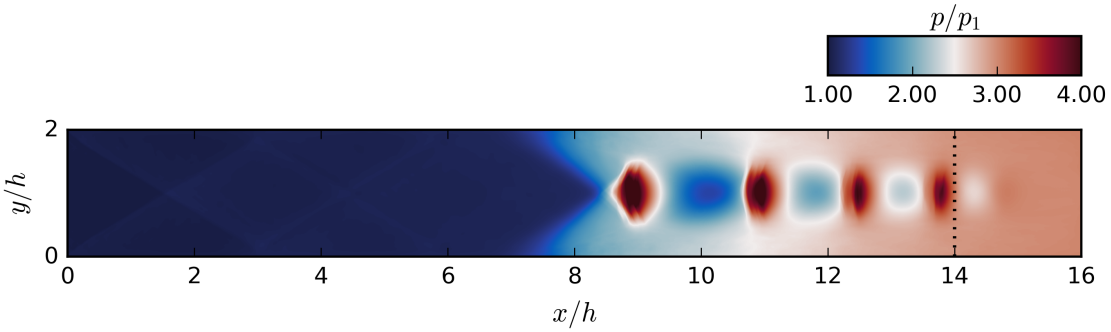

(c) Static pressure.

FIGURE 4.17: Contours of time-averaged flow properties in the x-y plane of the span-periodic shock train case. The limit of the sponge zone is indicated by the dashed line.

The density gradient plot (figure 4.17b) reveals the inflow compression waves which appear as the "X" on the left of the figure. Both waves reflect at around $x = 3h$ producing another, fainter,"X" further downstream. The third set of compression waves is, however, too weak to be visible. The unsteadiness of the shock

wave positions is indicated in this figure where the averaging period has captured a number of locations for each shock as they have moved in response to upstream conditions. The flow averaging means that the regions of subsonic flow are smaller in figure 4.17a than the instantaneous flow field in figure 4.14a.

Overall, these results demonstrate that the sponge zone can effectively enforce the pressure condition and generate a shock train. Since the sponge zone imparts a body force term, the sponge region itself should be considered strictly non-physical.

4.3 Grid Refinement Study

The purpose of the grid refinement study is to gain a good understanding of which properties of the flow converge at which particular grid resolution. Due to resource constraints, it is not always feasible to run every case at the finest possible grid, so understanding which details are captured at which resolutions is a vital step. The study is performed on the same shock train channel arrangement as the previous section (span-periodic, top and bottom solid boundaries, 3:1 pressure ratio). Three different grid resolutions are used here and are outlined in table 4.2. Two of these grids have been used previously in section 4.1 (ILES & DNS) while the CDNS (coarse DNS) grid has an intermediate degree of grid refinement.

Grid	N_x	N_y	N_z	Δx^+	Δy^+ (min/max)	Δz^+	Δt
ILES	800	320	60	9	0.8/5	8	0.016
CDNS	1200	480	90	6	0.5/3.5	5	0.008
DNS	1600	480	120	4.5	0.5/4.0	4	0.008

TABLE 4.2: Summary of grid resolutions used in the grid refinement study. Viscous grid spacing values are calculated with the local u_τ value at $x = 6h$.

Despite the very low reported viscous grid spacings for the ILES case (similar to that of other DNS studies), it is still assumed that not all of the Kolmogorov-scale structures are resolved and that the dissipation at this level is implicitly modelled by the natural dissipation in the TENO scheme.

The main results from the study are given in figures 4.18 and 4.19, where distributions of eight flow properties are shown. These charts reveal the relative grid convergence of different aspects of the flow. Starting with the first four charts (figure 4.18), all three grid resolutions produce similar distributions of inertial properties

(i.e. pressure and Mach number) albeit with offsets in the streamwise direction. In general ILES grid is able to capture accurately the upstream undisturbed flow and provides a reasonable fit for the location of the shocks and the pressure distribution throughout the shock train. The ILES and CDNS grids underestimate the the shock positions (compared to the DNS) by $0.65h$ and $0.15h$ respectively and these values appear to remain consistent throughout the shock train.

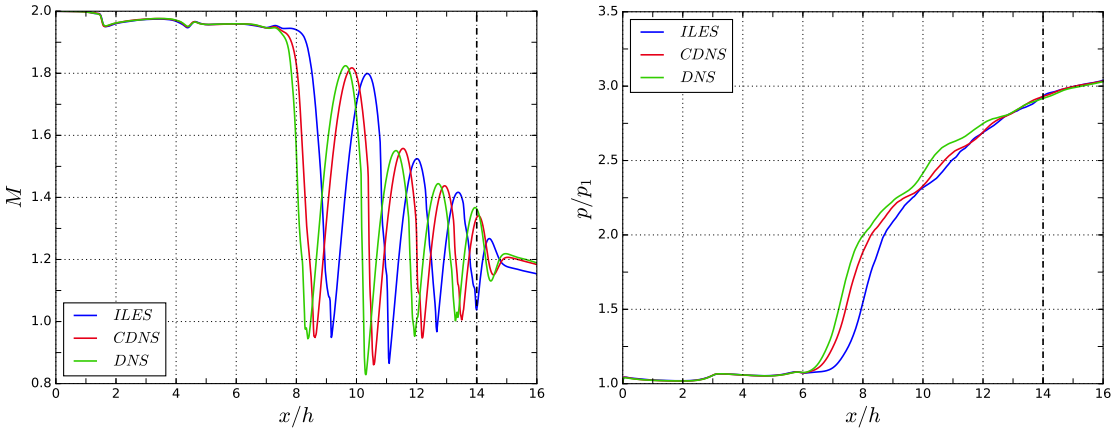

(a) Centreline Mach number.

(b) Wall static pressure.

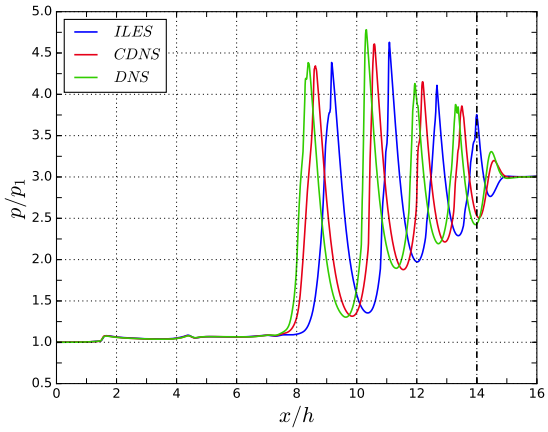

(c) Centreline static pressure.

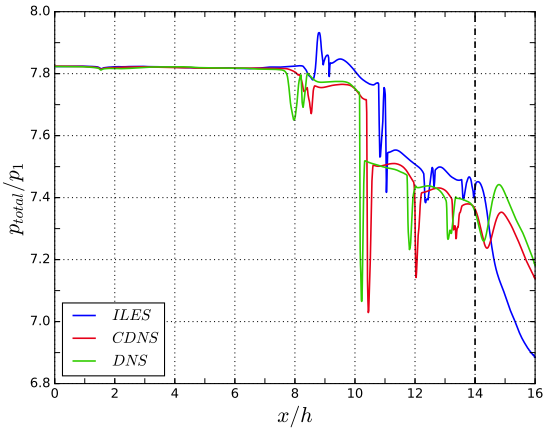

(d) Centreline stagnation pressure.

FIGURE 4.18: Streamwise variation of averaged inertial flow properties comparing different grid resolutions.

The pressure peaks are similar for each case, suggesting similar shock strengths and a similar degree in shock wave unsteadiness (the averaging period is consistent

between all of the cases at $64h/u_1$). The distribution of stagnation pressure through the shock train generally seems to be poorly matched when compared to the finer grids, although scale on the y-axis suggests that the relative difference is quite small.

A similar story can be told about the boundary layer properties in figure 4.19, namely that the ILES grid is able to capture the overall shape of the shock train but misses some of the finer details, which are only revealed in the finer grids. The skin friction distribution produces probably the biggest difference (certainly in the undisturbed region), as discussed previously in section 4.1.1.

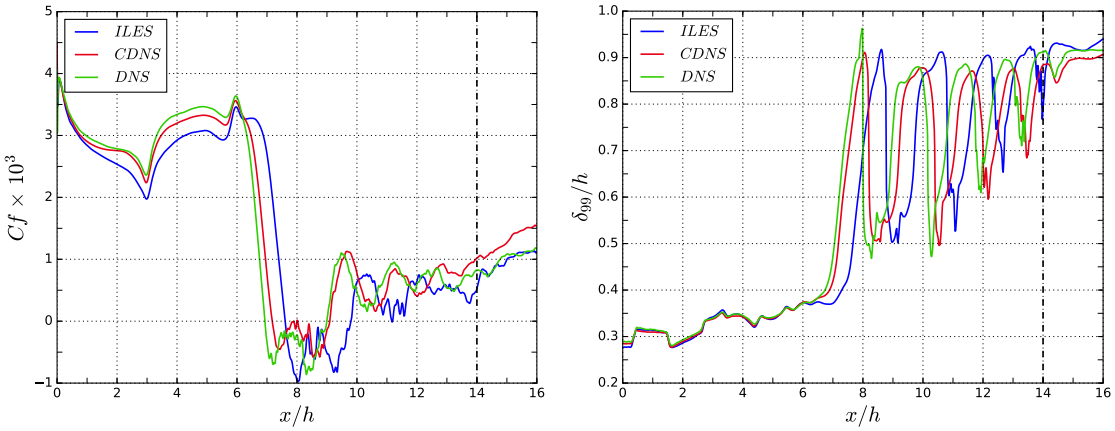

(a) Skin friction coefficient.

(b) Boundary layer thickness (δ_{99}).

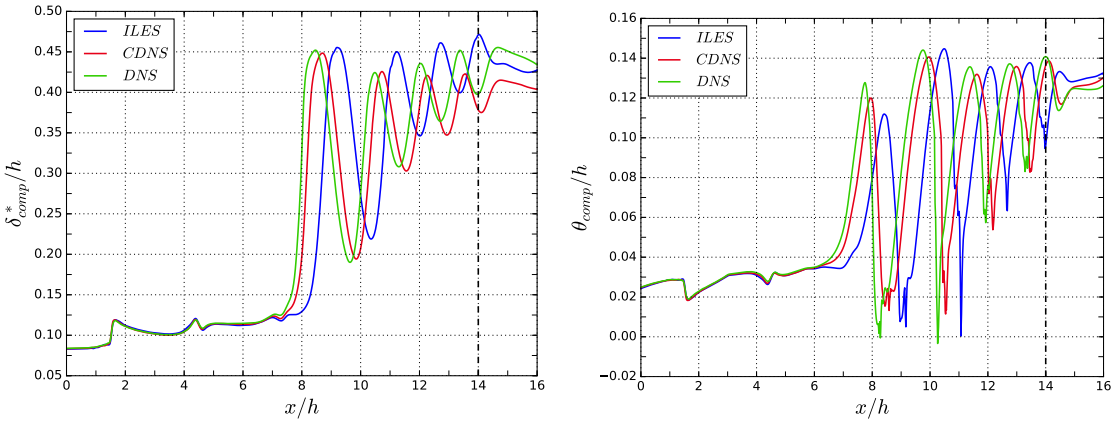

(c) Compressible displacement thickness.

(d) Compressible momentum thickness.

FIGURE 4.19: Streamwise variation of averaged boundary layer flow properties comparing different grid resolutions.

The CDNS once again appears to be very well converged, although there do appear to be some slight differences with the DNS grid, such as with the skin friction just ahead of the shock train and the displacement thickness near the exit.

Illustrations of the respective flow fields of each of the grids can be seen in figure 4.20. Generally there seems to be very little qualitative differences in the overall structures of the turbulent boundary layer and shock train, although there is a suggestion that the shock structures in the finer grids are more well-defined.

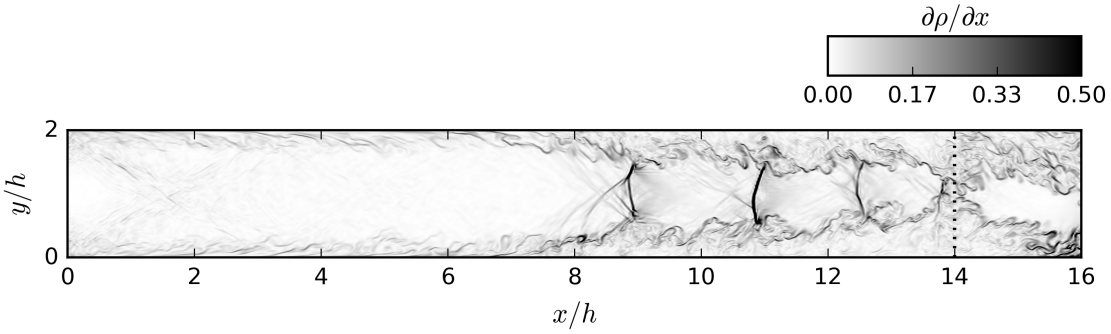

(a) ILES grid.

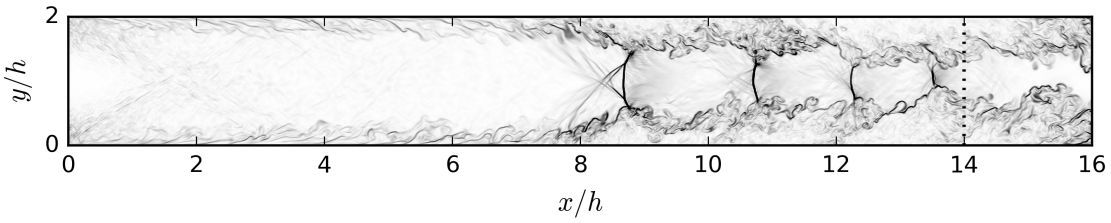

(b) CDNS grid.

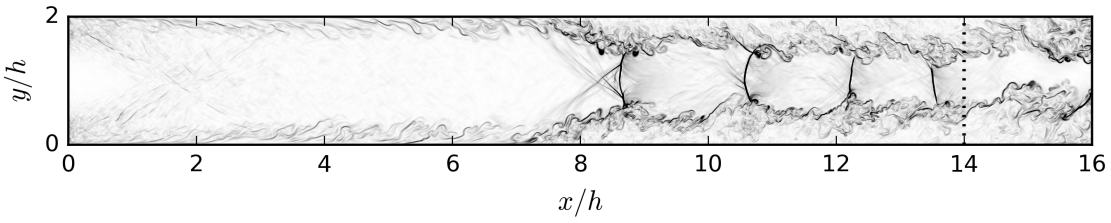

(c) DNS grid.

FIGURE 4.20: Contours of instantaneous density gradient for each of grid resolution. The limit of the sponge zone is indicated by the dashed line.

As the grid study is used to understand the limitations of each grid and therefore allocate resources accordingly, a summary of the grid resolutions is given below. The

relative computational cost of each grid (including adjustment for the CFL number) is given in brackets.

- ILES (×1.0): Appropriate for understanding the overall structure and dynamics of the shock train.
- CDNS (×5.0): Provides very good prediction of all properties. For use when accurate distributions are required.
- DNS (×10.7): More resolution than is needed to capture the turbulent flow properties in the shock train. Required for very accurate shock wave positions.

A summary of the computational performance of each of the grid cases is given in 4.3. All of the cases were run using Nvidia Telsa P100 GPU machines at the University of Cambridge HPC facility. The number of GPUs used for each case is given as well as the wall time required to process 100,000 time steps - this is a good proxy for the scaling capacity of the code. The last column gives the computational cost (GPU-hours) which is required to complete one convective cycle.

Grid	# GPUs (# nodes)	Wall time per 100k iters	Cost per FTT (GPU-hr)
ILES	2 (1/2)	12hrs	9.6
CDNS	4 (1)	15hrs	48.0
DNS	8 (2)	18hrs	102.4

TABLE 4.3: Outline of the computational performance of each of the grid cases.

4.4 TENO Scheme Sensitivity

The final stage of the validation process is to test how the dissipation level of the TENO scheme affects the shock train behaviour. Such is the nature of shock capturing schemes, there is always a trade off between high dissipation (which provides stability) and low dissipation (which provides accuracy). The controlling parameter for dissipation in the TENO scheme is the cut-off parameter (C_T) which determines which candidate stencils are included in the final formulation. The benchmark value of C_T (i.e. the value which generally produces acceptably accurate and stable simulations) is 10^{-6}, however some of the moving shock train cases in chapter 6 were found to be numerically unstable, having to resort to a value of $C_T = 10^{-5}$ instead. It was therefore important to test for the effect of different C_T values and these results are given in figure 4.21. Both cases use the ILES grid since this was used in the unstable cases in question.

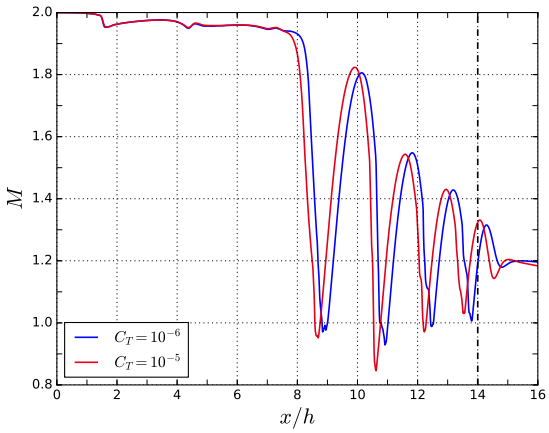

(a) Centreline Mach number.

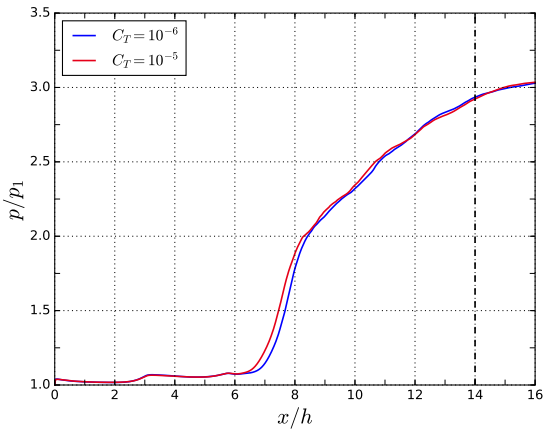

(b) Wall static pressure.

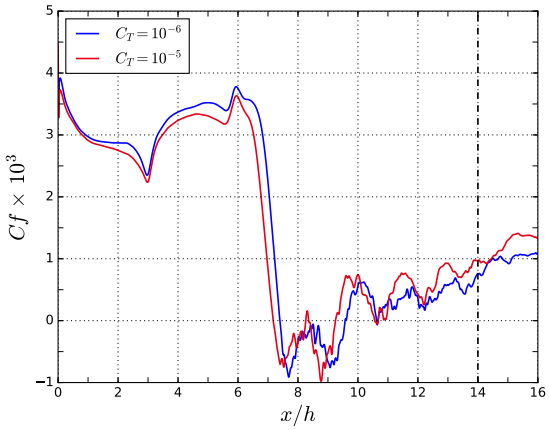

(c) Skin friction coefficient.

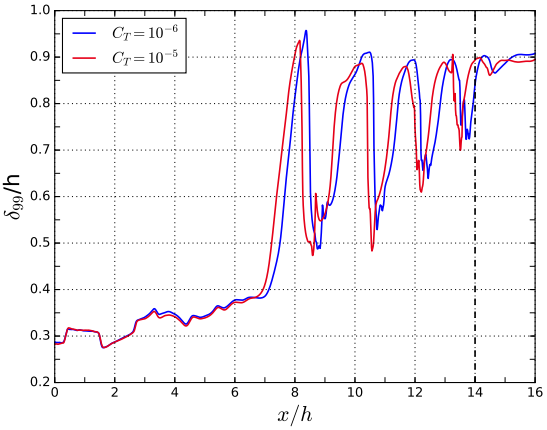

(d) Boundary layer thickness (δ_{99}).

FIGURE 4.21: Streamwise variation of averaged flow properties comparing different dissipation levels.

The results show that the effect of increasing the cut-off threshold (i.e. increasing the dissipation) by an order of magnitude is similar to that of moving from a finer grid to a coarser grid; namely that the structure of the shock train is preserved with only a slight mismatch in the streamwise position. Interestingly, the initial location of the shock train in the high dissipation case is slightly upstream, meaning that it is closer to the position predicted by the finer grid resolutions. Generally, there does not seem to be any appreciable penalty to increasing the dissipation that is not already caused by the lower grid resolution.

4.5 Summary

The purpose of this chapter is to validate the underlying numerical methods and techniques, thereby providing a foundational basis for the main research in this project. Additionally, the non-shock train cases provide a useful counterfactual to the study of shock trains throughout the remainder of this thesis. The main findings are as follows:

1. **Turbulent boundary layer:**
   (a) We show that the inflow turbulence method is able to generate and sustain a supersonic turbulent boundary layer.
   (b) Analysis of the turbulence statistics shows that most properties are fully developed by $x = 6h$ and all properties by $x = 8h$.
   (c) Comparison with established DNS data at matching flow conditions shows very good agreement with the current work.
2. **Effect of sidewalls on boundary layer:**
   (a) The added confinement effect of the sidewalls causes an increase in exit pressure and increase in boundary layer thickness compared to the infinite-span channel case.
   (b) The sidewalls cause corner vortex pairs to form which subsequently grow large enough to cover the entire duct cross section.
3. **Shock train and grid study:**
   (a) We are able to demonstrate that the sponge zone method is able to enforce a high back pressure and cause a stable shock train to form.
   (b) By considering three different grid resolutions, a good understanding was gained of the grid convergence.
   (c) The coarsest grid (ILES) is able to capture most of the detail of the shock train and is therefore sufficient for most purposes.
   (d) The CDNS grid provides fully converged distributions of the shock train properties while the finer DNS grid is only required for very precise boundary layer/turbulent statistics and shock placements.
   (e) A study of the numerical scheme was conducted demonstrating the flexibility of the code to a higher dissipation mode of the TENO scheme.

Chapter 5

Parametric Studies

This chapter quantifies the effects of a number of governing parameters on the shock train behaviour. Due to the particularly low Reynolds number of the current work, it is important to document such responses. The principal parameters studied here are back pressure (p_b), Reynolds number (Re_θ) and confinement ratio (δ_{99}/h). Additionally, we will consider the effect of the sidewalls and spanwise confinement. The latter sections are devoted to a modelling comparison and a detailed examination of the shock train structure.

5.1 Effect of Back Pressure

Due to the use of dynamic back pressures in the following chapter, it was necessary to understand the specific effects of a steady back pressure. In order to do this, three separate back pressures were tested on the baseline span-periodic case. The grid resolution chosen for each was the CDNS grid which, as discussed in section 4.3, captures all of the necessary flow details.

The cases in this study are outlined in table 5.1. The back pressures are selected such that the pressure ratios (p_b/p_1) over the channel are 3.0, 2.75 and 2.5. All of these back pressure values allow for a stable shock train to form within the domain without extending into the boundary layer development region. The Baseline case discussed here is identical to the CDNS grid case considered in grid refinement study. Given that shock trains are formed in response to high back pressures it is expected that, all else being equal, a lower back pressure will result in a shorter shock train with fewer shock waves (Klomparens et al. (2015) for example, found a linear relationship between the back pressure and the location of the shock train leading edge). Indeed, a positive relationship is confirmed in figure 5.1 where the a typical flow field of each case is shown.

Case	Grid	p_b	p_b/p_1
Baseline	CDNS	0.536	3.0
BP2.75	CDNS	0.446	2.75
BP2.5	CDNS	0.357	2.5

TABLE 5.1: Summary of cases for the back pressure study.

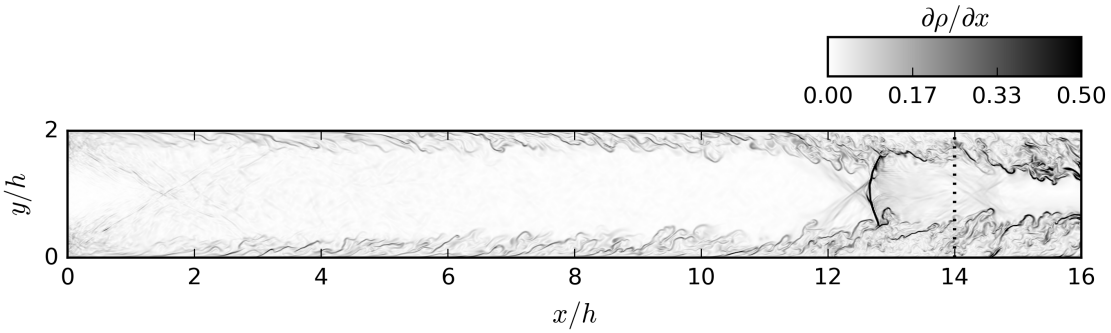

(a) BP2.5.

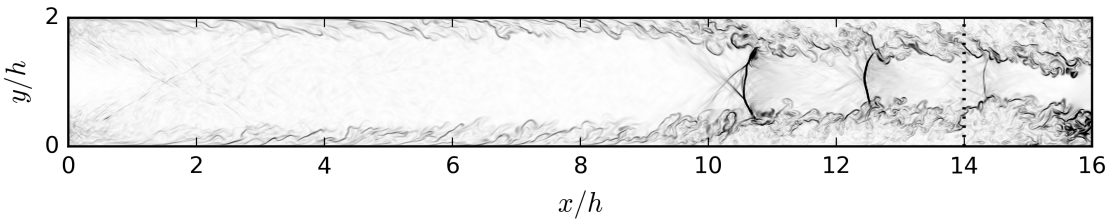

(b) BP2.75.

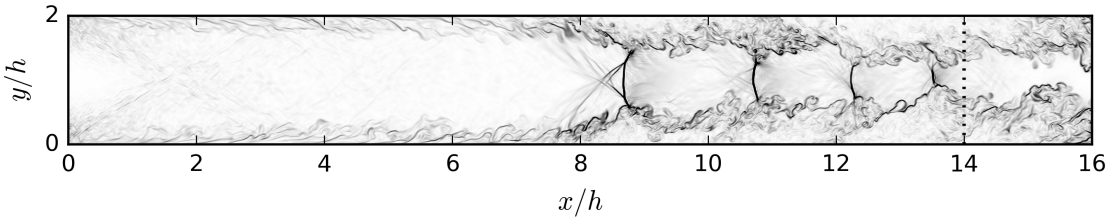

(c) Baseline.

FIGURE 5.1: Contours of instantaneous density gradient for different applied back pressures. A higher back pressure is associated with an upstream shift of the shock train due to the fact that a larger shock system is needed to accommodate the higher pressure rise.

The higher the back pressure, the further upstream the leading shock is located and the more shock waves form. The lowest back pressure only results in a single shock forming, compared with three shocks in the intermediate case and four in the Baseline case. The structure of the leading shock remains consistent in each case.

The data from each case has been averaged over a period of $64h/u_1$ and the results are shown in figure 5.2. Each chart shows how the upstream flow field remains undisturbed, with the data ahead of the shock train collapsing together. The length of the shock train here is taken to be $l_{ST} = l_x - x_2$, where l_x is the domain length and x_2 is the location where the wall pressure rises 5% above the zero pressure gradient case (discussed in section 4.1.1). Thus, we can find the overall shock train length for each case (note that this includes the sponge zone).

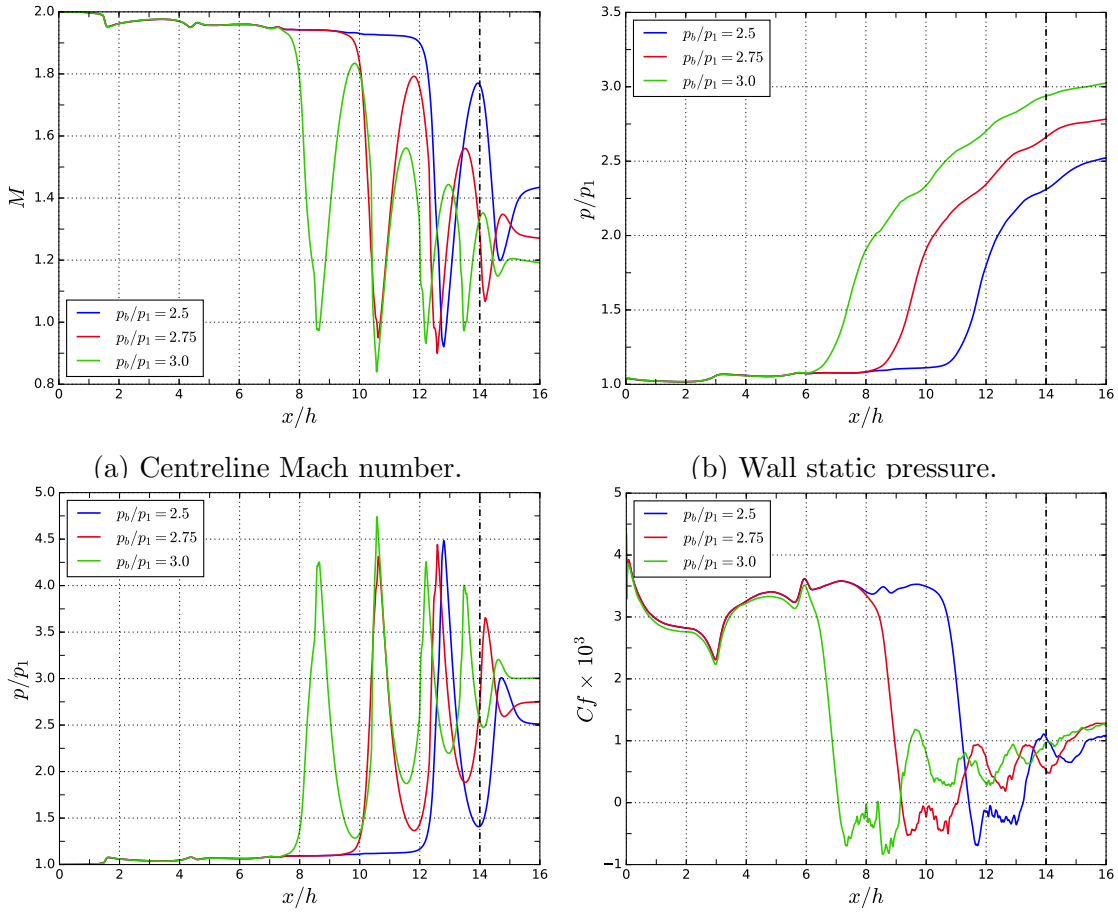

(a) Centreline Mach number.

(b) Wall static pressure.

(c) Centreline static pressure.

(d) Skin friction coefficient.

FIGURE 5.2: Streamwise variation of averaged flow properties comparing different applied back pressures.

For the three cases the shock train length is found to be $9.43h$, $7.36h$ and $5.10h$ in order of decreasing back pressure. In figure 5.3 we plot the shock train length against the total pressure change between inlet and outlet, Δp, along with a linear best-fit. Given the low number of data points, the statistical power of this regression is limited and thus are any inferences that can be made. However there is a suggestion of a linear relationship between the pressure gradient and the shock train length. It should be noted that the best fit line does not intersect the $(0, 0)$ coordinate and instead intersects the x axis at $\Delta p/p_1 = 0.91$. This suggests that a minimum pressure ratio of 1.91 is required for a shock train to form in the channel.

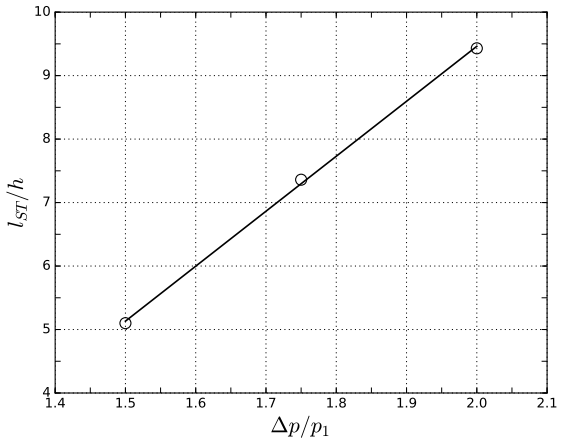

FIGURE 5.3: Effect of pressure gradient on shock train length with linear regression line.

As is typical for wall pressure distributions for shock trains (and other forms of SBLI), the slope is steeper near the beginning of the shock train before gradually levelling out towards the exit. This means that most of the pressure rise is associated with the first shock and helps explain why the lower back pressure only required a single shock wave despite the fact that the pressure gradient is only 33% larger compared to the Baseline case.

Its notable in both figure 5.1 and 5.2 that the shock structure appears to be very similar between the different cases and this idea is further explored in figure 5.4. Here the same properties are plotted but normalised by the location of the first shock (x_3). Each of the distributions collapse extremely well, demonstrating that not only are the spacing and relative positions of the shock waves well matched, but that the Mach number and pressure distributions through the first and second shocks are in agreement also. Even the skin friction distribution, which is highly sensitive, shows very good agreement though the first shock, only diverging later.

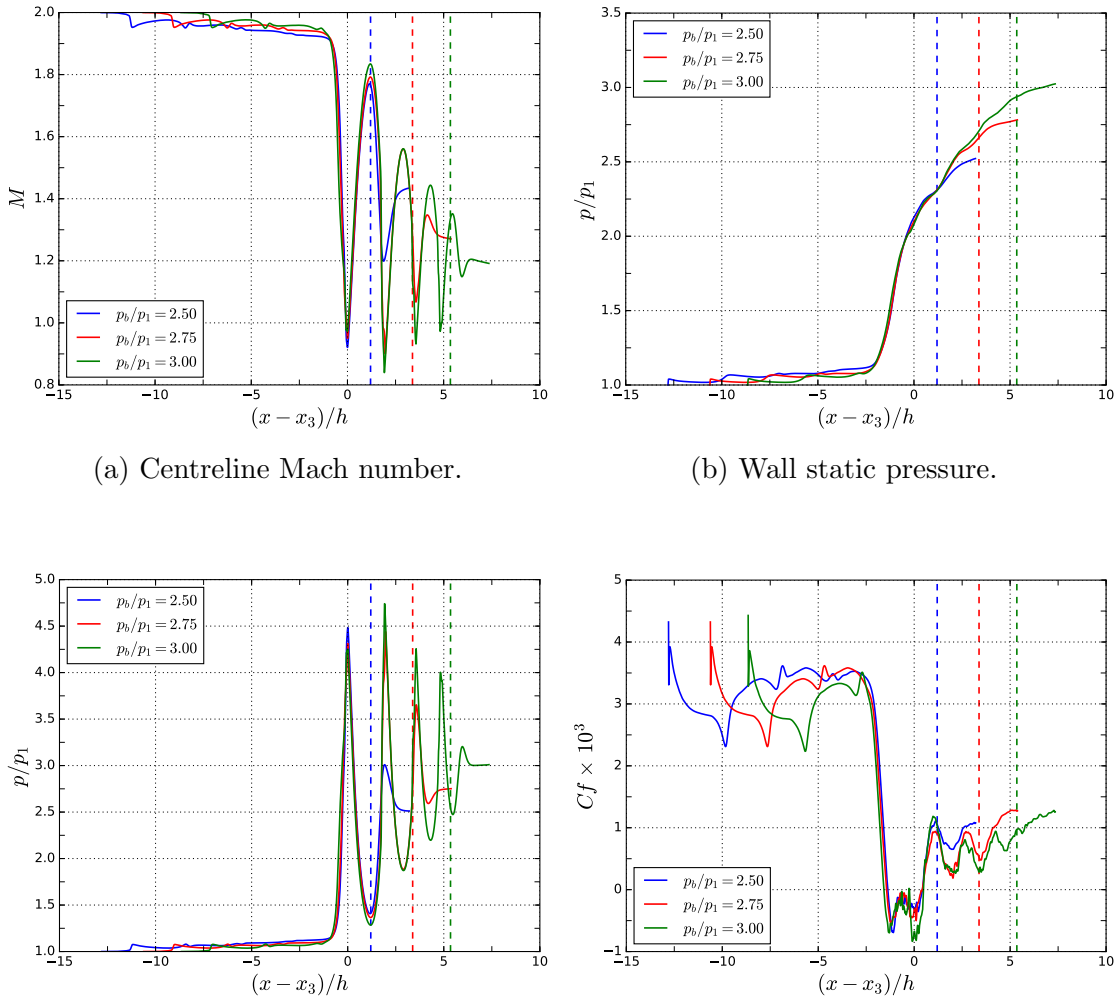

(a) Centreline Mach number.

(b) Wall static pressure.

(c) Centreline static pressure.

(d) Skin friction coefficient.

FIGURE 5.4: Streamwise variation of averaged flow properties comparing applied back pressures, normalised by location of the first shock. The shifted sponge zones are given by the dashed lines in the respective colours.

This is in general agreement with Free Interaction Theory (FIT), which shows that for shock interactions, the pressure rise due to separation is independent of downstream conditions (therefore independent of the prescribed back pressure). Since the upstream condition of each case is very similar (Mach number and confinement differ slightly due to the varying length of undisturbed flow), one would expect from the FIT assumption that the shapes of the wall pressure curves would be in agreement. This finding was also noted by Klomparens et al. (2016), although only with wall pressure.

5.2 Effect of Reynolds Number

Generally, Reynolds number is considered to only weakly affect the behaviour and structure of shock trains (see Billig, 1993; Matsuo et al., 1999), but this has only been verified for the range of Reynolds numbers at least one order of magnitude higher than those of the current work (see for example the simulations in Morgan et al., 2014). In order to be sure that the main features of the flow are representative, it is important to find out if this assumption holds with lower Reynolds numbers.

The baseline Reynolds number used in this project (in terms of the van Driest displacement thickness) is $Re_{\delta^*_{vd}} = 500$ which corresponds to approximately $Re_\theta = 500$ or $Re_\tau = 130$ at the inflow (these figures approximately double before reaching the outlet). In this section we compare the shock train response with two additional inflow Reynolds numbers: $Re_\theta = 790$ & 1100. The configuration considered is span-periodic and the grids are adjusted in each case in order to conserve the same approximate viscous grid spacing. All other parameters are kept consistent with previous sections. A summary is provided in table 5.2.

$Re_{\delta^*_{vd}}$	Re_θ	Grids available	$l_x \times l_y \times l_z$	N_x, N_y, N_z (ILES)
500	500	ILES, CDNS, DNS	$16h \times 2h \times 1h$	800, 320, 60
750	790	ILES, CDNS	$16h \times 2h \times 1h$	1200, 480, 90
1000	1100	ILES	$16h \times 2h \times 1h$	1600, 640, 120

TABLE 5.2: Summary of Reynolds number cases.

As demonstrated in figure 5.5 the structure of the flow field is generally well-conserved across the different Reynolds numbers. The crossed compression waves at the head of the shock train as well as the series of normal shocks are present in each case, albeit with a more defined structure at higher Reynolds numbers.

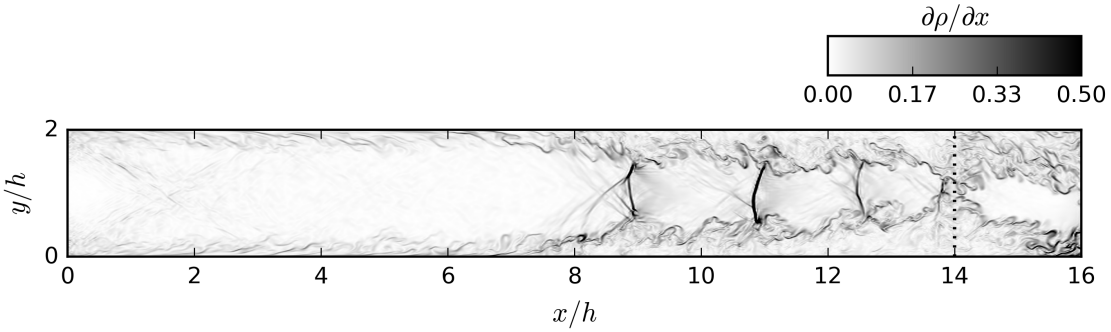

(a) $Re_\theta = 500$

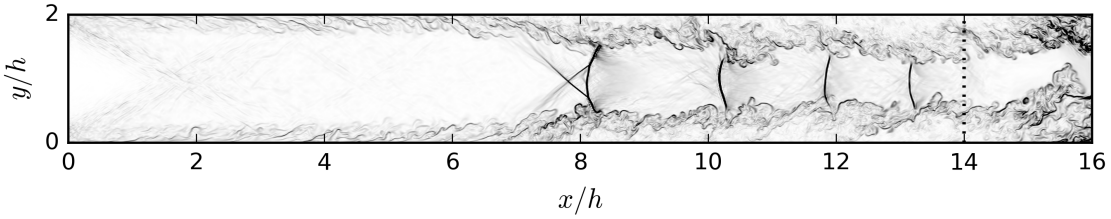

(b) $Re_\theta = 790$

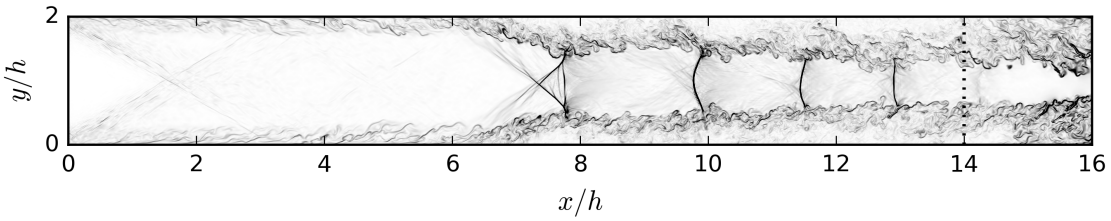

(c) $Re_\theta = 1100$

FIGURE 5.5: Contours of instantaneous density gradient for different Reynolds numbers. All case are run at the ILES resolution. The shock structure appears to be largely unaffected by the Reynolds number.

The two higher Reynolds number produce noticeably longer shock trains. As seen in figure 5.6 both these cases produce very similar distributions of pressure and stabilise roughly half a shock cell upstream of that of the $Re_\theta = 500$ case. It is strongly suggested from the literature that Reynolds number correlates with longer shock trains, however it is surprising that the difference in shock train length between $Re_\theta = 790$ and $Re_\theta = 1100$ is so small.

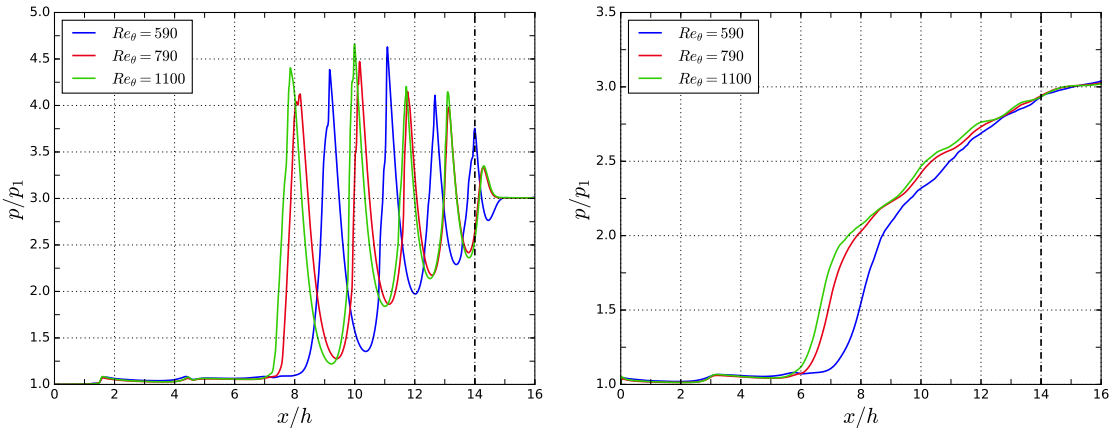

(a) Centreline static pressure. (b) Wall static pressure.

FIGURE 5.6: Streamwise variation of averaged pressure comparing different Reynolds numbers.

The pressure distributions have been normalised by the leading shock position and these are shown in figure 5.7. The distributions match closely at the head of the shock train but begin to diverge further downstream. There appears to be a positive relationship between the Reynolds number and the observed shock spacing (as measured by the gaps between pressure peaks). The intermediate and high Reynolds number cases increase the shock spacing above the baseline by an average of 1.8% and 8.3% respectively.

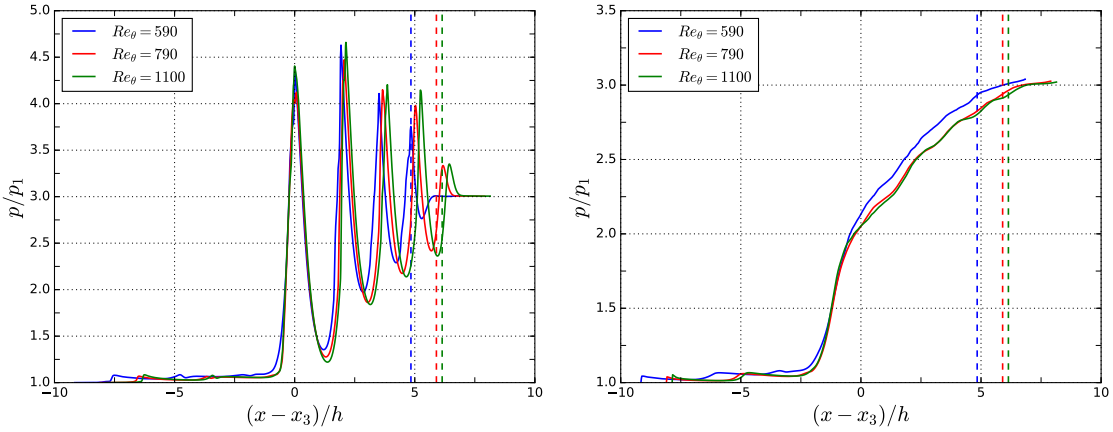

(a) Centreline static pressure. (b) Wall static pressure.

FIGURE 5.7: Streamwise variation of averaged pressure comparing different Reynolds numbers normalised by the location of the leading shock.

A comparison of the ILES and CDNS grid resolutions at $Re_\theta = 790$, is given in figure 5.8. As with the main grid refinement study (section 4.3) the ILES grid under-predicts the shock train length, although the gap between the profiles is larger in figure 5.8a is larger than in figure 4.18c. It should be noted that the leading edge of the shock train in the CDNS case occurs at approximately $x = 5h$ meaning that it occurs within the boundary layer development region. Resource limitations meant that a CDNS case at $Re_\theta = 1100$ was not feasible.

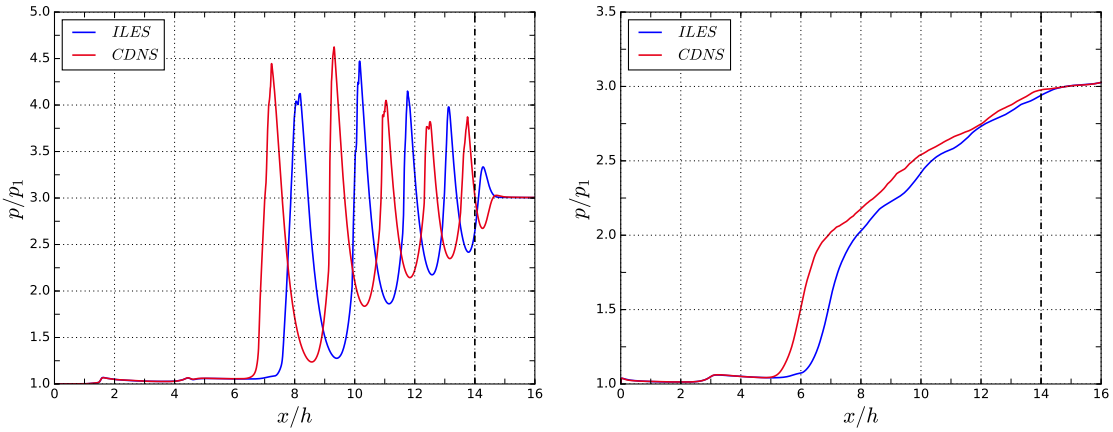

(a) Centreline static pressure.

(b) Wall static pressure.

FIGURE 5.8: Comparison between ILES and CDNS resolutions running with $Re_\theta = 790$. The grid resolution has a similar effect on the shock train length as it does with the baseline Reynolds number.

The results from this section allow for us to conclude that the Reynolds number effect near the lower end of turbulence-sustaining Reynolds numbers is fairly weak, as expected. Despite the shock position differing somewhat, the overall shape of the shock waves and spacing within the shock train appears to be relatively insensitive, even at these particularly low values of Re_θ.

5.3 Confinement Ratio Effects

The third parametric study in this chapter will consider the effect of inflow confinement ratio on the span-periodic arrangement. This test is performed by examining the shock train response in cases with inflow confinement ratios of $\delta_{99}/h = 0.19$ and 0.14 and comparing these to the baseline value ($\delta_{99}/h = 0.28$). The baseline case here is identical to the basic ILES from the grid study and Reynolds number study,

albeit with a domain which is 50% longer in x. For the other cases, the confinement is altered by running larger grids, where the domain lengths in x and y are multiplied by constant factors (respectively 1.5 and 2.0). This allows the boundary layer to remain consistent with each case while maintaining the same aspect ratio ($l_x/h = 24$). All other values (including grid resolution) are kept constant. The domain sizes and grid numbers are summarised in table 5.3.

δ_{99}/h (inflow)	l_x, l_y, l_z (δ^*_{vd})	N_x, N_y, N_z
0.28	960, 320, 40	1200, 320, 60
0.19	1440, 120, 60	1800, 480, 90
0.14	1920, 160, 40	2400, 640, 60

TABLE 5.3: Summary of cases for studying the confinement ratio. The lowest confinement case has the same span size of the baseline case in order to reduce the computational cost.

The resulting flow fields of each case are shown in figure 5.9. Despite significant reduction in inflow confinement ratio, the shock trains in the low confinement cases are very similar to the baseline; the positions of the first shock as well as the shock structure do not appear to change significantly. Although the overall structure of the shock interactions are the same (crossed oblique waves and Mach stem at the first shock, followed by a series of normal shocks) their shape becomes more well-defined at the lower level of confinement, most likely due to having less viscous-dominated flow at the centreline.

Certain time-averaged flow properties are given in figure 5.10. The distributions of static pressure (5.10a & 5.10b) show more clearly the impact of the confinement ratio on the shock train length. It is particularly interesting to note that the intermediate case has the shortest shock train of any of the three cases. This is in contradiction to the established literature which suggests a linear relationship between the confinement ratio at the start of the shock train and shock train length (Carroll and Dutton, 1988; Fiévet et al., 2017).

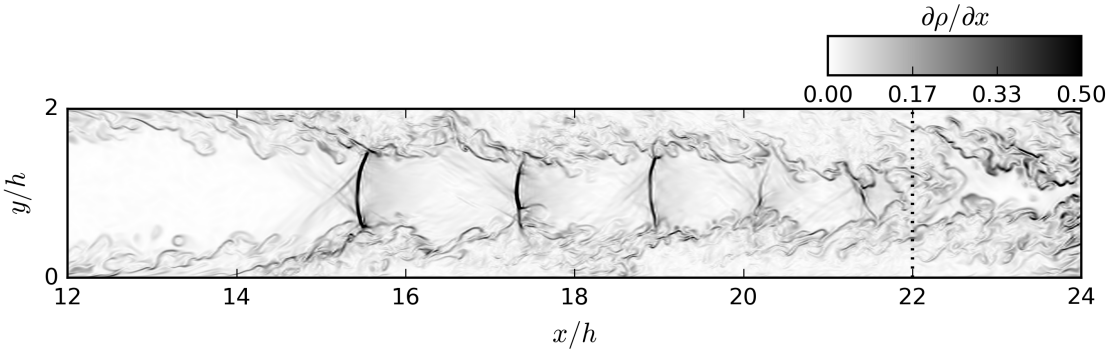

(a) $\delta_{99}/h = 0.28$.

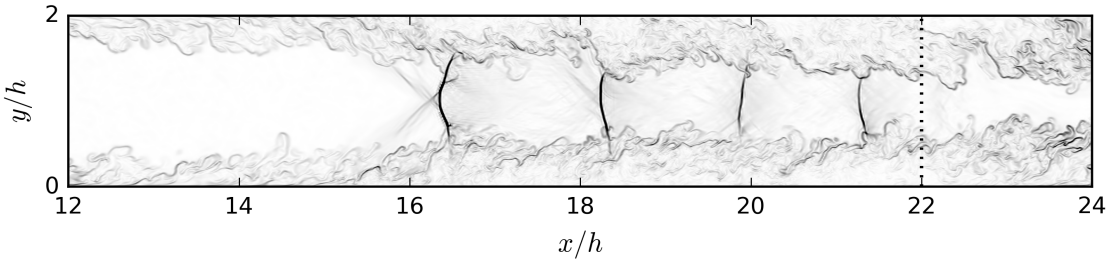

(b) $\delta_{99}/h = 0.19$.

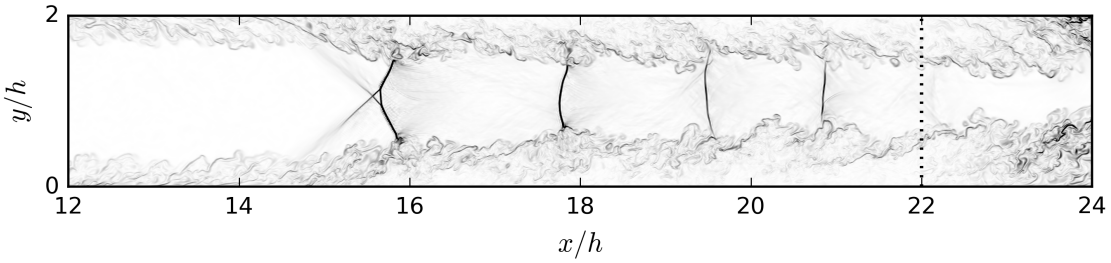

(c) $\delta_{99}/h = 0.14$.

FIGURE 5.9: Contours of density gradient comparing the effect of boundary layer confinement. The domain has been truncated at $x = 12h$ in order to provide better detail on the shock train.

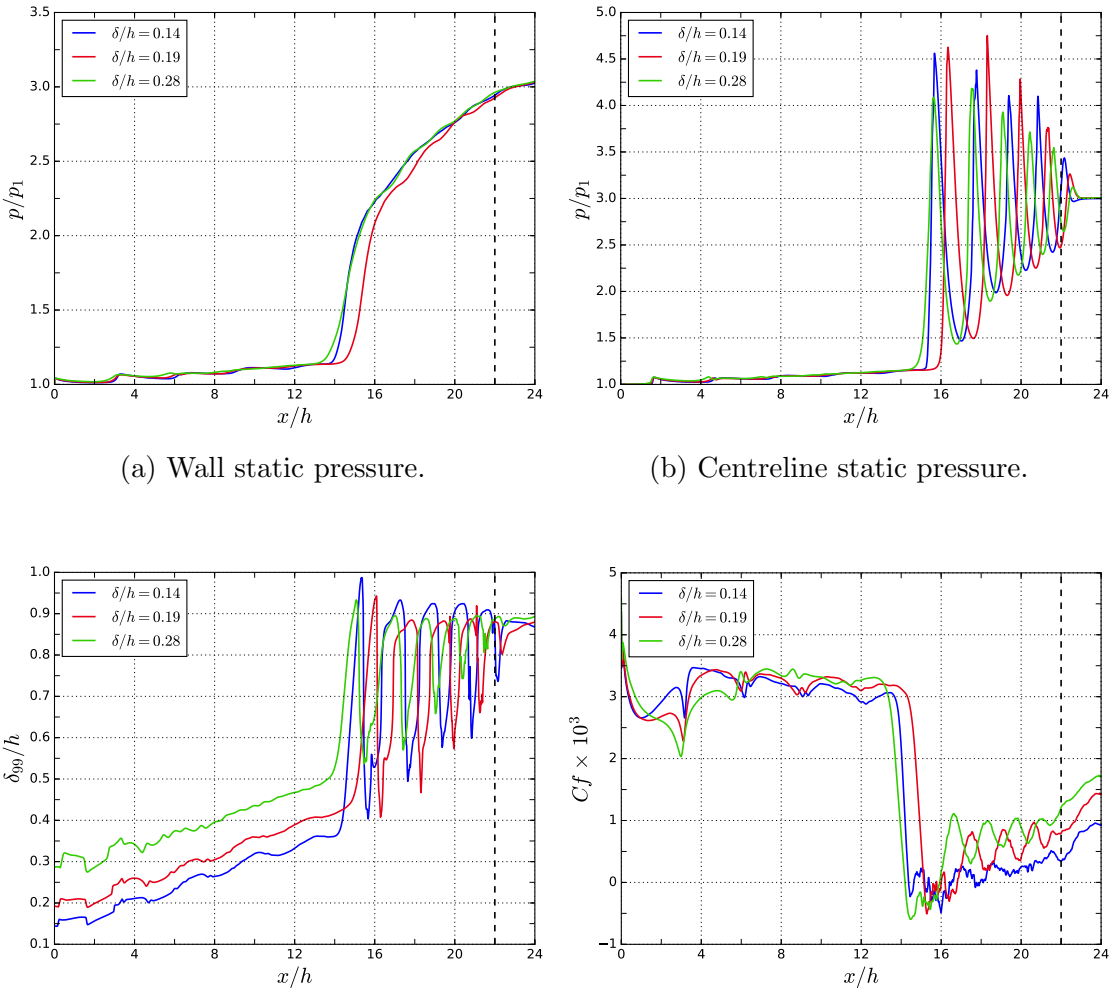

(a) Wall static pressure.

(b) Centreline static pressure.

(c) Boundary layer thickness.

(d) Skin friction coefficient.

FIGURE 5.10: Streamwise variation of averaged flow properties comparing the effect of inflow confinement ratio.

The distribution of boundary layer thickness in figure 5.10c provides a useful visualisation of how the confinement ratio develops along the domains. Although the initial values of confinement have a large spread, the gap between them (rather that the proportion) is maintained since each boundary layer thickens more or less linearly at the same slope. This means that the actual confinement ratios at the leading edge of the shock trains are much higher than at the inflow. Using the definition of the leading edge of the shock train from section 5.1, the shock train confinement ratios ($\delta_{99,2/h}$) are respectively 0.50, 0.44 & 0.36. The shock train lengths as well as the confinement/length ratios are given in table 5.4. The confinement/length ratio for the lowest confinement case is the notable outlier and, if the ratio of the other

two cases were conserved and boundary layer growth is linear, one would expect a shock train length of $8.36h$.

$\delta_{99,0}/h$	$\delta_{99,2}/h$	l_{ST}/h	$\delta_{99,2}/l_{ST}$
0.28	0.50	10.32	0.048
0.19	0.44	9.26	0.048
0.14	0.36	9.92	0.036

TABLE 5.4: Summary of results for the confinement ratio study.

In figure 5.11 we plot the change in the leading shock position over time for the lowest confinement case. The statistics for this case were gathered between $tu_1/h = 100$ and 140 when it was assumed that the flow field had converged. However, the trend appears to show that the shock train is still drifting downstream at approximately 1% of the freestream velocity. Although this speed is lower than for the convergence seen in other cases, this is the most likely explanation for the discrepancy in shock train length. Based on the trajectory in figure 5.11, the simulation would require an additional 160 time units (6.5 convective cycles) in order to reach the expected shock train length of $8.36h$.

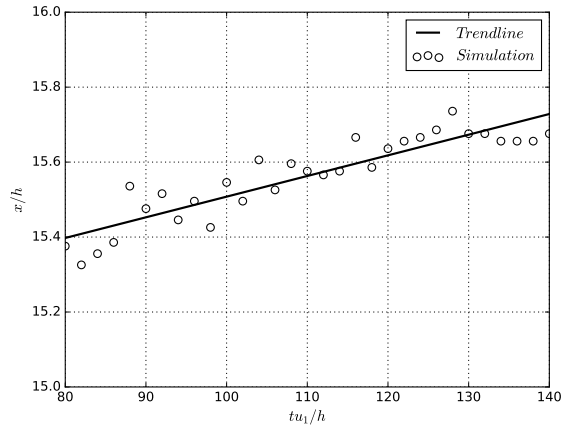

FIGURE 5.11: Change in the leading shock position over time ($\delta_{99}/h = 0.14$ case), with the trend line suggesting a lack of a converged solution.

As in previous sections, the pressure distributions have been normalised by the leading shock position, shown in figure 5.12. Again, the wall and centreline pressure distributions are surprisingly well conserved. It is interesting how well the spacing of the shock waves is maintained despite the lower confinement. This strongly suggests

that the approximate geometry of the shock cells (supersonic flow regions between shock waves) are very similar in each case. At the centreline, the shock pressure rise for the baseline case is noticeably lower which is most likely a consequence of the variations in the leading shock structure. For the lower confinement ratios, the normal shocks are much closer to the crossing point of the oblique shocks leading to a more concentrated pressure rise at that location.

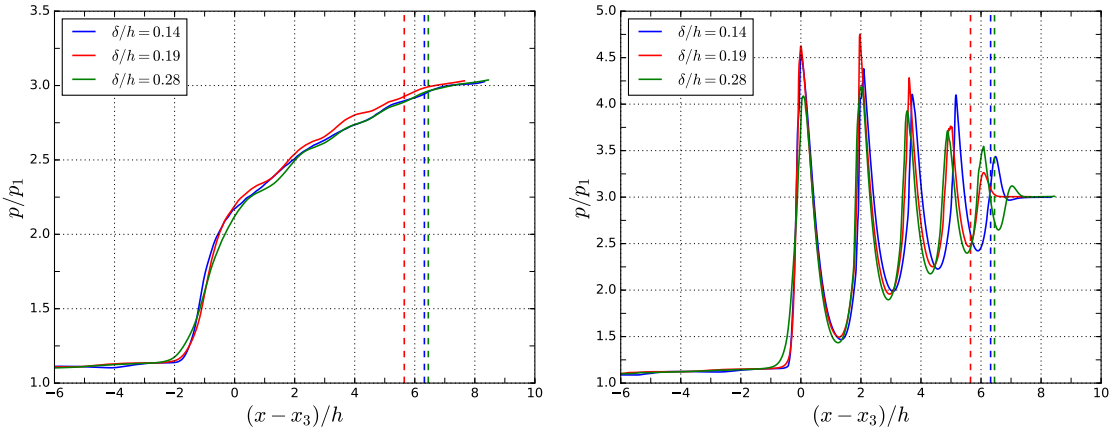

(a) Wall static pressure.

(b) Centreline static pressure.

FIGURE 5.12: Streamwise variation of normalised properties comparing the effect of inflow confinement ratio. As with other parametric studies, the distributions are very similar between cases.

5.4 Sidewall and Blockage Effects

5.4.1 Spanwise Confinement and Sidewalls

In order to assess the impact of spanwise confinement on the shock train, two cases have been set up such that they differ only by the presence of sidewalls. The sidewall case is identical to the square duct case discussed in section 4.1.3, except with an active sponge zone. The span-periodic (channel) case allows for an approximation of infinite span and is the same as the baseline case in the previous section (the longer ILES channel is used so that the domain lengths match). Both cases run with the ILES grid resolution and have identical inlet Mach numbers ($M = 2.0$), Reynolds numbers ($Re_\theta = 500$) and pressure ratios ($p_b/p_1 = 3.0$). A summary is given in table 5.5.

Case	Grid	$l_x \times l_y \times l_z$	$N_x \times N_y \times N_z$	p_b/p_1
Span-periodic	ILES	$24h \times 2h \times 1h$	$1200 \times 320 \times 60$	3.0
Square duct	ILES	$24h \times 2h \times 2h$	$1200 \times 320 \times 320$	3.0

TABLE 5.5: Summary of cases in the spanwise confinement study.

From an examination of the resulting flow fields it is immediately clear that the sidewalls have the effect of producing a significantly longer shock train. Figures 5.13, 5.14 and 5.15 compare the typical flow fields (of Mach number, total density gradient and pressure) at the mid-span location of each case. In addition to a longer shock train and higher number of shocks, the structure of the shocks is also considerably different. The first two shocks in the square duct are much weaker and it is only until the third shock at $x = 12h$ that there is subsonic flow at the centreline.

As discussed in section 4.1.3, the sidewalls introduce a higher degree of boundary layer confinement and this has the effect of reducing the exit Mach number at the centreline. While the span-periodic case produces a stable shock train position, there is no equilibrium solution with the square duct - instead the shock train slowly drifts towards the inlet (see further discussion of this in section 6.1.1).

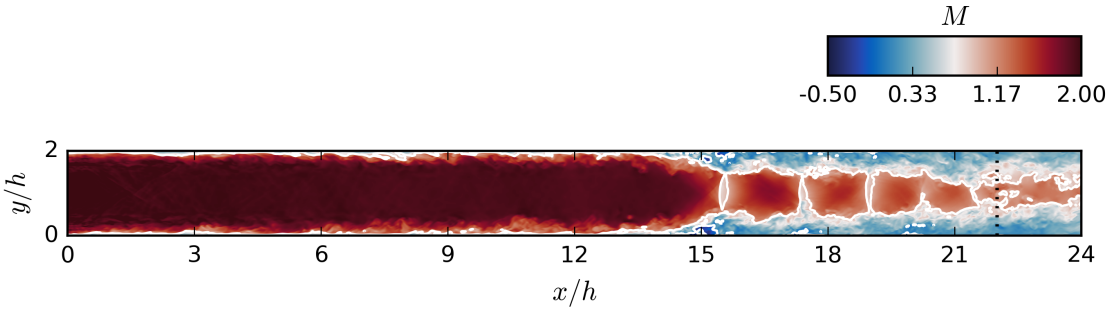

(a) Span-periodic.

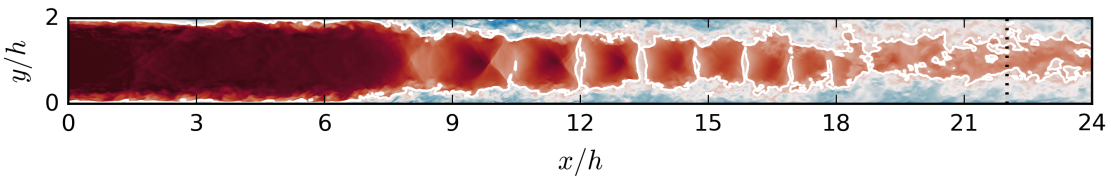

(b) Square duct.

FIGURE 5.13: Contours of instantaneous Mach number comparing the effect of sidewalls.

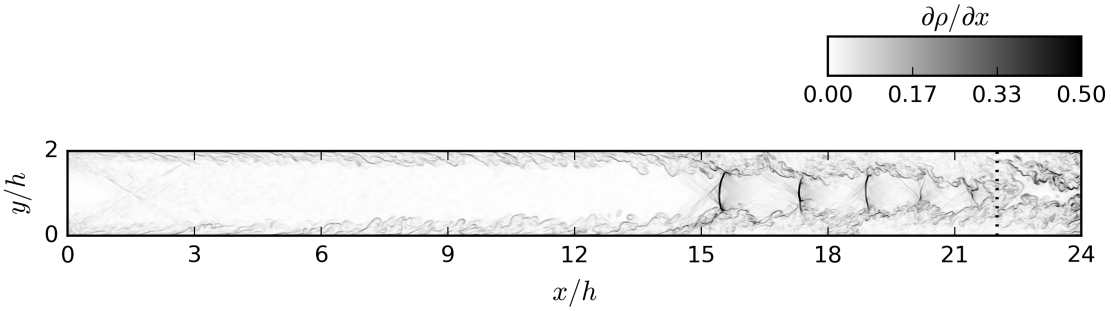

(a) Span-periodic.

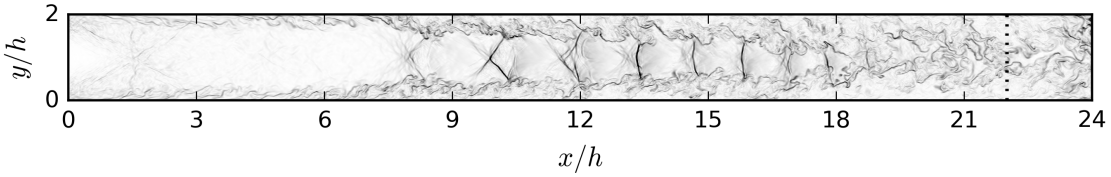

(b) Square duct.

FIGURE 5.14: Contours of instantaneous density gradient comparing the effect of sidewalls.

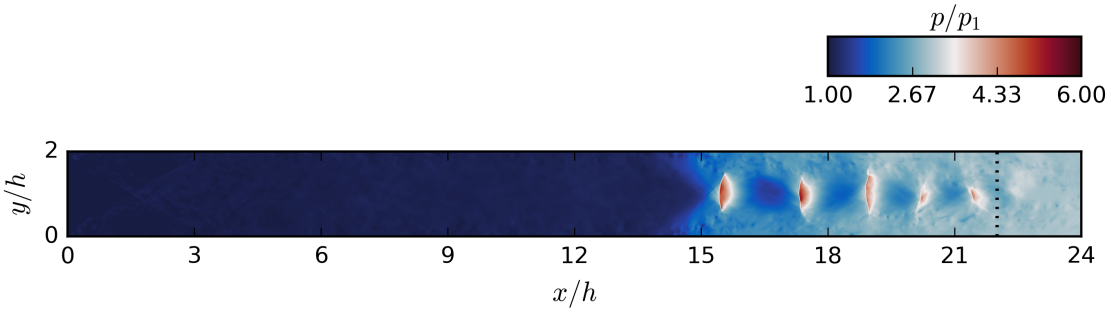

(a) Span-periodic.

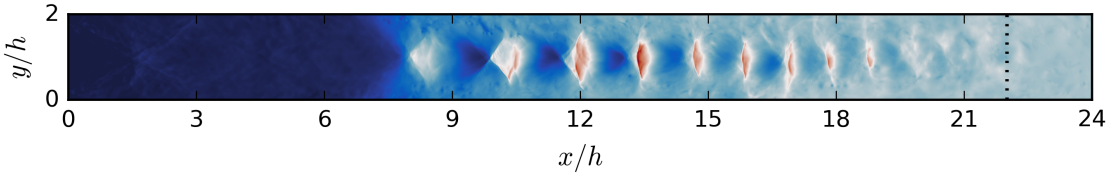

(b) Square duct.

FIGURE 5.15: Contours of instantaneous static pressure comparing the effect of sidewalls.

Statistical time-averaged data has been collected for each case. The time periods are 96 and $48h/u_1$ for the span-periodic and duct cases respectively - the lower sampling time for the latter accounts for the fact that the shock train is moving upstream. Streamwise plots of Mach number, pressure and skin friction are shown in figure 5.16. The data confirms the findings from the instantaneous flow - namely the higher number of weaker shocks which form in the square duct. The furthest upstream instance of the shock train occurs at around $x = 6h$ which is right at the limit of the boundary layer development region, hence any shock train movement beyond this point would give inaccurate results.

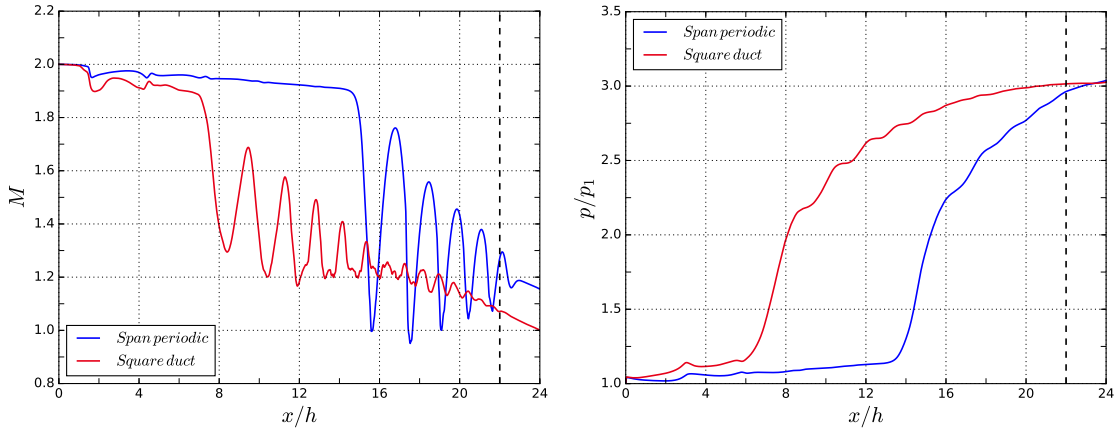

(a) Centreline Mach number.

(b) Wall static pressure.

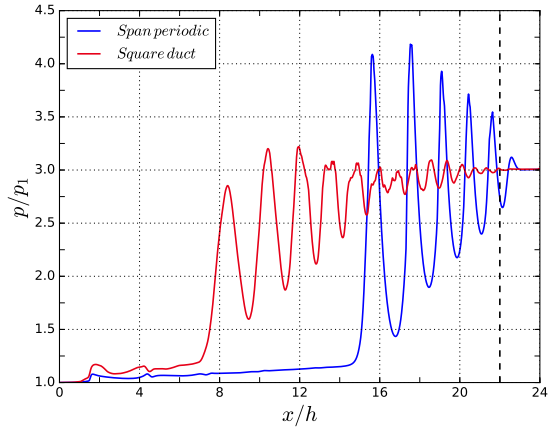

(c) Centreline static pressure.

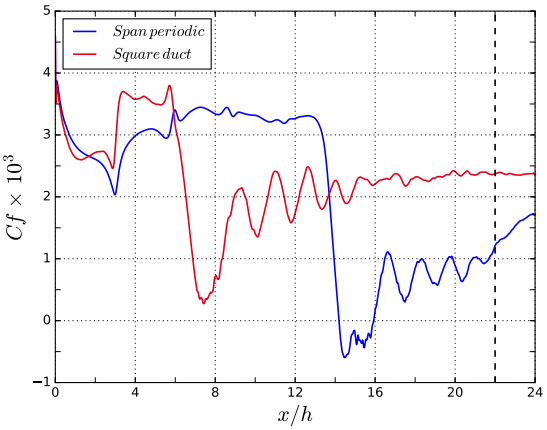

(d) Skin friction coefficient.

FIGURE 5.16: Streamwise variation of time-averaged flow properties comparing span periodic and square duct cases. The sidewalls cause a much longer shock train to form where the individual shock waves are much weaker.

By adjusting the results to match the location of the first shock (figure 5.17) we can see that despite the differences in shock strength, the actual shock spacing is well preserved (especially over the first three shock waves). This suggests that the spacing between the shock waves is more strongly governed by the Mach number and the 2D geometry of the domain than by the strength of the individual shock waves.

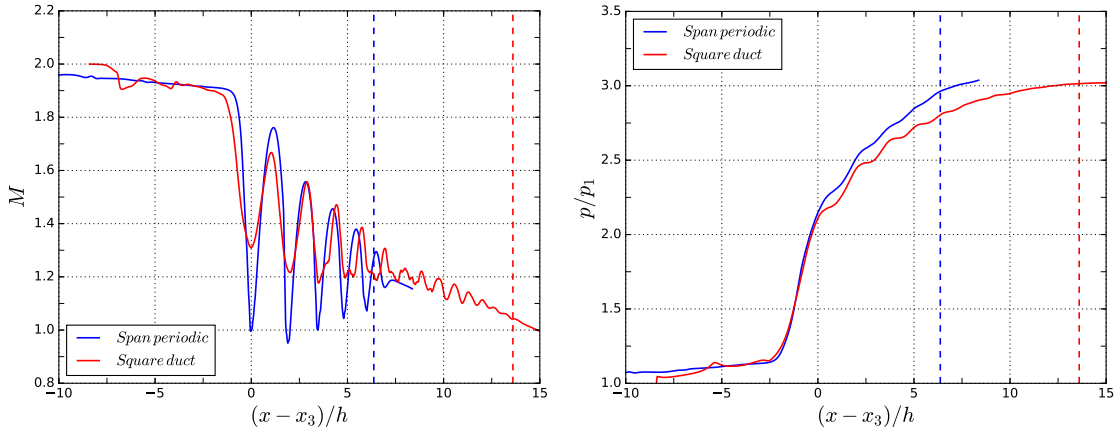

(a) Centreline Mach number.

(b) Wall static pressure.

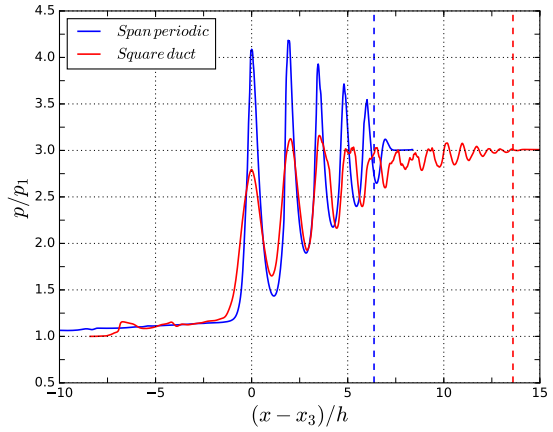

(c) Centreline static pressure.

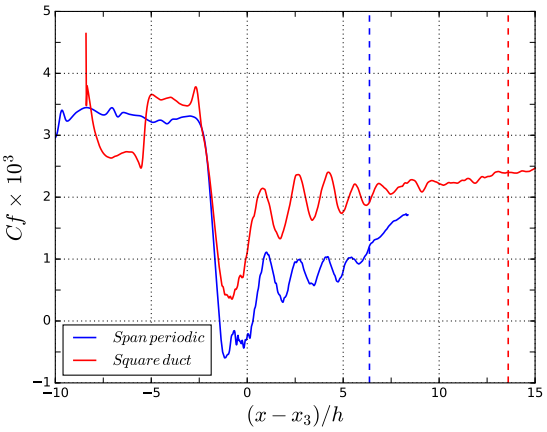

(d) Skin friction coefficient.

FIGURE 5.17: Streamwise variation of averaged flow properties showing the effect of sidewalls. Plots are normalised by the position of the first shock.

The Mach number and pressure distributions between the first, second and third shocks is also well preserved (there is only a significant mismatch at the shocks themselves) suggesting that the flow behaviour at these locations is similar between the two cases. The skin friction distribution remains permanently higher in the square

duct. In the undisturbed region before the shock train this difference is due to the spanwise confinement of the sidewall boundary layers, while through the shock train itself it appears to be a result of the lower pressure gradient which allows the boundary layer to recover more quickly.

The weaker shock strengths seen in the square duct case appears to be a result of the sidewall boundaries causing a more gradual pressure rise at each shock location. A similar effect was suggested by Babinsky et al. (2013) with oblique SBLI problems whereby the shock interaction with the sidewall produces compression waves which reach the main interaction region ahead of the oblique shock and thereby smear out the pressure rise and produce smaller separation bubbles. For the square duct case, the succession of weaker shocks means that the wall pressure rises more slowly. By the time that the mixing layer of the shock train reaches the centreline, the pressure rise cannot be achieved by shock waves, and so must be caused by entropic pressure losses in the mixing turbulent flow (a slower process), thereby further increasing the length of the shock train.

Figure 5.18 shows a comparison of skin friction at the bottom wall. The separation regions are given in dark blue and bounded by white lines. While the span-periodic case has a very large separation bubble (covering the whole width of the domain) at the head of the shock train, the separation in the square duct only exists in the corner region, where the low-momentum flow is more susceptible to separating. Again, it is clear that there is a much better recovery of the skin friction in the duct case.

The velocity streamlines just above the bottom wall are overlaid on the contour plot in figure 5.18b. There is significant convergence of streamlines under the first shock, where the flow is diverted round the separation regions. There is also subsequent downstream convergence of streamlines, demonstrating the increased boundary layer confinement.

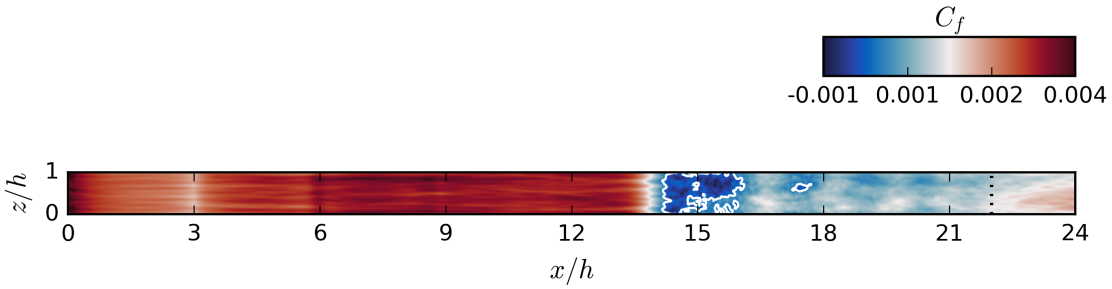

(a) Span-periodic case.

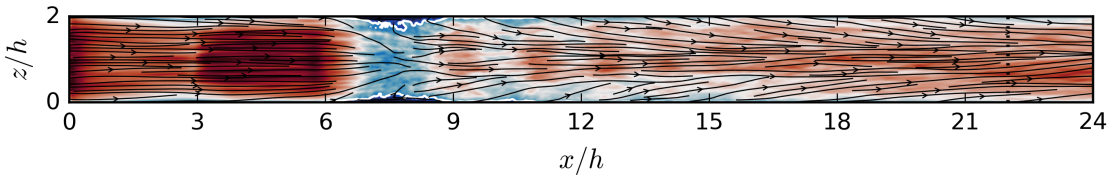

(b) Square duct case with velocity streamlines at the first grid point from the bottom wall ($y^+ = 0.6$).

FIGURE 5.18: Contours of time averaged skin friction coefficient on the bottom ($y = 0$) wall. Separation regions are marked by the solid white lines.

Another flow feature that occurs with the presence of sidewalls is secondary flow vortex structures. As shown with the shock-less duct case in section 4.1.3 vortex pairs form in each of the corners after a streamwise distance of around $6h$, eventually dominating the time-averaged transverse flow. In incident-reflected SBLI problems involving sidewalls (such as Wang et al., 2015), the corner vortices are completely disrupted by the strong spanwise pressure gradient in the interaction region so there is a question of whether a similar phenomenon occurs with a ducted shock train.

In figure 5.19 we compare the transverse velocity fields at various streamwise locations with and without the presence of the shock train. The locations are chosen to demonstrate the effect of the leading shock wave which occurs at approximately $x = 6.0h$. The impact of the shock train is felt as early as $x = 5.5h$ and the initial interaction region appears to last until $x = 8.0h$. Although the initial shock affects the entire flow field cross section by inducing transverse flow towards the centreline, the corner vortices do not disappear. Indeed, instead of completely disrupting the secondary flow structures, the vortices downstream of the initial interaction region are larger and stronger than the case with no shock train. Since the secondary flow is driven by the turbulent Reynolds stresses, it is clear that the increase in mixing in the shock train subsonic region is more than enough to overcome any pressure gradients which may inhibit the corner vortices.

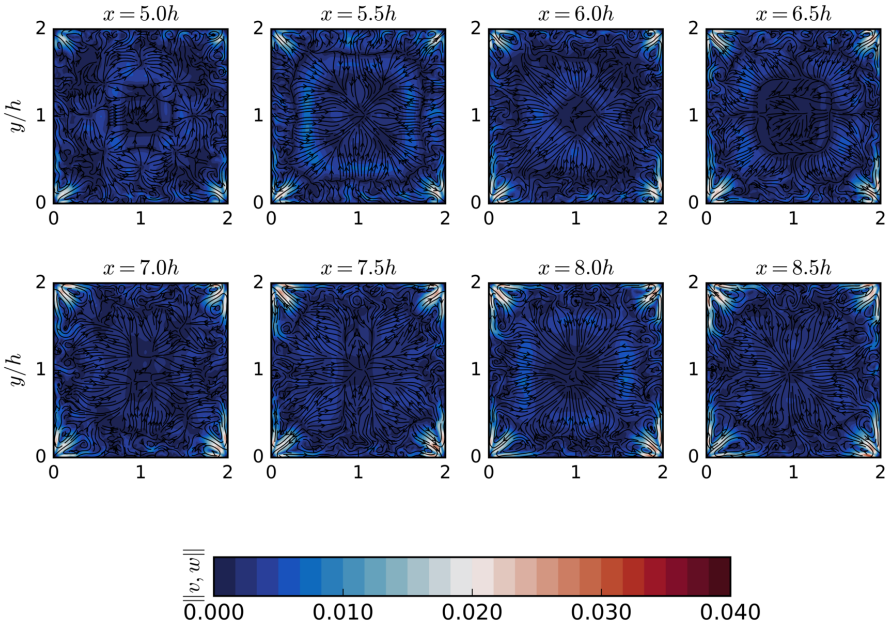

(a) Without shock train present.

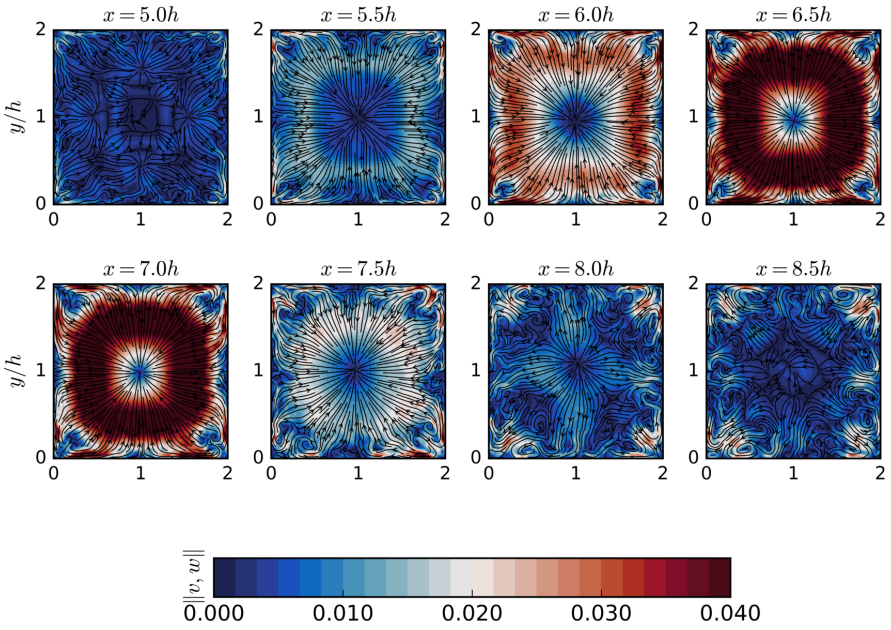

(b) With shock train present.

FIGURE 5.19: Comparison of transverse velocity contours with and without the presence of the shock train. The effect of the shock train appears to be that it hastens the development of secondary flow structures.

The results from this study are in general in agreement with the established literature on sidewall effects. For example, Morgan et al. (2014) found that a span periodic arrangement produced a shorter shock train, even when a higher back pressure was applied. Additionally, the span periodic case exhibited a slower recovery of the skin friction, as is observed with the current work. Cox-Stouffer and Hagenmaier (2001) compared shock trains within isolators of different aspect ratios (W/H), finding (for $M = 2.0$ at least) that aspect ratios of 1 (square cross sections) produced the longest shock train as well as the weakest individual shocks.

5.4.2 Blockage Considerations

It is clear from the previous section that despite having a matching confinement ratio at the inlet, the square duct produces a shock train which is approximately twice as long as that of the span-periodic case and is located much further upstream, even accounting for the faster rate of the boundary layer growth. While the confinement ratio provides a 1D measure of boundary layer blockage, it may be more useful to consider the total blockage across the cross section, thus accounting for the boundary layers on the sidewalls. An approximate measure of total blockage is defined here as

$$B = \frac{A_{\delta^*}}{A_{yz}}, \tag{5.1}$$

where A_{yz} is the cross sectional area of the duct and A_{δ^*} is the area within one displacement thickness of the walls, such that for a square duct with identical boundary layers on each wall:

$$A_{\delta^*} = 8h\delta^* - 4(\delta^*)^2. \tag{5.2}$$

With a cross sectional area of $4h^2$, the total blockage can be written

$$B = 2\frac{\delta^*}{h} - \left(\frac{\delta^*}{h}\right)^2. \tag{5.3}$$

For a span periodic arrangement with two boundary layers, the total blockage is the same as the 2D blockage:

$$B = \frac{\delta^*}{h}. \tag{5.4}$$

Considering the two cases, we find that the figures for total blockage at $x = 5h$ are 0.11 and 0.21 for the span-periodic and square duct respectively. Therefore we can assume that the boundary layer occupies approximately twice the cross section in the latter case. This is effect can be seen clearly when looking at the cross sectional flow of the upstream boundary layer, as in figure 5.20.

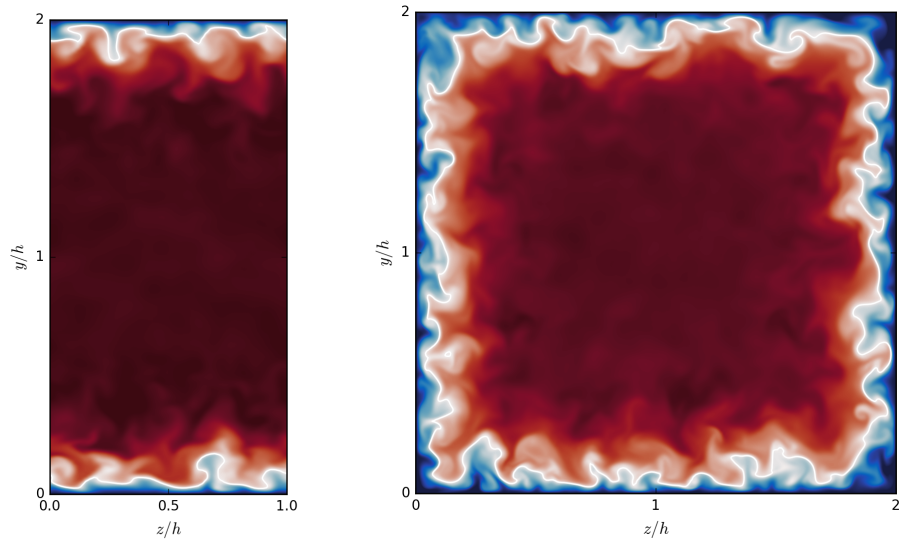

(a) Span-periodic. (b) Square duct.

FIGURE 5.20: Flow cross sections showing contours of Mach number. The sidewalls approximately double the boundary layer blockage.

The question here is whether matching the total blockage may allow for a much better shock train comparison - this has been suggested by Vane and Lele (2013). In order to assess this, a high confinement span-periodic case was set up such that the total blockage matched that of the square duct. The boundary layer generation is unchanged and therefore the higher confinement is achieved by reducing the height of the domain relative to the boundary layer thickness. Other than the confinement ratio, the other main flow parameters are consistent. All three cases are summarised in table 5.6. The duct lengths are given in the simulation length scale (δ^*_{vd}) in order to demonstrate the reduced domain size. As seen in the rightmost column, the high blockage case provides a much better comparison of total blockage.

Case	Grid	$l_x \times l_y \times l_z$ (δ^*_{vd})	$N_x \times N_y \times N_z$	δ_{99}/h (inflow)	B
High blockage	ILES	$510 \times 42.5 \times 40$	$640 \times 170 \times 60$	0.53	0.20
Span-periodic	ILES	$960 \times 80 \times 40$	$1200 \times 320 \times 60$	0.28	0.11
Square duct	ILES	$960 \times 80 \times 80$	$1200 \times 320 \times 320$	0.28	0.21

TABLE 5.6: Summary of cases used to study blockage effects. The blockage value is taken at $x = 5h$

The time-averaged data is compared in figure 5.21. The increase in blockage has the expected effect of shifting the location of the shock train upstream, but not to

the extent that the shock train length matches that of the square duct. It is notable also that the strength of the shock waves are considerably weaker than either of the two other cases, such that the slope of the centreline stagnation pressure is almost entirely smooth. This suggests that the shock train consists of a series of weak compression waves instead of shock waves.

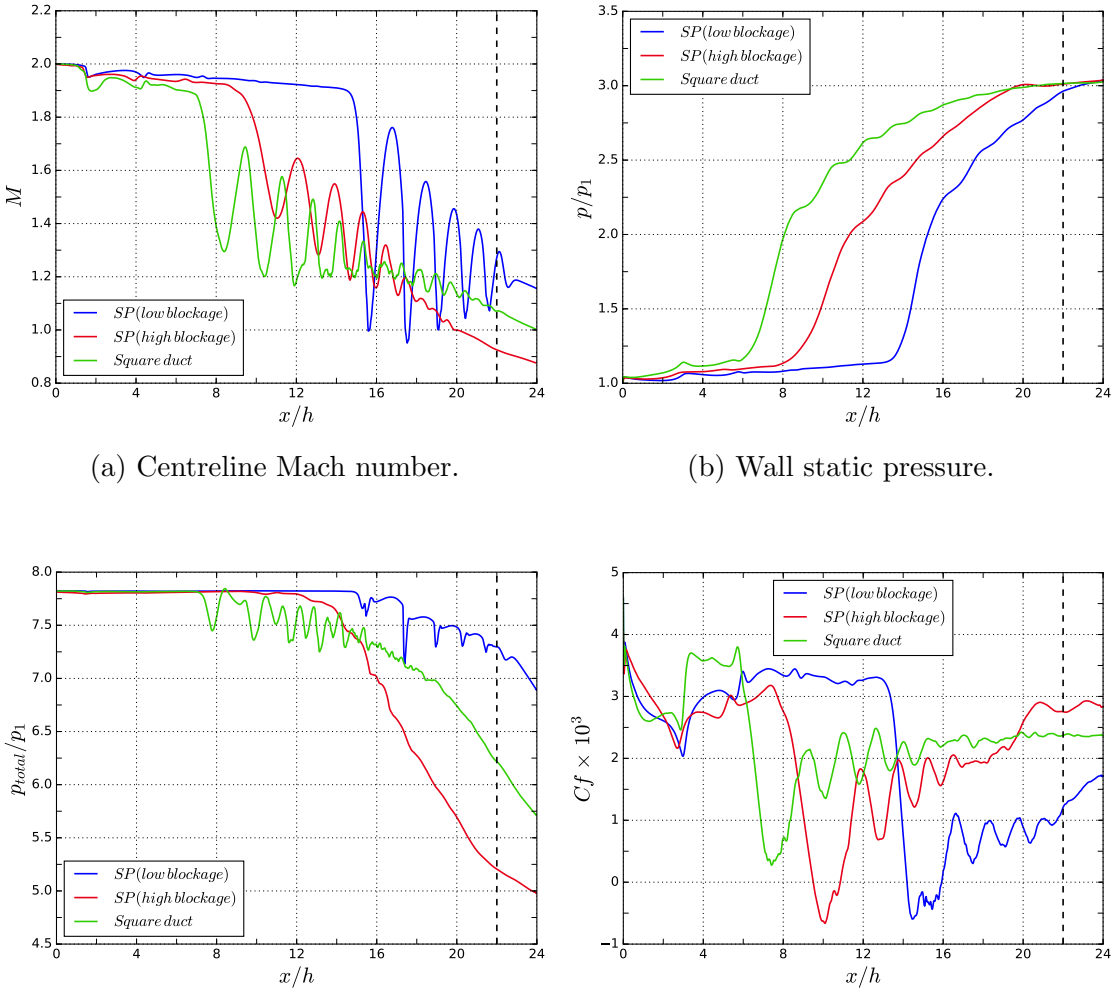

(a) Centreline Mach number.

(b) Wall static pressure.

(c) Centreline stagnation pressure.

(d) Skin friction coefficient.

FIGURE 5.21: Streamwise variation of averaged flow properties comparing the effect of total blockage.

A comparison of the instantaneous flow fields (figures 5.22 and 5.23) confirms this finding, where the shock waves in the high confinement case have all but disappeared. It is clear that the very high level of confinement combined with the low Reynolds number has allowed for the flow all the way to the centreline to become dominated

by viscous dissipation, whereas the supersonic regions in the other two cases can be assumed to be inviscid. The viscous flow has led to the compression waves being smeared out, such that their strength is significantly weakened. The much larger degree of flow dissipation explains why the outlet is almost entirely subsonic and why there is a higher stagnation pressure loss.

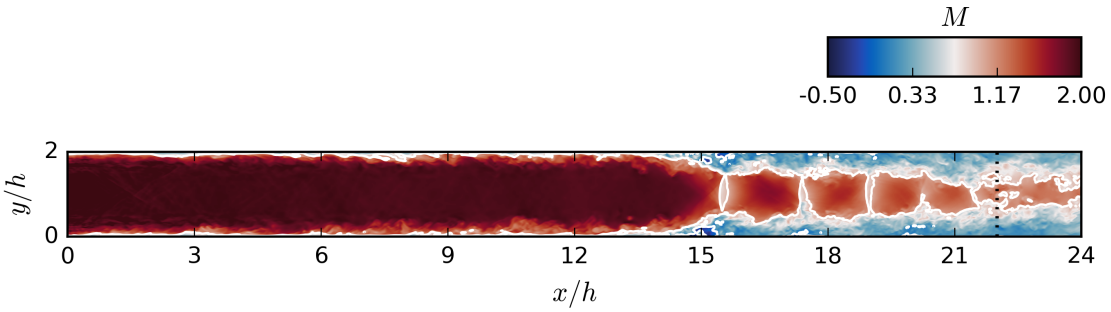

(a) Span-periodic.

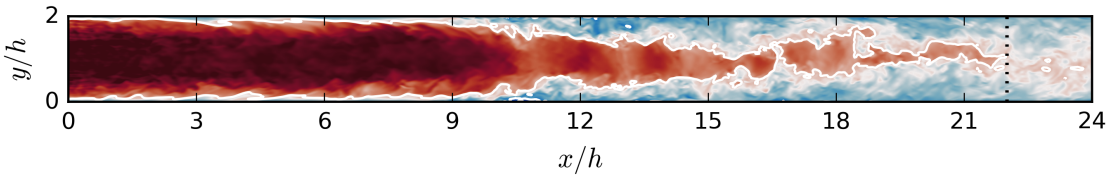

(b) Span-periodic (high blockage).

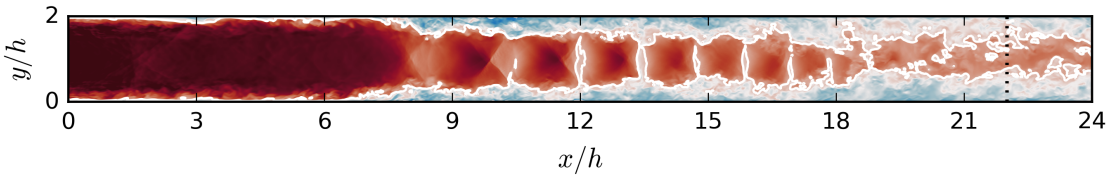

(c) Square duct.

FIGURE 5.22: Contours of instantaneous Mach number comparing the effect of blockage.

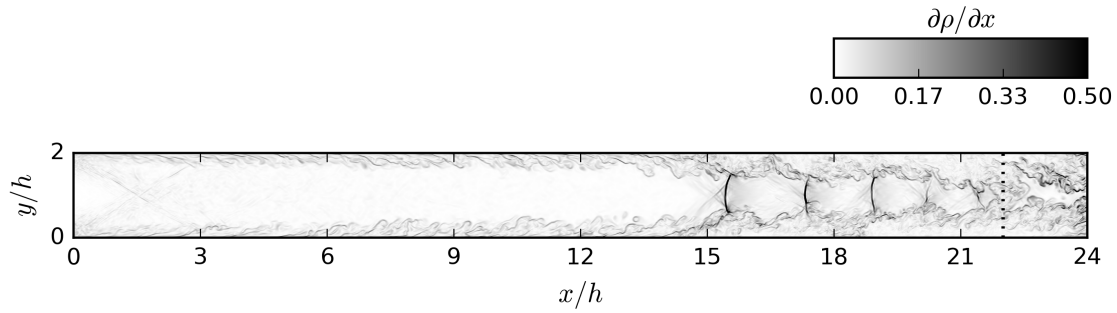

(a) Span-periodic.

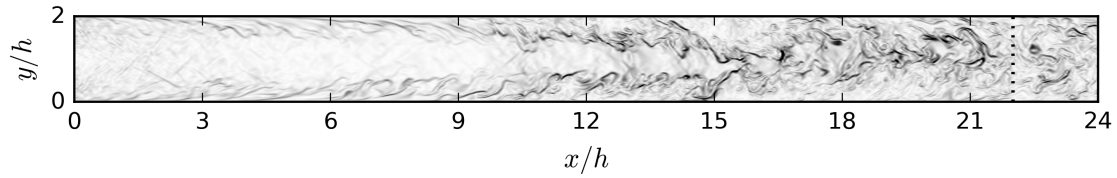

(b) Span-periodic (high blockage).

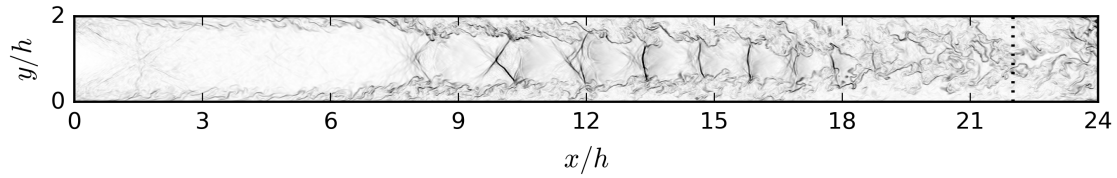

(c) Square duct.

FIGURE 5.23: Contours of instantaneous density gradient comparing the effect of blockage.

These findings show that for cases where the level of boundary layer confinement is reasonably high (e.g. $\delta/h >= 0.3$) sidewalls cannot be accounted for merely by controlling for the overall blockage of the boundary layer, although it is inconclusive as to whether this is applicable at all confinement levels.

5.5 Double Symmetry Plane

Given the doubly-symmetric geometry of the duct arrangement, there is an interesting question of whether the wall bisector planes may be implemented as symmetry planes. This has practical consequences given the possibility of replicating results on only a quarter the number of grid points. This study was initially pursued as a potential way to circumvent GPU memory limits and reduce computational costs,

however the results are included here due to possible academic interest.

In this study we compare the baseline ILES duct case (full duct) with an ILES double symmetry case (quarter duct). The quarter duct has a domain size of $24h \times h \times h$ (half the size in y and z) and the y_p and z_p boundaries implement standard symmetry boundary conditions. A full account of the numerical arrangement is given in section 3.4. As with the other studies, all other parameters are kept constant in order to provide a fair comparison.

In figures 5.24 and 5.25 we compare the flow field cross sections of the two cases (the quarter duct has been mirrored in the wall normal direction for clarity). While it is clear that the shock train with similar features is able to form in the quarter duct, there are significant differences with the reference case. The overall shock train is noticeably shorter and the subsonic layer grows more quickly such that the outflow is almost entirely subsonic. Judging by the density gradient images, there appears to be significantly less turbulent mixing towards the rear 50% of the shock train - compare for example the smoothness of the flow in the region between $18h$ and $21h$ in figure 5.25.

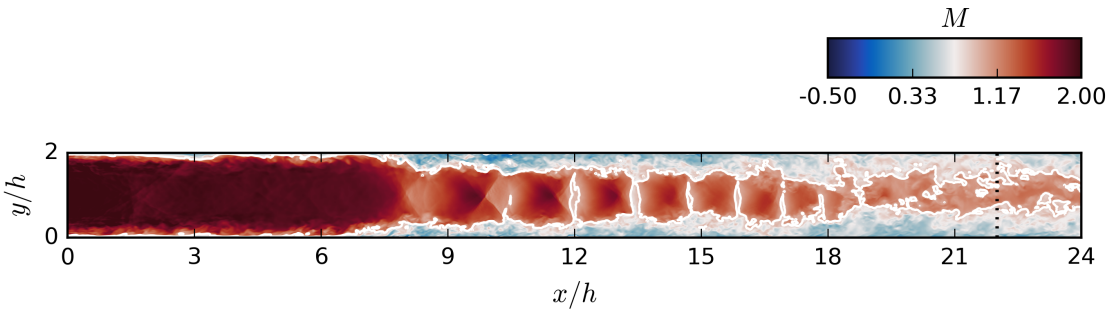

(a) Full duct.

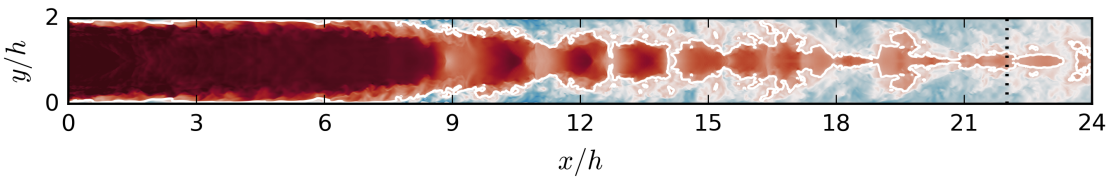

(b) Quarter duct.

FIGURE 5.24: Contours of instantaneous Mach number comparing the effect of the double symmetry plane.

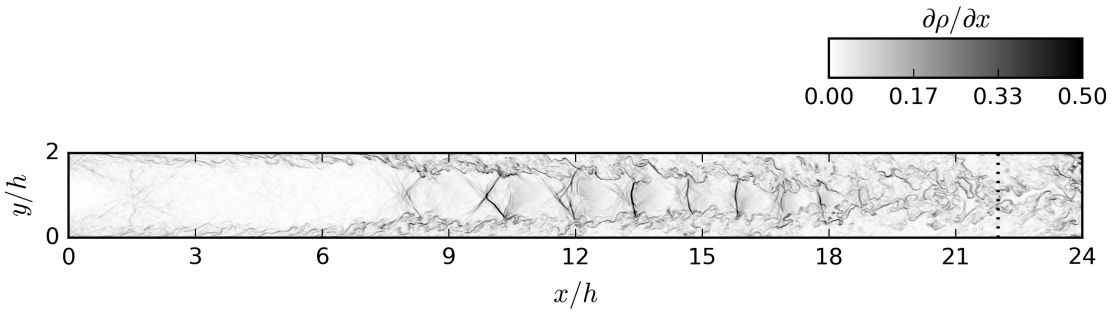

(a) Full duct.

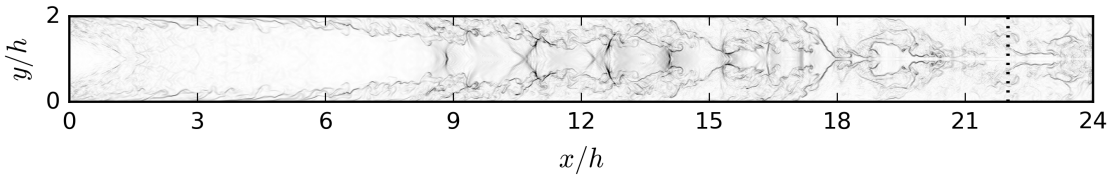

(b) Quarter duct.

FIGURE 5.25: Contours of density gradient comparing the effect of the double symmetry plane.

As with previous sections, it is particularly useful to plot the flow properties aligned by the leading shock - this is shown in figure 5.26. The first thing to note is that the wall pressure profiles are very well matched, despite the differences which exist between the two cases. The centreline flow conditions through the first two shocks are also reasonably well matched but diverge significantly further downstream. While the shocks in the full duct case continue to decrease in strength, the pressure peaks in the symmetry case remain high for the next four shocks. The stronger shocks cause the core Mach number to drop more rapidly.

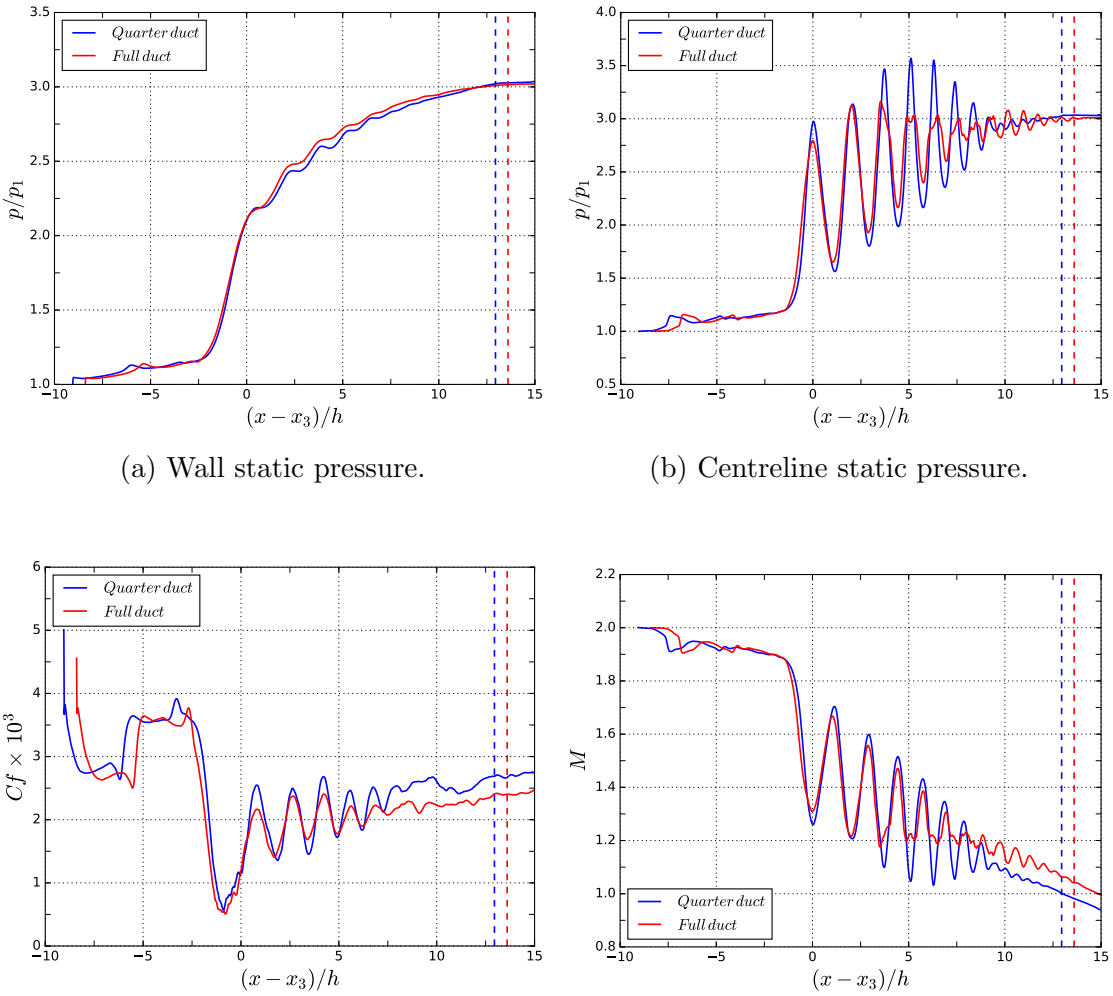

(a) Wall static pressure.

(b) Centreline static pressure.

(c) Skin friction Coefficient.

(d) Centreline Mach number.

FIGURE 5.26: Distributions of normalised flow properties. The double symmetry condition allows for a good estimation of wall pressure and skin friction. The main divergence occurs within the shock train at the centreline.

The main impact of the symmetry plane is that it appears to prevent the growth of turbulent mixing in the core flow which would naturally dissipate the strength of the shock waves. The freestream behaviour, boundary layer flow and the first and second shock cells are all well predicted by the application of the double symmetry planes and it is only downstream of this that the divergence occurs. It is unlikely that this is caused by the explicit filter, which is applied to the corner region between the symmetry planes, since similar filtering techniques have been applied in other shock train problems (e.g. Roussel, 2016). It appears that the double symmetry condition constrains the structure of the flow at the core of the duct enough to

affect the growth of the mixing layer.

The conclusion from these results is that the quarter duct arrangement provides only an approximate estimation of the structure of the shock train. Although it may be suitable for a reduced-cost exploratory case, any interpretations from the results will be limited. On the other hand, given the good match with the freestream and boundary layer properties, the quarter duct arrangement would be appropriate for simple ducted flow cases. In figure 5.27 there is a comparison between the upstream temperature cross sections of the two cases. Note that the nature of the symmetry implementation means that any flow along the centreline must be either a local maximum or minimum.

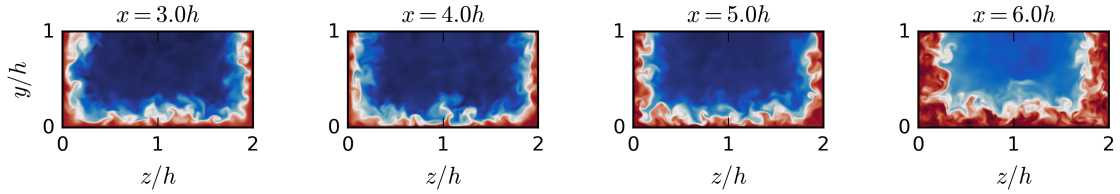

(a) Full duct.

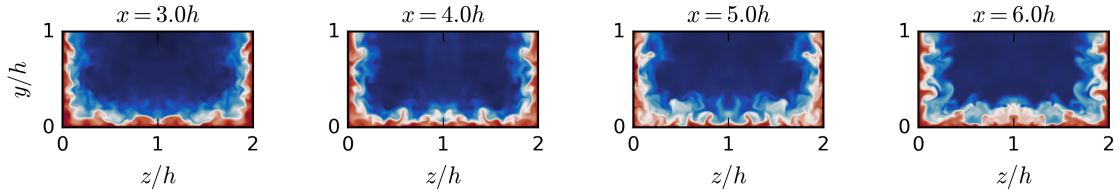

(b) Quarter duct.

FIGURE 5.27: Flow cross sections of temperature upstream of the shock train. Flow structures at the symmetry plan must represent either a local minimum or maximum.

5.6 Shock Train Modelling Comparison

As discussed in section 2.3.2, the most favoured predictive models for shock trains are those based on the one originally developed by Waltrup and Billig (1973) - referred to from now on as the Billig model. The model combines the main shock train parameters (Mach number, Reynolds number, confinement ratio) and uses them to predict a streamwise wall pressure distribution. The Billig model for rectangular ducts is repeated here for convenience:

$$\frac{(s/h)(M_2^2-1)Re_\theta^{1/4}}{(2\theta_2/h)^{1/2}} = 50\left(\frac{p}{p_1}\right) + 170\left(\frac{p}{p_1}\right)^2. \tag{5.5}$$

The coordinate variable s is equal to $x - x_2$ with location 2 referring to the leading edge of the shock train. The work done on the parametric studies in this chapter provides a large number of cases for us to compared to the Billig model and the results of this are shown in figure 5.28. Figure 5.28a compares all of the span-periodic cases whereas figure 5.28b compares the baseline channel and duct cases.

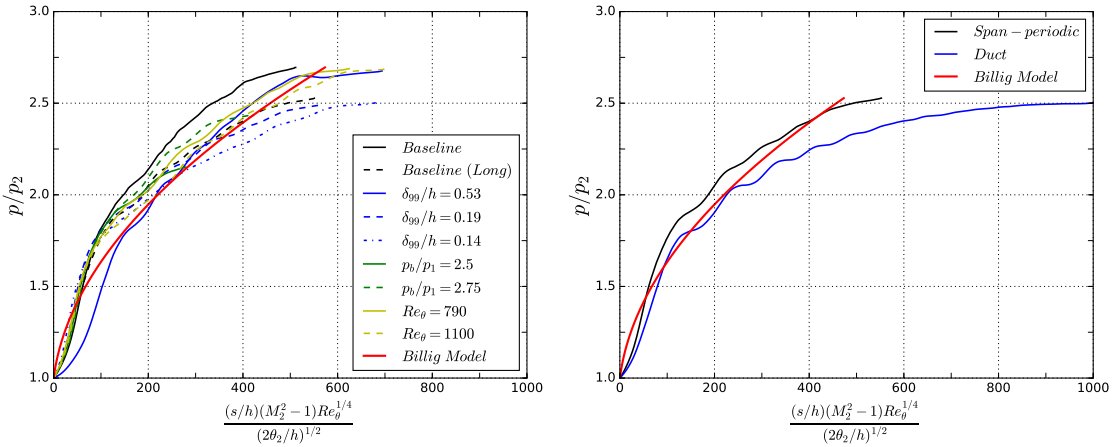

(a) Span periodic cases.

(b) Span periodic/duct comparison.

FIGURE 5.28: Comparison of all main parameter study cases and the prediction of the Billig model.

For the span periodic cases, the curves appear to collapse reasonably well and are in good agreement with the Billig model. The deviation from the pressure estimation is within $+/-0.5p_1$. The collapse is especially good close to the leading edge of the shock train ($p/p_2 < 1.75$), although in this region the estimation of the Billig model is poor. One limitation of the model is that it does not account for the spanwise confinement and this is especially clear in figure 5.28b where there is a large deviation between the channel and duct cases. The significant 3D confinement causes a much longer shock train than is predicted by the Billig model.

In figure 5.29 we plot the underlying wall pressure distributions. These curves produce a similar collapse to those in 5.28 which suggests that the strength of the model is based on the inherent pressure distributions of shock trains. Similar observations were made in previous sections of this chapter. The one exception to this is the high confinement case ($\delta_{99}/h = 0.53$) which has a more unique pressure

distribution, especially near the leading edge. As noted in section 5.4.2, the shock train in this case is highly dominated by viscous flow which dissipates the shock waves and this probably explains why its pressure curve is such an outlier.

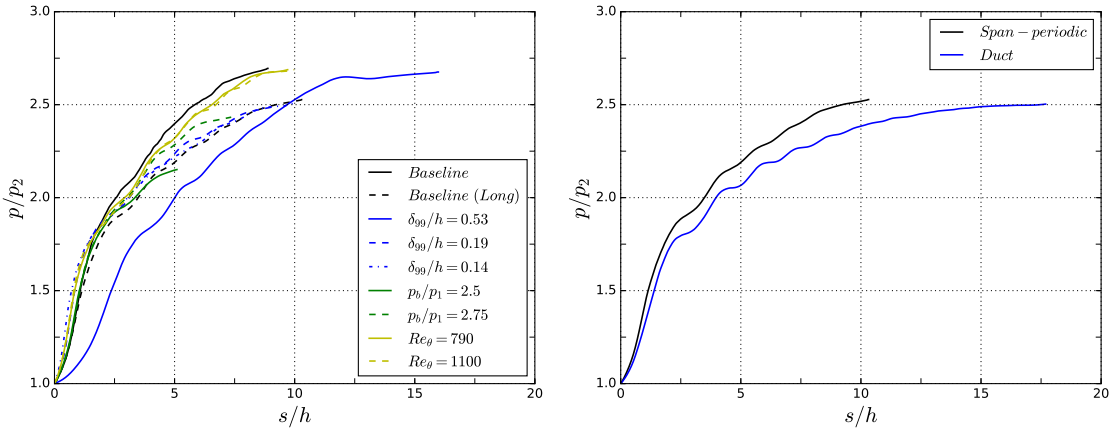

(a) Span periodic cases.

(b) Span periodic/duct comparison.

FIGURE 5.29: Comparison of wall pressure distributions, normalised by the shock leading edge, x_2.

In addition to the lack of sidewall considerations, the model is limited by the lack of tapering that occurs at the trailing edge of the shock train. Additionally, due the low-order polynomial fit and the large range of pressure ratios considered (up to $p/p_2 \sim 9$), the fine detail of the leading edge distribution is missed. Nevertheless, the model produces an acceptable prediction of the current work.

5.7 Analysis of Shock Train Structure

In this section we will consider in detail the structure of the shock trains discussed in this chapter. The range of cases available, as well as the resolution of the current simulations, means there is a good opportunity to make some observations of the various flow fields.

In section 2.3.1 we discussed the various SBLI structures that occur in shock trains. Some examples of leading shock waves from the current work are given in 5.30. As noted in previous sections in this chapter, the leading shock is typically composed of two crossed oblique shock waves followed by a stronger normal shock. The structure of the leading shock in the duct case is more difficult to discern but appears to be composed of a number of transient oblique shock waves and no normal shock wave. For the span-periodic cases, although the same basic structure

is observed for each case, there are noticeable differences when the Reynolds number and confinement ratio are varied. Increasing Re_θ or decreasing δ_{99}/h results in more well-defined oblique shock waves. Additionally, the distance between the oblique shock crossing point and the normal shock is generally reduced with a lower confinement ratio.

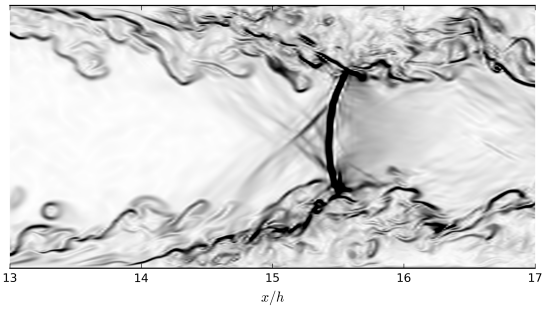

(a) Baseline span periodic case (long).

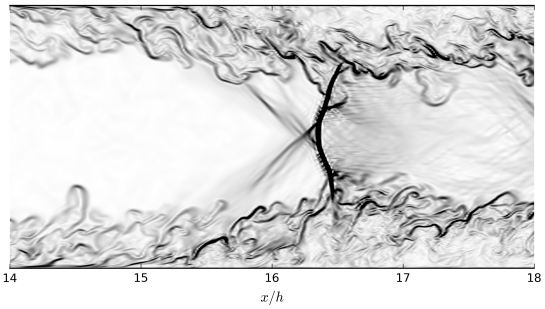

(b) $\delta_{99}/h = 0.19$ case.

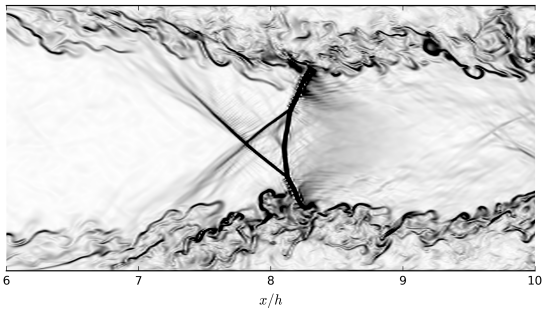

(c) $Re_\theta = 790$ case.

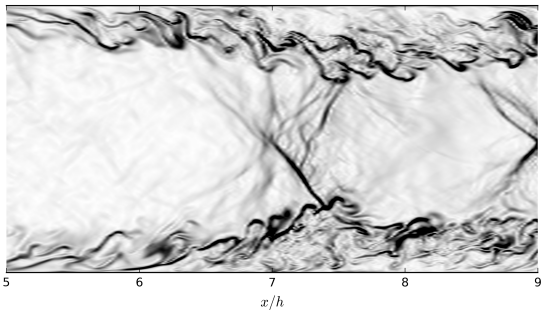

(d) Square duct case.

FIGURE 5.30: Numerical schlieren plots of the leading shock wave for a range of cases studied in chapter 5.

For each of the parameter studies in this chapter (including the sidewalls and symmetry comparisons) it was noted how well conserved the shock spacing was for the range of cases considered. The first three studies also showed a remarkable consistency between the normalised centreline pressure and Mach number distributions. This is further explored in figure 5.31 which compares the inner structure of each of the shock waves via traces of sonic lines. Position x_3 relates to the location of the peak pressure of the leading shock.

Figures 5.31a - 5.31c show the effects of back pressure, Reynolds number and confinement ratio. The shock train structure is very consistent in each case; the

traces of the sonic lines collapse together extremely well from the leading edge "ramp" all the way through the successive shock waves. As noted previously, the shock spacing is weakly dependent on the Reynolds number and the confinement ratio. Additionally, the confinement appears to be partly conserved through the shock train as shown by the slightly wider supersonic region between shock waves (referred to here as shock cells) in figure 5.31c. Despite the similarity in the shock spacing observed in section 5.4.1, it is clear from figure 5.31d that the sidewalls have a strong effect on the shock train structure. The duct case exhibits a consistently wider supersonic region as well as a lower angle of the leading edge "ramp".

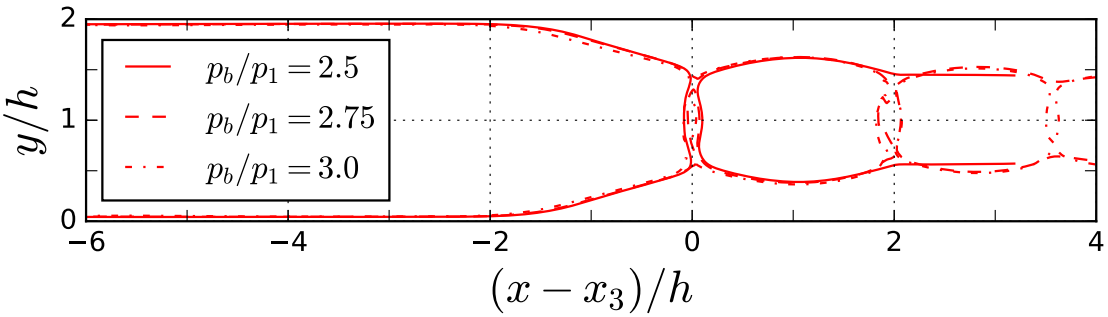

(a) Back pressure variation (all CDNS).

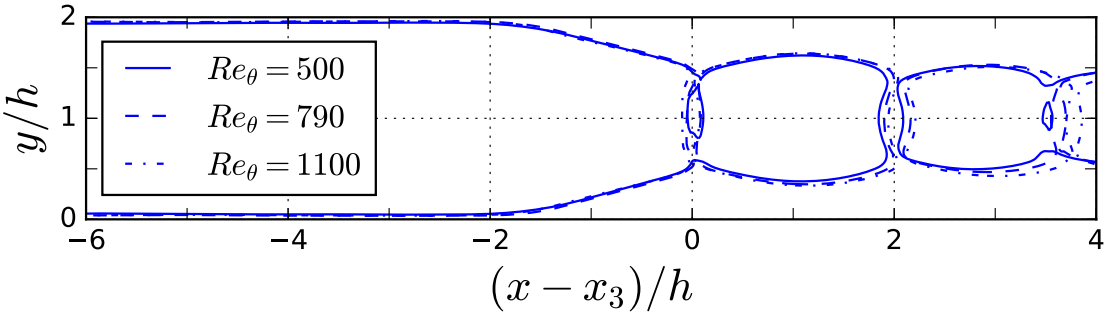

(b) Reynolds number variation.

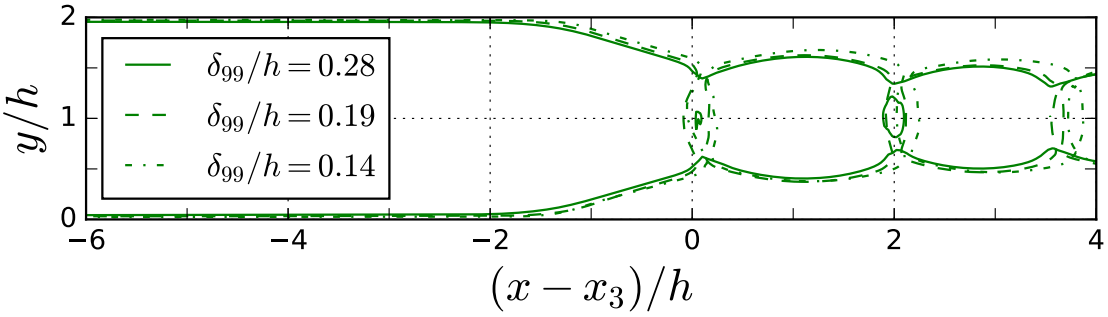

(c) Confinement ratio variation.

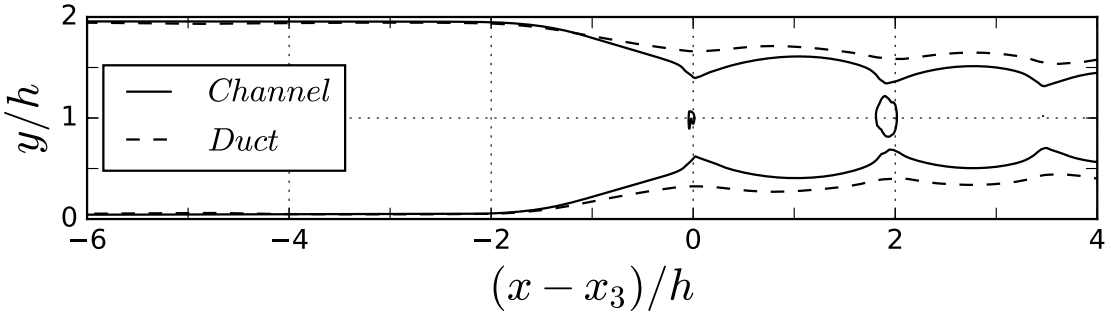

(d) Spanwise confinement.

FIGURE 5.31: Shock train structure comparisons with sonic line traces of time averaged data, normalised by the leading shock position, x_3. The shock train structures for the span periodic cases are very similar despite the range of flow parameters.

In many instances of SBLIs, the sonic region within the interaction can be considered to act as a solid boundary. In the current work, the oblique shocks at the leading edge of the shock train are caused by the wedge of subsonic flow which acts as a solid ramp. For the span periodic cases, the angle of this wedge remains apparently constant for the various parameters considered. In table 5.7 we list the recorded shock angles (column 5) as well as the freestream Mach number at the beginning of the interaction (column 2). The shock angles were calculated from time -averaged data using a shock detection algorithm and have an uncertainty value of $\pm 1°$. The CDNS and DNS cases from the grid study in section 4.3 as well as the square duct case have also been included. All shock angle values (with the exception of the square duct case) lie within within 3°, as would be expected given the shape of the subsonic wedges in figure 5.31.

Case	M_2	α_{max}	β_{max}	β (recorded)
Baseline	1.95	12.3°	43.0°	43°
Baseline (long)	1.91	11.8°	43.4°	42°
CDNS	1.96	12.4°	43.0°	40°
DNS	1.96	12.4°	43.0°	40°
$Re_\theta = 790$	1.97	12.5°	42.9°	41°
$Re_\theta = 1100$	1.96	12.4°	43.0°	41°
$pb/p1 = 2.50$	1.93	12.1°	43.2°	40°
$pb/p1 = 2.75$	1.94	12.2°	43.1°	43°
$\delta_{99}/h = 0.19$	1.91	11.8°	43.4°	42°
$\delta_{99}/h = 0.14$	1.91	11.8°	43.4°	41°
Square Duct	1.90	11.7°	43.5°	35°

TABLE 5.7: Recorded Mach numbers, deflection angles and shock angles at the shock train leading edge.

Additionally, in table 5.7 we have included the limit values of flow deflection (α_{max}) and shock angle (β_{max}) beyond which one would expect a Mach stem to occur at the centreline. These are the maximum values (based on M_2) where the post-shock flow can be still be returned to the streamwise direction with a regular oblique shock. For inviscid reflections this occurs at either the Detachment Criterion or the Von Neumann Criterion, although for Mach numbers around 2.0, these are virtually identical (see Chapman, 2000, chapter 11). For the range of cases, the maximum shock is around 43° and typically within a few degrees of the actual recorded shocks, and therefore close to the Mach stem transition-point. It is unclear whether this holds for this type of SBLI over a wider range of parameters, although it is an interesting observation nonetheless.

The shock angle for the square duct case is considerably lower than the theoretical β_{max} value and is instead much closer to the Mach angle ($\mu_2 = 31.8°$). This is consistent with the considerably weaker shock waves that are observed within the duct as well as the lower angle of the subsonic wedge. In figure 5.32 we compare contours of streamwise density gradient ($\partial\rho/\partial x$) for span periodic and duct arrangements, with the edge of the subsonic regions drawn in black. The contours are coloured as to distinguish between compression (red) and expansion (blue) regions, allowing for the compression-expansion cycle of the shock trains to be seen clearly. As well as the weaker leading shock, the square duct case has noticeably taller shock cells due to the fact that the subsonic layer thickens much more slowly.

Additionally, the mixing region in the latter half of the shock train can be seen clearly while it is not present in the span-periodic case at all.

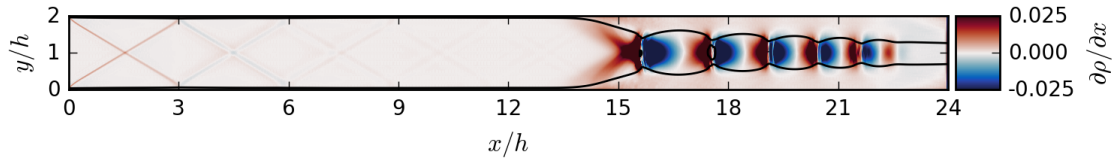

(a) Baseline span periodic (long).

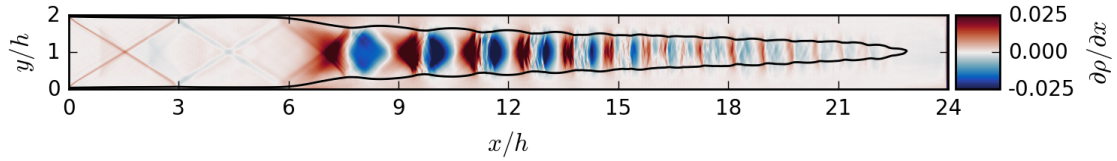

(b) Square duct.

FIGURE 5.32: Contours of span- and time-averaged streamwise density gradient with clearly demarcated contraction (red) and expansion (blue) regions.

Enhanced views of the the first two shock cells in each case are given in figure 5.33. The plots have been overlaid with flow deflection-adjusted characteristic lines indicating the pattern of expansion and compression waves. Expansion waves (diverging characteristic lines) are reflected on the sonic line as compression waves (converging lines), similar to the shock diamond pattern seen in jet exhausts. Comparing the two different cases reveals that the sidewalls have a strong affect on the shape of the expansion and compression regions - the two regions inside the shock cell are significantly more distinct in the duct case. Despite the differences in the structure of the two shock trains it is interesting to consider that the initial shock spacing is very similar in each case. Measuring between the pressure peaks, the lengths of the first two shock cells are $2.02h$ & $1.51h$ for the duct and $1.90h$ & $1.51h$ for the channel.

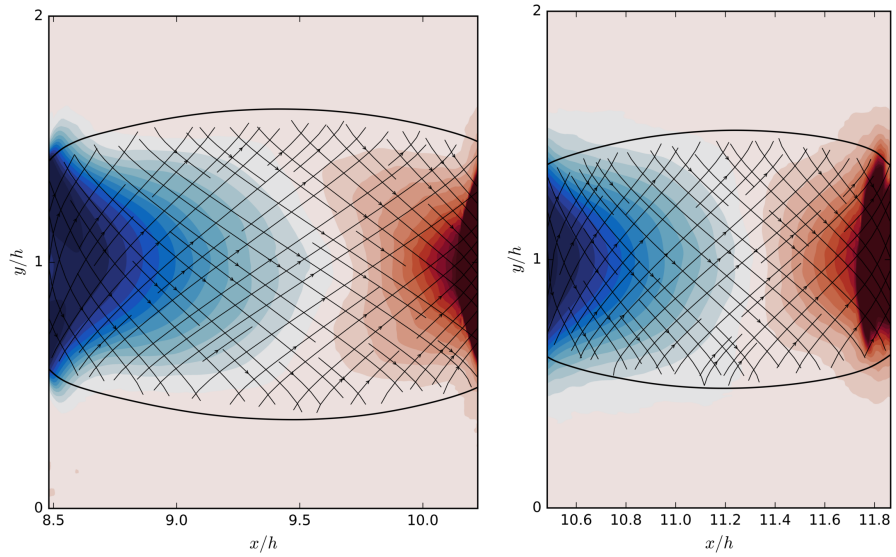

(a) Channel, 1st shock cell. (b) Channel, 2nd shock cell.

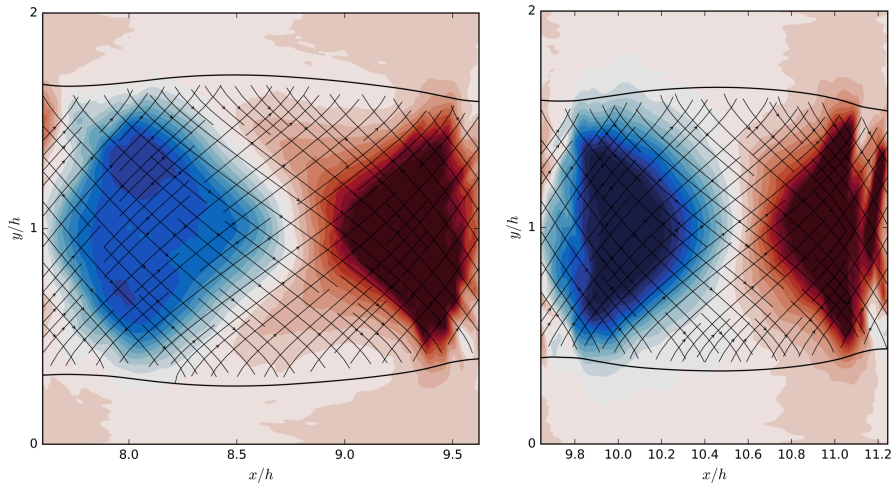

(c) Square duct, 1st shock cell. (d) Square duct, 2nd shock cell.

FIGURE 5.33: Detailed views of the first two shock cells for both span periodic and duct cases. Contours of streamwise density gradient are overlaid with left- and right-running characteristic plots.

5.8 Summary

This chapter provides a number of parametric studies in order to better understand the main controlling parameters of the shock train, especially at the particularly low Reynolds number of the current work. A number of these studies have been considered elsewhere, however, the rich datasets available with the ILES/DNS allow for a very detailed view on these effects. The main findings of this chapter are listed below.

1. **Effect of back pressure:**
   (a) A higher back pressure is associated with a longer shock train.
   (b) From the three cases considered, the size of the applied pressure gradient varies linearly with the length of the shock train, although the low number data points limits the statistical significance of this finding.
   (c) The distribution of centreline pressure (and Mach number) for each back pressure are extremely well matched once the shock train length is taken into consideration.
2. **Effect of Reynolds number:**
   (a) We are able to demonstrate the relatively weak effects of Reynolds number on the shock train.
   (b) Higher Reynolds numbers are correlated with slightly longer shock trains and longer shock spacing, as was expected.
   (c) We also find that at the intermediate Reynolds number has is a similar degree of grid sensitivity to that of the main grid refinement study.
3. **Effect of confinement ratio:**
   (a) The confinement ratio is found to have a weak effect on the shock train structure and shock spacing.
   (b) All cases exhibit very similar shock wave patterns and centreline pressure distributions (when adjusted for shock train length).
   (c) For the two more confined cases ($\delta_{99}/h = 0.28$, 0.19) we find that the shock train length is proportional to the confinement ratio. The least confined case, however, produces a longer shock train than expected, although this may be due to a very slow convergence process.
4. **Effect of sidewalls and blockage:**

(a) By directly comparing the effects of spanwise confinement we find that the sidewalls are responsible for a very large increase in shock train length (roughly by a factor of two).

(b) With sidewalls, the shock waves are considerably weaker than in the reference (channel) case although the shock spacing is initially well conserved.

(c) The shock train appears to encourage (rather than hinder) the development of corner vortices within the duct.

(d) The sidewall effects are thought to be largely caused by the additional blockage of the sidewall boundary layers, although when controlling for the blockage effects we find that there are still significant differences.

5. **Double symmetry plane:**

(a) A test is conducted to understand the impact of using a double symmetry plane as a means of only simulating one quarter of the duct.

(b) There are significant differences in the centreline flow throughout most of the shock train.

(c) The double symmetry plane arrangement appears suitable for simulating boundary layer and freestream flow.

6. **Modelling comparison and shock train structure:**

(a) All of the cases from this chapter are compared to a well-known, semi-empirical model where we find generally good agreement.

(b) We find that this model is most limited by its non-inclusion of 3D geometry.

(c) An analysis of the shock structures from the first three parameter studies reveals that the supersonic regions of the shock train are nearly identical for each case.

(d) Additionally we find that the leading shock angles all lie within 3° of the limiting angle for regular oblique shocks.

(e) A comparison between infinite and finite span cases show the strong effect of the sidewalls on the shock structure.

Chapter 6

Dynamic Shock Train Behaviour

This chapter is primarily concerned with the dynamic behaviour of the shock train, as opposed to the static behaviour in previous chapters. The chapter is in two parts: the first concerned with back pressure forcing and the other on a Fourier analysis (PSD) of the wall pressure fluctuations. All of the cases in this chapter are run at the ILES grid resolution in order to minimise the computational costs. Additionally, the TENO scheme is implemented with a higher dissipation threshold ($C_T = 10^{-5}$ rather than $C_T = 10^{-6}$) in order to provide better numerical stability around the moving shock waves without a large accuracy penalty.

6.1 Dynamic Back Pressure Response

Whereas in the previous chapters we have assumed that the back pressure is fixed, here the back pressure varies in time and we examine the time history of the shock train behaviour as it adjusts to this. In particular, we will consider step and sinusoidal forcing of the back pressure.

In figure 6.1 contours of wall and centreline pressure are plotted in $x-t$ space. This data is produced by storing slices of simulation data at fixed intervals and allows for an intuitive understanding of the time-dependent behaviour of the shock train. In this case the pressure is fixed at $p_b/p_1 = 3.0$ so the location of the shocks (ridges of high pressure) remain more-or-less fixed in space, with some slight movements due to natural disturbances. The units of time are in h/u_1 where $u_1 = 1$ is the inlet freestream velocity. The time axis represents roughly 7.5 flow-though-times of the channel. These plots will be used to provide analysis throughout this section.

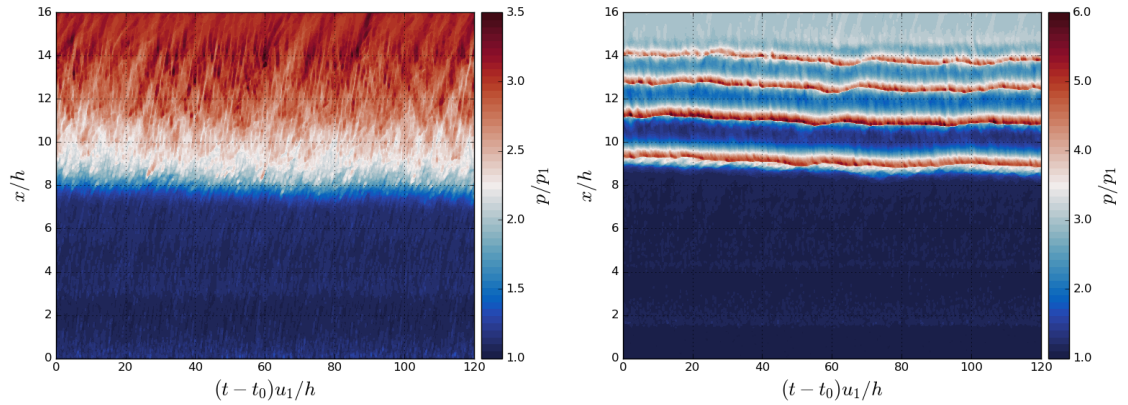

(a) Wall pressure.

(b) Centreline pressure.

FIGURE 6.1: Space-time plots with contours of pressure for a fixed pressure ratio of $p_b/p_1 = 3.0$. Data is from the ILES channel case. The four ridges in (b) correspond to the four shock waves. The shocks oscillate around their equilibrium positions due to perturbations from the inflow - these appear as the diagonal streaks in (a).

6.1.1 Back Pressure Step Forcing

The response of the shock train to step changes in back pressure is studied using four primary test cases where the sidewall arrangements and the back pressure values are varied. These are outlined in table 6.1. The step change in back pressure is applied in the simulation as a heavyside step function, such that the sponge target pressure, p_{target} is set to:

$$p_{target} = \begin{cases} p_{initial} & t < t_0 \\ p_{final} & t > t_0 \end{cases} \tag{6.1}$$

where t_0 is a chosen time such that the shock train at the initial pressure condition has converged. Over the time-scales considered, the adjustment time of the sponge zone can be negated and therefore the p_{target} value can be assumed equal to the actual back pressure, p_b. The pressure values are chosen such that the step up/step down conditions are symmetrical and therefore allow for a fairer comparison.

This matrix of test cases allows for a good understanding of how a shock train adjusts to the change in back pressure as well as the specific effects of the sidewalls and the direction of the back pressure change (step up vs. step down). Space-time plots of the centreline pressure response can be seen for each case in figures 6.2 and 6.3.

Test case	Arrangement	Initial p_b/p_1	Final p_b/p_1	$\|\Delta p/p_1\|$
C25-30	Channel	2.5	3.0	0.5
C30-25	Channel	3.0	2.5	0.5
D25-30	Duct	2.5	3.0	0.5
D30-25	Duct	3.0	2.5	0.5

TABLE 6.1: Summary of cases used to study of back pressure change.

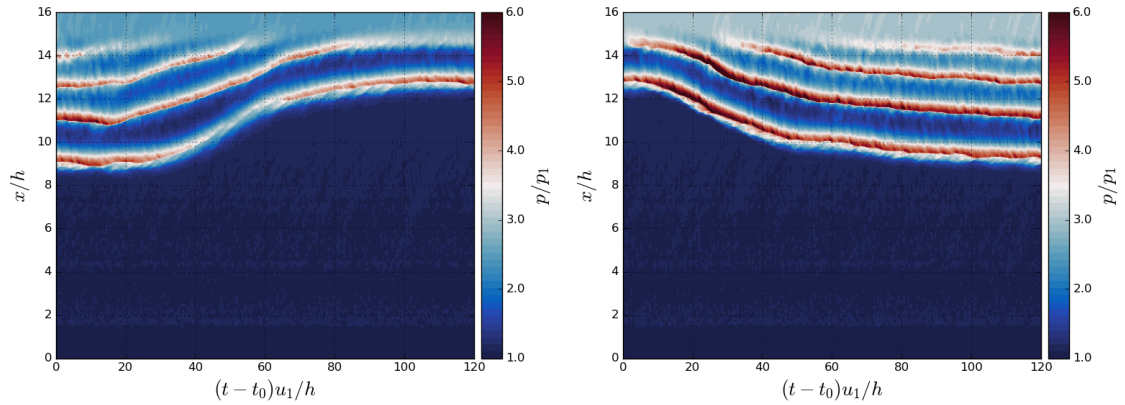

(a) Step change from $p_b/p_1 = 3.0$ to 2.5. (b) Step change from $p_b/p_1 = 2.5$ to 3.0.

FIGURE 6.2: Space-time plots showing the shock train response to step changes in back pressure (channel case). A sudden increase in back pressure will cause the shock waves to travel upstream, and vice-versa.

It is clear that a reduction in back pressure leads to the shock train moving downstream and the number of shock waves reducing. When moving downstream, the strength of the shock waves decreases (lower pressure on the colour scale) due to the reduction in the effective Mach number of the shock train. As is expected, these effects are mirrored when the back pressure is increased. The disappearance/emergence of the shock waves as the shock system moves downstream/upstream occurs gradually and the spacing between the shock waves appears to be reasonably well conserved throughout. As observed in section 5.1 spacing of n'th and $(n-1)$'th shocks is independent of the pressure ratio across the domain.

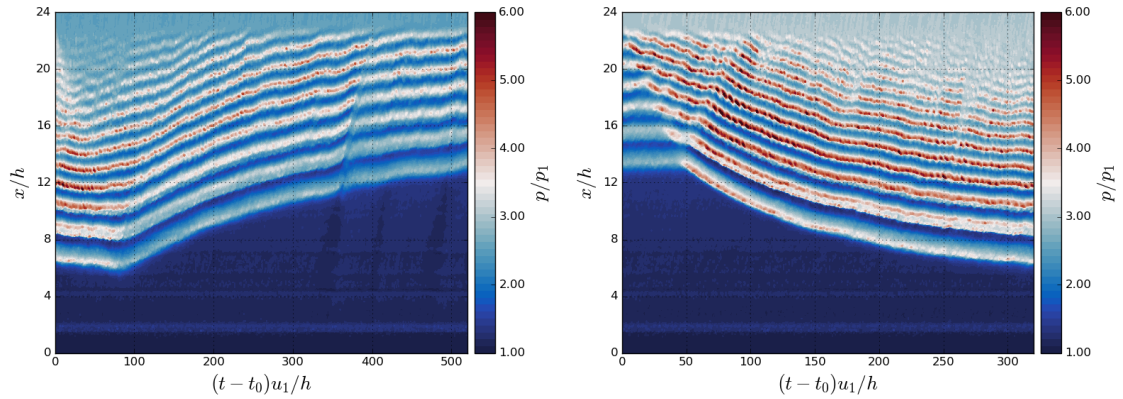

(a) Step change from $p_b/p_1 = 3.0$ to 2.5. (b) Step change from $p_b/p_1 = 2.5$ to 3.0.

FIGURE 6.3: Space-time plots showing the shock train response to step changes in back pressure (duct case). The inflow disturbances in (a) are caused by temporary laminarisation due to errors with the inflow method. Although there is a noticeable effect on the shock train, it is not assumed to be permanent.

The results from the duct cases provide a clear insight into the behaviour of the back pressure signal. Due to the supersonic nature of the core flow, the information from the back pressure change must propagate upstream via the subsonic boundary layer flow. The duct cases are long enough and with enough shock waves for there to be a very clear progression of the back pressure signal where the shock waves only respond once the signal reaches the correct part of the duct.

In figure 6.4 we plot the time history of duct case static pressure at two different y locations in each case. The plots are overlaid with the corresponding $u-c$ acoustic lines for reference (where c is the local speed of sound). Considering the two wall plots, it is clear that the back pressure propagates at a slower speed than the natural $-c$ acoustic signal. The other two figures are plotted at wall distances of $0.08h$ and $0.15h$ for the D30-25 and D25-30 case respectively, where the $u - c$ lines match with the back pressure propagation. The propagation speed appears to be relatively constant at approximately $u_1/6$ ($M \sim 0.33$) for all wall distances in both cases.

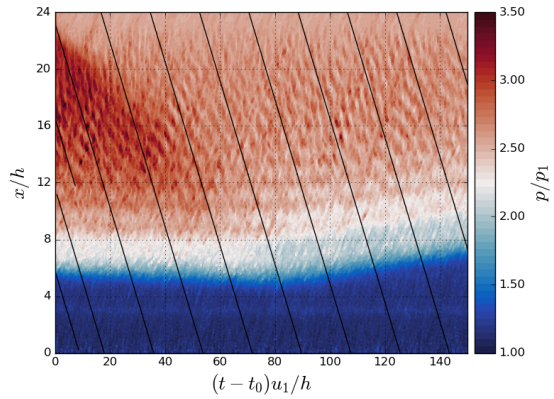

(a) D30-25, wall pressure.

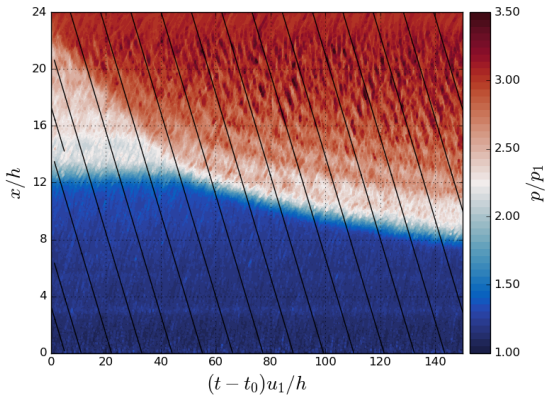

(b) D25-30, wall pressure.

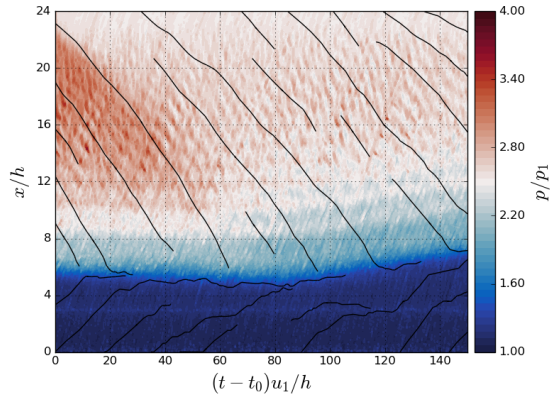

(c) D30-25, pressure at $y = 0.08h$.

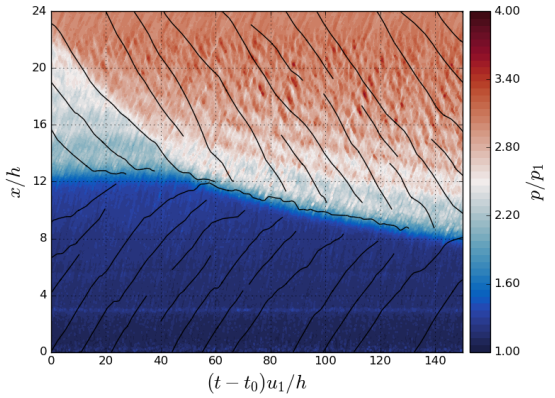

(d) D25-30, pressure at $y = 0.15h$.

FIGURE 6.4: Space-time plot of static pressure at various y locations and overlaid with acoustic lines $(u - c)$. The back pressure signal propagates at the same rate for all y locations.

The most noticeable difference between the channel and the duct cases is the much larger number of shocks in the duct. This fact has already been established in the previous chapter, although it is interesting to note that at the lowest back pressure, the converged shock train in the duct is composed of 6 shock waves compared to a single shock wave in the corresponding channel case. By comparing the time axes in figures 6.2 and 6.3 it is clear the duct cases exhibit much larger response times, even accounting for the fact that the duct is 50% longer in x.

Considering the different axis scales and domain sizes, it is difficult to directly compare the four cases from the data presented in these figures. To provide a better comparison, the space-time trajectories of the leading shock wave in each case are

plotted together in figure 6.5. These coordinates are extracted from the centreline pressure fields and a Gaussian filter has been applied to produce smoother curves. These trajectories provide a relatively good guide to the movement of the entire shock train since the shock spacing is well conserved. It is clear that the duct cases have a much larger response time, even accounting for the time it takes the back pressure change to reach the leading shock.

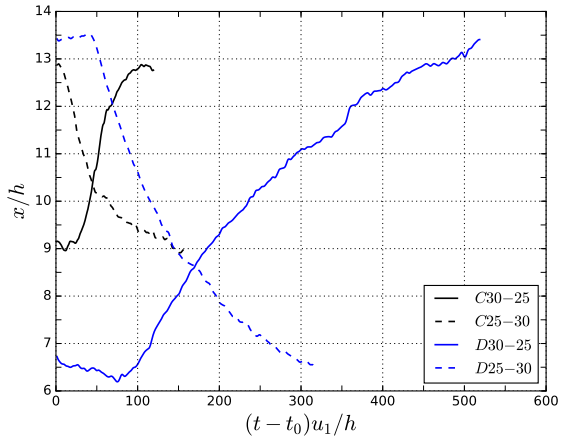

FIGURE 6.5: Trajectories of the leading shock wave in space-time for each of the four comparison cases. The initial downward slope of the D30-25 line indicates a non-steady-state initial condition.

In figure 6.6a these trajectories have been normalised by t_1 and x_1 which are respectively the time and position where the leading shock begins to adjust to the back pressure change. Additionally, the absolute value of the normalised shock position ($\|x - x_1\|$) is taken in order to better compare the trajectories. What is immediately clear is that all cases bar D30-25 have a very similar initial response such that the trajectories within the period $(t - t_1)u_1/h < 75$ collapse together. This is an important observation since it suggests that the initial response of the shock train may be generalisable for a range of conditions and geometries, albeit with some exceptions. The D30-25 case (duct arrangement, step down) is the outlier in that the response is considerably slower. The overall time it takes to adjust to the new time is approximately 50% longer that the corresponding D25-30 case.

The relative velocity of the leading shock wave for each case is plotted in figure 6.6b. For the two channel cases, the shock train peaks at around 10% of the freestream velocity before quickly slowing as the shock train reaches its new equilibrium position. The D25-30 case follows a similar pattern but peaks at a lower speed of 6% of u_1. For the D30-25 case there is also an early peak (4% of u_1) but

this occurs much later at around $(t - t_1)u_1/h = 50$ and the acceleration is significantly lower than the other cases - hence the initial divergence in the shock position.

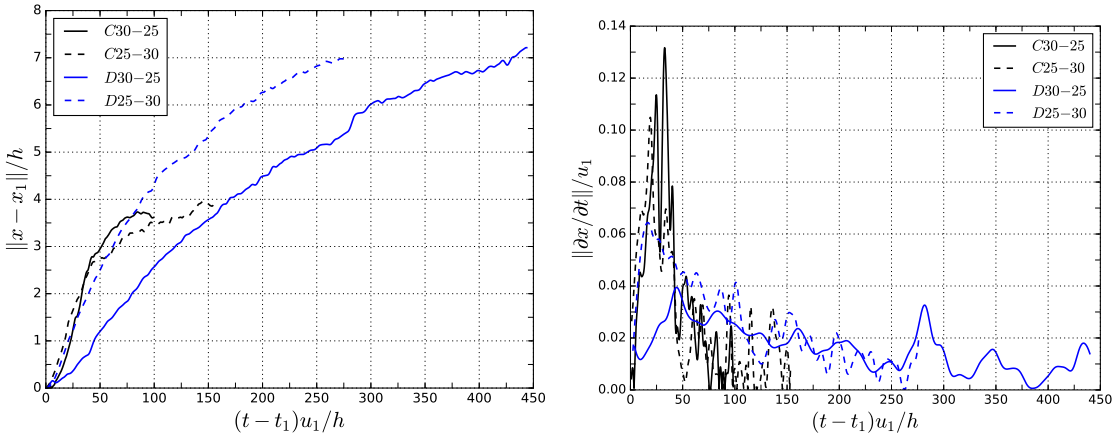

(a) Normalised position.

(b) Relative velocity.

FIGURE 6.6: Absolute position and velocity of the leading shock wave (adjusted for the back pressure lag). The D30-25 case is the clear outlier.

In the following pages we will consider two possible explanations for the lack of symmetry in the duct cases. The first of these is the natural drift in the back pressure that occurs when no sponge zone treatment is applied to the duct. As was discussed briefly in section 4.1.3, when there is no outflow treatment in the duct, the natural boundary layer confinement leads to an upstream drift in the back pressure that eventually causes a shock train to form. This process is shown in figure 6.7 where the centreline pressure drifts over time, leading to distinct pressure waves which then become shock waves.

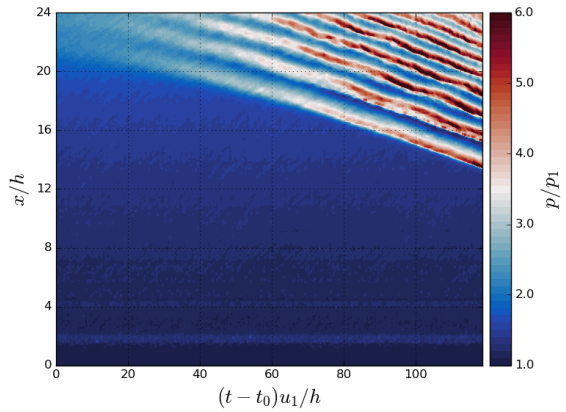

FIGURE 6.7: Space-time plot of duct centreline pressure with no sponge zone active, showing the natural formation of the shock train.

As with the previous cases, the leading shock position can be tracked and this is shown in figure 6.8a with the results from the D25-30 case included as a reference. The trajectory of the leading shock appears approximately linear and from the corresponding plot of velocity (figure 6.8b) we can see that there is no drop off in velocity seen with the other cases. This is explained by the fact that the back pressure continues to drift higher meaning there is no equilibrium position for the shock to reach. While the sponge zone in the channel arrangement is used to raise the exit pressure above its natural level, it appears that in the duct arrangement the opposite is true. Therefore, any situation where the back pressure is decreased (such as with D30-25), the sponge must fight against the natural tendency for the shock train to drift upstream. This seems like a plausible explanation for why the D30-25 case is such an outlier.

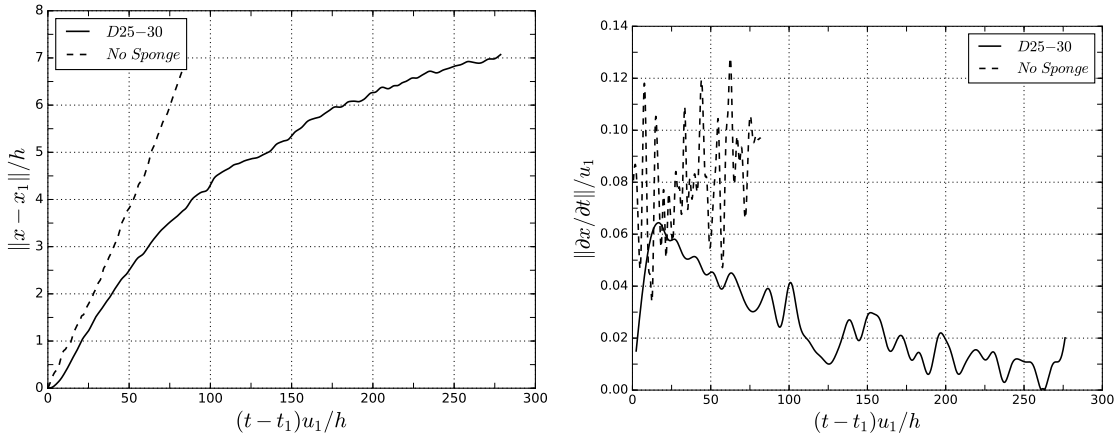

(a) Normalised leading shock trajectory. (b) Leading shock relative velocity.

FIGURE 6.8: Normalised leading shock trajectories comparing the D25-30 to the sponge-less duct case.

Another possible explanation for the slow response of D30-25 can be seen by examining the trajectory of the leading shock prior to the pressure change. In figure 6.5, within the period $(t - t_0)u_1/h < 100$, the shock can be seen slowly drifting upstream before the back pressure change causes it to move downstream. The pressure change was done at this point to avoid the shock train travelling into the boundary layer development region. Figure 6.9 shows the natural drift of the shock train where no pressure change is applied. The movement of the shock train suggests that the equilibrium position lies within the development region.

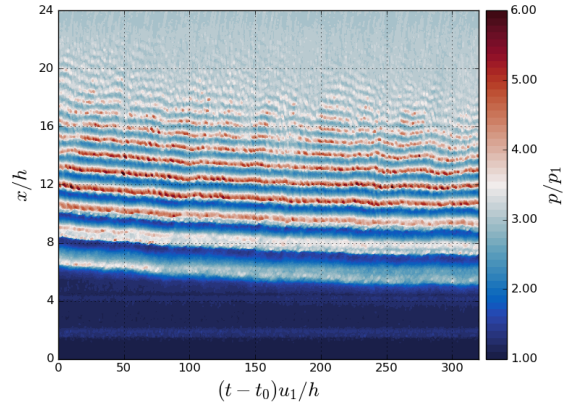

FIGURE 6.9: Space-time plot of centreline pressure showing the drift in shock position with a fixed back pressure. t_0 here is the same as with the D30-25 case but with no step change imposed.

In order to test whether the lack of steady-state is the reason for the slow response, a set of additional test cases were run such that the equilibrium position occurs at $x > 6h$. The details of these cases are listed in table 6.2. The lower peak pressure (2.75) allows for the shock train in the duct case to avoid the development region before the step change is applied. Due to resource constraints, it was not possible to run a fourth duct case. Additionally, the D275-25 case was not run all the way to its new equilibrium position, but the initial linear response was captured.

Test case	Arrangement	Initial p_b/p_1	Final p_b/p_1	$\|\Delta p/p_1\|$
C25-275	Channel	2.50	2.75	0.25
C275-25	Channel	2.75	2.50	0.25
D275-25	Duct	2.75	2.50	0.25

TABLE 6.2: Additional test cases for studying the step change response.

Space-time plots of the C275-25 and D275-25 cases are shown in figure 6.10. The results are similar to their higher step size counterparts in figures 6.2 and 6.3 - albeit with shorter initial shock trains and lower response speeds. The position of the leading shock in D275-25 is initially fixed at around $x = 9h$.

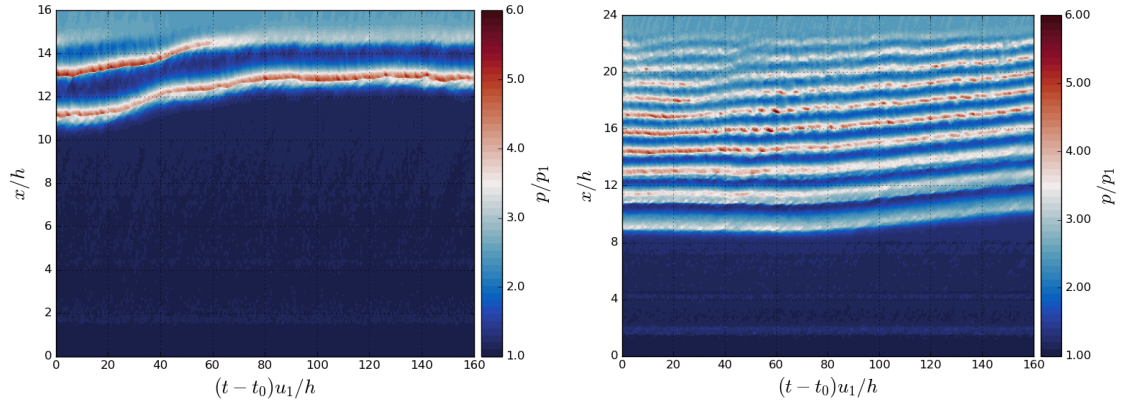

(a) C275-25. (b) D275-25.

FIGURE 6.10: Space-time plots of the channel and duct responses to a smaller step size.

A plot of normalised leading shock trajectories of all three cases is given in figure 6.11. The first thing to note is that the channel cases exhibit the same symmetrical response as with the larger step size - this adds strength to the argument that the direction of step size does not affect the speed of the moving shock wave, at least

for the channel cases. The second important observation is that the duct case once again has a significantly slower response than the channel cases. The average speed of the D275-25 leading shock is about 25% lower than C275-25, compared to around 50% lower for the larger step size (C30-25 and D30-25). This suggests that the non-steady state condition seen in D30-25 only partially accounts for its slower speed and therefore the sidewalls must play an important role in determining the dynamic behaviour of the shock train. In addition to the much longer shock train, there is a different composition of shock losses and mixing losses which may contribute to the slower step response. The shock train moves in response to the back pressure change partly in order to increase/decrease the relative Mach number and therefore the strength of each shock (this effect can be seen with back pressure forcing of normal SBLIs - Bruce and Babinsky, 2008). Given the different compositions of the channel and duct shock trains, it is perhaps then unsurprising that their step change response should be different. Determining whether or not the duct arrangement exhibits the step up/down symmetry (as occurs with the channel cases) would require running an additional duct case (D25-275).

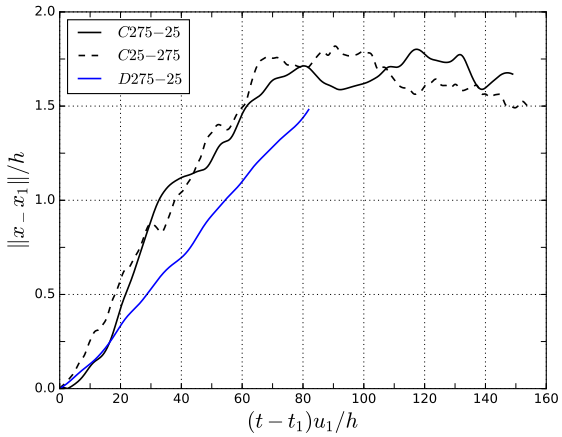

FIGURE 6.11: Normalised leading shock trajectories of the reduced step size cases. The slope for the D275-25 is approximately 25% lower.

Unstart Process

The cases discussed thus far 6.1 are designed to contain the shock train within the numerical domain and away from the boundary layer development region ($x/h < 6$). One additional channel case (C30-35) was tested where the back pressure was increase from 3.0 to 3.5. In this case, the shock train was not contained within the post-development region and an unstart-like process occurred where the shock train moved all the way to the inlet of the domain.

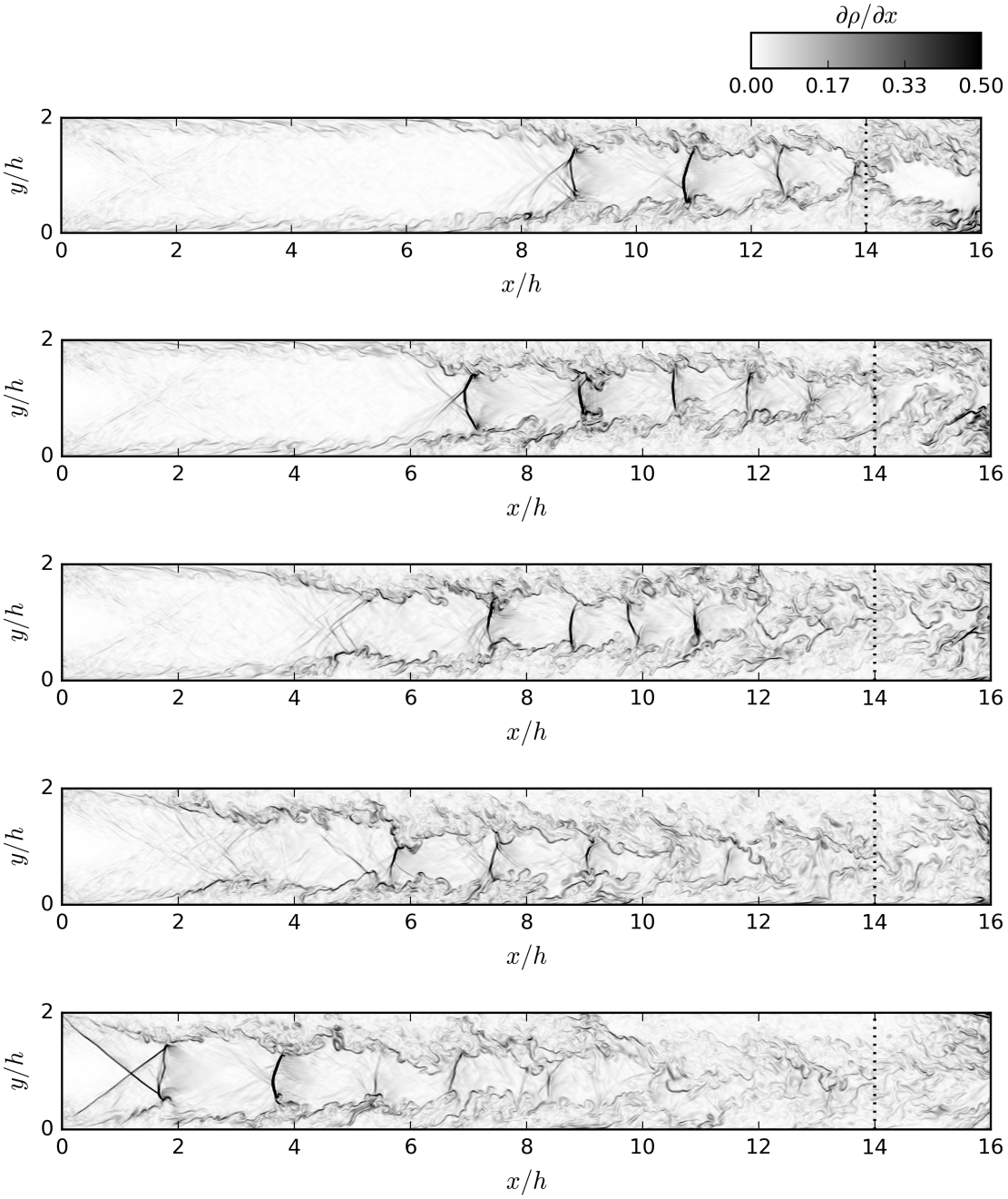

FIGURE 6.12: Density gradient plots showing the process of unstart. Data is taken at instances of $(t - t_0)u_1/h = 0$, 50, 100, 200, 270. The leading shock becomes substantially weaker as it moves upstream, before becoming stronger upon reaching the inlet.

Flow fields at various time frames are shown in figure 6.12. The shock train starts at the equilibrium state at $p_b/p_1 = 3.0$ and begins the familiar upstream movement after the back pressure is increased. As the shock train moves upstream the strength of the leading shock actually decreases significantly. Once the leading edge of the front shock wave reaches the inlet, the shock becomes anchored and again increases in strength.

This process is also demonstrated by the space-time plot of centreline pressure in figure 6.13. Due to the shock train moving into the boundary layer development region, the interpretations from this case are limited. For example, the reduction in leading shock strength occurs briefly after reaching $x/h = 6$ suggesting that this may be a caused by the un-physical flow.

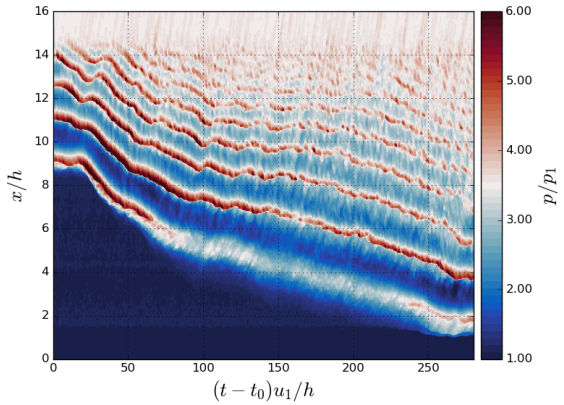

FIGURE 6.13: Space-time plot showing the process of unstart. The pressure ratio is increased from 3.0 to 3.5.

In figure 6.14a the normalised trajectory of the leading shock is compared to another step-increase case (C25-30). As with figure 6.6a the initial trajectories $(t-t_1)u_1/h < 50$ collapse together very well. This again suggests that the movement of the shock train in response to a back pressure jump may be independent of the initial state of the shock train and independent of the direction of the pressure change.

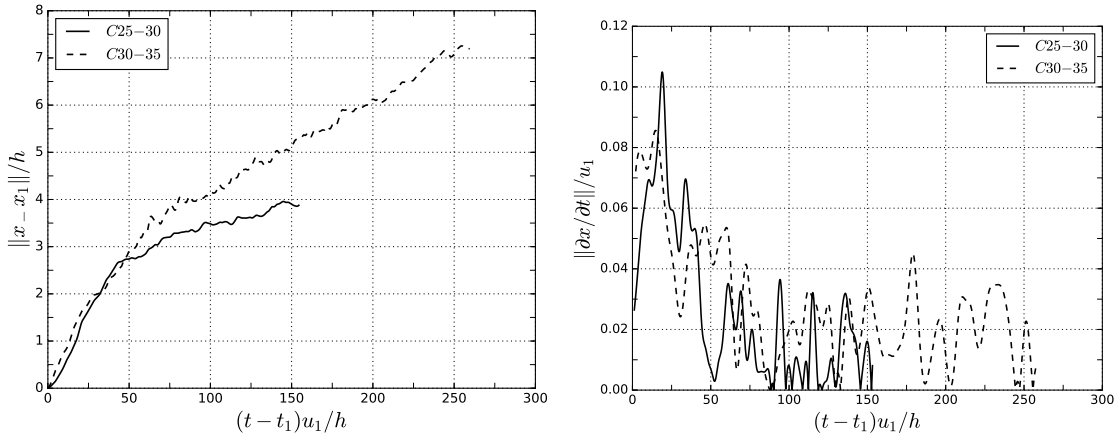

(a) Normalised trajectory.

(b) Relative velocity.

FIGURE 6.14: Leading shock trajectories and relative velocities comparing the C25-30 and C30-35 cases. The trajectories are initially well matched before diverging after $(t - t_1)u_1/h = 50$.

It is interesting to note that beyond the divergence point of the two shock trains, the shock in the C30-35 case moves linearly upstream rather than levelling-off (as occurs with C25-30). It is most likely that this behaviour is due to the shock train encountering the boundary layer development region. Within this region, the wall shear stress is considerably lower, as seen by the skin friction distribution of the shock-less case in figure 6.15.

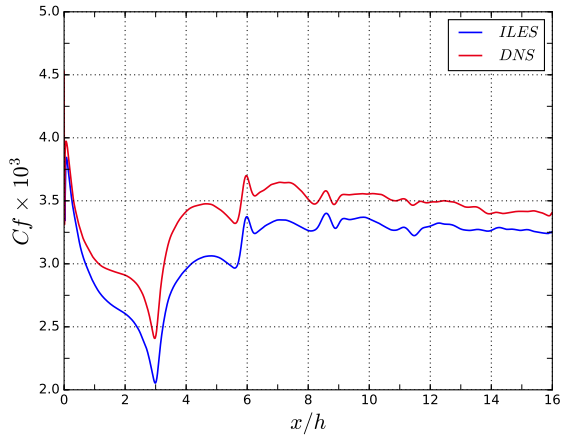

FIGURE 6.15: Distribution of skin friction coefficient through the zero-pressure-gradient channel.

The shock train behaviour in this region is similar to that of a shock train within laminar boundary layers; the weak leading shock and linear unstart behaviour are typical of laminar shock trains (see the results in appendix A). As the shock train in C30-35 moves through the un-physical development region, it encounters a more laminar-like boundary layer (lack of coherent turbulent structures, lower wall shear stress). This observation may explain the unexpected unstart behaviour of the C30-35 shock train.

Effect of Back Pressure Step Size

So far we have only compared cases where magnitude of the back pressure change has been constant. For the channel arrangement, the initial response speed of the shock train has been very similar, regardless of whether the change is positive or negative. However, the question remains whether this holds true if the magnitude of the pressure change is different. In the remainder of this section we will address this question by comparing the C25-275 and C25-30 cases which have been discussed previously in this section. These two cases have identical initial conditions and only differ by the size of the pressure step change. In figure 6.16 we compare the responses of the C25-30 and C25-275 cases. As seen in section 5.1, a back pressure of 2.75 only causes one additional shock to form in the shock train.

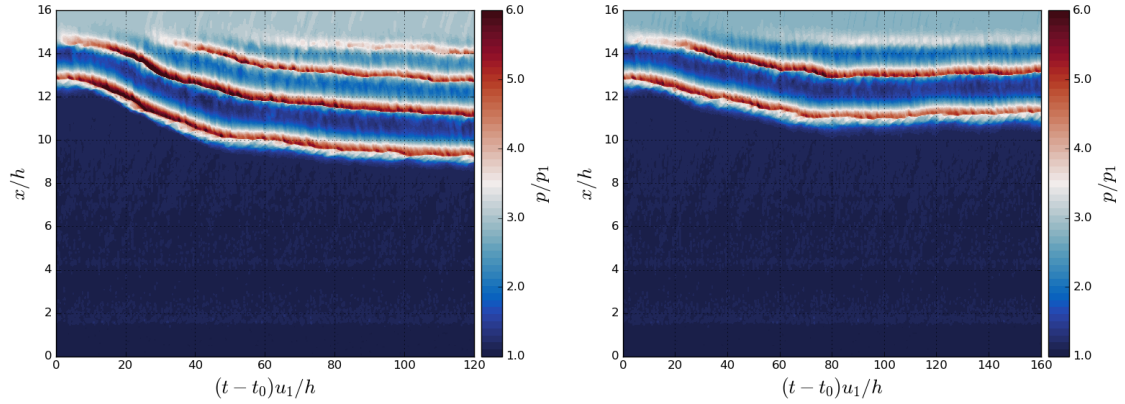

(a) C25-30. (b) C25-275.

FIGURE 6.16: Comparison of centreline pressure history showing the effect of back pressure step size.

Judging by the slope of the shock trajectory, it appears that the response rate for the smaller back pressure change is slower and this is confirmed by the tracked leading shock trajectories in figure 6.17a. There is no matching trajectory in the initial shock response as seen in other comparisons which strongly suggests that the

response is dependent on the magnitude of the back pressure change. Within the time period $(t - t_1)u_1/h < 40$ the C25-30 case moves a distance of approximately $2.5h$ compared with $1.1h$ for the C25-275 case. This is a factor of 2.27 difference whereas the pressure change differs by a factor of 2.0, suggesting an approximately linear relation of the response rate to the imposed step amplitude. Having only two cases to compare limits any further interpretation of the relationship that can be inferred between these two variables but it is clear that a higher back pressure change has a positive effect on the initial response of the shock train.

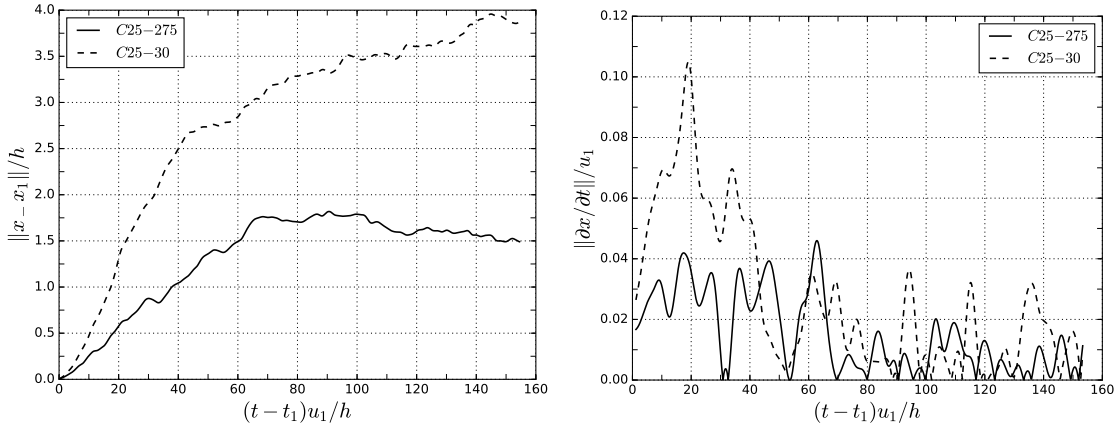

(a) Normalised trajectory.

(b) Relative velocity.

FIGURE 6.17: Leading shock trajectories and relative velocities comparing the C25-30 and C25-275 cases.

6.1.2 Sinusoidal Forcing

Due to the flow conditions experienced by a typical shock train within an air-breathing engine, it is important to understand the response of shock trains to harmonic back pressure variations. For example, the operation cycle of a combustion chamber can induce periodic loads which may reach the shock train within the isolator section. In this section we will study the response of a shock train to three separate back pressure forcing frequencies. Here, the time varying back pressure takes the form

$$p_b(t)/p_1 = \begin{cases} 3.0 & t < t_0 \\ 3.0 + \sin\left(\frac{2\pi(t-t_0)}{T_0}\right) & t > t_0, \end{cases} \tag{6.2}$$

where T_0 is the period of oscillation. This results in an average back pressure of 3.0 and maxima and minima of 4.0 and 2.0. The chosen oscillation periods and the

corresponding frequencies are listed in table 6.3. The conversion into kHz is done using an assumed reference freestream velocity of $680m/s$ and a channel length, l_x, of $70mm$ [1]. The oscillation periods are designed to allow for a factor of four between each case. Since the flow-through time period is approximately $16h/u_1$ the three cases allow for respectively 4, 1 and 0.25 oscillation periods per convective cycle.

Case	$T_0\,(h/u_1)$	$f\,(u_1/h)$	$f\,(kHz)$
T-04	4	0.25	40
T-16	16	0.0625	10
T-64	64	0.015625	2.5

TABLE 6.3: List of back pressure forcing frequencies.

All three of these cases implement the same Reynolds number, Mach number, confinement ratio and grid resolution as the baseline ILES channel case. None of the frequencies were tested within the duct arrangement. The oscillation commencement time, t_0, is chosen such that the shock train is initially at a converged position. Oscillation data is captured over a long enough time frame that the shock train responses become suitably cyclic. The time variance of back pressure in each case is shown in figure 6.18.

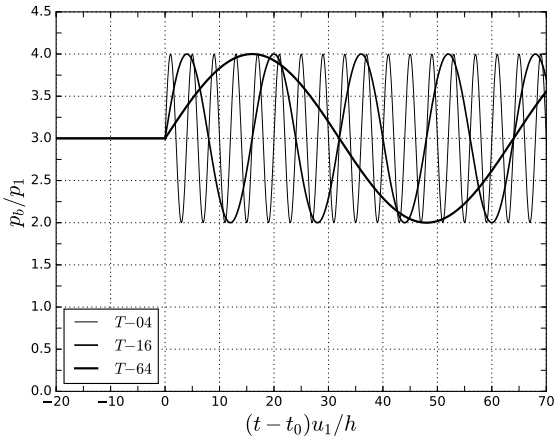

FIGURE 6.18: Variation of back pressure over time for all three forcing frequencies.

In figure 6.19 the time history of centreline pressure is shown for each frequency. The back pressure oscillations apply uniformly across the sponge zone ($x/h > 14$)

[1] These values are based on assuming a reference pressure of $10kPa$ and reference temperature of $273K$.

when they then travel upstream via the subsonic region of the shock train. It is immediately clear that the different forcing frequencies induce very distinct shock train responses. The highest frequency case (T-04) only noticeably affects the two downstream shock waves, causing them to oscillate slightly. Any disturbances upstream of this are quickly dissipated.

The intermediate forcing frequency in T-16 causes much larger oscillations in the shock wave positions. All but one of the shock waves oscillate in the streamwise direction at the applied forcing frequency. The leading shock oscillates initially (at roughly half the applied frequency) before converging to an equilibrium position which is noticeably offset upstream from the initial equilibrium position.

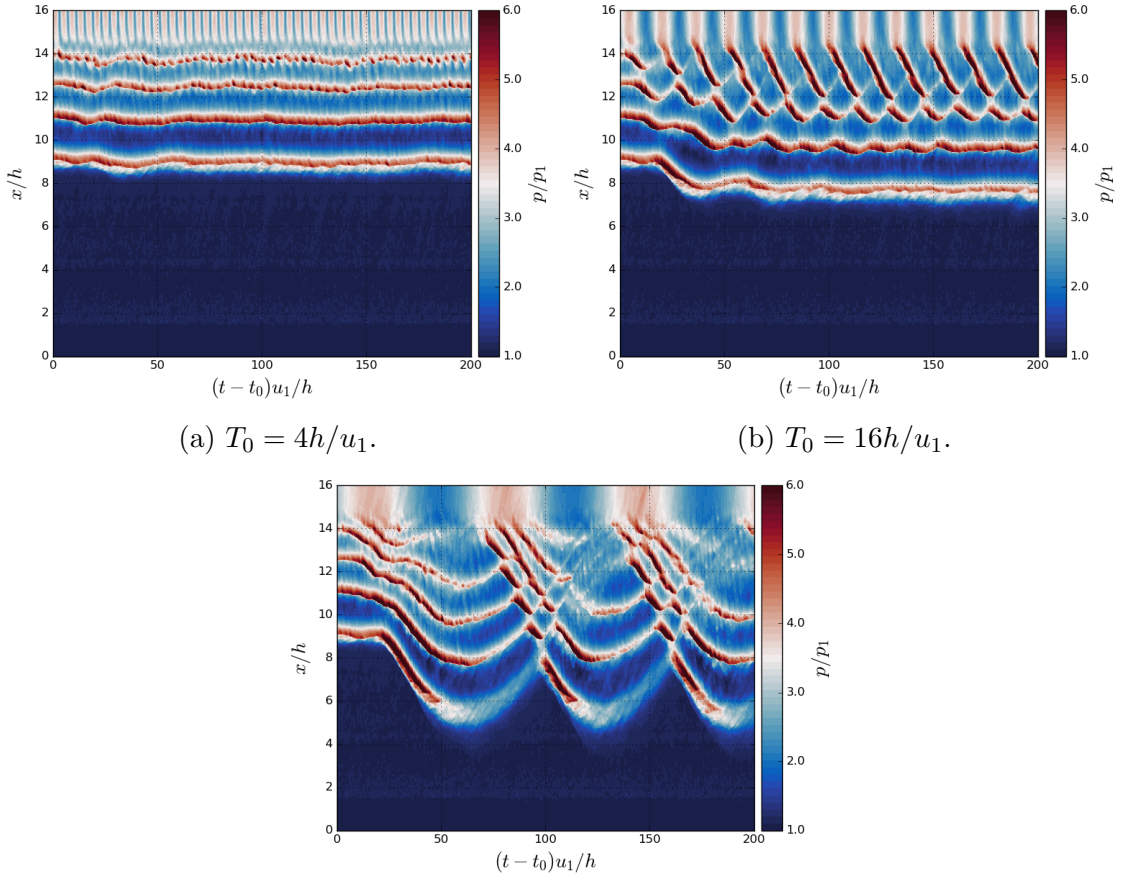

(a) $T_0 = 4h/u_1$.

(b) $T_0 = 16h/u_1$.

(c) $T_0 = 64h/u_1$.

FIGURE 6.19: Shock train response to harmonic back pressure forcing at different frequencies. Each frequency induces a very distinct response from the shock train.

By decreasing the frequency further still (T-64), the shock wave oscillations be-

come even larger. Each forcing cycle causes the production and subsequent destruction of 3 separate shock waves. During the high pressure ($p_b/p_1 > 3.0$) periods 3 individual shocks form and begin to travel upstream where they are met with retreating shocks from the previous cycle. At this point there is a complex but repeatable merging process between the retreating and advancing shocks. Each time two shock waves converge there is a dominant upstream and weaker downstream component. Therefore, the merging process may be considered as two moving shock waves either passing through each other or reflecting off each other. In the former interpretation, a shock wave which forms at the outlet can pass through the entire shock train to eventually become the leading shock, before eventually retreating back to the outlet.

The combined effect of the back pressure lag and the shock train merging process is for the oscillation pattern of the leading shock to have a saw-tooth wave form, rather than a smooth sinusoidal shape. As with the T-16 case, the average position becomes significantly offset from the initial state. As seen in figure 6.20, all of these results are independent of the phase in the forcing function, albeit after two complete oscillation cycles.

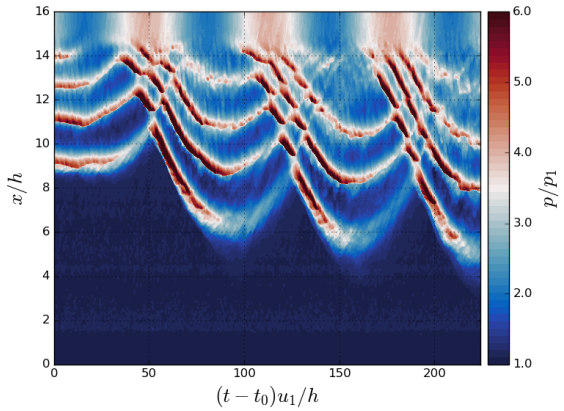

FIGURE 6.20: T-64 shock train response with 180°phase difference in forcing function. The effect of the phase difference disappears after 3 complete cycles.

The large oscillation amplitudes are enough to move the leading shock temporarily into the boundary layer development region so the T-64 case was run again on a longer domain (up to $24h$) in order to avoid this and the results are shown in figure 6.21. Other than the higher number of shock waves, the same interference pattern occurs in this case. Additionally, the strength (pressure peak) of the leading shock does not drop before reaching the maximum oscillation amplitude and instead more is gradually reduced as the shock moves downstream.

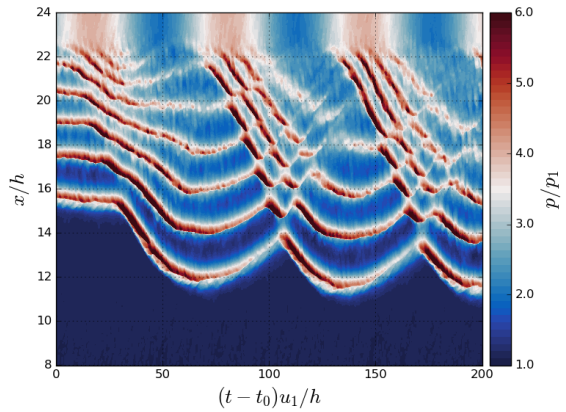

FIGURE 6.21: Longer domain version of the T-64 case.

It is interesting to note that, despite having the same average back pressure, the average length of the shock train for the T-16 and T-64 cases is longer than when the back pressure is fixed in time. As seen in the previous sections, when accounting for the back pressure lag, the initial response of the shock train is independent of the direction of the pressure change (within the time-scales considered here). This suggests that there should be no inherent bias towards upstream or downstream movement - which contradicts the observed bias of the sinusoidal cases towards the upstream direction. To explain this effect we will consider a simplified shock train model, as discussed in the following section.

The range of frequencies considered here are significantly higher than those that have been applied in the open literature. Even when adjusting for the domain size, the applied back pressure forcing in both Klomparens et al. (2016) and Gnani et al. (2018a) occurs at frequencies at least one order of magnitude below that of the current work. At such frequencies the lag effect between the head and tail of the shock train becomes negligible and each of the shock waves can be assumed to adjust instantaneously to the back pressure change. Hence, these cases did not observe any of the frequency-dependent behaviour (shock merging, dissipation of disturbances) that are seen here.

6.1.3 Dynamic Shock Modelling

Background

From the observations presented in sections 6.1.1 and 6.1.2 it is clear that the behaviour of a shock train with a time-dependent back pressure is determined by the following factors:

1. Positive changes in back pressure induce an upstream movement of the shock waves, and vice-versa for negative changes. The absolute size of the back pressure appears to determine the target position of each of the shock waves. The trajectory of the shock waves has a parabolic-like shape with an initial slope approximately proportional to the size of the pressure change.

2. Back pressure changes are associated with the emergence and disappearance of shock waves. Longer shock trains with higher back pressures have more shock waves.

3. The back pressure changes propagate upstream via the subsonic region. For the current arrangement this was observed to occur at approximately $u = -0.17$.

4. For sinusoidal back pressures, the frequency of forcing affects how the back pressure signal dissipates as it travels upstream. With high frequency forcing (frequencies less than one order of magnitude of the response time) the disturbances are dissipated before reaching the leading shock.

5. The shocks are coupled such that there is a "natural" shock separation that appears to be independent of the size of the back pressure.

With these thoughts in mind, we will attempt a rudimentary model of the time-dependent shock wave position. This model is based on the results from the channel arrangement only, although the conclusions drawn from the results are also applicable to the duct cases.

We start with the assumption of n shock waves arranged in a one-dimensional space of size $0 \geq x \geq l_x$ with an unbounded time variable. The back pressure is applied at $x = l_x$ and is varied with an arbitrary time-dependent function $p_b(t)$. The initial arrangement of the shock train is based on the empirical shock spacing results and the linear relationship between back pressure and shock position. For shock $i = 0...n-1$ (where 0 is the leading shock) the initial position is given by

$$x_i(t=0) = s_i - \sigma(p_b(t=0) - p_{b,0}), \tag{6.3}$$

where s_i is the reference shock distribution at reference back pressure, $p_{b,0}$. For the current model these are based on the $l_x/h = 16$ shock train results where $p_{b,0} = 3.0$ and $s_i = [9.0, 10.9, 12.5, 13.9, 15.2, 16.4, 15.5, 16.5, 17.5...]$. The parameter σ determines the how strongly the back pressure affects the shock position. From the results in section 5.1 we find that $\sigma = 8.0$.

The back pressure lag effect is applied to the model such that disturbances travel upstream at characteristic speed $u_c = -0.17$. Therefore each shock is affected by the back pressure with the following time delay:

$$t_{lag} = (l_x - x_i(t))/u_c. \tag{6.4}$$

The dissipation of high frequency disturbances is applied to the model with a position-depended, low-pass filter. The filtered back pressure, $\tilde{p}(t)$ has been passed though a Butterworth filter (Butterworth, 1930) with a cut-off frequency that varies linearly from 10^{-2} at $x = 0$ to 10^{-1} at $x = l_x$. Therefore, the back pressure experienced by each shock wave (after the lag and filtering is applied) is $\tilde{p}(t - t_{lag})$. The basis of the model is that the back pressure and shock spacing determine a moving target, $x_{target,i}$, for each shock wave to move towards. For the most downstream shock, $x_{target,i}$ is determined in a similar way to the initial position:

$$x_{target,i} = s_i - \sigma(\tilde{p}(t - t_{lag}) - p_{b,0}). \tag{6.5}$$

For the upstream shocks, the target position is not just determined by the back pressure but also by the proximity to the other shock waves. The back pressure component, $x^{(bp)}_{target,i}$ is identical to the $x_{target,i}$ value in equation 6.5. The shock spacing component, $x^{(ss)}_{target,i}$, is equal to

$$x^{(ss)}_{target,i} = s_i - s_{i+1} + x_{i+1}, \tag{6.6}$$

i.e. one shock spacing upstream of the nearest downstream shock. The final target position is determined with a simple blending formula:

$$x_{target,i} = w x^{(bp)}_{target,i} + (1 - w) x^{(ss)}_{target,i}, \tag{6.7}$$

where w depends on the the strength of the low-pass filter and is given by

$$w = \frac{\max(\tilde{p}_b) - \overline{\tilde{p}}_b}{\max(p_b) - \overline{p}_b}, \tag{6.8}$$

where $\overline{()}$ denotes time averaging. The value of w ranges from 0 (all disturbances filtered) to 1 (no filtering). This technique prevents the shocks acting independently of each other and allows the natural shock spacing to assert itself even when disturbances are small. Next, the shock velocity, u_i, is defined such that it is proportional to the distance between the current location and the target:

$$u_i = u_0(x_{target,i} - x_i). \tag{6.9}$$

A limit is applied to the velocity magnitude such that $|u_i| \leq |u_c|$. The reference speed, $u_0 = 0.05$, matches approximately the results from the shock train step

response. The shock velocity then allows the shock position to be updated with a simple 1st-order forward Euler update. When a shock reaches the exit plane, it is removed from the model and the next upstream shock becomes the new rear-most shock. A new shock is added at the exit when the following condition is met: $l_x - x_{n-1} > s_{n+1} - s_n$ (where n is the current number of shocks in the shock train).

Results

The plots in figure 6.22 show the results of the model response to step forcing. The domain exit is taken to be the edge of the sponge zone ($l_x = 14$). By comparing the step response of the model to those in figures 6.23 it becomes clear that the model is able to provide a reasonably accurate prediction of the shock train behaviour, including the number of shock waves and the approximate response times.

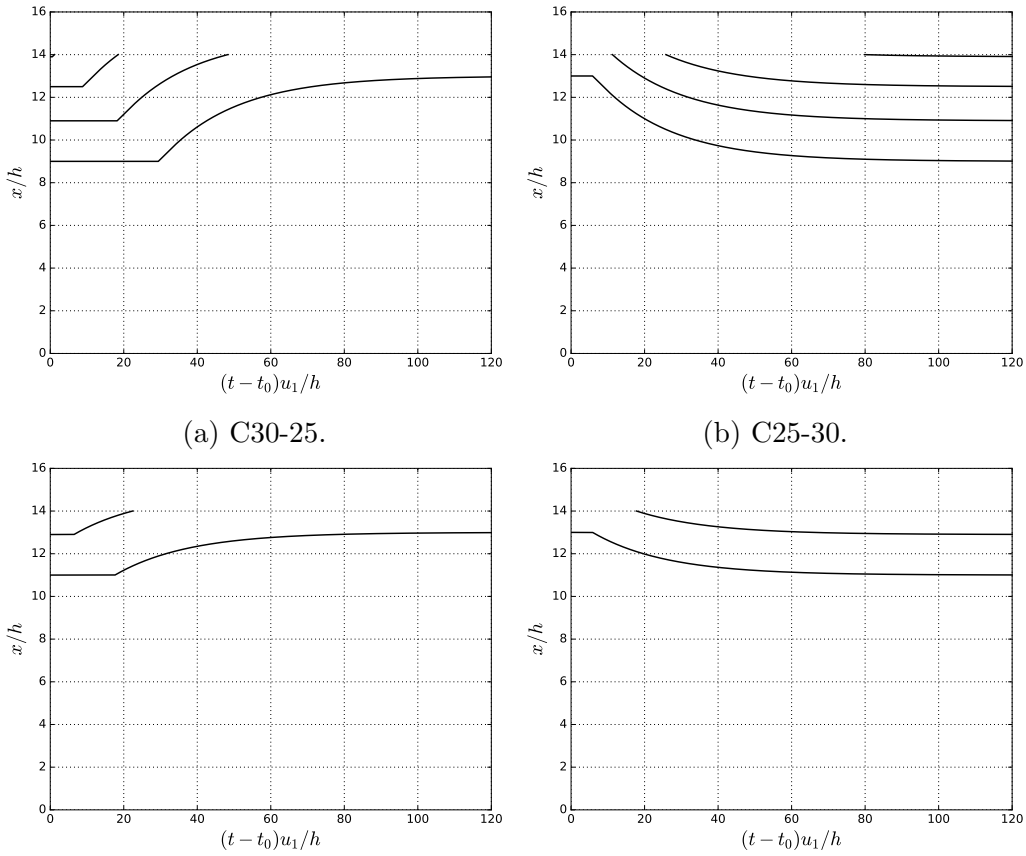

(a) C30-25.

(b) C25-30.

(c) C275-25.

(d) C25-275.

FIGURE 6.22: 1D shock model with step forcing. Simulation units are used for comparison purposes.

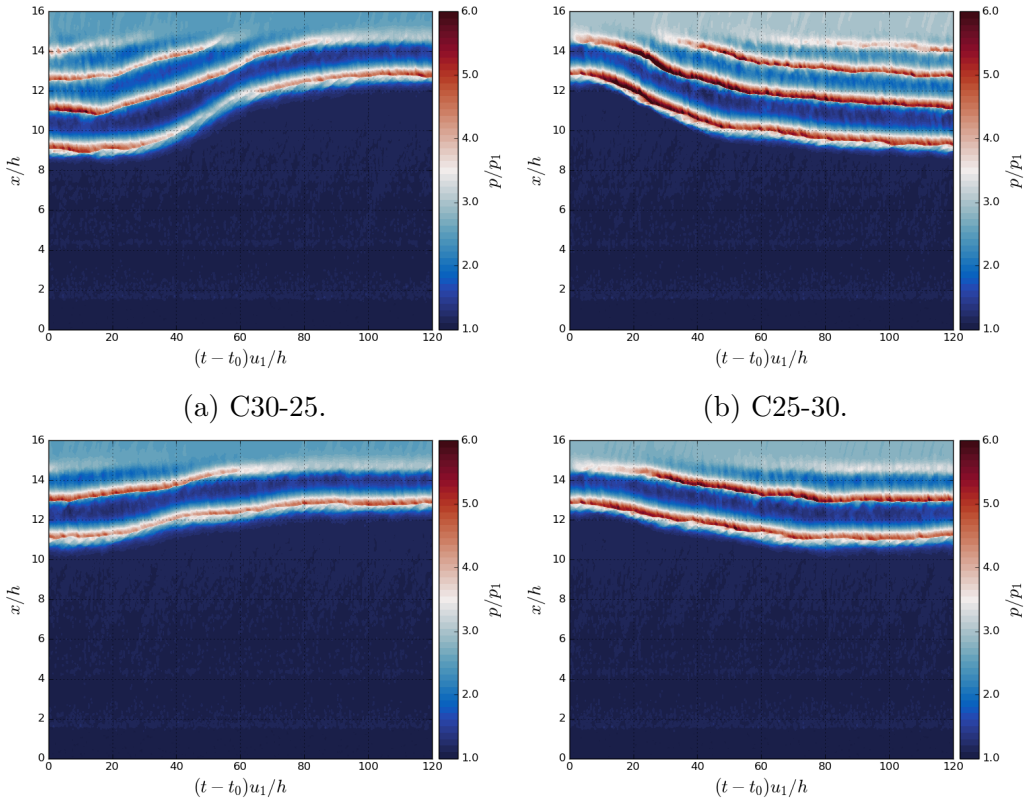

(a) C30-25.

(b) C25-30.

(c) C275-25.

(d) C25-275.

FIGURE 6.23: Step response simulation results (channel case).

These results are generally to be expected since model inputs are mostly based on observations of the simulation results. Therefore, the step response provides a good validation of the underling assumptions of the model but does not reveal anything fundamental about the shock train behaviour.

The more interesting application of the model comes with applying the same sinusoidal forcing as discussed in section 6.1.2. The results from each of the forcing frequencies are shown in figure 6.22 which can be directly compared to the simulation results in figure 6.19. As with the step responses, the basic dynamic behaviour of each case has been captured by the model. The shock oscillations in the T-04 case are barely noticeable and hence the shock positions are entirely static, as they are in the respective simulation case. When the oscillation period is increased to T-16, the oscillations of the downstream shocks become noticeable. Although the leading shock does not oscillate, its location becomes offset from the initial position - as it is with the T-16 simulation. The lowest forcing frequency has predictably large shock oscillations as well as the clustering of shocks that occurs when they travel

upstream. There is, however, no shock merging process that occurs when advancing and retreating shocks encounter one another.

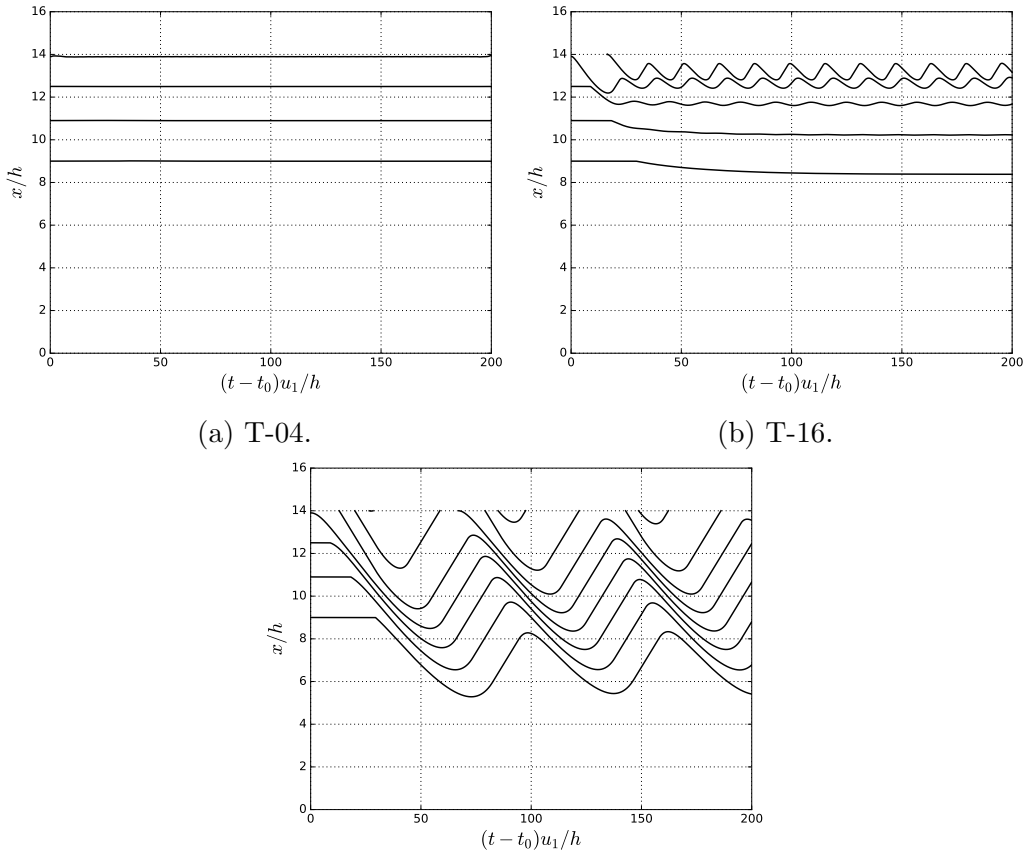

(a) T-04.

(b) T-16.

(c) T-64.

FIGURE 6.24: 1D shock model with sinusoidal forcing.

When the lag effect is turned off in the model (by setting $u_c = -\infty$) the upstream offset in the latter two cases disappears, suggesting that the back pressure lag is responsible for the upstream shift observed in section 6.1.2. This is fairly intuitive when considering that shocks which are further upstream respond more slowly to back pressure changes and so there is a certain "stickiness" to back pressure increases where the effects on the shock train are longer lasting. Additionally, for the T-16 case, the shock spacing component of the target velocity ($x^{(ss)}_{target,i}$) is also required for the upstream offset to occur at the leading shock. Therefore, despite the complete dissipation of disturbances, the leading shock is still affected by the dynamic back pressure. This occurs due to the geometric requirements of the shock spacing which allows the oscillating downstream shocks to push the whole shock train upstream,

hence the leading shock is still affected even though the disturbances have been dissipated.

6.2 Spectral Analysis

6.2.1 Fixed Back Pressure

In this section we consider the power spectra of wall pressure fluctuations in order to gain a better understanding of the shock train dynamic behaviour. Both channel and duct cases (ILES grid) are considered here and both have a fixed back pressure applied. Here we apply a non-dimensional frequency unit, the Strouhal number (equation 6.10) where the reference length is taken as the channel half-height, h. Spectral analysis of this type is common with incident-reflected SBLI problems and it is typical to use separation lengths or interaction lengths as the reference value. Due to the lack of permanent separation bubble in the duct case and the lack of any interaction lengths, it was deemed that the half-height would provide a more suitable reference value.

$$St_h = \frac{fh}{u_1}. \tag{6.10}$$

Both cases are averaged over a time period of $200h/u_1$ (respectively 12.5 and 8.3 convective cycles for the channel and duct), sampled at an interval of $0.08h/u_1$ and captured over an entire wall. The spectra are computed at each x and z position using Welch's method (Barbe et al., 2009) with a Blackman filter applied to each segment in order to remove any windowing effects. The spectral data at each streamwise position is then span-averaged in order to provide a smoother result. A non-weighted PSD was preferred in this case so that all the key features can be seen using the same color scale.

In figures 6.25 and 6.26 we show contours of power spectral density (PSD) in $St_h - x$ space for respectively the channel and duct cases. Spectra computed using 3 and 13 segments are both shown in order to provide low frequency information as well as smooth data at higher frequencies.

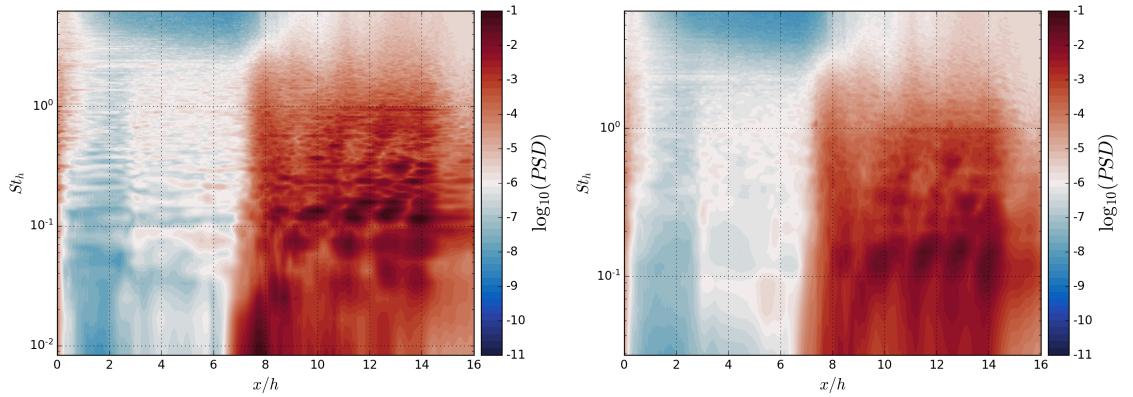

(a) 3 segments. (b) 13 segments.

FIGURE 6.25: Contour maps of power spectral density (PSD) of wall pressure fluctuations (channel case).

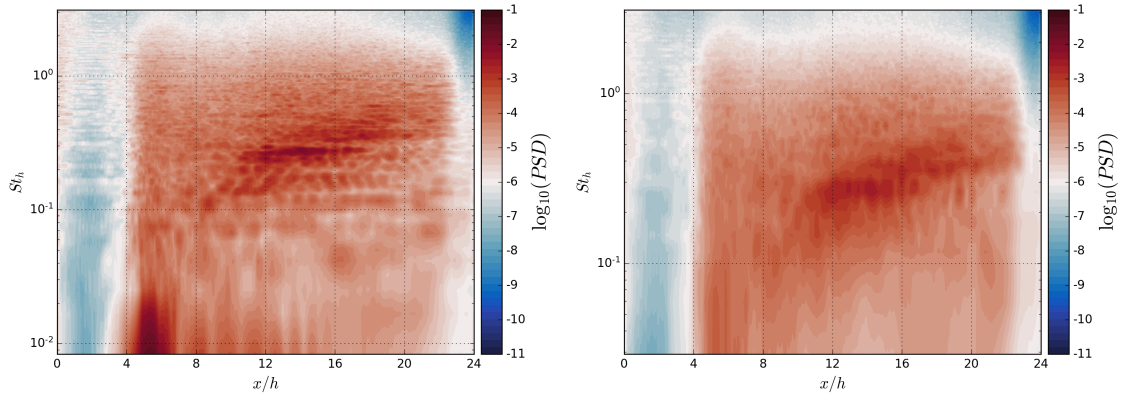

(a) 3 segments. (b) 13 segments.

FIGURE 6.26: Contour maps of power spectral density of wall pressure fluctuations (duct case). The shock train induces a broadband increase in fluctuation intensity for both cases. The 3-segment profiles provides clearer information at low frequency at the cost of smoothness.

The shock train is responsible for a broadband increase in pressure fluctuations. This is directly caused by the increase in turbulent mixing which occurs within the subsonic region. The pressure fluctuations in the channel case exhibit higher intensity than the duct case. Within the shock train region there are regions of higher intensity peaking at around $St_h = 0.1{-}0.2$ in the channel and $St_h = 0.2{-}0.3$ in the duct. Similarly intense lines were identified by Roussel (2016) at similar Strouhal number - these were shown to be due to cavity-type acoustic resonances caused by

the enclosed geometry of the shock train problem. This is most likely occurring in the present work and the shift in frequency can be explained by the factor of two difference in spanwise length between the duct and channel.

A feature that is only detected by the low frequency data in figures 6.25a and 6.26a is the high intensity region at the leading edge of the shock train. For both cases the peak intensity occurs at approximately $St_h = 0.01$. Such low frequency movement has also been observed at the shock foot location in incident-reflected SBLI problems. For example, Touber and Sandham (2009) observed a peak in low frequency oscillations at the leading edge of the separation bubble, with the peak intensity at $St = fL_{sep}/u_1 = 0.03$. Since the separation length, L_{sep}, in that case is of a similar order of magnitude to the reference length in the current work ($L_{sep} \sim 6.0\delta_{99}$ compared with $h \sim 3.6\delta_{99}$) the peak Strouhal numbers are of comparative size. As was also suggested by Xiong et al. (2017), the same leading shock motion (as well as the underlying mechanism) may occur in shock train problems as it does with oblique and normal SBLIs.

6.2.2 Sinusoidal Back Pressure

The same spectral analysis has also been applied to three sinusoidal back pressure cases [2]. The pressure data for these cases was captured over a period of $360h/u_1$. The spectral maps are shown for each case in figure 6.27 and the range of the contour colouring is adjusted in order to reveal the high intensity oscillations. The applied forcing frequencies correspond to Strouhal numbers of 0.25, 0.0625 and 0.0156 for the T-04, T-16 and T-64 cases respectively. The effect of the back pressure forcing is immediately obvious in each case due to the high-intensity line stretching from the outflow.

For the T-04 and T-16 cases, the back pressure forcing appears to have limited influence on the flow outside of a narrow band of frequencies and the dissipation of the disturbances can be seen by the decay in intensity fluctuation as they are pushed further upstream. In both these cases, the low frequency peak at the leading shock can be seen suggesting that this phenomenon remains unaffected (other than the offset in position in T-16). It may be useful to consider the shock train as a low-pass filter, whereby high frequency disturbances from the outflow are dissipated before reaching the leading edge of the shock train. A similar filtering effect was observed by Fiévet et al. (2017) with high frequency inlet disturbances.

[2]For the T-64 the longer ($L_x = 24h$) case is considered to avoid interference with the development region.

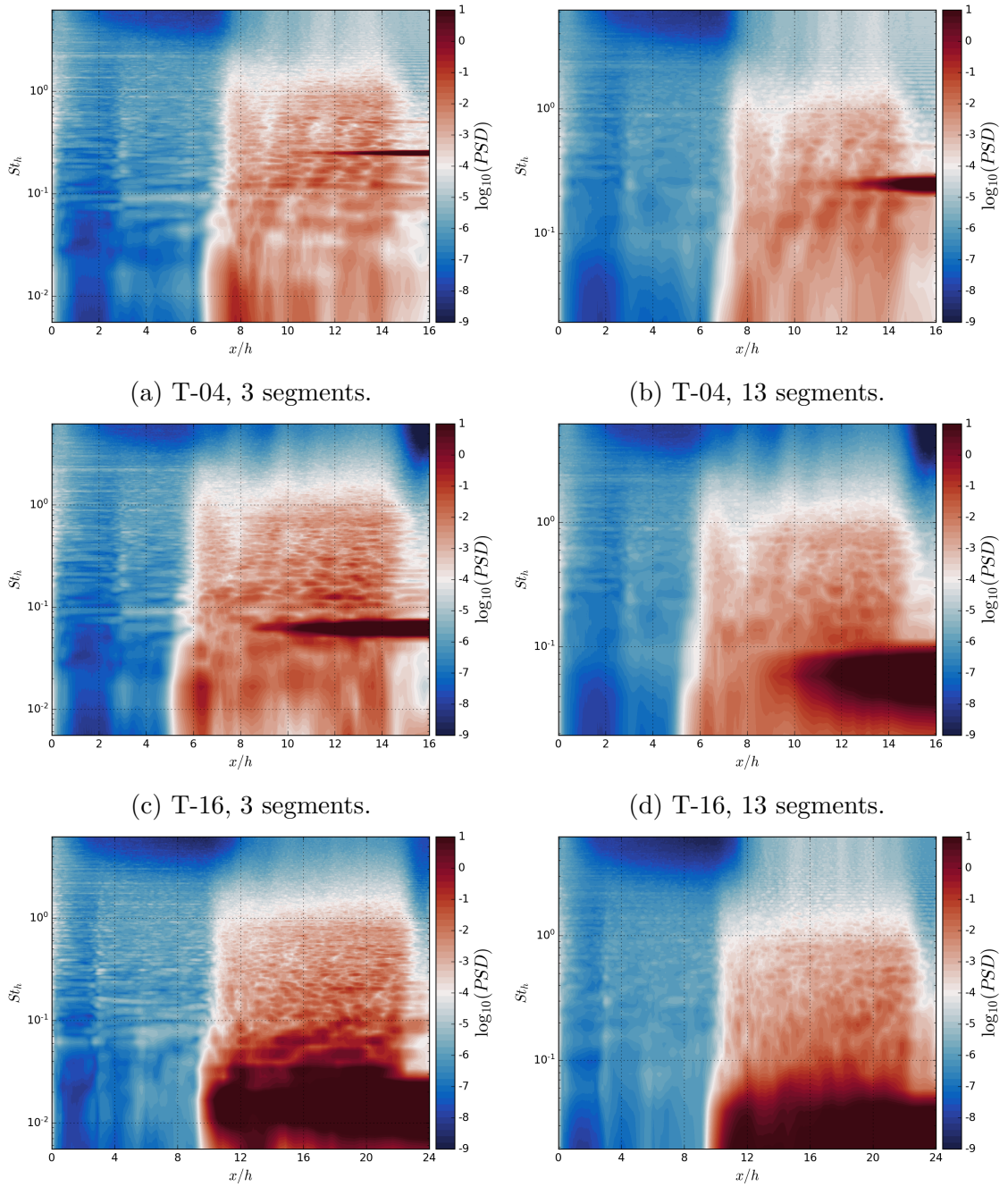

(a) T-04, 3 segments.

(b) T-04, 13 segments.

(c) T-16, 3 segments.

(d) T-16, 13 segments.

(e) T-64, 3 segments.

(f) T-64, 13 segments.

FIGURE 6.27: Contour maps of power spectral density of wall pressure fluctuations for all sinusoid cases. The higher frequency oscillations are filtered as the pass through the shock train.

The low frequency forcing in T-64 has a much larger impact on the PSD field. Not only do the disturbances dominate the frequencies $St_h = 0.1$ and below, but the influence extends all the way to the leading shock. The oscillation of the leading shock becomes locked-in to the applied frequency, as is observed in section 6.1.2 with the sawtooth-like waveform in $x - t$ space. It is clear that the period of oscillation is large enough to prevent the disturbances becoming dissipated as they pass upstream. It is interesting to note that the Strouhal number of the back pressure forcing ($St_h = 0.0156$) matches closely with the natural low frequency motion of the leading shock [3]. It may be worth a closer examination of any links between the natural low frequency motion and the low-pass filter effect of the shock train (more information on this suggestion in section 7.4).

6.3 Summary

The purpose of this chapter was to gain an insight into the time-dependent behaviour of shock trains, mostly through the use of dynamic back pressures. The main results are summarised below.

1. **Step change back pressure**

   (a) The response of a shock train to a sudden change in back pressure is characterised by three distinct processes: a lag period whereby the signal of the new back pressure is transmitted upstream, the initial linear response of each of the shock waves, and the subsequent deceleration of the shock waves as they approach the new equilibrium position.

   (b) The speed of the linear shock wave response depends strongly on the size of the pressure jump but appears to be largely independent of the direction of the pressure change and the initial back pressure of the shock train.

   (c) The inclusion of sidewalls were also found to have an effect on the speed of the moving shock, although only in cases where the pressure was stepped down.

2. **Sinusoidal back pressure**

   (a) Each forcing frequency induces streamwise oscillations of the shock train and the amplitude of oscillation is positively correlated with the period of oscillation.

[3] It is worth noting that this purely is coincidental since the forcing frequencies were not chosen based on any natural low frequency behaviour

(b) Additionally, there is a noticeable lag in the oscillations of each of the shocks due to the back pressure time lag.

(c) For the medium and low frequency cases, significant shock-shock interaction occurs due to the interference of advancing and receding shock waves.

(d) The sinusoidal forcing causes an upstream offset in the average shock wave position.

(e) A basic one dimensional model of the sinusoidal behaviour is able to capture most of these observations and proves that the upstream offset is an artefact of the back pressure lag period.

3. **Spectral analysis**

(a) We are able to identify a peak low frequency motion at the leading shock, a feature which is common in other SBLI problems.

(b) The sinusoidal forcing at the medium and higher frequency are shown to have a limited impact on the upstream flow as the disturbances are gradually dissipated.

(c) At the lower applied frequency, however, the entire shock train becomes locked-in with the back pressure forcing.

Chapter 7

Conclusions and Future Work

In the introductory chapter the main objectives for this project were outlined. For convenience, they are repeated here here:

1. Develop and characterise eddy resolving (DNS or near DNS) simulations of shock trains.
2. Better understand the unique effect of sidewalls and spanwise confinement.
3. Provide a detailed examination of other governing parameters (Back pressure, Reynolds number, confinement ratio).
4. Gain an insight into the time-dependent shock train behaviour, particularly via back pressure forcing.

The objectives are largely driven by sparsely researched problems in the wider literature on shock trains which are discussed in detail in chapter 2. Chapter 3 contains the research methodology and the remaining chapters are devoted to the research objectives. Objective 1 was addressed largely in chapter 4, objectives 2 and 3 in chapter 5 and the final objective in chapter 6. The main findings of each of the research chapters are summarised in the following sections. The final section outlines possible avenues for further study.

7.1 Validations

Chapter 4 provides a robust validation of all of the numerical methods used for the simulations in this project. This is hugely important due to the relative novelty of the inflow and outflow treatment. The first part of the chapter is devoted to the development of the boundary layer and the turbulence which is triggered by the inflow boundary condition. By examining the instantaneous flow field we are

able to observe the development of coherent turbulent flow structures. Additionally, by considering the time-averaged flow properties and turbulence statistics (at two grid resolutions), we can be confident that the boundary layer becomes sufficiently developed at around $x = 6h$, although the density-adjusted velocity profile appears to develop until around $x = 8h$. The boundary layer data is compared to established DNS data where a good match is found with the scaled velocity profiles and turbulent fluctuations. There is some divergence between the momentum thickness distribution, which is attributed to the boundary layer confinement effect in the channel.

In section 4.1.3 a comparison is made between infinite and finite span cases. The square duct case exhibits a more significant increase in exit pressure, which is seen to be directly caused by the spanwise confinement of the additional boundary layers. This higher adverse pressure gradient causes a subsequent increase in confinement via a thickening of the boundary layers. The positive feedback loop eventually increases the exit pressure to a sufficiently high level to force a shock train to form at the duct outlet. Secondary flow structures in the form of corner vortex pairs are observed in the duct case. These are observed to have fully formed by $x = 6h$ and continue to grow in size until they dominate the flow cross section by $x = 20h$.

By applying a sponge zone at the domain outlet, we are able to demonstrate the formation of a stable shock train composed of four individual shock waves. The shock train produces the expected distribution of pressure, Mach number and skin friction. An example shock train is tested with three separate grid resolutions (ILES, CDNS & DNS) in order to understand the grid convergence of various flow properties. The coarsest (and therefore the most economical) grid resolution, ILES, is able to capture the overall shock structure. The shock location and spacing, as well as most flow properties, are well matched to the finer grids. This suggests that the ILES grid is suitable for most purposes although it does under-predict the skin friction distribution and the boundary layer growth. The CDNS and DNS grids are very well matched; almost all flow properties collapse together very well which suggests that most grid convergence occurs before the CDNS resolution. It is recommended that the DNS resolution is only used when very accurate boundary layer data and shock positions are required.

The final validation process is a brief examination of the effect of numerical scheme sensitivity. For stability reasons, several of the cases in chapter 6 are required to run in a higher dissipation mode of the TENO scheme. In general, the effect of the higher dissipation is small and is therefore acceptable to use when running on the ILES grid.

7.2 Parametric Studies

In chapter 4 we perform a parametric study on the shock train, covering a wide range of governing parameters. The first study considers the effect of the size of the back pressure. This was performed using three test cases with differing back pressures, each forming a stable shock train. As expected, a higher back pressure is correlated with a longer shock train. The relationship appears to be linear, although additional cases would be needed to confidently confirm this. The most notable result can be seen by comparing the freestream pressure distributions - by normalising the position by the location of the leading shock, the distributions for each case collapse together very well for all but the final shock. This suggests that the shock structure and spacing is largely independent of the absolute size of the back pressure.

Due to the particularly low Reynolds number of the current work, it was felt important to test the effect of a higher Re on the shock train behaviour in order to be confident of the wider applicability of the results. By testing two additional Reynolds numbers up to a factor of two higher than the baseline we are able to demonstrate that the structure is well conserved. The main differences observed are the improved distinction of the shock waves and moderate increases in shock train length.

The third parameter study considers the effect of boundary layer confinement. Three confinement ratio cases are designed such that the actual boundary layers are identical and only the domain sizes are differed. The comparison shows that the centreline flow properties in each case are very similar (once the shock train length is taken into account) and the shock wave structure and spacing were only weakly effected by the confinement ratio. The ratio between boundary layer thickness and shock train length was conserved for the two most confined cases, though not for the remaining case which produced a longer than expected shock train.

The fourth study in this chapter is on the effect of span-wise confinement (i.e. the influence of the sidewalls). To perform this study two cases are tested which only differ by their spanwise boundary treatment and domain width: an infinite span (channel) case and a square duct. The effect of the sidewalls is to significantly increase the overall size of the shock train - approximately doubling it in length. Additionally, the shocks were individually weaker, although the spacing between the initial shocks appears to be conserved. Permanent corner vortices are present throughout the shock train in the duct case and the increase in turbulent mixing after the leading shock appears to encourage their growth faster than compared to the shockless counterfactual.

The increase in shock train length due to the sidewalls is presumed to be a direct result of the higher blockage - i.e. the effect of the sidewalls is similar in principle to increasing the confinement ratio. The higher blockage results in weaker individual shock waves and the pressure rise is then achieved by entropic pressure losses in the mixing region, thereby causing a longer shock train. Within this section we also consider an additional channel case with an overall blockage (by area) equal to that of the duct. This allows us to test whether the higher blockage in the duct fully accounts for the longer shock train. The results show that, while the new high blockage case does increase the length of the shock train, it does not match that of the duct case. Additionally, the viscous-dominated flow at the centreline means the shocks are significantly weaker than either of the other cases. Overall this suggests that, at least in some situations, controlling for the total blockage is not a sufficient proxy for the effect of sidewalls.

In the fifth section we consider the effects of only simulating one quarter of the duct cross section with the use of a double symmetry plane arrangement. The results show significant differences in the shock train structure, with strong shocks persisting further downstream when the symmetry arrangement is implemented. Other properties, such as the upstream boundary layer flow, provide a much better match with the full duct arrangement.

The results from all of the cases are compared to a well-known semi-empirical model (Billig, 1993; Waltrup and Billig, 1973) that considers the Mach number, Reynolds number and momentum thickness to predict a streamwise distribution of wall pressure. Each case is generally in good agreement with the model predictions although there is a notable deviation near the leading edge of the shock train. The strength of the Billig model appears to be that the underlying, un-scaled pressure distributions collapse together reasonably well. One significant limiting factor of the Billig model is that it does not take into account the sidewall geometry.

The last section in chapter 5 is a more detailed analysis of the shock train structure. We find that for the first three parameter studies (back pressure, Reynolds number, confinement ratio), the shape of the supersonic regions of the shock train are almost entirely conserved. Additionally we find that the angle of the oblique shocks at the shock train leading edge are all very similar and occur at the very limit of forming a Mach stem at the centreline. These similarities do not hold once sidewalls are included; instead there is a much lower shock angle and smaller subsonic region. The sidewalls also strongly influence the internal expansion and compression pattern observed between each of the shock waves.

7.3 Dynamic Shock Train Behaviour

The final research chapter in this thesis is concerned with the time-dependent response of the shock train to back pressure forcing. Extensive time-histories were collected and analysed for many different cases detailing the behaviour of the shock train under different conditions.

In section 6.1.1 we consider the response of various shock trains to step changes in back pressure. By starting with shock trains at a fixed back pressure and in an equilibrium or near-equilibrium state and subjecting them to sudden increases or decreases in back pressure we are able to observe the time-dependent response. The back pressure change is transmitted via the subsonic region (travelling approximately at $M = 0.33$) and when reaching each of the shock waves causes them to move at an approximately constant speed (upstream movement for positive changes and vice-versa). After an initial period, the trajectory becomes sub-linear where the shock speed gradually reduces before converging on the new equilibrium position.

From the cases considered, the magnitude of the initial response speed of the shock train appears to be independent of the initial back pressure and the direction of the back pressure change. The main factor affecting the initial response was found to be the size of the pressure jump where a larger step change will induce a faster response. When sidewalls were included, the speed of the moving shocks were lower, although only in cases where the back pressure was stepped down.

In section 6.1.2 we apply a sinusoidal-type back pressure to the shock train and again record the response. Three different oscillation frequencies were considered and each produced noticeably different responses but all induce streamwise oscillations of the shock waves. The periods of oscillation for the the low, medium and high frequency cases were chosen such that they would equal respectively 4.0, 1.0 and 0.25 flow-through-times. The results confirm that the magnitude of the shock oscillation is highly dependent on the forcing frequency. For example there is no observed oscillation of the leading shock in the high frequency case. For the medium and low frequency cases, each oscillation cycle is associated with the production and destruction of one or more shock waves. The time lag of the back pressure propagation means that there is significant interference between advancing and retreating shock waves. In both of these cases there was also an observed upstream offset in the average shock position.

A basic 1D model that aims to capture some of the dynamic shock train behaviour is presented in section 6.1.3. This model is primarily based on empirical results from static back pressure results but also considers the lag effect of the back

pressure as well as the upstream/downstream response to pressure changes and the filtering of oscillations at higher frequencies. The model is able to capture the basic dynamics of step and sinusoidal forcing, including frequency effects. The model allows us to deduce that the upstream offset of the shock waves is most likely caused by the lag effect of the back pressure.

By examining the power spectral density of wall pressure fluctuations we are able to identify a number of features of the shock train behaviour. This analysis was performed with a fixed back pressure in both the channel and duct arrangement. The increase in turbulent mixing through the shock train causes a broadband increase in pressure fluctuations. Peaks of intensity in PSD within the shock trains were observed which are thought to be the result of cavity-type resonances (as shown by Roussel, 2016) due to the confined geometry of both the channel and duct. A peak of low frequency motion is identified at the foot of the leading shock in both cases. This matches closely to both the non-dimensional frequency and location of low frequency motion commonly observed in canonical SBLI problems. Spectral analysis was also performed on the three sinusoidal back pressure cases where we are able to further demonstrate the upstream dissipation of the higher frequency disturbances. Additionally, the spectral analysis captures how the leading shock becomes locked-in with the back pressure forcing in the lowest frequency case.

7.4 Future Work

The work conducted over the course of this projects presents a number of opportunities for further study. One example is the back pressure study in section 5.1 where the limited number of cases meant that there could be no solid conclusion as to the exact relationship between back pressure and shock train length. Expanding this study a higher number different back pressures would provide a much clearer picture of this relationship.

In section 5.4 an attempt was made to control for the blockage induced by the sidewalls. This was done by running a high blockage channel case but, due to the very confined nature, the viscous effects limited the conclusions of the test. During this project there was a plan to develop and run a low-confinement duct case where the overall blockage would match that of the baseline channel case. However, due to the required grid size of this case (around 1 billion grid points), the memory requirement was too large to be able to run at the available HPC facility. Running this case with an LES formulation may make it more feasible and it would be able to provide more conclusive results of the effect of sidewall blockage.

Of the main governing parameters, the only one not considered here was the effect of Mach number. Given that Mach number has a stronger effect on the length of the shock train and the shock wave structure, this would be an interesting follow-on activity to the current work, as well as being particularly feasible. As noted in the confinement study in section 5.3, the very low confinement ratio case showed signs that it was still converging, albeit very slowly. Carrying out an extended simulation of this case would allow for more conclusive results.

Considering the dynamic back pressure study in section 6.1.1, the sidewalls appear to have a non-trivial impact on the response speed. Compared to the channel arrangement, the shock speed was lower but only when the back pressure was reduced. Conducting another step up case (D25-275 for example) or even another set of cases would provide more information on this problem. For the sinusoidal forcing cases it was particularly interesting how the higher frequency disturbances were so thoroughly dissipated before reaching the leading edge of the shock train, despite the large oscillation amplitude. Additionally, such dissipation did not occur at the lowest forcing frequency (T-64) and it would be worthwhile testing whether this fact is related in any way to the natural low frequency motion of the leading shock. Testing a tighter range of frequencies could provide a better understanding of the filtering effect of the shock train.

References

J. Ackeret, F. Feldmann, and N. Rott. Investigations of compression shocks and boundary layers in gases moving at high speed. 1947.

H. Babinsky and J. K. Harvey. *Shock wave-boundary-layer interactions*, volume 32. Cambridge University Press, 2011.

H. Babinsky, J. Oorebeek, and T. Cottingham. Corner effects in reflecting oblique shock-wave/boundary-layer interactions. In *51st AIAA Aerospace Sciences Meeting including the New Horizons Forum and Aerospace Exposition*, page 859, 2013.

K. Barbe, R. Pintelon, and J. Schoukens. Welch method revisited: nonparametric power spectrum estimation via circular overlap. *IEEE Transactions on Signal Processing*, 58(2):553–565, 2009.

O. Bardsley and W. Mair. III. The interaction between an oblique shock-wave and a turbulent boundary-layer. *The London, Edinburgh, and Dublin Philosophical Magazine and Journal of Science*, 42(324):29–36, 1951.

F. Barry. The interaction of shock waves with boundary layers on a flat surface. *Journal of the Aeronautical Sciences*, 18(4):229–238, 1951.

G. Ben-Dor, O. Igra, T. Elperin, and J. Délery. *Handbook of Shock Waves: Shock wave interactions and propagation*. Academic Press, 2001.

F. S. Billig. Research on supersonic combustion. *Journal of Propulsion and Power*, 9(4):499–514, 1993.

P. Bruce and H. Babinsky. Unsteady shock wave dynamics. *Journal of Fluid Mechanics*, 603:463–473, 2008.

P. Bruce, D. Burton, N. Titchener, and H. Babinsky. Corner effect and separation in transonic channel flows. *Journal of Fluid Mechanics*, 679:247–262, 2011.

S. Butterworth. On the theory of filter amplifiers. *The Wireless Engineer*, 7(6): 536–541, 1930.

B. Carroll and J. C. Dutton. Characteristics of multiple shock wave/turbulent boundary layer interactions in rectangular ducts. In *1st National Fluid Dynamics Conference*, page 3803, 1988.

B. F. Carroll and J. C. Dutton. Characteristics of multiple shock wave/turbulent boundary-layer interactions in rectangular ducts. *Journal of Propulsion and Power*, 6(2):186–193, 1990.

M. Castro, B. Costa, and W. S. Don. High order weighted essentially non-oscillatory weno-z schemes for hyperbolic conservation laws. *Journal of Computational Physics*, 230(5):1766–1792, 2011.

C. J. Chapman. *High speed flow*, volume 23. Cambridge University Press, 2000.

D. R. Chapman, D. M. Kuehn, and H. K. Larson. Investigation of separated flows in supersonic and subsonic streams with emphasis on the effect of transition. *Technical Report, NACA*, 1958.

S. Cox-Stouffer and M. Hagenmaier. The effect of aspect ratio on isolator performance. In *39th Aerospace Sciences Meeting and Exhibit*, page 519, 2001.

L. Crocco. *One dimensional treatment of steady gasdynamics*. Princeton Univ. Press, 1958.

D. S. Dolling. Fifty years of shock-wave/boundary-layer interaction research: what next? *AIAA Journal*, 39(8):1517–1531, 2001.

P. Dupont, C. Haddad, and J. Debieve. Space and time organization in a shock-induced separated boundary layer. *Journal of Fluid Mechanics*, 559:255–277, 2006.

L. M. Edelman and M. Gamba. Rigid body response of a mach 2 shock train to downstream forcing. In *2018 Fluid Dynamics Conference*, 2018.

A. Fage and R. Sargent. Shock-wave and boundary-layer phenomena near a flat surface. *Proc. R. Soc. Lond. A*, 190(1020):1–20, 1947.

A. Ferri. Experimental results with airfoils tested in the high-speed tunnel at guidonia. Technical report, 1940.

R. Fiévet, H. Koo, V. Raman, and A. H. Auslender. Numerical investigation of shock-train response to inflow boundary-layer variations. *AIAA Journal*, pages 2888–2901, 2017.

L. Fu, X. Y. Hu, and N. A. Adams. A family of high-order targeted eno schemes for compressible-fluid simulations. *Journal of Computational Physics*, 305:333–359, 2016.

B. Ganapathisubramani, N. Clemens, and D. Dolling. Effects of upstream boundary layer on the unsteadiness of shock-induced separation. *Journal of Fluid Mechanics*, 585:369–394, 2007.

B. Ganapathisubramani, N. Clemens, and D. Dolling. Low-frequency dynamics of shock-induced separation in a compression ramp interaction. *Journal of Fluid Mechanics*, 636:397, 2009.

F. Gnani, H. Zare-Behtash, C. White, and K. Kontis. Effect of back-pressure forcing on shock train structures in rectangular channels. *Acta Astronautica*, 145:471–481, 2018a.

F. Gnani, H. Zare-Behtash, C. White, and K. Kontis. Numerical investigation on three-dimensional shock train structures in rectangular isolators. *European Journal of Mechanics-B/Fluids*, 72:586–593, 2018b.

I. J. Grossman and P. J. Bruce. Confinement effects on regular–irregular transition in shock-wave–boundary-layer interactions. *Journal of Fluid Mechanics*, 853:171–204, 2018.

C. Horstman and C. Hung. Computation of three-dimensional turbulent separated flows at supersonic speeds. *AIAA Journal*, 17(11):1155–1156, 1979.

R. Humble, G. Elsinga, F. Scarano, and B. Van Oudheusden. Three-dimensional instantaneous structure of a shock wave/turbulent boundary layer interaction. *Journal of Fluid Mechanics*, 622:33–62, 2009.

R. L. Hunt and M. Gamba. Shock train unsteadiness characteristics, oblique-to-normal transition, and three-dimensional leading shock structure. *AIAA Journal*, 56(4):1569–1587, 2018.

T. Ikui, K. Matsuo, and M. Nagai. The mechanism of pseudo-shock waves. *Bulletin of JSME*, 17(108):731–739, 1974.

T. Ikui, K. Matsuo, and K. Sasaguchi. Modified diffusion model of pseudo-shock waves considering upstream boundary layers. *Bulletin of JSME*, 24(197):1920–1927, 1981.

C. T. Jacobs, S. P. Jammy, and N. D. Sandham. OpenSBLI: A framework for the automated derivation and parallel execution of finite difference solvers on a range of computer architectures. *Journal of Computational Science*, 18:12–23, 2017.

X. Jiao, J. Chang, Z. Wang, and D. Yu. Periodic forcing of a shock train in a scramjet inlet-isolator at overspeed condition. *Acta Astronautica*, 143:244–254, 2018. doi: 10.1016/j.actaastro.2017.12.005.

Y. Kim, Z.-T. Xie, and I. P. Castro. A forward stepwise method of inflow generation for les. In *Proceeding of the 6th International Conference on Fluid Dynamics*, volume 1376, pages 134–136. AIP, 2011.

A. Kistler. Fluctuating wall pressure under a separated supersonic flow. *The Journal of the Acoustical Society of America*, 36(3):543–550, 1964.

M. Klein, A. Sadiki, and J. Janicka. A digital filter based generation of inflow data for spatially developing direct numerical or large eddy simulations. *Journal of Computational Physics*, 186(2):652–665, 2003.

R. Klomparens, J. Driscoll, and M. Gamba. Unsteadiness characteristics and pressure distribution of an oblique shock train. *AIAA Paper*, 1519:2015, 2015.

R. Klomparens, J. F. Driscoll, and M. Gamba. Response of a shock train to downstream back pressure forcing. In *54th AIAA Aerospace Sciences Meeting*, 2016.

Q. Li. Numerical study of Mach number effects in compressible wall-bounded turbulence. *PhD thesis, University of Southampton*, 2003.

H. W. Liepmann. The interaction between boundary layer and shock waves in transonic flow. *Journal of the Aeronautical Sciences*, 13(12):623–637, 1946.

H. W. Liepmann, A. Roshko, and S. Dhawan. On reflection of shock waves from boundary layers. Technical report, California Institute of Technology, 1951.

J. Lukasiewicz. Diffusers for supersonic wind tunnels. *Journal of the Aeronautical Sciences*, 20(9):617–626, 1953.

T. S. Lund, X. Wu, and K. D. Squires. Generation of turbulent inflow data for spatially-developing boundary layer simulations. *Journal of Computational Physics*, 140(2):233–258, 1998.

D. J. Lusher, S. P. Jammy, and N. D. Sandham. Shock-wave/boundary-layer interactions in the automatic source-code generation framework opensbli. *Computers & Fluids*, 173:17–21, 2018.

J. Matheis and S. Hickel. On the transition between regular and irregular shock patterns of shock-wave/boundary-layer interactions. *Journal of Fluid Mechanics*, 776:200–234, 2015.

K. Matsuo, Y. Miyazato, and H. D. Kim. Shock train and pseudo-shock phenomena in internal gas flows. *Progress in Aerospace Sciences*, 35(1):33–100, 1999.

B. Morgan. Large-eddy simulation of shock/turbulence interactions in hypersonic vehicle isolator systems. *PhD thesis, Stanford University*, 2012.

B. Morgan, K. Duraisamy, and S. K. Lele. Large-eddy simulations of a normal shock train in a constant-area isolator. *AIAA Journal*, 52(3):539–558, 2014.

E. P. Neumann. Supersonic diffusers for wind tunnels. *J. Appl. Mech.*, 16:195–202, 1949.

S. Piponniau, J. Dussauge, J. Debieve, and P. Dupont. A simple model for low-frequency unsteadiness in shock-induced separation. *Journal of Fluid Mechanics*, 629:87–108, 2009.

D. C. Reda and J. D. Murphy. Shock wave/turbulent boundary-layer interactions in rectangular channels. *AIAA Journal*, 11(2):139–140, 1973.

I. Z. Reguly, G. R. Mudalige, M. B. Giles, D. Curran, and S. McIntosh-Smith. The ops domain specific abstraction for multi-block structured grid computations. In *2014 Fourth International Workshop on Domain-Specific Languages and High-Level Frameworks for High Performance Computing*, pages 58–67. IEEE, 2014.

C. Roussel. Modelisation et simulation de l'interaction onde de choc/couche limite turbulente en écoulement interne avec effets de coins. *PhD thesis, ENSAM Paris*, 2016.

P. Sagaut, E. Garnier, E. Tromeur, L. Larcheveque, and E. Labourasse. Turbulent inflow conditions for large-eddy-simulation of compressible wall-bounded flows. *AIAA Journal*, 42(3):469–477, 2004.

P. Schlatter and R. Örlü. Assessment of direct numerical simulation data of turbulent boundary layers. *Journal of Fluid Mechanics*, 659:116–126, 2010.

A. H. Shapiro. *The dynamics and thermodynamics of compressible fluid flow*. John Wiley & Sons, 1953.

C.-W. Shu. Essentially non-oscillatory and weighted essentially non-oscillatory schemes for hyperbolic conservation laws. In *Advanced numerical approximation of nonlinear hyperbolic equations*, pages 325–432. Springer, 1998.

P. R. Spalart. Direct simulation of a turbulent boundary layer up to $Re_\theta = 1410$. *Journal of Fluid Mechanics*, 187:61–98, 1988.

P. R. Spalart and M. K. Strelets. Mechanisms of transition and heat transfer in a separation bubble. *Journal of Fluid Mechanics*, 403:329–349, 2000.

E. Touber. Unsteadiness in shock-wave/boundary layer interactions. *PhD thesis, University of Southampton*, 2010.

E. Touber and N. D. Sandham. Large-eddy simulation of low-frequency unsteadiness in a turbulent shock-induced separation bubble. *Theoretical and Computational Fluid Dynamics*, 23(2):79–107, 2009.

E. Touber and N. D. Sandham. Low-order stochastic modelling of low-frequency motions in reflected shock-wave/boundary-layer interactions. *Journal of Fluid Mechanics*, 671:417–465, 2011.

Z. P. Vane and S. K. Lele. Simulations of a normal shock train in a constant area duct using wall-modeled les. In *43rd AIAA Fluid Dynamics Conference*, page 3204, 2013.

I. Veloudis, Z. Yang, J. J. McGuirk, G. Page, and A. Spencer. Novel implementation and assessment of a digital filter based approach for the generation of LES inlet conditions. *Flow, Turbulence and Combustion*, 79(1):1–24, 2007.

P. Waltrup and F. Billig. Structure of shock waves in cylindrical ducts. *AIAA Journal*, 11(10):1404–1408, 1973.

B. Wang, N. D. Sandham, Z. Hu, and W. Liu. Numerical study of oblique shock-wave/boundary-layer interaction considering sidewall effects. *Journal of Fluid Mechanics*, 767:526–561, 2015.

A. Weiss, A. Grzona, and H. Olivier. Behavior of shock trains in a diverging duct. *Experiments in Fluids*, 49(2):355–365, 2010.

C. Wenzel, B. Selent, M. Kloker, and U. Rist. DNS of compressible turbulent boundary layers and assessment of data/scaling-law quality. *Journal of Fluid Mechanics*, 842:428–468, 2018.

J. Williamson. Low-storage Runge-Kutta schemes. *Journal of Computational Physics*, 35(1):48–56, 1980.

Z.-T. Xie and I. P. Castro. Efficient generation of inflow conditions for large eddy simulation of street-scale flows. *Flow, Turbulence and Combustion*, 81(3):449–470, 2008.

B. Xiong, X. Q. Fan, Y. Wang, L. Zhou, and Y. Tao. Back-pressure effects on unsteadiness of separation shock in a rectangular duct at Mach 3. *Acta Astronautica*, 141:248–254, 2017.

Appendix A

Laminar Shock Train

In this section we will outline briefly the results of tests conducted on shock train in fully-laminar isolators. Such flows are not particularly important for industrial applications but they are nonetheless interesting and worthwhile including here. All of the cases here were conducted with inflow values of $M = 2.0$, $Re_\theta = 200$ & $\delta_{99}/h = 0.13$ and a constant back pressure of $p_b/p_1 = 1.8$ is applied. As with the simulation in the main body of this work, a 6th-order TENO scheme is used and the Navier-Stokes equations solved directly. At the inlet a pressure extrapolation condition is applied and the back pressure at the outlet is applied with a fixed pressure condition (no sponge treatment). Six cases are presented here; five 2D cases with varying domain lengths ($l_x/h = 25$, 30, 40, 50, 60) and one fully 3D square duct case ($l_x/h = 40$). The details of the domain and grid sizes are listed in table A.1.

Case	Dimensions	L_x, L_y, L_z (δ^*)	N_x, N_y, N_z
2D-L25	2	375, 30, 0	1125, 175, 1
2D-L30	2	450, 30, 0	1350, 175, 1
2D-L40	2	600, 30, 0	1800, 175, 1
2D-L50	2	750, 30, 0	2250, 175, 1
2D-L60	2	900, 30, 0	2700, 175, 1
3D-L40	3	600, 30, 30	1800, 175, 175

TABLE A.1: Summary of laminar flow shock train cases.

Flow-field contours from the shortest 2D case is shown in figure A.1. The resulting shock train is composed of a chain of weak compression and expansion waves. Despite the low pressure ratio (significantly lower than all of the turbulent cases) the shock train has fully reached the inlet. For the 2D cases, the boundary layer

is highly separated all through the shock train (see the white $u = 0$ lines in figure A.1a). Additionally, the pattern is for compression waves to increase in strength in the streamwise direction, rather than decrease.

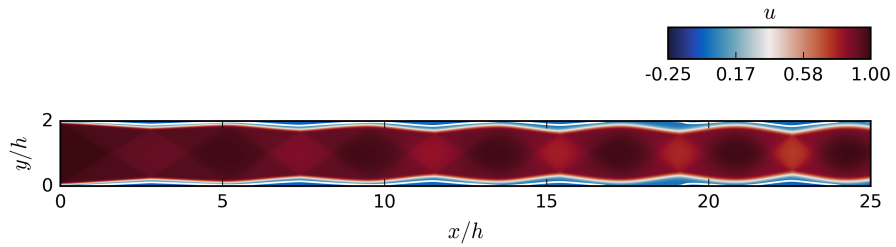

(a) Streamwise velocity.

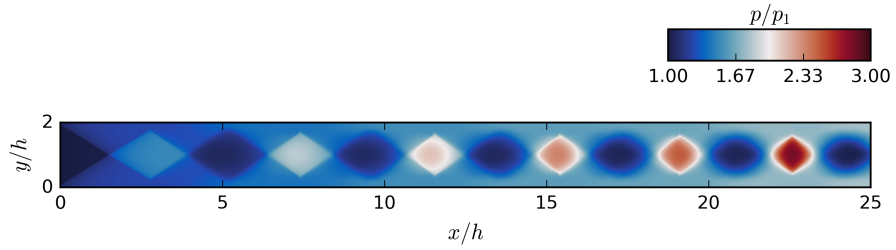

(b) Static pressure.

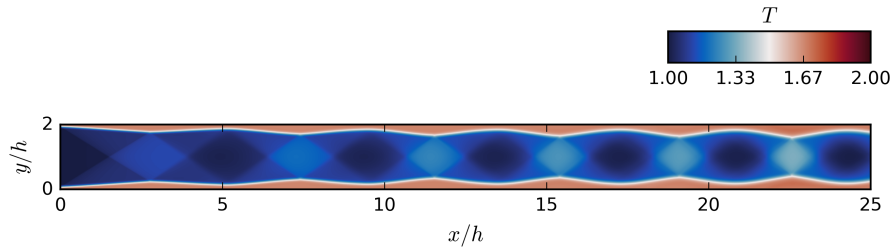

(c) Temperature.

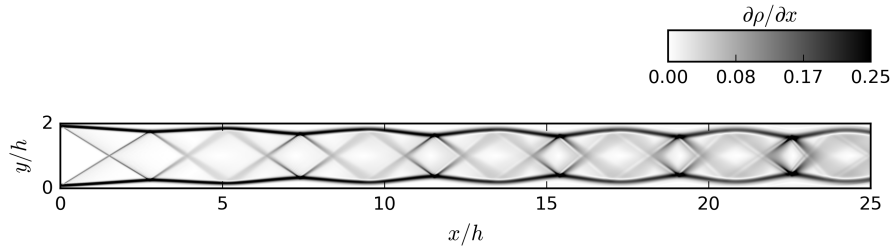

(d) Total density gradient.

FIGURE A.1: Instantaneous flow-field contours from the $l_x/h = 25$ 2D case.

Centreline and wall properties are plotted for each of the 2D cases in figure A.2. Again, it is clear that the compression waves increase towards the outlet for each case. The distribution of skin friction (figure A.2d) shows that once the boundary layer becomes separated it does not reattach and therefore there exists very large regions of separated flow. The strength of the compression waves is higher for shorter domains and only the longer cases ($l_x/h \geq 40$) are able to stabilise and contain the shock train. This unstart problem is due to the shallower velocity profile of the laminar boundary layer near the walls and is the same feature which causes laminar flows to be more susceptible to separation.

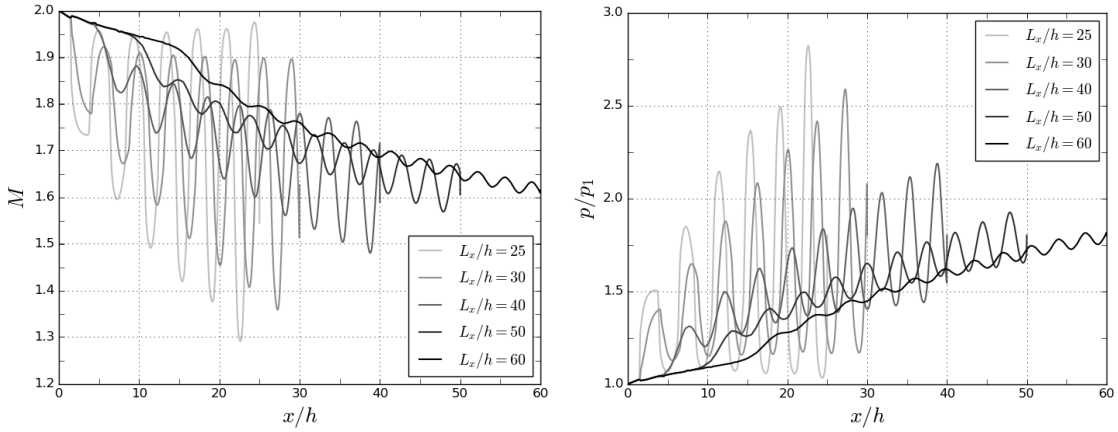

(a) Centreline Mach number.

(b) Centreline static pressure.

(c) Wall static pressure.

(d) Skin friction coefficient.

FIGURE A.2: Plots of streamwise flow properties comparing all of the 2D cases.

The same properties are considered in figure A.3 where we compare the matching 2D and 3D cases. The 3D case produces a very different shock train with weaker

and more complex compression waves. Despite the matching length and pressure ratio, the 3D case has reached the inlet, suggesting the sidewalls makes it more susceptible to unstart. Additionally, there is an immediate reattachment of the separated boundary layer and gradual recovery of the skin friction distribution which does not occur in any of the 2D cases.

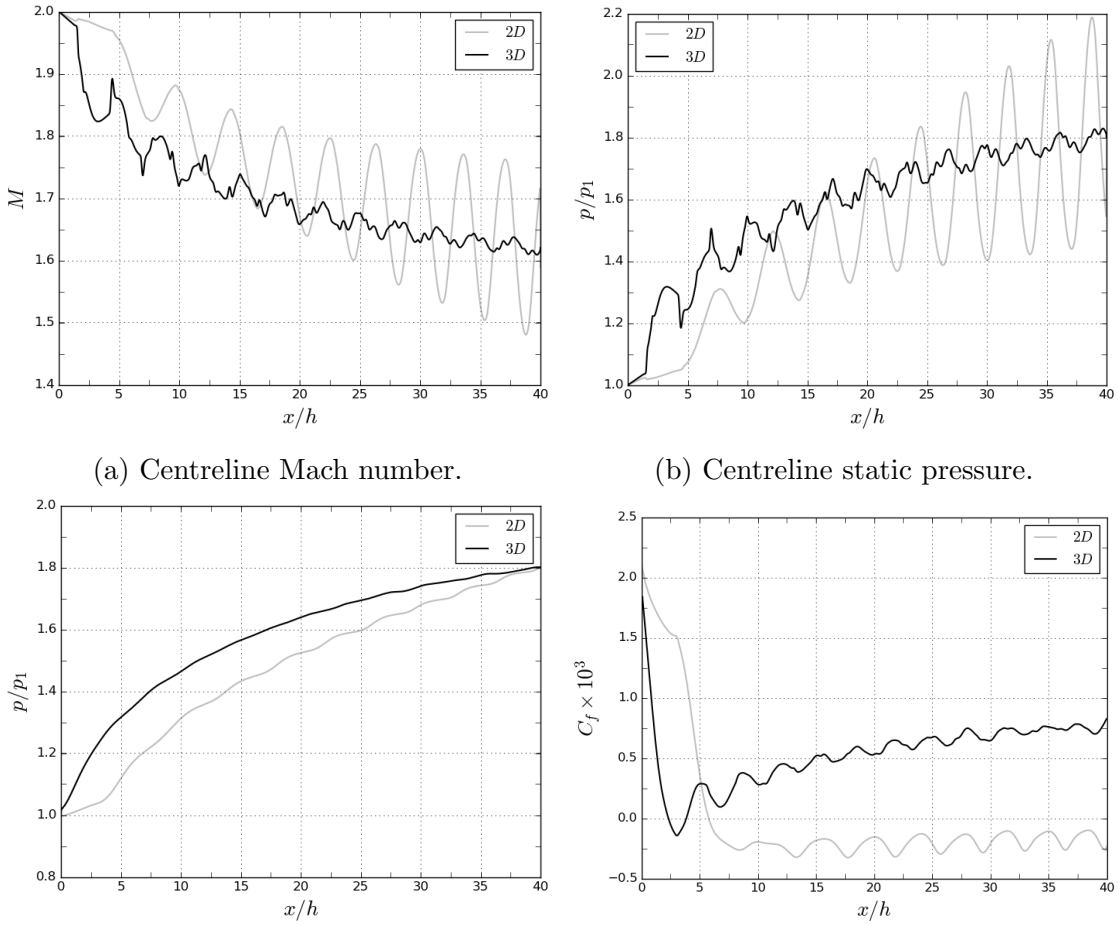

(a) Centreline Mach number.

(b) Centreline static pressure.

(c) Wall static pressure.

(d) Skin friction coefficient.

FIGURE A.3: Plots of streamwise flow properties comparing 2D and 3D cases ($l_x/h = 40$).

Appendix B

Code Listings

This appendix contains code for running the inflow turbulence generation and the sponge zone. The code is in the form of self-contained functions which are called within the main simulation routine. The code is machine-generated OPSC-code (very similar to C-code) which then needs to be translated further in order to match the targeted HPC architecture. Each of the functions are parallel kernels meaning that they are applied to individual grid points. Some clarity regarding functions and variables is given bellow.

- The function `OPS_ACC1(i,j,k)` is used to access grid-dependent variables with relative indices in the (x, y, z) directions.
- The function `random_generator()` calculates normally-distributed random numbers ($\bar{r} = 0$, $\sigma = 1.0$).
- `Seed1_B0` - `Seed6_B0` are grid-dependent seed values for the random number generator. Pre-calculated random numbers uniformly distributed between 0 and 10^7.
- `Umean_B0`, `Vmean_B0` & `Wmean_B0` are the mean inflow velocity profiles.
- `A11_B0` variables refer to the grid-dependent mean fluctuations a_{ij}.

Additionally, the following constants were used in the implementation of this code:

```
Lx0 = 1920.0;
Lx1 = 160.0;
Lx2 = 40.0;
block0np0 = 2400;
block0np1 = 640;
block0np2 = 60;
```

```
Delta0block0 = Lx0/(block0np0-1);
Delta1block0 = Lx1/(block0np1-1);
Delta2block0 = Lx2/(block0np2);
eps = 1e-15;
TENO_CT = 1e-6;
niter = 100000;
double rkold[] = {1.0/4.0, 3.0/20.0, 3.0/5.0};
double rknew[] = {2.0/3.0, 5.0/12.0, 3.0/5.0};
dt = 0.016;
Minf = 2.0;
gama = 1.4;
restart_iteration_no = 600000;
Twall = 1.676;
SuthT = 110.4;
RefT = 288.0;
Pr = 0.72;
Re = 500.0;
gamma_m1 = gama - 1;
inv_0 = 1.0/Delta2block0;
inv_1 = 1.0/Delta0block0;
inv_2 = 1.0/Delta1block0;
inv_3 = pow(Delta0block0, -2);
inv_4 = pow(Delta2block0, -2);
inv_5 = pow(Delta1block0, -2);
back_pressure = 0.535000000000000;
sponge_length = 180.0000000000000;
sa = 0.050000000000000;
sb = 1.00000000000000;
rc6 = 1.0/12.0;
rc7 = 2.0/3.0;
rcinv8 = pow(Minf, -2);
rcinv9 = 1.0/gama;
rcinv10 = 1.0/sponge_length1;
rcinv11 = 1.0/sponge_length2;
rcinv12 = pow(Minf, -2.0);
rc13 = 1.0/2.0;
rcinv14 = 1.0/RefT;
rc15 = 1.0/4.0;
rc16 = 13.0/12.0;
rc17 = 3.0/2.0;
rc18 = 781.0/1440.0;
rc19 = 781.0/480.0;
rc20 = 5.0/2.0;
rc21 = 1.0/36.0;
rc22 = 11.0/2.0;
rc23 = 9.0/2.0;
rc24 = 1.0/6.0;
rc25 = 231.0/500.0;
rc26 = 3.0/10.0;
```

```
rc27 = 27.0/500.0;
rc28 = 23.0/125.0;
rc29 = 5.0/12.0;
rc30 = 7.0/12.0;
rc31 = 11.0/12.0;
rc32 = 1.0/8.0;
rc33 = 13.0/24.0;
rc34 = 5.0/24.0;
rc35 = 1.0/24.0;
rc36 = 781.0/720.0;
rcinv37 = 1.0/gamma_m1;
rc38 = 19.0/2.0;
rc39 = 35.0/12.0;
rc40 = 14.0/3.0;
rc41 = 26.0/3.0;
rc42 = 1.0/3.0;
rc43 = 5.0/3.0;
rc44 = 4.0/3.0;
rcinv45 = 1.0/Re;
rcinv46 = 1.0/Pr;
rcinv47 = 1.0/niter;
```

B.1 Turbulence Generation

There are four kernel functions used for the generation of synthetic turbulence. The method for generating the mean profiles is not given here, although it is likely to be included in the next publicly available version of OpenSBLI. Each of the kernels listed here is applied over the entire inflow plane.

Generating $\phi_{ij}(y, z)$

```
void opensbliblock00Kernel001(const double *seed2_B0, const double
    *phi_u_old_B0, const double *seed3_B0, const double
*seed1_B0, const double *seed6_B0, const double *seed4_B0, const
    double *seed5_B0, const double *x1_B0, const double
*phi_w_old_B0, const double *phi_v_old_B0, double *phi_w_B0, double
     *phi_u_B0, double *phi_v_B0, const int *iter)
{
  //Declare variables
  double rand_v = 0.0;
  double rand_u = 0.0;
  double rand_w = 0.0;
  double dy = 0.0;
  dy = -x1_B0[OPS_ACC7(0,0,0)] + x1_B0[OPS_ACC7(0,1,0)];

  //Generate random numbers
```

```
13   rand_u = random_generator(restart_iteration_no +  *iter, seed1_B0
       [OPS_ACC3(0,0,0)], seed2_B0[OPS_ACC0(0,0,0)]);
14
15   rand_v = random_generator(restart_iteration_no +  *iter, seed3_B0
       [OPS_ACC2(0,0,0)], seed4_B0[OPS_ACC5(0,0,0)]);
16
17   rand_w = random_generator(restart_iteration_no +  *iter, seed5_B0
       [OPS_ACC6(0,0,0)], seed6_B0[OPS_ACC4(0,0,0)]);
18
19   //Generate Phi values
20   phi_u_B0[OPS_ACC11(0,0,0)] = rand_u*sqrt(1 - exp
       (-1.33333333333333*dy)) +
21     exp(-0.666666666666667*dy)*phi_u_old_B0[OPS_ACC1(0,-1,0)];
22
23   phi_v_B0[OPS_ACC12(0,0,0)] = rand_v*sqrt(1 - exp
       (-1.14285714285714*dy)) +
24     exp(-0.571428571428571*dy)*phi_v_old_B0[OPS_ACC9(0,-1,0)];
25
26   phi_w_B0[OPS_ACC10(0,0,0)] = rand_w*sqrt(1 - exp(-2.0*dy)) + exp
       (-1.0*dy)*phi_w_old_B0[OPS_ACC8(0,-1,0)];
27
28 }
```

Generating $\psi_{ij}(y,z)$

```
1  void opensbliblock00Kernel002(const double *psi_w_old_B0, const
       double *psi_u_old_B0, const double *psi_v_old_B0, const
2  double *phi_w_B0, const double *phi_u_B0, const double *phi_v_B0,
       double *psi_u_B0, double *psi_v_B0, double
3  *psi_w_B0)
4  {
5    //Generate Psi values
6      psi_u_B0[OPS_ACC6(0,0,0)] = sqrt(1 - exp(-1.33333333333333*
       Delta2block0))*phi_u_B0[OPS_ACC4(0,0,0)] +
7        exp(-0.666666666666667*Delta2block0)*psi_u_old_B0[OPS_ACC1
       (0,0,-1)];
8
9      psi_v_B0[OPS_ACC7(0,0,0)] = sqrt(1 - exp(-2.0*Delta2block0))*
       phi_v_B0[OPS_ACC5(0,0,0)] +
10       exp(-1.0*Delta2block0)*psi_v_old_B0[OPS_ACC2(0,0,-1)];
11
12     psi_w_B0[OPS_ACC8(0,0,0)] = sqrt(1 - exp(-1.14285714285714*
       Delta2block0))*phi_w_B0[OPS_ACC3(0,0,0)] +
13       exp(-0.571428571428571*Delta2block0)*psi_w_old_B0[OPS_ACC0
       (0,0,-1)];
14
15 }
```

Generating $u^*_{ij}(y,z)$

```
void opensbliblock00Kernel003(const double *psi_v_B0, const double
    *psi_w_B0, const double *psi_u_B0, const double
*Umean_B0, const double *phi_w_B0, const double *phi_u_B0, const
    double *phi_v_B0, double *phi_u_old_B0, double
*psi_w_old_B0, double *phi_w_old_B0, double *psi_u_old_B0, double *
    psi_v_old_B0, double *phi_v_old_B0, double *vstar_B0,
double *wstar_B0, double *ustar_B0)
{
  //Generate ustar values
  ustar_B0[OPS_ACC15(0,0,0)] = sqrt(1 - exp(-0.2*dt*Umean_B0[
    OPS_ACC3(0,0,0)]))*psi_u_B0[OPS_ACC2(0,0,0)] +
     exp(-0.1*dt*Umean_B0[OPS_ACC3(0,0,0)])*ustar_B0[OPS_ACC15
    (0,0,0)];

  vstar_B0[OPS_ACC13(0,0,0)] = sqrt(1 - exp(-0.5*dt*Umean_B0[
    OPS_ACC3(0,0,0)]))*psi_v_B0[OPS_ACC0(0,0,0)] +
     exp(-0.25*dt*Umean_B0[OPS_ACC3(0,0,0)])*vstar_B0[OPS_ACC13
    (0,0,0)];

  wstar_B0[OPS_ACC14(0,0,0)] = sqrt(1 - exp(-0.5*dt*Umean_B0[
    OPS_ACC3(0,0,0)]))*psi_w_B0[OPS_ACC1(0,0,0)] +
     exp(-0.25*dt*Umean_B0[OPS_ACC3(0,0,0)])*wstar_B0[OPS_ACC14
    (0,0,0)];

  //Update t-1 reference values
  phi_u_old_B0[OPS_ACC7(0,0,0)] = phi_u_B0[OPS_ACC5(0,0,0)];

  psi_u_old_B0[OPS_ACC10(0,0,0)] = psi_u_B0[OPS_ACC2(0,0,0)];

  phi_v_old_B0[OPS_ACC12(0,0,0)] = phi_v_B0[OPS_ACC6(0,0,0)];

  psi_v_old_B0[OPS_ACC11(0,0,0)] = psi_v_B0[OPS_ACC0(0,0,0)];

  phi_w_old_B0[OPS_ACC9(0,0,0)] = phi_w_B0[OPS_ACC4(0,0,0)];

  psi_w_old_B0[OPS_ACC8(0,0,0)] = psi_w_B0[OPS_ACC1(0,0,0)];

}
```

Generating $U_{ij}(y, z)$

```
void opensbliblock00Kernel004(const double *Dmean_B0, const double
    *Vmean_B0, const double *A31_B0, const double
*Umean_B0, const double *wstar_B0, const double *A11_B0, const
    double *A32_B0, const double *A22_B0, const double
*A21_B0, const double *A33_B0, const double *vstar_B0, const double
     *Wmean_B0, const double *ustar_B0, double *rhoE_B0,
double *rhou1_B0, double *rhou0_B0, double *rho_B0, double *
    rhou2_B0)
```

```
{
   //Define variables
   double Ptotal = 0.0;
   double Utotal = 0.0;
   double Dtotal = 0.0;
   double Wtotal = 0.0;
   double Vtotal = 0.0;

   //Compute total values for velocity, density, pressure
   Utotal = A11_B0[OPS_ACC5(0,0,0)]*ustar_B0[OPS_ACC12(0,0,0)] +
   Umean_B0[OPS_ACC3(0,0,0)];

   Vtotal = A21_B0[OPS_ACC8(0,0,0)]*ustar_B0[OPS_ACC12(0,0,0)] +
   A22_B0[OPS_ACC7(0,0,0)]*vstar_B0[OPS_ACC10(0,0,0)] +
      Vmean_B0[OPS_ACC1(0,0,0)];

   Wtotal = A31_B0[OPS_ACC2(0,0,0)]*ustar_B0[OPS_ACC12(0,0,0)] +
   A32_B0[OPS_ACC6(0,0,0)]*vstar_B0[OPS_ACC10(0,0,0)] +
      A33_B0[OPS_ACC9(0,0,0)]*wstar_B0[OPS_ACC4(0,0,0)] + Wmean_B0[
   OPS_ACC11(0,0,0)];

   Dtotal = Dmean_B0[OPS_ACC0(0,0,0)];

   Ptotal = 1.0*rcinv8*rcinv9;

   //Compute state space variables
   rho_B0[OPS_ACC16(0,0,0)] = Dtotal;

   rhou0_B0[OPS_ACC15(0,0,0)] = Dtotal*Utotal;

   rhou1_B0[OPS_ACC14(0,0,0)] = Dtotal*Vtotal;

   rhou2_B0[OPS_ACC17(0,0,0)] = Dtotal*Wtotal;

   rhoE_B0[OPS_ACC13(0,0,0)] = 0.5*Dtotal*(pow(Utotal, 2) + pow(
   Vtotal, 2) + pow(Wtotal, 2)) + Ptotal/(gama - 1);

   //Apply to halo points
   rho_B0[OPS_ACC16(-1,0,0)] = Dtotal;

   rhou0_B0[OPS_ACC15(-1,0,0)] = Dtotal*Utotal;

   rhou1_B0[OPS_ACC14(-1,0,0)] = Dtotal*Vtotal;

   rhou2_B0[OPS_ACC17(-1,0,0)] = Dtotal*Wtotal;

   rhoE_B0[OPS_ACC13(-1,0,0)] = 0.5*Dtotal*(pow(Utotal, 2) + pow(
   Vtotal, 2) + pow(Wtotal, 2)) + Ptotal/(gama - 1);

```

```
48    rho_B0[OPS_ACC16(-2,0,0)] = Dtotal;
49
50    rhou0_B0[OPS_ACC15(-2,0,0)] = Dtotal*Utotal;
51
52    rhou1_B0[OPS_ACC14(-2,0,0)] = Dtotal*Vtotal;
53
54    rhou2_B0[OPS_ACC17(-2,0,0)] = Dtotal*Wtotal;
55
56    rhoE_B0[OPS_ACC13(-2,0,0)] = 0.5*Dtotal*(pow(Utotal, 2) + pow(
      Vtotal, 2) + pow(Wtotal, 2)) + Ptotal/(gama - 1);
57
58    rho_B0[OPS_ACC16(-3,0,0)] = Dtotal;
59
60    rhou0_B0[OPS_ACC15(-3,0,0)] = Dtotal*Utotal;
61
62    rhou1_B0[OPS_ACC14(-3,0,0)] = Dtotal*Vtotal;
63
64    rhou2_B0[OPS_ACC17(-3,0,0)] = Dtotal*Wtotal;
65
66    rhoE_B0[OPS_ACC13(-3,0,0)] = 0.5*Dtotal*(pow(Utotal, 2) + pow(
      Vtotal, 2) + pow(Wtotal, 2)) + Ptotal/(gama - 1);
67
68 }
```

B.2 Sponge Zone and Outflow

The sponge generation requires a single kernel function, although there is an additional kernel for the pressure outflow boundary - both are listed here. The sponge kernel is applied to all grid points where $x \geq l_x - l_{sponge}$ while the outflow is only applied to the exit plane.

Sponge Zone

```
1  void opensbliblock00Kernel005(const double *x0_B0, double *rhoE_B0,
       double *pressure_sponge_weight_B0,
2  const double *rho_B0, const double *rhou1_B0, const double *
     rhou0_B0, const double *rhou2_B0)
3  {
4    //Declare variables
5    double local_pressure = 0.0;
6    double x0 = 0.0;
7    double xsp = 0.0;
8
9    //Get x coordinate
10   x0 = x0_B0[OPS_ACC0(0,0,0)];
11
12   //Gefine coordinate at the edge of the sponge zone
```

```
13    xsp = Lx0 - sponge_length;
14
15    //Calculate the sponge weight function
16    pressure_sponge_weight_B0[OPS_ACC2(0,0,0)] = dt*sa*pow(-0.5*cos(
       rcinv11*M_PI*(x0 - xsp)) + 0.5, sb);
17
18    //Curent static pressure value
19    local_pressure = (gama - 1.0)*(-(0.5*pow(rhou0_B0[OPS_ACC5(0,0,0)
       ], 2) + 0.5*pow(rhou1_B0[OPS_ACC4(0,0,0)], 2) +
20       0.5*pow(rhou2_B0[OPS_ACC6(0,0,0)], 2))/rho_B0[OPS_ACC3(0,0,0)
       ] + rhoE_B0[OPS_ACC6(0,0,0)]);
21
22    //New static pressure value
23    local_pressure = local_pressure + (back_pressure - local_pressure
       )*pressure_sponge_weight_B0[OPS_ACC7(0,0,0)];
24
25    //Update Energy term
26    rhoE_B0[OPS_ACC6(0,0,0)] = local_pressure/(gama - 1.0) + (0.5*pow
       (rhou0_B0[OPS_ACC5(0,0,0)], 2) +
27       0.5*pow(rhou1_B0[OPS_ACC4(0,0,0)], 2) + 0.5*pow(rhou2_B0[
       OPS_ACC6(0,0,0)], 2))/rho_B0[OPS_ACC3(0,0,0)];
28
29  }
```

Outflow

```
1   void opensbliblock00Kernel006(double *rhoE_B0, double *rhou1_B0,
       double *rhou0_B0, double *rho_B0, double *rhou2_B0)
2   {
3       rho_B0[OPS_ACC3(0,0,0)] = rho_B0[OPS_ACC3(-1,0,0)];
4
5       rhou0_B0[OPS_ACC2(0,0,0)] = rhou0_B0[OPS_ACC2(-1,0,0)];
6
7       rhou1_B0[OPS_ACC1(0,0,0)] = rhou1_B0[OPS_ACC1(-1,0,0)];
8
9       rhou2_B0[OPS_ACC4(0,0,0)] = rhou2_B0[OPS_ACC4(-1,0,0)];
10
11      rhoE_B0[OPS_ACC0(0,0,0)] = rhoE_B0[OPS_ACC0(-1,0,0)];
12
13      rho_B0[OPS_ACC3(1,0,0)] = rho_B0[OPS_ACC3(-1,0,0)];
14
15      rhou0_B0[OPS_ACC2(1,0,0)] = rhou0_B0[OPS_ACC2(-1,0,0)];
16
17      rhou1_B0[OPS_ACC1(1,0,0)] = rhou1_B0[OPS_ACC1(-1,0,0)];
18
19      rhou2_B0[OPS_ACC4(1,0,0)] = rhou2_B0[OPS_ACC4(-1,0,0)];
20
21      rhoE_B0[OPS_ACC0(1,0,0)] = rhoE_B0[OPS_ACC0(-1,0,0)];
22
```

```
23    rho_B0[OPS_ACC3(2,0,0)] = rho_B0[OPS_ACC3(-1,0,0)];
24
25    rhou0_B0[OPS_ACC2(2,0,0)] = rhou0_B0[OPS_ACC2(-1,0,0)];
26
27    rhou1_B0[OPS_ACC1(2,0,0)] = rhou1_B0[OPS_ACC1(-1,0,0)];
28
29    rhou2_B0[OPS_ACC4(2,0,0)] = rhou2_B0[OPS_ACC4(-1,0,0)];
30
31    rhoE_B0[OPS_ACC0(2,0,0)] = rhoE_B0[OPS_ACC0(-1,0,0)];
32
33    rho_B0[OPS_ACC3(3,0,0)] = rho_B0[OPS_ACC3(-1,0,0)];
34
35    rhou0_B0[OPS_ACC2(3,0,0)] = rhou0_B0[OPS_ACC2(-1,0,0)];
36
37    rhou1_B0[OPS_ACC1(3,0,0)] = rhou1_B0[OPS_ACC1(-1,0,0)];
38
39    rhou2_B0[OPS_ACC4(3,0,0)] = rhou2_B0[OPS_ACC4(-1,0,0)];
40
41    rhoE_B0[OPS_ACC0(3,0,0)] = rhoE_B0[OPS_ACC0(-1,0,0)];
42
43    rho_B0[OPS_ACC3(4,0,0)] = rho_B0[OPS_ACC3(-1,0,0)];
44
45    rhou0_B0[OPS_ACC2(4,0,0)] = rhou0_B0[OPS_ACC2(-1,0,0)];
46
47    rhou1_B0[OPS_ACC1(4,0,0)] = rhou1_B0[OPS_ACC1(-1,0,0)];
48
49    rhou2_B0[OPS_ACC4(4,0,0)] = rhou2_B0[OPS_ACC4(-1,0,0)];
50
51    rhoE_B0[OPS_ACC0(4,0,0)] = rhoE_B0[OPS_ACC0(-1,0,0)];
52
53 }
```

Appendix C

Data Management

Three data files are submitted alongside this document containing data produced over the course of the project (DOI: https://doi.org/10.5258/SOTON/D1770). The file formats are HDF5 and they can be easily accessed with MATLAB, Python, R and other common scientific software. The data is non-dimensionalised by the relevant simulation reference values (see section 3.2). Some larger data files (such as instantaneous flow fields and spectral data) will be kept in storage and can be accessed by contacting the author [1].

Time-averaged flow field data from the shock train cases described in chapters 4 and 5 are contained within the file `shock_train_data.h5`. The data is grouped by test case and for each the following variables are given: x, y, ρ, ρu, ρv, ρw, ρE. All data is averaged in time and in the spanwise direction (for duct cases only the homogeneous core is averaged).

Data from the three boundary layer (shock-less) cases from section 4.1 are stored in the file `boundary_layer_data.h5`. In addition to the variables listed above we include the six unique components of the $\overline{\rho u_i u_j}$ tensor in order to allow for a full reconstruction of the Reynolds stresses.

The centreline and wall time-history data for the step and sinusoidal forcing cases can be found within `time_history_data.h5`. The main flow variables (ρ, ρu, ρv, ρw, ρE) are given as well as 1D arrays of x and t. The datasets are named in the format `[casename]_[wall/centre]`.

[1] alexmgillespie@gmail.com. Bear in mind that not all data will be retained.